Adaptive Observing Synthetic Aperture Radar with Digital Beamforming

Zur Erlangung des akademischen Grades einer

DOKTORIN DER INGENIEURWISSENSCHAFTEN (Dr.-Ing.)

von der KIT-Fakultät für
Elektrotechnik und Informationstechnik
des Karlsruher Instituts für Technologie (KIT)

angenommene

DISSERTATION

von

M.Sc. Fairouz Stambouli
geb. in Tunis

Tag der mündlichen Prüfung: 25.10.2024

Hauptreferent: Prof. Dr.-Ing. Marwan Younis
Korreferent: Prof. Dr. Koen Mouthaan

To my mother, my unwavering pillar of strength and love,
and in loving memory of my father, whose wisdom and dreams live on within me.

Acknowledgements

This dissertation marks the culmination of years of learning, research, and growth, and I am deeply grateful to everyone who has accompanied me on this path and contributed to the accomplishment of this work. It was developed during my time as a research scientist at the Microwaves and Radar Institute at the German Aerospace Center (DLR) in Oberpfaffenhofen.

First and foremost, I would like to express my deepest gratitude and most sincere thanks to my doctoral advisor, Prof. Dr.-Ing. Marwan Younis. His exceptional guidance and mentorship have been invaluable throughout this journey. With his encouragement, trust, and insightful feedback on my work, I learned how to navigate challenges, think, and grow as a researcher.

I would also like to extend my deep appreciation and gratitude to my supervisors, Markus Limbach and Dr.-Ing. Tobias Rommel. Their invaluable expertise, support, and long brainstorming discussions helped shape my research questions and develop new ideas and techniques. They always guided me through challenges and encouraged me to give my best at every step. I couldn't have asked for better support on this journey.

I am equally grateful to Prof. Dr.-Ing. habil. Alberto Moreira for his continuous support and motivating spirit. Our regular status meetings were invaluable, filled with insightful discussions, new ideas, and thoughtful feedback that helped me refine my work. I feel truly honored and fortunate to have had the opportunity to learn from his expertise and work under his leadership.

My special thanks and appreciation go to my co-advisor, Dr. Koen Mouthaan, for his insightful questions, constructive feedback, and invaluable advice on my research and dissertation. I would also like to extend my deep appreciation to all my examination committee members, Prof. Dr.-Ing. Eric Sax, Prof. Dr. Dr. h.c. Dipl.-Phys. Manfred Thumm, Prof. Dr. Ivan Peric, and Prof. Dr.-Ing. Dr.h.c. Dr.-Ing. E.h. mult. Werner Wiesbeck for their support, valuable feedback, and guidance throughout the examination process.

I also extend my sincere thanks to my former department head, Dr.-Ing. Andreas Reigber, whose vast expertise and support were instrumental throughout my doctoral journey. Furthermore, I am also truly grateful to all my colleagues for always being supportive. I am especially thankful to Dr.-Ing. Stefan Valentin Baumgartner, Dr.-Ing. Matthias Jirousek, Dr.-Ing. André Barros Cardoso da Silva, Marc

Jäger, and Dr.-Ing Sushil Kumar Joshi for their constructive feedback and technical support. Their insights and help, particularly in assessing the practical feasibility of my ideas, were invaluable throughout my research. A special thanks goes also to Diego Lorente Catalan, Bernd Gabler, Alicja Schreiber, and Michael Pircher for their valuable discussions and for contributing to a positive and enjoyable group atmosphere. It was an absolute pleasure working with everyone in such a professional yet friendly environment. I will always remember the fun time we spent together. I also would like to extend my heartfelt thanks to Sandra Hillegeist, Petra Deutinger, Sibylle Radzuweit, and Barbara Gülzow for their support and encouragement. Their invaluable assistance with the administrative work throughout my doctoral journey made everything smoother and more manageable.

Last but not least, I express my warm gratitude to my lovely mother, my unwavering source of strength and inspiration. Her belief in my dreams and constant encouragement to keep reaching higher have shaped me into the person I am today. Her support and love have been the foundation of my journey, always pushing me to become the best version of myself. I want to thank my sister for being a constant source of encouragement, and always reminding me to believe in myself. I'm also deeply thankful to my significant other for his unwavering love and support throughout this journey, and to all my close friends who always knew when to pull me out of my research bubble. I can never adequately express my sincere gratitude for their steadfast support through all the ups and downs during these years. Finally, I dedicate this work to the memory of my father, whose belief in me still gives me strength and encouragement every step of the way. Though he is no longer here, his guidance and love have always been by my side.

Oberpfaffenhofen, November 2024
Fairouz Stambouli

Zusammenfassung

Die Beliebtheit von abbildenden Erdbeobachtungsradaren und die Vielfalt ihrer Anwendungen haben in den letzten Jahrzehnten erheblich zugenommen. Luft- und weltraumgestützte Radarsysteme mit synthetischer Apertur (SAR) sind leistungsstarke bildgebende Sensoren, die in der Lage sind, verschiedene Erdphänomene bei Tag und Nacht, unabhängig von den Wetterbedingungen, zu überwachen. Der weltweit steigende Bedarf an Umwelt-, Krisen- und Sicherheitsüberwachung hat die Entwicklung innovativer SAR-Konzepte und Datenverarbeitungstechniken vorangetrieben. Ein großer Erfassungsbereich mit einer feinen Auflösung ist jedoch typischerweise erwünscht, was ein enormes Datenvolumen und hochkomplexe Verarbeitungstechniken zu Folge hat. Daher ist eine hohe Downlink-Kapazität erforderlich, und die Datenverarbeitung sowie Informationsgewinnung sind üblicherweise am Boden durchgeführt. Die schnelle Beschaffung der erforderlichen Informationen stellt eine große Herausforderung für moderne SAR-Systeme, insbesondere für nutzergesteuerte Anwendungen, die eine Überwachung und Identifizierung in nahezu Echtzeit erfordern. Darüber hinaus sind alle Beobachtungsgebiete mit einer festen Konfiguration für jeden Betriebsmodus abgebildet, unter Einsatz eines offenen Regelkreises, der ohne szenenabhängiges Feedback operiert. Die Datenerfassung und -auswertung erfordert menschliche Aufsicht, was die erforderliche Flexibilität für schnell entwickelnden Umgebungen deutlich einschränkt.

Um diese Herausforderungen zu beseitigen, stellt die vorliegende Doktorarbeit ein innovatives SAR-Konzept namens ADaptive OBserving SAR (ADOB-SAR) vor. Das vorgeschlagene Konzept hat das Ziel, SAR in einen intelligenten Sensor umzuwandeln, der eine zielgerichtete und selektive Datenerfassung ermöglicht. Es operiert gleichzeitig in zwei Bildgebungsmodi, die von demselben Radarinstrument gesteuert werden, um einen geschlossenen Regelkreis mit der Umgebung zu schaffen. Die gesamte Szene wird zunächst grob mit niedriger Auflösung und minimalem Leistungs- sowie Ressourcenverbrauch analysiert. Der Sensor passt dann autonom die Beleuchtung in Echtzeit an, um spezifische Gebiete von Interesse mit höherer und optimaler Genauigkeit zu überwachen. Die Integration dieses Systems auf einer Höhenplattform (eng. HAP) wird eine neue Ära intelligenter Sensoren ermöglichen, die durch wissensgestützte Steuerung, eine kontinuierliche Überwachung interessanter Bereiche bieten. Bei dem adaptiven Beobachtungsverfahren werden ausschließlich relevante Gebiete erfasst und gespeichert, was das Downlink-Datenvolumen signifikant reduziert. Zur Aufrechterhaltung dieses

adaptiven Mehrmodusbetriebs, wird eine rekonfigurierbare mehrkanalige phasengesteuerte Gruppenantenne entworfen, Sie bietet digitale Strahlformung (eng. DBF) und agile zweidimensionale Schwenkung sowohl beim Senden als auch beim Empfangen. Dabei werden neuartige Hardware-Techniken konzipiert, die es ermöglichen, diese DBF-Verfahren bei minimaler Komplexität des Antennenarrays zu nutzen und mehrere gleichzeitige Sendestrahlen zur Verfolgung mehrerer Ziele zu erzeugen. Das entworfene Instrument kann die SAR-Parametern während des gleichen Fluges einstellen und von Puls zu Puls zwischen den Modi umschalten. Es wendet zeit- und raumorthogonale Techniken sowie Wellenform- und Frequenzdiversität an, um Sende-/Empfangs- sowie gegenseitige Empfangsinterferenzen zwischen allen gleichzeitig aktiven Modi zu vermeiden. Ein adaptiver Scheduling-Algorithmus wird hergeleitet, der unter Berücksichtigung der Gesamtdynamik des Szenarios und die gesamte abwechselnd Operation, den optimalen Zeitpunkt für die Übertragung neuer Pulse und den Empfang ihrer Rückerechos wählt. Dieser Algorithmus entscheidet sich auch automatisch für die am besten geeignete Orthogonalitätstechnik für jedes Szenario aus. Ein adaptives Entscheidungsmodell wird hergeleitet, um die optimale Kombination aus Instrumentenkonfiguration und -parametern zu bestimmen. Es adaptiert die Performanz und minimiert die Ressourcen anhand der extrahierten Szeneneigenschaften und Nutzeranforderungen. Es basiert auf einer dynamischen Optimierungsfunktion, die ihre Rahmenbedingungen entsprechend dem Szenario anpassen kann. Dabei werden adaptive zielgerichtete Modelle zur Strahl- und Zeitzuweisung sowie variable Prioritätseinstellungen für verschiedenen Optimierungsziele entworfen.

Im Rahmen dieser Arbeit wurde ein Referenzsystem für ein HAP unter Berücksichtigung eines maritimen Szenarios entworfen. Zudem wurde ein Simulator entwickelt, um das ADOB-SAR-Konzept zu validieren und dessen dynamische Entscheidungs- und Scheduling-Algorithmen zu verifizieren. Die Ergebnisse zeigen, dass der vorgeschlagene Sensor eine erhebliche Datenreduktion und effiziente Nutzung der Radarressourcen erreicht, was insbesondere den Energieverbrauch deutlich senkt. Die abgeleiteten Algorithmen zur Anpassung der Instrumentenparameter und zur Planung der Pulse sind für verschiedene Anwendungen geeignet und können an Bord eingesetzt werden, da sie die zusätzliche Rechenkomplexität verwalten und somit die Anforderungen nahezu Echtzeit-fähiger benutzergesteuerter SAR-Anwendungen erfüllen.

Abstract

The popularity of Earth Observation imaging radars and the diversity of their applications have been growing tremendously over the past few decades. Airborne and spaceborne Synthetic Aperture Radars (SAR) are powerful imaging sensors capable of monitoring various Earth phenomena day and night, regardless of weather conditions. The increasing global need for environmental and crisis monitoring and security surveillance has driven the advancement of innovative SAR concepts and data processing techniques. A wide coverage at a fine resolution is typically desired, which implies a huge data volume and highly complex processing techniques. Therefore, a high downlink capacity is required, and data processing and information extraction are typically conducted on the ground. Getting the necessary information quickly is a major challenge for state-of-the-art SAR systems, particularly for user-driven applications requiring near real-time monitoring and identification. Furthermore, all observed areas are imaged with a fixed configuration for each operating mode, employing an open loop system without scene-dependent feedback. The data acquisition and evaluation process relies on human oversight, which limits the flexibility typically required for evolving environments.

To tackle these challenges, this doctoral thesis introduces an innovative concept named ADaptive OBserving Synthetic Aperture Radar (ADOB-SAR). The proposed concept aims to transform SAR into an intelligent sensor capable of performing targeted and selective data acquisition. It operates in two concurrent imaging modes managed by the same radar instrument to create a closed loop with the environment. The overall scene is broadly analyzed at low resolution and minimal performance and resource consumption. The sensor then autonomously adapts the illumination on the fly to monitor specific areas of interest with higher optimum accuracy. Integrating this system on a High-Altitude Platform (HAP) will facilitate a new era of smart sensors, providing persistent monitoring over regions of interest via knowledge-aided control. With the adaptive observing approach, only the relevant spots are imaged and saved, thus reducing the downlinked data volume. To cope with this adaptive multi-mode operation, a reconfigurable multi-channel phased array antenna architecture is designed. It features Digital Beamforming (DBF) and two-dimensional agile beam steering on transmit and receive. Novel hardware techniques are designed to enable the use of these DBF techniques with minimal antenna array complexity and to generate multiple simultaneous transmit beams to track multiple targets. The instrument can adjust the SAR parameters during flight and switch between modes using pulse-to-pulse interleaving. It utilizes temporal and

angular orthogonality techniques, as well as waveform and frequency diversity to avoid transmit/receive and mutual receive interference across all concurrent modes. An adaptive scheduling algorithm is derived, which selects the optimal timing for transmitting new mode pulses and receiving their return echoes, considering the overall interleaved multi-target operation. This algorithm also automatically selects the most suitable orthogonality technique for each scenario. An adaptive decision-making model is implemented to determine the optimal combination of instrument configuration and parameters, adjusting system performance and minimizing resources based on extracted scene properties and user requirements. It is based on a dynamic optimization function capable of changing its framework in response to the observed scenario using adaptive target-specific beam and time allocation models, along with variable multi-objective priority settings.

A reference system for a HAP was designed considering a maritime scenario, and a simulator was developed in the framework of this thesis to validate the ADOB-SAR concept and verify its dynamic decision-making and scheduling algorithms. The results show that the proposed sensor achieves a huge data reduction and efficient use of radar resources, notably lowering power consumption. The algorithms derived to adapt the instrument parameters and schedule the pulses can be applied to any application and operate onboard, while managing the additional computational complexity, and effectively meeting the demands of near real-time user-driven SAR applications.

Contents

Acknowledgements iii

Zusammenfassung v

Abstract vii

Acronyms and Symbols xiii

1 Introduction 1

1.1 State-of-the-Art Imaging Radars 1
1.2 Toward Cognitive Radars 4
1.3 Objectives and Scope of the Work 6
1.4 Structure of the Thesis 8

2 Fundamentals of Multi-Channel SAR and Beamforming 11

2.1 SAR Principles 11
2.1.1 Geometry and Synthetic Aperture Formation 11
2.1.2 Pulse Compression 13
2.1.3 Doppler Basics 14
2.1.4 Backscattering Mechanism 16
2.1.5 Image Formation 17
2.1.6 Data Rate 18
2.2 Phased Array and Beamforming Principles 19
2.2.1 Introduction to Phased Arrays 19
2.2.2 Antenna Pattern of a Planar Phased Array 19
2.2.3 Antenna Pattern of a Linear Phased Array 21
2.2.4 Element Spacing and Grating Lobes 25
2.2.5 Digital Beamforming (DBF) 26
2.2.6 Sub-Aperture Formation 30
2.2.7 Tapering and Reduction of Sidelobes 31
2.2.8 Noise Figure 32
2.3 SAR-GMTI Principles 32
2.3.1 SAR-Based Moving Target Detection 33

2.3.2 Sea Clutter Influence on Detection . . . 36
2.3.3 GMTI Performance Metrics . . . 37

3 Adaptive Observing SAR Concept . . . 41
3.1 Operation Concept . . . 41
3.1.1 User-Driven SAR Application . . . 41
3.1.2 Platform Considerations . . . 42
3.1.3 Adaptive Observing SAR Principle . . . 44
3.2 Mode Concept . . . 46
3.2.1 Operational Modes . . . 46
3.2.2 Mode Rational: from Uncertainty to Certainty . . . 49
3.2.3 Multi-Mode Timing Principle . . . 50
3.3 System Concept . . . 51
3.4 ADOB-SAR Concept Summary . . . 52

4 Reconfigurable Multi-Mode SAR System Design . . . 53
4.1 MapSearch Mode Imaging Technique . . . 53
4.1.1 MapSearch Detection Technique . . . 56
4.1.2 SCORE Imaging Technique . . . 57
4.2 MapSearch Instrument Design . . . 59
4.2.1 Azimuth Front-End Architecture . . . 59
4.2.2 Elevation Front-End Architecture . . . 62
4.3 MapSearch Antenna Configuration . . . 62
4.3.1 Azimuth Squint Angle . . . 63
4.3.2 Azimuth Antenna Parameters . . . 67
4.3.3 Staggered Array Configuration . . . 69
4.3.4 Elevation Transmit Beam Broadening . . . 72
4.3.5 Elevation SCORE Hybrid Beamforming . . . 79
4.3.6 MapSearch Antenna Gain . . . 87
4.4 Tracking Imaging Techniques . . . 87
4.4.1 Follow Spot SAR . . . 89
4.4.2 Circular Trajectory SAR . . . 92
4.5 Tracking Antenna Configuration . . . 94
4.5.1 Elevation Antenna Parameters . . . 94
4.5.2 Azimuth Antenna Parameters . . . 96
4.6 Tracking Mode Instrument Design . . . 96
4.6.1 Multi-Beam Transmit Configuration . . . 96
4.6.2 Elevation Receive Configuration . . . 100
4.6.3 Azimuth Receive Configuration . . . 101
4.6.4 Tracking Antenna Gain . . . 102

5 Multi-Mode SAR: Signal Space Orthogonality 105
5.1 MapSearch Mode Timing 105
5.1.1 Transmit and Receive Timing 106
5.1.2 SCORE Timing 108
5.1.3 Pulse Repetition Frequency Timing Considerations 109
5.1.4 MapSearch Burst Mode with Alternating PRF 112
5.1.5 Scenario-Based Adaptation of MapSearch PRF 113
5.1.6 MapSearch Burst Mode with Alternating Frequency 115
5.2 Interleaved Tracking Mode Timing 117
5.2.1 Transmit and Receive Timing 117
5.2.2 Interleaved Multi-Mode PRF Condition 121
5.2.3 Tracking Mode Transmit Timing Strategy 122
5.2.4 Adaptive Tracking Scheduling Algorithm 125
5.3 Suppression of Tracking Echo Overlapping with Multi-Mode Transmit Pulses 129
5.4 Temporal Orthogonality of Interleaved Multi-Mode Echoes 130
5.5 Angular Orthogonality of Multi-Mode Temporal Overlapped Echoes 135
5.5.1 Angular Diversity of Overlapped Echoes via DBF 135
5.5.2 SCORE Angular Orthogonality 137
5.6 Multi-Mode Frequency Orthogonality 140
5.7 Multi-Mode Waveform Diversity 143
5.8 Multi-Mode Interleaving Simulation 145

6 Adaptive Observing SAR Decision-Making 147
6.1 Smart Control Decision Rules 147
6.1.1 Adaptive Spatial Resolution Control 148
6.1.2 Adaptive Energy Control 152
6.2 Adaptive Forcing Models 157
6.2.1 Multi-Target Single-Beam Model 159
6.2.2 Time Assignment Model 160
6.2.3 Multi-Target Multi-Beam Model 168
6.2.4 Target Assignment Examples 172
6.3 Beamforming Execution 174
6.4 Dynamic ADOB-SAR Optimization Model 176
6.4.1 Input and Output Vectors 176
6.4.2 Adaptive Multi-Objective Function 177
6.4.3 Dynamic Optimization Framework 179
6.4.4 Examples of Adaptive Priority Weighting and Ideal Parameter Vectors 182

7 Adaptive Observing SAR Reference System and Simulation . 187
7.1 Reference System Design 187
7.1.1 Performance Requirements 187
7.1.2 Designed Antenna System 189
7.1.3 SAR Instrument Parameters 193
7.2 DECISION Simulator 199
7.3 Simulated Experiment 201
7.3.1 MapSearch Target Scenario 201
7.3.2 Dynamic Tracking Optimization and Scheduling 202

8 Conclusions and Outlook 213

Bibliography 217

A ADOB-SAR Optimization Objective Function 237

Acronyms and Symbols

Constants

π	Pi (ratio of circle's circumference to its diameter)	3.14159265359
c_0	speed of light in vacuum	2.99792458×10^8 m/s
K	Boltzmann constant	$1.380\,649 \times 10^{-23}$ J/K
j	imaginary unit	$\mathrm{j} = \sqrt{-1}$

Mathematical Notations and Symbols

$\approx$	approximately equal
$\in$	element of
$\notin$	not element of
$\subset$	subset of
$\not\subset$	not subset of
$\mathbb{Z}$	set of integer numbers
$\forall$	for all
$\lvert a \rvert$	absolute value of complex quantity a
$\otimes$	convolution
a^*	complex conjugate of complex quantity a
$a^\star$	ideal value of a in optimization
$\mathbf{a}$	vector nomenclature
$\mathbf{A}$	matrix nomenclature
$\sum_k a_k$	sum versus the summands a_k
∂	partial derivative
$\arg\min$	argument of the minimum
$\arg\max$	argument of the maximum
$\exp\{\cdot\}$	exponential function
$\log_{10}\{\cdot\}$	base 10 logarithm
$\overline{a}$	average value of a
$\mathrm{erfc}(\cdot)$	complementary error function

Acronyms

1-D	One-Dimensional
2-D	Two-Dimensional
3-D	Three-Dimensional
ABF	Analog Beam Forming
A/D	Analog / Digital
ADC	Analog-to-Digital Converter
ADOB	ADaptive OBserving
AI	Artificial Intelligence
AIS	Automatic Identification System
ATI	Along-Track Interferometry
BAQ	Block-Adaptive Quantization
CFAR	Constant False Alarm Rat
CNR	Clutter-to-Noise Ratio
CPI	Coherent Processing Interval
CR	Cognitive Radar
DAC	Digital-to-Analog Converter
dB	Decibel
DECISION	Dynamic Evaluation and Control of Instrument Scheduling and Interleaved OptimizatioN
DBF	Digital Beam-Forming
DoA	Direction of Arrival
DR	Data Rate
DPCA	Displaced Phase Center Antenna
DLR	Deutsches Zentrum für Luft- und Raumfahrt
DSP	Digital Signal Processing
FFT	Fast Fourier Transform
FNBW	First Null Beam Width
HAP	High Altitude Platform
HAPS	High Altitude Pseudo-Satellite
HBF	Hybrid Beam Forming
HH	Horizontal transmit, Horizontal receive (polarisation)
HPA	High Power Amplifier
HPBW	Half Power Beam-Width
HRWS	High-Resolution Wide-Swath
IFFT	Inverse Fast Fourier Transform
GaN	Gallium nitride
GL	Grating Lobe
GMTI	Ground Moving Target Indication
KA	Knowledge-Aided

LMS	Least-Mean-Square
LNA	Low Noise Amplifier
MDV	Minimum Detectable Velocity
ML	Machine Learning
MMIC	Monolithic Microwave Integrated Circuit
MMTI	Maritime Moving Target Indication
NESZ	Noise Equivalent Sigma Zero
NF	Noise Figure
PDF	Probability Density Function
PRF	Pulse Repetition Frequency
PRI	Pulse Repetition Interval
Radar	RAdio Detection And Ranging
RCS	Radar Cross Section
RCM	Range Cell Migration
RDA	Range Doppler Algorithm
RC	Range-Compressed
RF	Radio Frequency
ROC	Receiver Operating Characteristic
Rx	Receive
SAR	Synthetic Aperture Radar
SCNR	Signal-to-Clutter-plus-Noise Ratio
SCORE	SCan On REceive
SCR	Signal-to-Clutter Ratio
SINR	Signal-to-Interference-plus-Noise Ratio
SNR	Signal-to-Noise Ratio
SLAR	Side-Looking Airborne Radar
SLR	SideLobe Ratio
STAP	Space-Time Adaptive Processing
TRC	Transmit/Receive Core
TRM	Transmit/Receive Module
Tx	Transmit
ULA	Uniform Linear Array
VV	Vertical transmit, Vertical receive (polarization)

Lower Case Letters

c_0	velocity of light
d	spacing or distance
d_c	duty cycle
d_e	antenna element spacing in elevation
d_ill	illumination distance

d_{sa}	subarray spacing in azimuth
$d_{\mathrm{sub,a}}$	receive sub-aperture spacing in azimuth
$d_{\mathrm{sub,e}}$	receive sub-aperture spacing in elevation
f_{a}	instantaneous frequency
f_{c}	center (carrier) frequency
f_{res}	resolution control function
f_{energy}	energy control function
f_{D}	Doppler frequency
h_{r}	reference signal in time domain
i	step index
k	target index
n	Tracking pulse index
n_{op}	number of modes in operation
m	MapSearch pulse index
o_{v}	echo overlapping factor
p	number of modes within the interval T_{int}
p_{GL}	grating lobe order
r_{up}	received up-chirp signal
r_{down}	received down-chirp signal
s_{a}	azimuth subarray size
s_{up}	up-chirp signal
s_{down}	down-chirp signal
s_{R}	received signal
s_{T}	transmitted chirp signal
t	time
t_0	transmit time of the first pulse
$t_{\mathrm{rs}}^{\mathrm{M}}$	MapSearch echo start time
$t_{\mathrm{re}}^{\mathrm{M}}$	MapSearch echo end time
$t_{\mathrm{rs}}^{\mathrm{T}j}$	Echo start time of Tracking tier j
$t_{\mathrm{re}}^{\mathrm{T}j}$	Echo end time of Tracking tier j
u_{rc}	range compressed receive signal
v_{blind}	blind velocity
v_{p}	platform velocity
v_{tg}	target ground velocity
$v_{\mathrm{t}x}$	target along-track velocity
$v_{\mathrm{t}y}$	target across-track velocity
$\mathbf{w}$	antenna complex weighting vector
w_n	complex weight of antenna element n
x	position
u_{rc}	matched filter output

Capital Letters

A_t	antenna area
A_n	amplitude excitation of antenna element n
A_f	beam footprint size
AF	array factor
B	bandwidth
B_D	Doppler bandwidth
B_Dc	clutter Doppler bandwidth
B_Dt	target Doppler bandwidth
B_sys	total system bandwidth
C	antenna pattern
C_e	antenna element pattern
C_array	total antenna array pattern
D_h	antenna height
D_l	antenna length
DR	data rate
F	noise figure
H	platform altitude
H_r	range reference signal in frequency domain
H_a	azimuth reference signal in frequency domain
G	antenna gain
G_e	gain of a single antenna element
$\mathcal{K}$	chirp rate
L	losses
L_t	target length
L_sa	synthetic aperture length
M_p	number of time spots
N	number of antenna elements
$N_\mathrm{sub,e}$	number of receive sub-apertures in elevation
N_sa	number of transmit subarrays in azimuth
$N_\mathrm{sub,a}$	number of receive sub-apertures in azimuth
N_b	number of bits per sample
N_p	number of pulses
N_px	number of pixels
N_s	number of received samples per pulse
N_shifter	number of phase shifters
N_t	number of targets
N_wait	number of Tracking tiers on hold
N_txch	number of transmit beams
N_ch	total number of digital channels
P_avg	average power

P_{d}	probability of detection
P_{fa}	probability of false alarm rate
P_{t}	peak power
P_{tv}	peak power variation factor
$\mathrm{PRI}^{\mathrm{M}}$	MapSearch pulse repetition interval
$\mathrm{PRI}^{\mathrm{T}}$	Tracking pulse repetition interval
R	slant range
R_0	slant range of the center beam
R_{near}	near slant range
R_{far}	far slant range
R_{max}	maximum slant range considering the squint
R_{min}	minimum slant range considering the squint
$\mathcal{R}_{\mathrm{f}}$	frequency range
R_{RCM}	range variation due to RCM
S_{echo}	echo span
T_{CPI}	CPI time duration
T_{dwell}	SAR dwell time
T_{echo}	echo duration
T_{free}	free time margin
T_{ill}	illumination/dwell time of the synthetic aperture
T_{int}	time interval of distinct MapSearch and Tracking events
T_{proCPI}	detection processing time of one CPI
T_{s}	receiver noise temperature
T_{td}	time delay between the last MapSearch echo and the start of the Tracking mode
T_{trans}	transition time between detection and activation of the Tracking
T_{tr}	dwell time of the Tracking mode
$\mathcal{T}_{\mathrm{idle}}$	idle time interval
$\mathcal{T}_{\mathrm{t}}$	transmit pulse time interval
$\mathcal{T}_{\mathrm{r}}$	receive echo time interval
W_{g}	swath width
W_{t}	target width
W	priority weighting vector
X_k	vector of SAR adaptive control parameters
$\mathcal{X}_\theta$	pulse extent
Y_k	vector of target properties
$Z^\star$	ideal parameter vector

Greek Symbols

α	antenna cell angle
β	phase excitation
γ_{b}	beam broadening gain loss factor
λ	wavelength
μ_{ant}	antenna efficiency
δ_{a}	azimuth resolution
δ_{a}	range resolution
δ_{D}	Doppler resolution
ϕ	azimuth angle
ϕ_{a}	Tracking azimuth steering angle
ϕ_{GL}	azimuth grating lobe angle
ϕ_{sq}	azimuth squint angle
Φ_{ms}	MapSearch azimuth half power beamwidth
Φ_{tr}	Tracking azimuth half power beamwidth
Φ_{sub}	azimuth subarray half power beamwidth
φ	azimuth phase variation
ψ_{a}	angular field of view in azimuth
τ_{delay}	echo time delay
τ_{g}	guard time
τ_{gap}	time gap between transmit pulses
τ_{p}	pulse duration
θ	elevation angle
θ_0	steering angle
Θ_{2N}	second null elevation beamwidth
θ_{d}	target depression angle
θ_{GL}	elevation grating lobe angle
θ_{gz}	grazing angle
Θ_{w}	swath width illumination beamwidth
θ_{c}	boresight incident looking angle
θ_{e}	steering angle in elevation
θ_{eA}	analog steering angle in elevation
θ_{L}	look angle
θ_{eD}	digital steering angle in elevation
θ_{s}	sub-aperture steering angle
Θ_{scr}	SCORE half power beamwidth in elevation
θ_{tilt}	mechanical antenna tilt angle
σ	reflectivity / radar cross section
σ_0	clutter reflectivity
$\Delta\vartheta$	phase shift
$\Delta\theta$	digital steering switch step

Δ_{ts}	time shift
Δ_{scr}	SCORE time shift
η	efficiency
ω	flight rotation angle
$\chi(\Delta f)$	frequency correlation function

Superscripts and Subscripts

a	azimuth
az	azimuth
b	broadened
cir	circular
D	Doppler
e	elevation
el	elevation
f	footprint
far	far range
FN	first null of the antenna pattern
fs	Follow Spot imaging mode
g	ground
GL	grating lobe
hcir	half circular
i	incident
max	maximum
min	minimum
ms	MapSearch
M	MapSearch mode
near	near range
ov	overlapping
R	receive
rc	range compressed
rs	receive start
rs	receive end
Rx	receive
s	sub-aperture
SA	synthetic aperture
scr	SCORE
sub	subarray or sub-aperture
t	target
te	transmit end
tr	Tracking

$_{\text{tri}}$ triangular lattice
$_{\text{ts}}$ transmit start
$_{\text{T}j}$ Tracking tier j
$_{\text{Tx}}$ transmit

1 Introduction

Radars have revolutionized the way humans perceive and interact with the environment through applications ranging from enhancing security to advancing meteorological and geoscience research. The essence of radar technology is embedded in its name, RADAR, an acronym for *RAdio Detection And Ranging*, highlighting its main objective of detecting objects and estimating their distance and direction through electromagnetic waves. The evolution of this technology was first driven by the demands of military air and maritime defense during the Second World War. The name was adopted by the United States Navy for the first time in 1940 [1]. However, the first idea that led to the concept of radar dates back to the late 19th century, specifically the 1880s, when Heinrich Hertz discovered that metallic and dielectric objects can reflect electromagnetic waves [2]. Christian Hülsmeyer was the first to demonstrate the radar mechanism in 1904 through his invention called the *Telemobilescope*, intended for the detection of ships in the Rhein river [3]. Between then and today many land and sea-based radars have been developed, expanding beyond their initial military applications to serve various civilian purposes, including air and land traffic control, weather forecasting, maritime navigation, and geological surveying [4–6]. The development of compact radar systems has increased mobility and versatility, thus enhancing efficiency and accuracy across diverse platforms. The radar system was and still is an exciting concept. Unlike optical sensors it can operate during both day and night times using its own illumination source, further, it offers a wide range of weather-independent observation capabilities that can advance environmental monitoring and disaster response, greatly aiding in the protection and sustainability of communities worldwide.

1.1 State-of-the-Art Imaging Radars

Radar technology has evolved significantly since its inception. Early systems processed the radar echo signals fully in the analog domain using electronic filters and displays. Over the decades, advancements in digital hardware and software have led to a sophisticated 'culture' of radar signal processing. A major leap in this evolution was the introduction of sampling and digitizing [7–10]. This allowed for the implementation of advanced detection techniques. Modern radar systems now feature amplified Radio Frequency (RF) signals that are down-converted, digitized, and processed via software before being displayed.

Initial radar systems, known as Side-Looking Airborne Radars (SLAR), utilized real aperture technology where the range resolution depends on pulse duration and the angular resolution on antenna beamwidth, making high-resolution challenging due to the need for long pulses and large antennas. Transitioning from these constraints, Synthetic Aperture Radar (SAR) emerged in 1954 as a pivotal innovation, addressing these limitations by employing a moving carrier coupled with signal processing to enhance azimuth resolution without physically enlarging the antenna. This invention by Carl Wiley marked a significant leap in radar technology [11]. It takes advantage of the Doppler effect captured in the echo returns at different azimuth positions throughout the flight to achieve a "Doppler beam sharpening" yielding an azimuth resolution which is independent of the distance to the imaged scene. It differs from SLAR by the method of processing the Doppler spectrum of the signal [4]. This opened the doors to the field of imaging radars, leading to the development of promising spatial imaging techniques. Since the launch of the first civil spaceborne SAR sensor, Seasat-A in 1978 [12], tens of satellite SAR missions have been successfully operated. SAR has developed into a powerful sensor used for military and civilian purposes in various applications including Earth observation, military reconnaissance, and even planetary exploration [13].

Nearly all spaceborne SAR systems developed in the last two decades operate in multiple imaging modes (Stripmap, ScanSAR, and Spotlight), including TerraSAR-X, Sentinel-1, and ALOS-2 [14–18]. The traditional SAR imaging modes are illustrated in Figure 1.1. Each mode has a unique mechanism for observing the scene and is distinguished by the technique used for data collection and processing.

- **Stripmap imaging mode:** It is considered the standard SAR acquisition mode. The antenna pattern is pointing toward a fixed direction and does not vary with time over the data take. Data are uniformly collected along the flight path, covering a consistent swath width. To achieve a fine azimuth resolution, the area should be observed for a long time with a wide azimuth beam.
- **ScanSAR imaging mode:** This mode can achieve a wider swath compared to Stripmap mode without necessitating a broader elevation beam. It operates by sequentially switching the antenna beam in elevation during data take to illuminate distinct sub-swaths. This mode, while increasing swath width (coverage), worsens the azimuth resolution due to the shorter illumination time duration for each sub-swath.
- **Spotlight imaging mode:** In this mode, the antenna pattern is steered in azimuth toward a specific patch on the ground throughout the flight to form a larger synthetic aperture. This steering results in an extended observation time over the same area of interest, thereby enhancing the azimuth resolution beyond what is possible with a Stripmap mode; this comes at the cost of imaging single patches instead of a continuous swath.

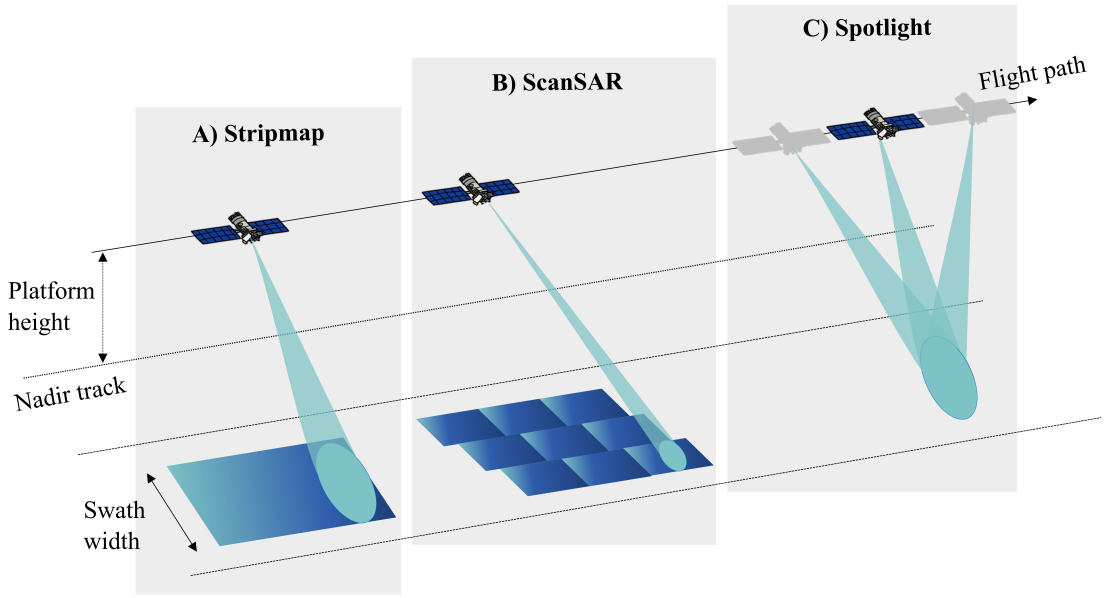

Figure 1.1: Illustration of typical state-of-the-art SAR imaging modes.

It has consistently been a significant challenge for SAR system designers to balance the trade-off between resolution and swath width [19]. The operating modes are designed to either enhance resolution or increase coverage, but not both at the same time. Besides, these modes are not operated simultaneously but are selectively activated during specific acquisition periods, limiting the system's multi-functionality.

Increasing user demand for a global interpretation of the different Earth phenomena with high resolution and large coverage has driven the development of innovative SAR concepts and data processing techniques. The advent of fast analog-to-digital converters and more powerful computers enabled the shift of digitization closer to the antenna, making use of the full potential of digital signal processing in the time and space domain and enhancing radar capabilities. Digital Beamforming (DBF) on receive has been a catalyst in the evolution of SAR technology, opening new horizons for the development of advanced and innovative imaging techniques achieving both high resolution and wide coverage [20–26]. The ability to capture digitized beams independently has inspired the research community to develop efficient post-processing algorithms. These address many acquisition challenges, including ambiguity suppression and interference mitigation [27–30]. Another promising technique, known as SCan-On-REceive (SCORE), significantly enhances the Signal-to-Noise Ratio (SNR) by dynamically forming a narrow antenna beam on receive and digitally steering it to follow the echo returns across a wide swath [21, 31].

Despite the advancement of many innovative imaging techniques based on DBF and bi-static configuration, SAR is still limited in flexibility. SAR hardware parameters are typically fixed during the design stage and cannot be updated during the opera-

tion. Besides, state-of-the-art SAR sensors operate on an open-loop system without feedback, i.e., the observed areas are imaged with fixed configurations, which are, in the best case, based on a priori knowledge about the scene during mission planning. If the scene is different from what is expected, the interpretation of the acquired data becomes challenging. User-driven applications, such as surveillance, crisis response, and disaster monitoring, require near real-time observation of specific areas to accelerate the decision-making process. They typically require high-resolution information of distinct objects within a large area. However, current sensors inefficiently attempt to cover a large area with fine resolution, resulting in excessive data and overhead. Therefore, they still cannot cope with real-time monitoring and prevent system adaptation to varying mission requirements and environmental conditions. Besides, they are mostly operated by a human under predefined fixed modes. For urgent monitoring requests of particular regions, users face a long waiting time to acquire the data, process it, and interpret it. This is considered an inefficient use of time and resources by imaging areas that are not interesting for a specific user-driven application.

1.2 Toward Cognitive Radars

There has been an increasing demand to transform the classical radar into an adaptive system that better manages resources and limits the amount of information to what is essential to the user. The desire to automate the radar operation shed light on many innovative techniques, which are widely used in modern radar systems today. The radar community has been trying to implement adaptivity for various radar concepts since the 1960s, with the Constant False Alarm Rate (CFAR) algorithm being one of the earliest examples. This technique adapts the detection threshold depending on the spatial and temporal variations in noise and clutter for a consistent false alarm probability [32, 33]. Many adaptive benchmarks were developed for detection and tracking, including adaptive processors to maximize the probability of detection [34] and achieve multi-target track maintenance [35]. Additionally, adaptive array antennas have emerged as a promising solution to mitigate the impact of jamming and interference using, for example, the Least-Mean-Squares (LMS) algorithm [34, 36, 37]. The antenna array weights are adapted in a time-varying environment to maximize the Signal to Noise Ratio (SNR) by reducing the sidelobe level or forming antenna pattern nulls [38]. Adaptive clutter suppression approaches have also been extensively studied, which led to the Space-Time Adaptive Processing (STAP) based on multiple digital channels [39–42]. A remarkable form of SAR adaptivity was introduced by an antenna array capable of performing null-steering in the elevation direction where range ambiguities occur [43].

These concepts have led to the development of numerous adaptive SAR image processing techniques [44–47], resulting in a significant increase in performance. How-

ever, they are mostly applied on the receiver, thus neglecting to adapt the illumination from the transmitter. This approach is not optimal as the transmitted energy is not tailored to the scene or the desired information, leading to a waste of resources. The adaptive techniques are typically applied a posteriori during processing, which causes a high data overhead and prevents the optimization of instrument resources. Therefore, the degree of adaptivity remains limited considering the dynamic nature of the observed environment. The subsequent stage involves adapting the transmitted signal and transforming the radar into an intelligent system capable of reacting to changes in the scene, particularly in fast-changing scenarios.

Simon Haykin introduced the concept of a fully adaptive radar, also known as Cognitive Radar (CR), for the first time in the 90s [48–51]. It is based on a perception-action cycle, illustrated in Figure 1.2, featuring a feedback loop with the observed environment, thereby imitating human perception. The radar system can thus in-

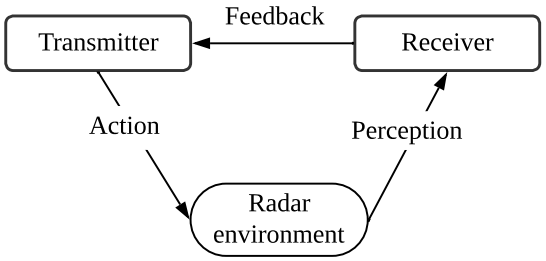

Figure 1.2: Block diagram of a cognitive radar featuring the perception-action cycle.

teract with the environment, extract relevant information, and use it to adapt its configuration for the next transmission. Applying this innovative concept, many ideas based on optimal waveform selection emerged in the last decades [52–56]. They are based on optimizing the radar waveform and maximizing performance in terms of modulation type, such as linear/non-linear frequency modulation or phase coding, as well as waveform parameters like bandwidth and operating frequency. Knowledge-aided signal processing was also considered a milestone in the concept of a fully adaptive radar. It is capable of using a priori knowledge about the surrounding environment to achieve a better performance [57]. It has also been applied to enhance target identification using embedded information sources like geospatial databases (e.g., road networks and location of strong clutter) [58]. An extended form of the Space-Time Adaptive Processing (STAP) concept called KA-STAP (Knowledge-Aided STAP) was developed, which relies on prior knowledge of the clutter environment to perform intelligent training methods and adaptive filtering [59, 60].

So far, there have only been a few implementations of the cognitive concept in SAR systems. In [61], SAR imaging with adaptive spatial resolution was applied based on the physical distance between two targets. However, many challenges still need to be addressed especially the real-time control of the operation mode, the hardware requirements and limitations, and the timing capability to adjust the transmitter on the fly. The overall SAR system and operation have not yet been addressed in terms of the hardware, modes, and task management.

1.3 Objectives and Scope of the Work

This thesis introduces a novel concept that transforms the existing state-of-the-art SAR system into intelligent and selective sensors. The designed system is named *ADaptive OBserving Synthetic Aperture Radar* (ADOB-SAR) and, in some ways, mimics human visual cognition by applying the most effective approach to observe specific areas. The sensor can automatically reconfigure itself on the fly to match the illumination to the scene properties by utilizing feedback from the environment gathered through acquired sensor data, utilized as a priori knowledge. It interacts with the environment to autonomously select the areas of high interest according to the user requirements and adapts its configuration on the fly. This is accomplished by interleaving multiple modes with different functionalities. Adaptive control of the SAR operation mode requires on-board processing because the delay and complexity involved in transferring massive amounts of data to the ground for processing, as well as computing a new set of operation parameters and re-transferring them to the platform, are too significant, particularly in dynamic environments. Therefore, a coarse scene analysis is continuously performed to get a quick overview of the surroundings. Then, the sensor decides on the optimal imaging technique and instrument configuration for specific areas of interest. Thus, it becomes feasible to control the different parameters and scanning combinations to reach a high imaging and tracking performance with fewer resources and less data volume compared to the state-of-the-art SAR sensors. The ADOB-SAR significantly reduces the stored and transferred data volume by only downlinking the relevant information from the adaptive mode, while omitting all other acquired data used for the adaptation.

The ADOB-SAR concept is generic and can be applied to airborne and spaceborne platforms. This thesis considers a high-altitude platform (HAP) as the potential platform, which autonomously flies in the stratosphere at approximately 20 km altitude above the Earth's surface. It is also called a high-altitude platform station, high-altitude pseudo satellite, high-altitude platform system, stratospheric platform, and near-space vehicle [62–66]. This platform's wide reach, long monitoring capabilities, and persistence make it a compelling choice for various applications, particularly for Earth observation tasks that require monitoring changing scenarios. The SAR community started giving importance to this platform as a potential candidate for

future missions and multiple concepts have been developed [63–67]. Three types of unmanned aerial vehicles can be utilized as HAP: fixed-wing aircraft, airships, and balloons, as listed in Table 1.1. Two key variables affecting their performance are the vehicle's speed and the flight duration [68–70]. Using such a platform presents

	Balloons	**Fixed-wing aircrafts**	**Airships**
Examples	Google Loon [71]	Zephyr [72] HAP alpha [62] SPL [73] SoftBank Sunglider [74]	Stratobus [75] Sceye [76] Stratosyst SkyRider [77] Ecosat [78]
Payload power	tens of watts	several kW	above 100 kW
Payload weight	tens of kg	≈ 100 kg	several 100 kg
Flight duration	few months	several months	$\approx$ one year
Speed	$0 - 20$ m/s	$20 - 100$ m/s	$0 - 40$ m/s

Table 1.1: Comparison of the different types of high-altitude platforms with the most important parameters.

several challenges, notably the limited payload size, weight, and power [79]. This is where the ADOB-SAR sensor comes into play, minimizing radar resource allocation based on the observation. HAP requires an energy source to reach its operational altitude, maintain forward motion, and power the payload. Due to their limited lifespan, traditional aviation fuels are not practical for use. Although power transmission via microwaves from ground stations to aircraft is an attractive option [80, 81], it remains impractical at present. Hence, HAP still needs to undergo further development to carry the ADOB-SAR payload and supply it with sufficient power. Recent advances in battery and solar panel technology have made solar power the leading candidate among potential energy sources for HAP.

To design such a fully adaptive SAR sensor, many trade-offs and considerations should be addressed. This thesis introduces a new perspective on a multi-mode SAR sensor, emphasizing its reconfigurable hardware design based on beamforming capabilities for both transmission and reception, as well as adaptive parameter control. This included a reconfigurable antenna front-end architecture with agile beam steering capabilities, and a dynamic decision-making processor, which selects the optimal instrument configuration based on acquired a priori knowledge about the scene, decision rules, and user performance requirements. The designed system takes into consideration the timing aspects of the operation and scene properties to obtain the optimal solution for each scenario over time. An adaptive pulse-to-pulse

interleaving strategy is derived, which operates multiple modes concurrently. The design uses different orthogonality techniques to avoid time and space ambiguities through a scheduling algorithm based on all changing timing constraints.

1.4 Structure of the Thesis

The work is divided into eight chapters that showcase the features of the proposed adaptive observing SAR sensor. Chapter 2 begins with the theoretical background necessary for comprehending the designed system and its operation. The SAR basics are first described, followed by the principles of multi-channel phased array antennas and digital beamforming. Ground Moving Target Indication (GMTI) fundamentals are then presented, highlighting the different detection procedures and clutter suppression techniques.

Chapter 3 presents the ADOB-SAR concept. It starts with the operation by describing the potential applications of the proposed sensor, its foreseen platform, and the methodology used to apply the cognitive radar concept to SAR. The mode concept is then introduced, which is based on two modes running concurrently, followed by an overview of the system concept.

Chapter 4 provides a detailed description of the ADOB-SAR instrument. The chapter delves into the design guidelines of a reconfigurable SAR system that is capable of operating multiple modes concurrently with the same antenna front-end and derives the corresponding design equations. It shows how a single compact antenna array can cope with the different requirements of each task by applying hybrid beamforming, which combines analog and digital beamforming. The imaging techniques of each mode are described, including SCORE and a novel mode named *Follow Spot* SAR. The front-end configurations to generate multiple beams on transmit and receive are provided along with a comparison between different beam broadening techniques. A staggered antenna array is examined, which can be utilized to reduce the number of elements.

The timings of the simultaneous modes and their interleaving techniques are detailed in Chapter 5. An intelligent scheduling algorithm is introduced, which selects the optimal time for transmitting pulses of each new adaptive mode while avoiding ambiguities with other concurrent events. Multidimensional space orthogonality techniques, including time, angular, frequency, and waveform orthogonality, are utilized to separate the echoes of different interleaved modes.

Chapter 6 describes the decision-making process for selecting the optimal instrument parameters. Smart decision rules are introduced based on adaptive spatial resolution and energy. Then, it delves into the mathematical derivation of adaptive

forcing models that impose constraints on specific parameters based on the changing scenario and other operating modes. A dynamic optimization model derived by combining all the adaptive models is presented. It is based on an objective function that changes its framework for each new scenario throughout the flight.

Chapter 7 introduces a designed reference system and a simulator to evaluate the performance of the proposed ADOB-SAR system. It showcases the parameter selection by the decision-making algorithm, followed by the resulting performance for each adaptive mode. Their corresponding pulse scheduling is simulated using the derived interleaving strategy. The simulated scenario demonstrates that the proposed sensor achieves data reduction and effective utilization of radar resources, including power consumption and data rate.

Chapter 8 concludes the thesis by discussing future research opportunities to enhance the capabilities of the ADOB-SAR sensor.

2 Fundamentals of Multi-Channel SAR and Beamforming

This chapter navigates through the necessary theoretical fundamentals for comprehending the concept, design, and operation of the adaptive observing synthetic aperture; the core of this thesis. It traces the evolution of key SAR basics and their system requirements that have paved the way for the current research. The first Section 2.1 explores radar fundamentals, focusing on synthetic aperture formation and the main components of imaging. Then, in Section 2.2, the antenna configurations and beamforming techniques typically used for SAR are presented, shedding light on phased arrays, which are considered the most promising antennas for modern radar systems. Section 2.3 explores the fundamental detection principles and performance requirements for a Ground Moving Target Indication (GMTI) system.

2.1 SAR Principles

The radar is an electromagnetic sensor that detects and locates targets. It accurately measures target information by transmitting electromagnetic energy and receiving the reflected signal. The term "target" broadly refers to any object or entity that is subject to detection. SAR applies these radar principles in a sophisticated way, leveraging its moving platform to generate detailed images of targets from the reflected electromagnetic signals. It takes advantage of the ranging and Doppler tracking capabilities of coherent radars to generate images with high resolution independently of the sensor altitude. This is achieved through target differential time delay and Doppler history. This section provides an overview of the SAR basics necessary for the following chapters.

2.1.1 Geometry and Synthetic Aperture Formation

The initial concept of SAR involves a deployment on a platform that moves at a constant velocity along a linear trajectory, as illustrated in Figure 2.1. A side-looking geometry is applied, where the antenna beam is directed obliquely to the scene to be imaged, with a specific elevation look angle. In azimuth, it looks perpendicular to the platform movement, which is known as the boresight direction. When the beam is looking forward or rearward, a squinted geometry is applied.

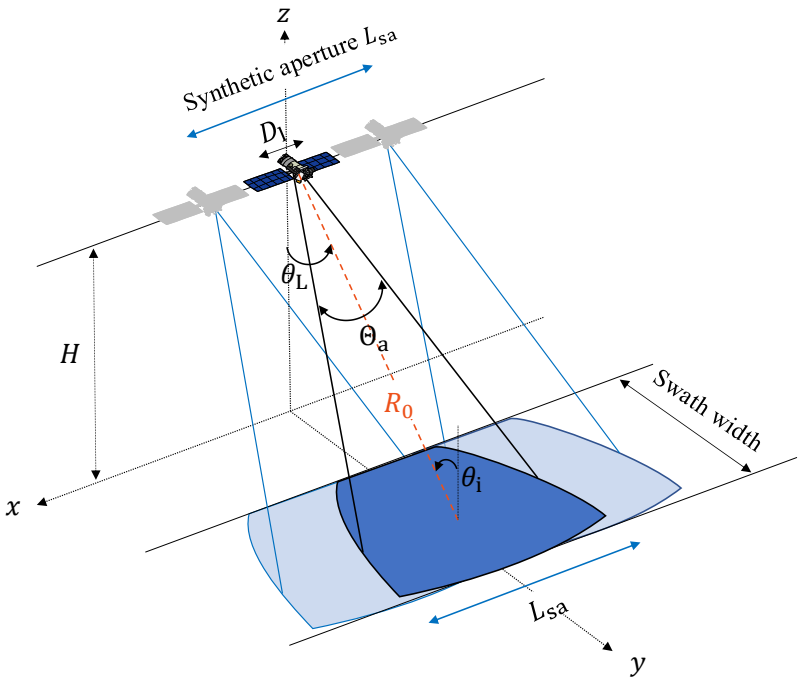

Figure 2.1: SAR imaging geometry with an antenna length of D_l mounted on a platform at a altitude H with the look angle θ_L.

As an analogy to optical imaging, capturing a panoramic view involves snapping multiple pictures while pivoting the camera in one spot to encompass the entire scene. If the camera is moving in a straight line and capturing photos at regular intervals, the individual snapshots are combined to create a larger and more detailed image. This is similar to how SAR works. SAR collects the backscattered signals at different points along its path and processes them to create a synthetic aperture as if they had been acquired with a much longer antenna that is physically impossible to mount on an aircraft or satellite. This is done by taking advantage of the motion. The synthetic aperture length depends on the physical antenna length D_l and azimuth beamwidth Θ_a and is given by [82]

$$L_\mathrm{sa} = R_0 \tan\Theta_\mathrm{a} \approx R_0 \Theta_\mathrm{a} = R_0 \frac{\lambda}{D_\mathrm{l}}, \tag{2.1}$$

with λ the signal wavelength. The synthetic beamwidth is $\Theta_\mathrm{sa} = \lambda / 2L_\mathrm{sa}$ taking into consideration the two-way path from transmission to reception. The azimuth resolution results in

$$\delta_\mathrm{a} = \Theta_\mathrm{sa} R_0 = \frac{\lambda}{2L_\mathrm{sa}} R_0 = \frac{\lambda D_\mathrm{l} R_0}{2\lambda R_0} = \frac{D_\mathrm{l}}{2}, \tag{2.2}$$

by substituting (2.1). It is thus independent of the signal wavelength and range. However, this theoretical resolution is only valid for a focused SAR and for a target

observed continuously along the formed synthetic aperture from the point where the beam starts seeing it until it leaves. In real scenarios, reaching this high resolution is challenging, especially for moving targets leaving the beam faster. Therefore, it is more practical to relate the azimuth resolution to the real target observation time, which is defined as

$$T_{\mathrm{dwell}} = \frac{L_{\mathrm{sa}}}{v_{\mathrm{p}}} = \frac{\lambda R_0}{v_{\mathrm{p}} D_{\mathrm{l}}}, \tag{2.3}$$

with v_{p} the platform velocity.

2.1.2 Pulse Compression

The SAR is typically a pulsed radar system, transmitting a linear frequency-modulated (LFM) chirp signal. Pulse compression is used to achieve a fine range resolution while keeping a high average power. The range resolution is inversely proportional to the bandwidth B and incident angle θ_{i} relative to the side-looking geometry. It is defined as [83]

$$\delta_{\mathrm{r}} = \frac{c_0}{2B \sin \theta_{\mathrm{i}}}, \tag{2.4}$$

where c_0 is the speed of light in free space. To use a high bandwidth, the pulse duration τ_{p} should be kept small, given that $B \approx 1/\tau_{\mathrm{p}}$ for unmodulated rectangular pulses. This leads to a smaller pulse energy (product of power and time) and thus to a low backscattered signal. Therefore, modulation techniques such as chirping are used to transmit a long pulse with a wide bandwidth dependent on the frequency sweep [84, 85]. The average transmitted power of a relatively long pulse is achieved, while obtaining the range resolution corresponding to a short pulse.

An up-chirp signal has an increasing instantaneous frequency over time and is given by

$$s_{\mathrm{up}}(t) = A \exp\left(\mathrm{j}\pi\mathcal{K}t^2\right) \operatorname{rect}\left[\frac{t}{\tau_{\mathrm{p}}}\right], \tag{2.5}$$

while a down-chirp signal is defined as

$$s_{\mathrm{down}}(t) = A \exp\left(-\mathrm{j}\pi\mathcal{K}t^2\right) \operatorname{rect}\left[\frac{t}{\tau_{\mathrm{p}}}\right], \tag{2.6}$$

where A is the amplitude and $\mathcal{K}$ is the chirp rate, which is related to the chirp bandwidth by

$$\mathcal{K} = \frac{B}{\tau_{\mathrm{p}}}. \tag{2.7}$$

The two different chirps are plotted in Figure 2.2. The same chirp rate is used in this example.

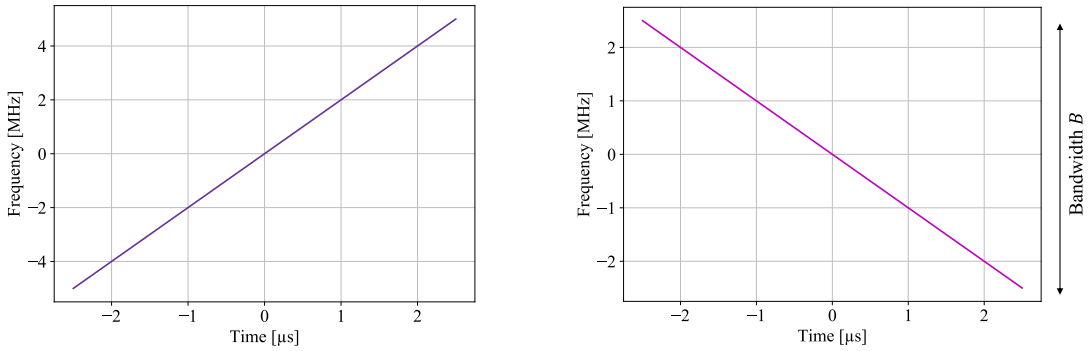

(a) Up-chirp (b) Down-chirp

Figure 2.2: Up- and down-chirp frequency variation over time for a pulse duration of $\tau_\mathrm{p} = 5\,\mu\mathrm{s}$ and a bandwidth of $B = 10\,\mathrm{MHz}$.

Proper range compression is applied on the backscattered signal after reception using matched filtering. This is achieved by cross-correlating the backscattered signal $s_\mathrm{R}(t)$ with a reference signal $h_\mathrm{r}(t)$, which is the complex conjugate and time-reverted replica of the transmitted chirp signal, $h_\mathrm{r}(t) = s_\mathrm{T}^*(-t)$. The matching filter output is therefore given by

$$u_\mathrm{rc}(t) = s_\mathrm{R}(t) \otimes h_\mathrm{r}(t) = \int_{-\infty}^{\infty} s_\mathrm{R}(\tau) h_\mathrm{r}(t-\tau) d\tau, \tag{2.8}$$

where $\otimes$ is the convolution operator. This matched filter convolution is typically done in the frequency domain for simplicity [84, 86].

To achieve the azimuth resolution described in (2.2), a pulse should be transmitted whenever the moving platform covers half of the antenna length to fulfill the sampling theorem in space. A minimum condition on the Pulse Repetition Frequency (PRF) is therefore required and given by [82]

$$\mathrm{PRF} > \frac{2v_\mathrm{p}}{D_\mathrm{l}} = \frac{v_\mathrm{p}}{\delta_\mathrm{a}}. \tag{2.9}$$

The radar should pulse faster while considering the range ambiguities by setting a maximum bound on the PRF as a function of the desired swath width. Range ambiguities occur when echoes from a target appear at multiple locations along the range direction due to the simultaneous reception of echoes from consecutive and different pulses. This is described in more detail in Chapter 5.

2.1.3 Doppler Basics

As SAR moves relative to the target on the ground, the frequency of the electromagnetic wave reflected from the ground and received will be different than that of

the transmitted wave according to the Doppler effect. For a target located at the slant range R_0 and having the incident angle θ_i, this Doppler shift is given by [87]

$$f_\mathrm{D} = \frac{2v \sin\theta_\mathrm{i}}{\lambda}. \tag{2.10}$$

where v can be the platform's velocity v_p or the across-track ground velocity of a moving target $v_{\mathrm{t}y}$, depending on the scenario. When targets are located at different azimuth positions, they display distinct range profiles evident through their variable echo phases, resulting in a shift in their respective Doppler. The slant range of a point target located in azimuth at $x(t) = tv_\mathrm{p}$ varies over time depending on the platform movement and is given by [88]

$$R(t) \approx \sqrt{R_0^2 + x(t)^2} \approx R_0 + \frac{x(t)^2}{2R_0} = R_0 + \frac{v_\mathrm{p}^2 t^2}{2R_0}. \tag{2.11}$$

This is referred to as the range history, which is approximated as a quadratic function. The azimuth phase is directly influenced by this range variation with $\varphi(t) = 4\pi R(t)/\lambda$. Using the same principle, the instantaneous frequency variation of the received azimuth signal is expressed as

$$f_\mathrm{a}(t) \approx \frac{-1}{2\pi}\frac{\partial\varphi(t)}{\partial t} = \frac{-2v_\mathrm{p}^2}{\lambda R_0}t, \tag{2.12}$$

which gives the Doppler frequency history. This Doppler information is crucial for enhancing the resolution through azimuth compression. Precise matched-filtering of the Doppler history requires accurate knowledge of both the range and velocity information to achieve proper image focusing. Azimuth compression is applied on the range-compressed (RC) data using the azimuth reference signal $h_\mathrm{a}(t)$, which is the complex conjugate and time-reversed replica of the transmitted chirp signal, $h_\mathrm{a}(t) = s_\mathrm{T}^*(-t)$.

The Doppler bandwidth of a non-moving target or clutter varies over the azimuth integration angle and is inversely proportional to the azimuth resolution with [89]

$$B_\mathrm{D} \approx \frac{2v_\mathrm{p}\Theta_\mathrm{a}}{\lambda} = \frac{2v_\mathrm{p}}{D_\mathrm{l}}, \tag{2.13}$$

when the integration angle Θ_a is equal to the antenna azimuth beamwidth. This shows that the Doppler bandwidth reflects the frequency range when the target is illuminated by the half-power beamwidth of the antenna beam [90].

For a moving target, the Doppler bandwidth additionally becomes dependent on the target's along-track velocity $v_{\mathrm{t}x}$ and is given by [89]

$$B_\mathrm{Dt} \approx \frac{2\left(v_\mathrm{p} - v_{\mathrm{t}x}\right)\Theta_\mathrm{a}}{\lambda}. \tag{2.14}$$

If the clutter is moving (e.g. sea clutter), the clutter bandwidth, denoted by B_{Dc}, becomes dependent on the clutter velocity v_{c} with

$$B_{\mathrm{Dc}} \approx \frac{2\,(v_{\mathrm{p}} - v_{\mathrm{c}})\,\Theta_{\mathrm{a}}}{\lambda}. \tag{2.15}$$

2.1.4 Backscattering Mechanism

SAR measures the backscattered signal, which depends strongly on the Radar Cross-Section (RCS). The transmitted pulse interacts with the Earth's surface and only a portion of it is backscattered to the receiving antenna depending on the physical and electrical properties of the imaged scene, as illustrated in Figure 2.3. A smooth surface typically reflects and scatters the signal away from the radar. The rougher the surface is, the more diffusely it reflects the signal in all directions [91].

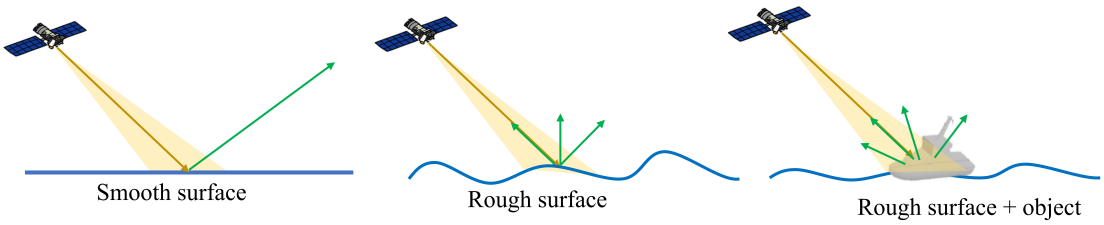

Figure 2.3: SAR Backscattering behavior over different surfaces and scene components.

The RCS, denoted by σ, is determined by the multiplication of the geometric cross-section, reflectivity, and directivity [4], and can be expressed as

$$\sigma = 4\pi \frac{\text{Backscattered power per unit solid angle}}{\text{Power density of intercepted signal}}. \tag{2.16}$$

The RCS is influenced mainly by the

- incident angle.
- surface roughness relative to the wavelength.
- target shape and physical size.
- polarization of the transmitted signal.
- frequency of the transmitted signal.
- target material and dielectric properties.

- target movement.

The backscattering behavior of the different objects in the scene can be easily interpreted in SAR images. Typically, dark areas represent low backscattering objects, such as oil spots. On the other hand, high backscattering elements are brighter. In regions where the characteristics remain consistent across more than a hundred resolution cells, like the sea surface, it is presumed that the average backscatter maintains a constant value throughout that particular section of the image.

2.1.5 Image Formation

The received SAR data are organized in a two-dimensional matrix, where different time delays, represented along the range axis, capture the varying distances of targets from the sensor. These time delays are a direct result of the pulse sequence connected to the PRF. Along the azimuth axis, distinct times reflect the sensor's movement, allowing for the synthesis of a larger aperture and thus, a more detailed spatial understanding of the scene [90]. After data acquisition, matched filtering is applied to create the final synthetic image. Many types of image formation algorithms are tailored for different resolution requirements and computational loads. The Range Doppler Algorithm (RDA) stands as a widely used SAR processing technique, characterized by its use of frequency domain operations for both range and azimuth compression, executed efficiently through multiplications [92].

The range Doppler algorithm is illustrated in Figure 2.4. The raw data are first converted to the frequency domain using a range Fast Fourier Transform (FFT), multiplied with the matching filter replica of the transmitted chirp $H_{\mathrm{r}}(f)$, and then transformed back into the time domain with a range Inverse Fast Fourier Transform (IFFT) to produce RC data. An FFT in the azimuth domain is then applied to transform the RC data into the range-Doppler domain.

After range compression, the energy signal from a point target in 2-D SAR data traces a path that is influenced by the varying range delay to the target as it moves through the antenna beam, an effect known as Range Cell Migration (RCM). This distance change is given by [88]

$$R_{\mathrm{RCM}}(t) = R(t) - R_0 \approx \frac{v_{\mathrm{p}}^2 t^2}{2R_0} \tag{2.17}$$

by substituting (2.11). It is approximated as a quadratic function, which is represented by the curvature of the range compressed response in Figure 2.4. If $R_{\mathrm{RCM}} > \delta_r/2$, an RCS correction is needed. In this case, aligning the signal energy from the point target within a single range bin is crucial for effective azimuth compression. This alignment is achieved by adjusting the range for each azimuth

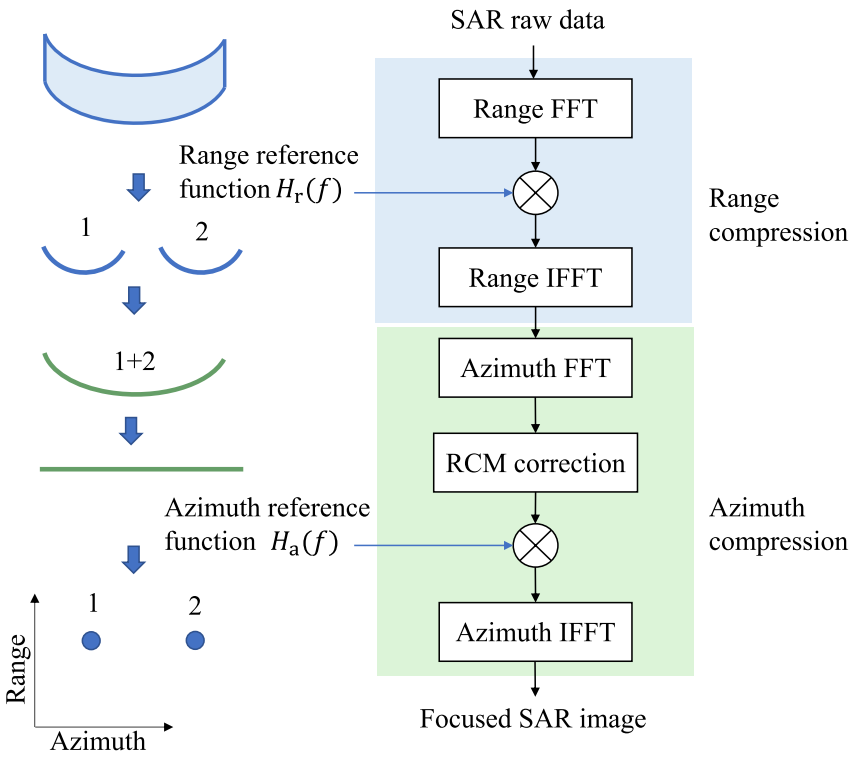

Figure 2.4: Range Doppler algorithm used to generate a focused SAR image.

frequency bin and employing interpolation in the range direction to capture all signal energy accurately.

Multiplication with the azimuth matching filter reference function $H_a(f)$ is then performed for each range bin and then transformed back to the time domain using an azimuth IFFT. All these steps lead to the focused complex SAR image.

2.1.6 Data Rate

The data rate of a SAR system is an important factor in assessing the volume of data to be downlinked or processed on board. It is expressed as the product of the number of samples per pulse N_s, the PRF, and the number of bits per sample N_b [85]

$$\mathrm{DR} = 2N_s N_b \,\mathrm{PRF}, \tag{2.18}$$

in bits per second. A coherent receiver is considered with both in-phase and quadrature (I and Q) channels, which justifies the factor 2 in (2.18). The number of samples N_s is given by the product of the pulse bandwidth B and the time duration of the sampling window, defined as the echo time window. For example, the DLR F-SAR system [93] has a data rate of $\mathrm{DR} = 245\,\mathrm{MB/s}$.

Diverse methods have emerged to reduce SAR raw data, such as data compression through Block-Adaptive Quantization (BAQ) and its advanced and adaptive forms [94–96], and signal coding [97, 98]. However, these techniques are not considered in this assessment to ensure that the data volume is evaluated uniformly, allowing for accurate comparisons with different systems in the next chapters.

2.2 Phased Array and Beamforming Principles

The antenna is an essential component of any radar system. It can be used in two different settings: monostatic and bistatic. When the same antenna is used for both transmission and reception, it is called monostatic. When the transmit antenna differs from the receive antenna and is separated by a large baseline, the setup is known as a bistatic configuration. This section highlights the key fundamentals of antenna arrays deployed in SAR systems.

2.2.1 Introduction to Phased Arrays

A single antenna element cannot achieve the necessary radiation characteristics for airborne and spaceborne synthetic aperture radar, as it lacks the capability of beam steering and shaping. Therefore, an array of radiating elements is typically used for such applications. The purpose of this electrical and physical arrangement is not only to boost the power output but also to exploit the constructive and destructive interference of the signals from each element, allowing the forming of the radiation pattern in ways that a single antenna cannot achieve. Array antennas are capable of electronically steering the beam, changing its shape, and dynamically focusing or spreading its energy, without any physical movement of the antennas. This is done by introducing variable phase shifts and amplitude scaling across the elements. The beamforming flexibility is crucial in applications that require high agility and precision, such as radar systems, and it constitutes the fundamental basis of phased array antennas.

2.2.2 Antenna Pattern of a Planar Phased Array

A phased planar array is a set of identical radiating antenna elements that work together to transmit or receive electromagnetic waves in a specific direction, as illustrated in Figure 2.5. The beam can be steered in both dimensions and the array factor is the product of the independent factors of two linear arrays.

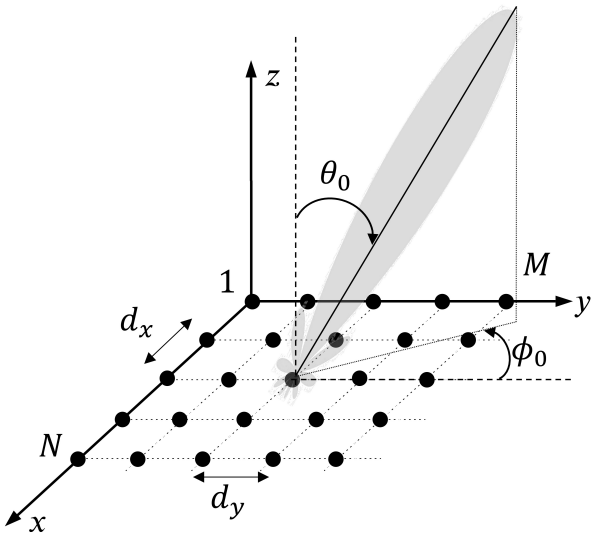

Figure 2.5: Rectangular planar array geometry of $N \times M$ elements.

The far-field radiation pattern is defined as the ratio of the electric field on a sphere of infinite radius centered at the antenna to the maximum electric field on that sphere with a constant distance from the antenna

$$C(\theta, \phi) = \left. \frac{E(\theta, \phi)}{E_{\max}} \right|_{r=\text{const} \to \infty}, \tag{2.19}$$

where the electric far-field is described by a local plane wave. $C(\theta, \phi)$ represents the spatial distribution of the radiation intensity generated by all elements. For an antenna array, it is expressed as the product of the two-dimensional element pattern $C_\text{e}(\theta, \phi)$, which describes the radiation characteristics of a single element, and the array factor $\text{AF}(\theta, \phi)$, which represents the impact of the array configuration including the excitation of its elements [99]

$$C_\text{array}(\theta, \phi) = C_\text{e}(\theta, \phi)\ \text{AF}(\theta, \phi). \tag{2.20}$$

This is valid for ideal considerations without mutual coupling effects between the antenna elements, which can influence the radiation characteristics depending on their relative separation and orientation [100, 101].

The array factor of a planar array having the same amplitude excitation is given by [86]

$$\text{AF}_\text{planar}(\theta, \phi) = \sum_{n=0}^{N-1} \sum_{m=0}^{M-1} A_{nm} e^{\text{j}k \sin\theta (n d_x \cos\phi + m d_y \sin\phi)}, \tag{2.21}$$

where the projection of each element point on a plane is taken into consideration with the following direction cosines

$$\begin{aligned} u &= \sin\theta\cos\phi \\ v &= \sin\theta\sin\phi. \end{aligned} \tag{2.22}$$

In antenna array theory, these cosines simplify and describe the beam's direction in a planar coordinate system. When the beam is steered to (θ_0, ϕ_0), the 2-D array factor is expressed as

$$\mathrm{AF}_{\mathrm{planar}}(\theta,\phi) = \sum_{n=0}^{N-1}\sum_{m=0}^{M-1} A_{nm} e^{\mathrm{j}k(nd_x(u-u_0)+md_y(v-v_0))}, \tag{2.23}$$

by substituting (2.22) in (2.21).

Planar Array Gain

The gain of an antenna aperture with $N \times M$ elements uniformly excited without losses and looking at the boresight depends on its physical area A and is given by [86, 102]

$$G_0 = \frac{4\pi A}{\lambda^2}, \tag{2.24}$$

where $A = Nd_xMd_y$.

The gain for a nonuniform amplitude distribution and a lossy aperture is reduced to [100]

$$G(\theta_0) = \frac{4\pi}{\lambda^2} A\eta\cos(\theta_0), \tag{2.25}$$

when the beam is steered to the angle θ_0. The cosine corresponds to the variation of the beamwidth with the scan, and η is an efficiency term relative to the losses.

2.2.3 Antenna Pattern of a Linear Phased Array

As a special case of the planar array, a linear array is investigated in the following considering the pattern in the xy-plan, $\phi = 90°$.

For a Uniform Linear Array (ULA) with N antenna elements spaced by d as shown in Figure 2.6, a linear phase progression is employed to steer the beam toward θ_0. For the element n, this phase shift is given by [103]

$$\Delta\phi(n) = n\Delta\phi = n\frac{2\pi}{\lambda} d\sin\theta_0, \tag{2.26}$$

with $n \in [0, 1...N]$.

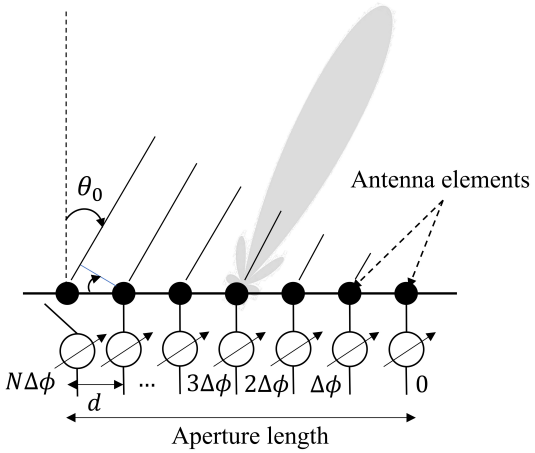

Figure 2.6: Linear phased array of N antenna elements, all contributing to steering the beam in a specific direction θ_0.

The array factor depends on the number of elements N and their spacing d and is given by

$$\mathrm{AF}_{\mathrm{array}}(\theta) = \sum_{n=1}^{N} A_n e^{\mathrm{j}k(n-1)\ d\ \sin(\theta)+\beta}, \tag{2.27}$$

with $k = 2\pi/\lambda$, A_n the amplitude weight of element n, and β the phase taper applied to steer the beam in a specific direction θ_0, which is given by

$$\beta = -kd\sin(\theta_0). \tag{2.28}$$

The expression in (2.27) may be simplified to [104]

$$\mathrm{AF}_{\mathrm{array}}(\theta) = \frac{\sin\left(\dfrac{Nkd(\sin\theta - \sin\theta_0)}{2}\right)}{N\sin\left(\dfrac{kd(\sin\theta - \sin\theta_0)}{2}\right)}, \tag{2.29}$$

for a uniform amplitude distribution $A_n = 1\ \forall\ n$.

Substituting (2.27) and (2.28) in (2.20) leads to the antenna array pattern given by

$$C(\theta) = C_{\mathrm{e}}(\theta)\ \sum_{n=1}^{N} A_n e^{\mathrm{j}k(n-1)\ d\ (\sin\theta - \sin\theta_0)}. \tag{2.30}$$

First-Null Beamwidth

the array factor nulls occur when the argument of the sinus in the nominator is equal to integer multiples of π. The first nulls of the pattern can be determined by setting the array factor (2.29) equal to zero and thus the argument of the sinus in the nominator equal to integer multiples of π, which leads to

$$\frac{Nkd(\sin\theta - \sin\theta_0)}{2} \stackrel{!}{=} \pm\pi. \tag{2.31}$$

The nulls closest to the main lobe also referred to as first nulls are of interest. Solving for θ gives the first-null angle

$$\sin\theta^{\mathrm{FN}} = \pm\frac{2\pi}{Nkd} + \sin\theta_0. \tag{2.32}$$

Substituting $k = 2\pi/\lambda$ in (2.32) leads to the

$$\theta^{\mathrm{FN}} = \sin^{-1}\left(\pm\frac{\lambda}{Nd} + \sin\theta_0\right). \tag{2.33}$$

The first nulls of the array pattern are plotted in Figure 2.7 as a function of the scan angle.

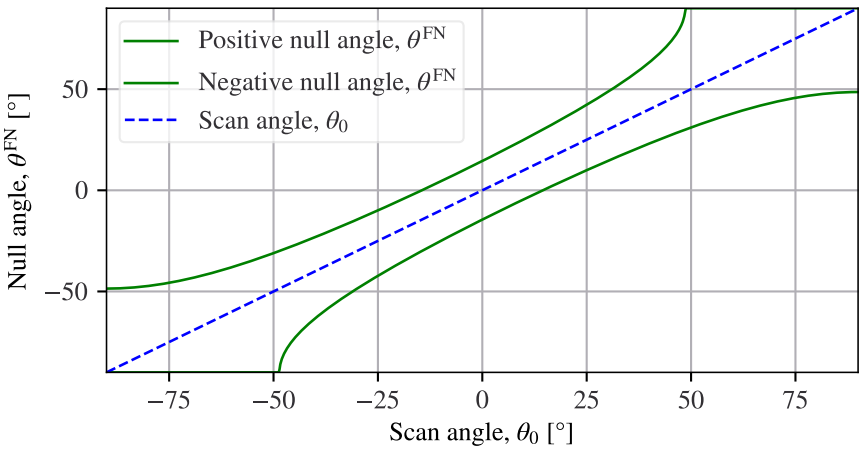

Figure 2.7: First nulls versus scan angle for an array of $N = 8$ antenna element spaced with $d = \lambda/2$.

The fist-null beamwidth, defined as the distance between the right and left nulls, is therefore given by

$$\Theta^{\mathrm{FN}} = \frac{2\lambda}{Nd}, \tag{2.34}$$

for $Nd \gg \lambda$.

Half-Power Beamwidth

The half-power beamwidth (HPBW) is defined as the beamwidth when the power density is reduced by 3 dB. It varies with the steering angle θ_0 and is given in radians by [99, 103]

$$\Theta_{3\mathrm{dB}}(\theta_0) = \frac{\Theta_{3\mathrm{dB}}(0)}{\cos\theta_0} \approx 0.886 \frac{\lambda}{D\cos\theta_0}, \tag{2.35}$$

for a uniformly illuminated array with the length D. This relation shows the slight broadening of the beam with steering caused by the decrease in the effective array aperture, as illustrated in Figure 2.8.

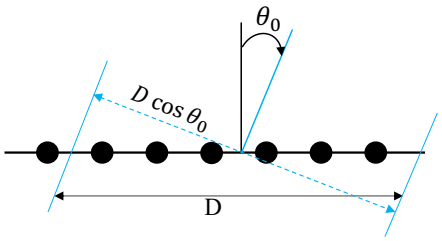

Figure 2.8: The effective array aperture variation with the steering angle θ_0.

Linear Array Gain

The gain of a large array depends on the gain of the single element G_e, as well as the array factor including the amplitude excitation, scan angle θ_0, and the number of elements N. It is given by [104]

$$G_\mathrm{array}(\theta) = G_\mathrm{e}(\theta)\mathrm{AF}_\mathrm{array}(\theta). \tag{2.36}$$

The maximal gain is typically achieved when the array is uniformly excited with amplitudes $A_n = 1$ in (2.27) and the beam is directed toward the boresight direction with $\theta_0 = 0$. The phase difference between adjacent elements, defined in (2.26), becomes $\Delta\phi = 0$. Consequently, the exponential term in the array factor (2.27) simplifies to 1 and the resulting array factor becomes equal to the number of elements N. This leads to the maximum gain of

$$G_\mathrm{array}(0) = G_\mathrm{e}(0)\mathrm{AF}_0 = G_\mathrm{e}(0)N. \tag{2.37}$$

In decibels, the maximum gain can be expressed by

$$G_{\text{array}\,\text{dB}}(0) = 10\log_{10}(NG_{\text{e}}(0)) = 10\log_{10}(G_{\text{e}}(0)) + 10\log_{10}(\text{N}). \tag{2.38}$$

Hence, adding two antenna elements to the array increases the array gain theoretically by 3 dB, assuming ideal conditions with no losses, perfect phase coherence, and minimal mutual coupling.

2.2.4 Element Spacing and Grating Lobes

Grating lobes in a phased array antenna are unwanted secondary lobes that decrease the radiation performance in the desired direction. They appear at the maxima of the array factor (2.29) when

$$\sin\left(\frac{\pi d}{\lambda}(\sin\theta - \sin\theta_0)\right) \stackrel{!}{=} 0, \tag{2.39}$$

leading to

$$\frac{\pi d}{\lambda}(\sin\theta - \sin\theta_0) \stackrel{!}{=} \pm\pi p_{\text{GL}}, \tag{2.40}$$

where $p_{\text{GL}} = \pm 1, \pm 2, \ldots$ is the order of the grating lobe, as multiple maxima can occur.

Solving for $\sin\theta$ yields the directions θ_{GL} of the grating lobes:

$$\sin\theta_{\text{GL}} = \sin\theta_0 \pm p_{\text{GL}}\frac{\lambda}{d}, \tag{2.41}$$

which is the general condition for the occurrence of grating lobes. The location of the grating lobes is determined by the scan angle θ_0, the distance between elements d, and the wavelength λ, with no impact from the number of antenna elements N. For practical antenna array applications, the first-order grating lobes with $p_{\text{GL}} = -1$ and/or $+1$ are most relevant.

The expression in (2.41) may be used in two ways:

- To determine the angle of the grating lobes for a given element separation and array scan angle, as illustrated in Figure 2.9.
- To determine the maximum allowable antenna element spacing such that the first-order grating lobes are either avoided or placed at the antenna pattern nulls of a sub-array.

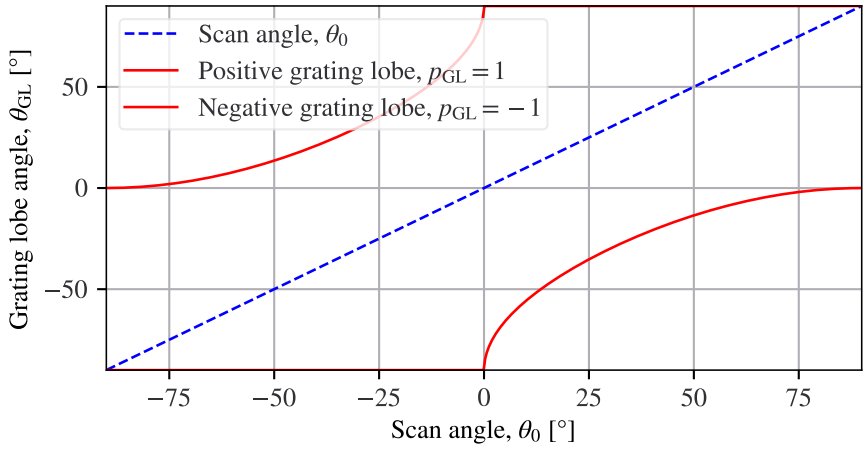

Figure 2.9: Grating lobe angles versus scan angle for an antenna element spacing of $d = \lambda$.

The required spacing is thus given from (2.41) for a desired grating lobe angle and maximum steering angle of the main beam $\theta_{\max}$ by

$$\frac{d}{\lambda} \leq \frac{1}{\sin|\theta_{GL}| + \sin|\theta_{\max}|}. \tag{2.42}$$

Considering a boresight-looking geometry and an antenna covering the angular sector $\psi = [-\frac{\pi}{2}, \frac{\pi}{2}]$, the spacing for a given wavelength λ should satisfy [105]

$$\frac{d}{\lambda} \leq \frac{1}{1 + \sin|\theta_{\max}|}. \tag{2.43}$$

by substituting $\theta_{GL} = \pm\pi/2$ in (2.40) and solving it. The condition (2.43) is thus considered a special case of (2.42).

2.2.5 Digital Beamforming (DBF)

Digital beamforming enhances the antenna array performance by moving control functions, such as phase and amplitude adjustment, to the digital domain [23]. It can be applied in both the transmit and the receive modes. DBF on transmit is achieved by placing the digital-to-analog converter (DAC) closer to the antenna element, having a waveform generator on each antenna element, and presetting the beam phase and amplitude characteristics in the digital domain [106–108]. This configuration is commonly used to generate multiple beams with different waveforms and Multiple Input Multiple Output (MIMO) systems.

DBF on receive involves connecting each antenna element (or sub-aperture) in the array to an analog-to-digital converter (ADC), which samples and converts each

received signal into a digital signal. Post-processing algorithms, e.g. Digital Signal Processing (DSP), are then used to shape and steer the beam in the desired direction by adjusting the phase and amplitude weights w_n in the digital domain. This configuration is also called a multi-channel system, where each channel corresponds to a digitized signal [109–111]. In contrast to analog beamforming which

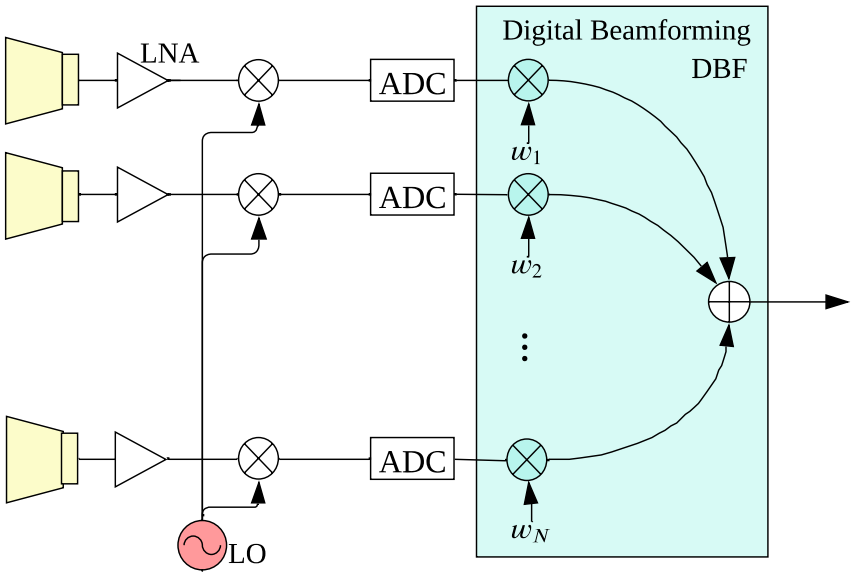

Figure 2.10: Digital beamforming array configuration: Each antenna element's signal independently undergoes amplification, down-conversion, and digitization. DBF is then implemented by multiplying it with a complex-valued weighting vector $\mathbf{w}$. The summation of all digitally processed signals results in the formation of the desired beam.

uses phase shifters and attenuators in hardware, the signals received by each element are individually amplified, down-converted, and digitized over time, as depicted in Figure 2.10. The digitized signals are then multiplied with complex coefficients to generate the desired beams. This offers more flexibility and agility in steering the beams. By digitizing individual channels, beams can be formed offline and made available for multiple uses. The direction, shape, and other beam characteristics can be dynamically adjusted through software. Several advantages can be achieved using DBF, including:

- Reduced analog radio frequency components and better beamforming and system efficiency.
- The suppression of interference and spatially ambiguous signals [112].

- Easy adaptation for different applications and conditions by changing the signal processing algorithms, without needing physical modifications to the antenna array.
- The possibility of applying frequency dispersive DBF [113].

Elevation DBF on Receive

Having multiple digital channels in elevation enables diverse offline beamforming operations on receive. A typical digital beamforming technology in elevation is known as Scan-On-Receive (SCORE) [21, 31, 112]. It is based on generating a high-gain narrow beam on receive, which follows the SAR echo signal on the ground while having a broad transmit beam that illuminates the entire swath width. An onboard DBF steers and combines the received signals over time. Therefore, it involves a weighted time-variant digital combination of the signals in elevation, followed by a summation, as shown in Figure 2.10. The weighting vector becomes variable with time and is defined as $\mathbf{w}(t)$, according to the echo reception time. The main objective of using DBF in elevation is to increase the gain of the received signal, thus the Signal-to-Noise Ratio (SNR), and to avoid the collection of backscattered signals from a wide footprint. With digital steering, the entire swath width illuminated during transmission can be reconstructed. Range ambiguities can be suppressed via spatial filtering thanks to DBF in elevation [114, 115].

The switch step of the DBF weights over time depends on many parameters, including the PRF, pulse duration, sampling, and antenna array size. In [116], it was demonstrated how the angular pulse extent directly affects the weight update rate. The condition is to ensure that the pulse edge stays within the half-power beamwidth of the radiation pattern. To maintain the pulse within the beamwidth, weights are updated as soon as the pulse moves beyond the pattern maximum. This strategy ensures that the SCORE beam transitions smoothly from one direction to another, mimicking a continuous movement. The angular pulse extent varies with the look angle θ and considering a flat Earth it is approximated as [117]

$$\mathcal{X}_\theta(\theta) = \frac{\tau_\mathrm{p} c_0 \cos^2\theta}{2H \sin\theta}, \tag{2.44}$$

where τ_p is the pulse duration and H the platform height. The angular difference between the antenna beamwidth Θ and $\mathcal{X}_\theta(\theta)$ gives the digital steering switch step as [116]

$$\Delta\theta = \Theta - \mathcal{X}_\theta(\theta) \qquad \text{for} \quad \Theta > \mathcal{X}_\theta(\theta). \tag{2.45}$$

DBF can simultaneously generate multiple beams from the same set of antenna elements. This is particularly useful in applications, like SAR, where desired features include scanning different areas and tracking multiple targets simultaneously.

DBF can efficiently determine the Direction of Arrival (DoA) [118], allowing for the separation of multi-mode echoes received simultaneously, which is described in Chapter 5.

Azimuth DBF on Receive

The receive antenna aperture is divided into N_{ch} individual channels in azimuth. Each channel is digitized and registered separately. The main objective of employing multiple channels in azimuth is to eliminate azimuth ambiguities that arise from undersampled Doppler bandwidth B_{D} [119]. An effect of aliasing occurs when targets appear several times instead of only once in the final SAR image. For an antenna length of D_{l}, the minimum PRF needed to prevent azimuth ambiguities is given in (2.9). It directly influences the azimuth resolution. A fine resolution requires a high Doppler bandwidth, which should be sampled with a sufficient PRF [83]. However, this reduces the unambiguous range of the radar. Thus, it is challenging for single-channel SAR systems to achieve high resolution while having a large swath width with a reduced Pulse Repetition Interval (PRI) leading to range ambiguities. This trade-off is a fundamental constraint, reflecting an inherent limitation in the design and operation of such systems. This is where azimuth DBF comes into play, as it offers both high resolution and wide coverage, thus providing enhanced imaging capabilities: N echo signals are received through the different channels for each transmitted pulse. The channels observe the same area on the ground, but from different phase centers, resulting in distinct angular Doppler. This idea was first proposed in [120] as a Displaced Phase Center Antenna (DPCA) technique, now widely employed in many radar signal processing algorithms. Enhancing it with DBF, the problem of resolution-swath trade-off is solved by using a lower PRF for each channel, $\mathrm{PRF}/N_{\mathrm{ch}}$, and then combining the different phase centers. DBF has opened the door for many promising SAR concepts, including the High-Resolution Wide-Swath (HRWS) [121].

DBF Limitations

Despite the flexible features of digital beamforming, it remains an expensive technique due to the cost of A/D converters. To overcome this challenge, a commonly used approach is partial implementation which involves forming sub-arrays instead of digitizing each antenna element. This approach decreases the number of digital channels and thus reduces the high digital data rate of N_{ch} channels, alleviates their calibration burden, and decreases the front-end power consumption.

2.2.6 Sub-Aperture Formation

In the configuration depicted in Figure 2.11, a set of array elements are grouped to form sub-apertures. The resulting array pattern is then derived from the multiplication of two key factors: the array factor, representing the collective behavior of the entire array, and the pattern of the individual sub-apertures, which details the radiation characteristics of the group of elements:

$$C_{\text{total}}(\theta) = C_{\text{e}}(\theta)\ \text{AF}_{\text{sub}}(\theta)\ \text{AF}_{\text{array}}(\theta). \tag{2.46}$$

In the context of this thesis, a sub-aperture refers to a specific subset of active

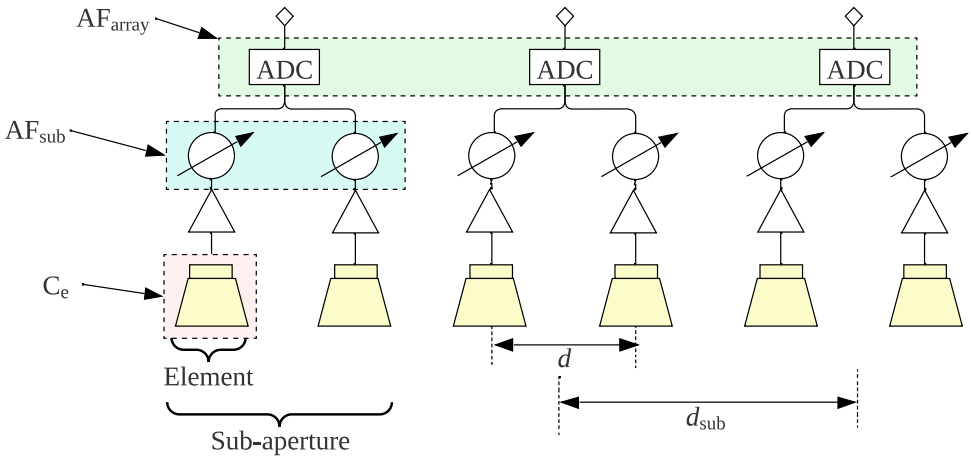

Figure 2.11: Active electronically steered phased array antenna system with formed sub-apertures.

elements within the array, capable of shaping the pattern. In contrast, a subarray combines passive elements without individual control.

The pattern of the sub-aperture can therefore be shaped and steered to a desired direction θ_{s0} by adding a progressive phase difference between the N_s sub-aperture elements. The total array pattern is then given by

$$C_{\text{total}}(\theta) = C_{\text{e}}(\theta) \sum_{n_{\text{s}}=1}^{N_{\text{s}}} A_{\text{n}_{\text{s}}} e^{\text{j}kn_{\text{s}}d\ (\sin\theta - \sin\theta_{\text{s0}})} \times \sum_{n=1}^{N} B_{\text{n}} e^{\text{j}knd_{\text{sub}}\ (\sin\theta - \sin\theta_0)}, \tag{2.47}$$

considering the spacing between sub-apertures d_{sub} in the total array factor.

To reduce the number of digital channels in a phased array system, it is common to use subarrays without the need for phase shifters. However, some applications require additional analog beamforming and thus sub-apertures, especially in the context of suppressing grating lobes with the first nulls, which is described in Chapter 4.

2.2.7 Tapering and Reduction of Sidelobes

The amplitude and phase required to generate the desired beam are determined using array synthesis methods and beamforming techniques [113, 122–124]. One of these techniques is amplitude tapering used to reduce the sidelobe level. An important characteristic of the antenna pattern is the sidelobe ratio (SLR), defined as the difference in gain between the main lobe and the first sidelobe. The larger the SLR is, the better the radiation dynamic range is. However, this leads to a decrease in directivity and a widening of the HPBW [104]. For systems that require transmitting the maximum power like spaceborne radars, amplitude tapering on transmit is typically not used to avoid any drop in the radiation efficiency. Hence, amplitude tapering is often more suitable for received signals. However, several applications require the shaping of the beam on transmit, and therefore a performance compromise is usually struck.

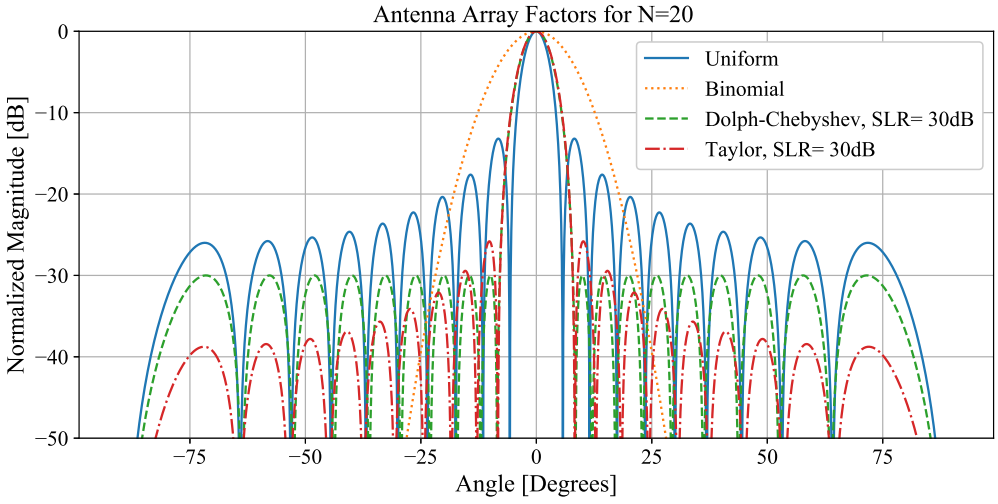

Figure 2.12: Simulated normalized array factors of a linear 20-element array with an element distance of $d = \lambda/2$ for different amplitude tapering functions: uniform, binomial, Dolph-Chebyshev, and Taylor.

Many amplitude tapering functions, such as the binomial, Dolph-Chebyshev, and Taylor functions can be used [100, 118]. Each method has a unique effect on the

array, as shown by the antenna array factor simulation in Figure 2.12. The use of binomial coefficients eliminates all sidelobes. However, it also leads to a significant broadening of the main beam. Consequently, the beamwidth increases to more than twice that of a uniformly distributed array. The Dolph-Chebyshev array generates a pattern where all sidelobes have the same level. On the other hand, the Taylor tapering maintains the first few lobes below a specific level.

2.2.8 Noise Figure

The noise figure (NF) is a key parameter in assessing the quality of the signal received by the antenna and how much noise the instrument adds to the signal path. It quantifies the noise contribution of all RF components, which are typically connected in cascade in an active phased array antenna. The total system noise figure F_{total} of the entire signal chain with N devices is measured by the Friis cascade formula [104]

$$F_{\text{total}} = F_1 + \frac{F_2 - 1}{G_1} + \frac{F_3 - 1}{G_1 G_2} + ... + \frac{NF_{\text{N}} - 1}{G_1 G_2 ... G_{\text{N}-1}}, \tag{2.48}$$

with G_i the gain of device i and F_i its respective noise figure. When the Low Noise Amplifier (LNA) has high gain, subsequent components contribute minimally to system noise, allowing them to be largely disregarded in noise analysis.

Many techniques can reduce the total noise figure, such as placing the LNA as close to the antenna as possible at the beginning of the signal chain. Gallium Nitride (GaN) amplifiers with their high electron mobility and saturation drift velocity can be utilized, leading to a low noise figure and increased output power [104]. The phase shifters should have a low insertion loss and a high phase accuracy. Therefore, digital phase shifters are typically used. They are also small and can be implemented using Monolithic Microwave Integrated Circuit (MMIC) technologies.

2.3 SAR-GMTI Principles

Combining SAR with GMTI is a powerful tool for detecting and tracking moving targets while leveraging the properties and imaging features of the SAR instrument [125]. While SAR and GMTI traditionally have different operational configurations, there has been a growing demand to merge the two modes for simultaneous operation. This can enhance the effectiveness of surveillance by achieving better recognition and classification of moving targets. This section provides an overview of the target detection criteria relevant to the design of SAR systems while emphasizing the GMTI performance metrics.

2.3.1 SAR-Based Moving Target Detection

To detect moving objects, the signal of interest needs to be separated from both the clutter and the receiver noise. Clutter is considered any undesired echoes received by a radar system, such as those caused by land, sea, or weather disturbances [92].

Doppler frequency-based techniques are commonly used to distinguish moving targets from stationary clutter, which is the basis of the GMTI radars. The Doppler effect is relevant when the target moves with a radial velocity relative to the platform. A pulsed radar like SAR sends a coherent set of pulses, then enhances moving target intensity while rejecting stationary clutter by filtering out zero Doppler shifts using a Doppler filter bank [86]. The detection of moving targets is often performed in the Doppler domain using a single-channel SAR system and only range compressed (RC) data [126].

Clutter Doppler Spectrum

Due to the Doppler effect, described in Section 2.1.3, the received target signal is shifted in Doppler based on its relative velocity compared to the platform's velocity. The clutter Doppler spectrum represents the distribution of the clutter energy as a function of the Doppler frequency and has two main regions [126, 127]:

- **The endo-clutter region** contains significant clutter energy centered around zero Doppler. Typically, clutter from stationary or slow-moving objects falls within this region.
- **The exo-clutter region** is free of clutter and typically contains only noise and target signals. Located outside the endo-clutter region, it is crucial for detecting moving targets with Doppler frequencies exceeding those of the clutter.

Hence, moving targets can be detected in the Doppler domain if they produce Doppler frequencies that lie outside of the endo-clutter region [128]. This means that their Doppler frequencies, defined in (2.10), are larger than half of the clutter Doppler bandwidth, B_{Dc} defined in (2.15), with $\mid f_{\mathrm{D}} \mid > B_{\mathrm{Dc}}/2$.

Figure 2.13 shows a simulated range-Doppler image including clutter and a target at 1.3 km moving with a velocity of 20 m/s in the exo-clutter region. As observed, the target Doppler frequency surpasses the limits of the endo-clutter region, making the target visible for detection.

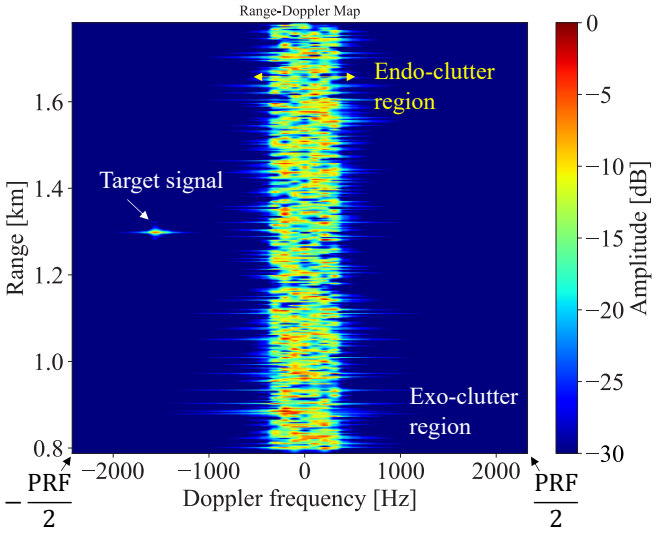

Figure 2.13: Simulated range-Doppler image after applying range and azimuth FFT on the backscattered signal showing the clutter Doppler spectrum centered at zero and a target within the exo-clutter region.

PRF Influence on Moving Target Detection

The clutter bandwidth is defined by the antenna beam footprint, and the clutter and platform velocities, but not on the PRF. A high PRF can help concentrate clutter energy closer to zero Doppler, effectively reducing its impact across the overall Doppler spectrum [129, 130]. Hence, the PRF expands the exo-clutter region and increases the maximum unambiguous Doppler frequency that can be measured, given by $\pm\,\mathrm{PRF}\,/2$. Hence, having a high PRF expands the system's capability of detecting fast-moving targets. It also helps improve the temporal coherence between successive pulses, which is crucial for effective clutter cancellation.

The PRF choice also influences the Doppler resolution δ_D, which is the ability of the radar to distinguish between two targets based on their relative Doppler shifts and hence their radial velocities. It is given by

$$\delta_\mathrm{D} = \frac{1}{T_\mathrm{CPI}} = \frac{\mathrm{PRF}}{N_\mathrm{p}}, \tag{2.49}$$

with T_CPI the coherent processing interval (CPI), which depends on the number of integrated pulses N_p [131].

Multi-Channel Detection

Moving targets characterized by a strong backscattering signal can be detected with one single azimuth channel even if their Doppler shift lies within the endo-clutter

region. The only condition here is that their intensity is higher than the clutter level. However, targets with low RCS and Doppler frequencies within the clutter bandwidth are hard to detect and need clutter suppression before detection. To tackle this challenge, a multi-channel SAR system is needed to receive the return echo with two different phase centers. The additional channel should be in the along-track direction of the platform and is used to suppress returns from the ground clutter before the target detection is performed [28,132]. Many promising techniques have been developed using this approach, including:

- **The Space-Time Adaptive Processing (STAP)** [39, 41, 133]: This joint angle-Doppler domain filtering technique decreases the ground clutter and enhances the moving target response even if it is embedded within the endo-clutter region.
- **The Displaced Phase Center Antenna (DPCA)**: This technique uses at least two receiving apertures or digital channels. The co-registered signal received by the first aperture is subtracted from the signal received by the second aperture when it reaches the same position in space. Thus, everything that is static can be canceled, and slowly moving targets can be identified [134, 135].
- **The Along Track Interferometry (ATI)**: This method employs two receive antennas to capture signals at offset times, then multiplies the first signal with the complex conjugate of the second antenna. Any change in the radial position of an object results in an ATI phase, while the stationary background has a zero phase [136, 137].

The computational complexities of these multi-channel GMTI techniques vary significantly. For instance, STAP requires the computation of a clutter covariance matrix, which can be time-consuming [60, 138, 139].

Target Size Estimation

When the most dominant scatterers are mapped across several range gates[1] and correlated with the backscattered power in each gate, a range profile of the target can be formed. The RCS of a target can therefore be measured [140], which can help estimate its length [141]. Other techniques include SAR or Inverse SAR imaging, which provides a more accurate estimation of the target shape and silhouette [142]. In ISAR imaging, the motion of an object is analyzed as a combination of translation and rotation relative to the radar's line of sight, causing distinct rates of phase change across the object. These phase history differences are then match-filtered

[1] A range gate is a digital bin assigned after signal sampling and corresponds to a particular distance from the radar

to resolve individual scatterers within a range cell, enabling the creation of detailed images [86].

2.3.2 Sea Clutter Influence on Detection

In maritime applications, particularly in Maritime Moving Target Indication (MMTI), understanding the influence of sea clutter on detection is crucial for optimizing system performance and accuracy [125, 143–147]. The sea surface is considered homogeneous if the sea state is moderate and the average range resolution is bigger than 30 m [148]. The backscattered sea reflectivity σ_0 depends on many factors including:

- The sea state, which is directly proportional to the wind strength and affects the ocean surface roughness.
- The radar look angle. Typically, sea clutter is more dominant in near range than in far range
- The used polarization. Horizontal transmit, horizontal receive (HH) polarization is less sensitive to surface roughness and has the best intensity contrast between ships and sea. On the other hand, vertical transmit, vertical receive (VV) polarization is suitable for sea surface scattering and can be used for wake detection [149, 150].

However, sea clutter remains a complex phenomenon, which varies drastically with the way the radar observes it. In contrast to applications where a fine resolution is always desired, the homogeneity of a smooth sea clutter can be lost when a fine range resolution is used. This leads to false alarms and makes target detection challenging. The detection of maritime targets relies on an intensity-based contrast criterion, where the maximum detection probability occurs when the power of a sea-surface object backscattering in a resolution cell exceeds the sea returns of neighboring cells. Spiky sea clutter may have a target-like intensity that can influence the target detection capability giving rise to large false alarms. Reducing sea clutter power is crucial, but high resolution is limited when a ship's surface area cannot fit within a single cell. A typical trade-off is to select a resolution cell size between 30 and 40 meters. This range maximizes the chances of detecting a ship within one or two cells, making the impact of sea clutter more dependent on the resolution cell size [148].

Various sea clutter models are typically used in CFAR algorithms to define a suitable detection threshold. This includes theoretical models based on the physical scattering behavior of the sea surface considering the received signal such as the Bragg Scattering, Burst Scattering, and Whitecap Scattering [151–153]. Statistical models are typically used such as Rayleigh and K-distribution, which are based on empirical

data collected through measurements under a wide range of real environmental conditions [126, 154–156]. To effectively address strong sea clutter, it is recommended to use multiple azimuth channels for clutter cancellation before detection. As discussed in the previous section, this method ensures clutter mitigation. However, it comes with the trade-off of increased system complexity and processing time.

2.3.3 GMTI Performance Metrics

In this section, the performance metrics of a GMTI system are described. The theory behind the probability of detection, false alarms, and their connection to the Signal-to-Clutter-plus-Noise Ratio (SCNR) is covered followed by the minimum detectable velocity (MDV).

Detection Statistics

In target detection problems, two hypotheses are used to evaluate the presence of a target within the received signal [4, 157]:

- H0: The null hypothesis, which consists of clutter and noise.
- H1: The non-null hypothesis, which includes signal, clutter, and noise.

The presence of a target is evaluated using the probability density functions (PDFs) corresponding to these hypotheses, as illustrated in Figure 2.14.

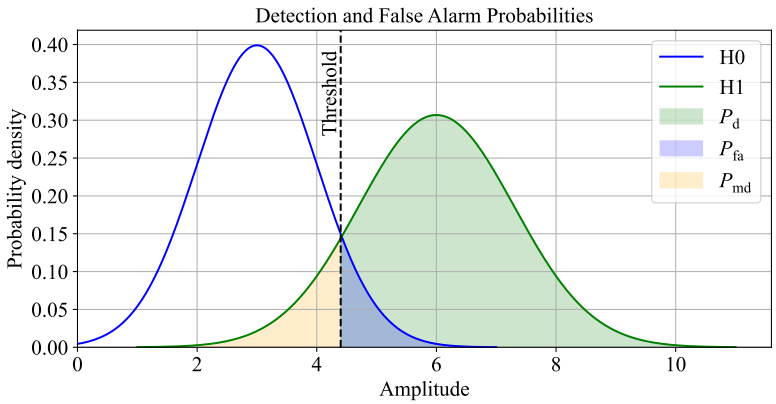

Figure 2.14: Probability density functions of noise ($H0$) and signal plus noise ($H1$) based on Gaussian distribution and highlighting the probability of detection P_{d}, the probability of false alarm P_{fa}, and the probability of missed detection P_{md} separated by the threshold.

Several performance metrics are derived from these PDFs:

- Probability of detection, P_{d}: The probability that the radar detects the target when it is present, represented by the area under the H1 to the right of the threshold.
- Probability of false alarm, P_{fa}: The probability that the radar declares the presence of a target when there is only noise, represented by the area under the H0 to the right of the threshold.
- Probability of missed detection, P_{md}: The probability that the radar fails to detect a target although it is present, represented by the area under the H1 to the left of the threshold. It is equal to $P_{\mathrm{md}} = 1 - P_{\mathrm{d}}$.

The decision threshold is a critical parameter determined based on a trade-off between P_{d} and P_{fa}. The goal of adjusting the threshold is typically to achieve the desired detection performance while minimizing false alarms. Hence, the probability of detecting a target in a radar system depends on several factors, including the user-set probability of false alarm rate P_{fa} and the SCNR. Determining the required SCNR for a given probability of detection is typically solved using approximations. In this context, there is a notable body of literature encompassing universal detection equations, which are recognized for their capacity to yield results with a high degree of accuracy [158, 159]. A commonly used expression for the probability of detection is given by [160–163]

$$P_{\mathrm{d}} = 0.5 \operatorname{erfc}(\sqrt{-\ln P_{\mathrm{fa}}} - \sqrt{\mathrm{SCNR} + 0.5}), \tag{2.50}$$

where the $\operatorname{erfc}(x)$ is the complementary error function defined as

$$\operatorname{erfc}(x) = \frac{2}{\sqrt{\pi}} \int_{x}^{+\infty} e^{-t^2}\, dt. \tag{2.51}$$

assuming that the noise and clutter in the radar system are Gaussian-distributed [164–166].

As a rule of thumb for a P_{fa} of 10^{-6}, an SCNR of at least 13 dB is typically required to achieve a P_{d} of 0.9, as depicted in Figure 2.15. These curves are referred to as receiver operating characteristic (ROC) curves and are widely utilized to check the detection performance during the design phase.

However, this may vary depending on factors such as target fluctuations, which are often determined using specific Swerling models [167].

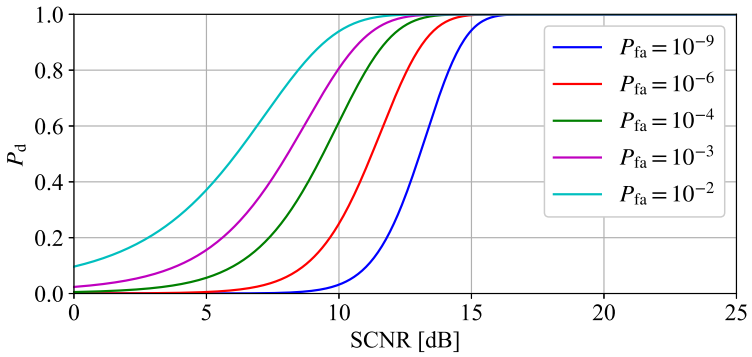

Figure 2.15: Probability of detection versus SCNR for different probabilities of false alarm (ROC curves).

SCNR Performance

The SNR is a critical performance parameter for GMTI radar systems as it directly impacts target detection, tracking accuracy, and overall system performance. It is based on the radar equation [86]. For a given slant range R and target RCS, denoted by σ_t, the SNR is expressed by [87, 138]

$$\text{SNR} \approx \frac{P_t \, G_{tx} \, G_{rx} \, \lambda^2 \, \sigma_t}{(4\pi)^3 \, R^4 \, K T_s \, F L} \, \tau_p \, N_p, \tag{2.52}$$

where P_t denotes the peak power, G_{tx} and G_{rx} are the gain of the transmit and receive antenna, respectively, considering a single azimuth channel, K the Boltzmann constant, T_s the effective noise temperature in degree Kelvin, F the noise figure, L the losses, and N_p the number of integrated pulses.

In every detection scenario, clutter exerts a significant influence on system performance. Its manifestation is contingent upon numerous environmental factors, including incident angles, surface roughness, and atmospheric phenomena such as wind-induced effects in the context of sea clutter, as described in Section 2.3.2. Consequently, it is imperative to thoroughly assess clutter behavior and its impact on detection performance during the system design phase. The Clutter-to-Noise Ratio (CNR) is given by [90]

$$\text{CNR} \approx \frac{P_t \, G_{tx} \, G_{rx} \, \lambda^2}{(4\pi)^3 \, R^4 \, K T_s \, F L} \sigma_0 A_{res} \, \tau_p \, N_p, \tag{2.53}$$

where σ_0 is the clutter reflectivity, also defined as the RCS per unit area of the illuminated surface and $A_{res} = \delta_a \delta_r$ is the resolution cell defined as the product of the azimuth δ_a and range resolution δ_r, respectively.

The SCNR combines both SNR and CNR and is widely used in assessing the performance of GMTI systems and the probability of detection. It is expressed as [168–170]

$$\mathrm{SCNR} = \frac{1}{\frac{1}{\mathrm{SCR}} + \frac{1}{\mathrm{SNR}}} = \frac{\mathrm{SNR}}{\mathrm{CNR}+1}, \tag{2.54}$$

where SCR is the Signal-to-Clutter Ratio when a noise-free scenario is assumed, which can be written as

$$\mathrm{SCR} = \frac{\mathrm{SNR}}{\mathrm{CNR}} = \frac{\sigma_\mathrm{t}}{\sigma_0 A_\mathrm{res}}. \tag{2.55}$$

This leads to

$$\mathrm{SCNR} = \frac{\sigma_\mathrm{t}}{\sigma_0 A_\mathrm{res} + \frac{1}{\mathrm{SNR}}}. \tag{2.56}$$

Substituting the SNR equation (2.52) results in

$$\begin{aligned}
\mathrm{SCNR} &\approx \frac{\sigma_\mathrm{t}}{\sigma_0 A_\mathrm{res} + \frac{(4\pi)^3 K T_\mathrm{s} F L R^4}{P_\mathrm{t}\lambda^2 G_\mathrm{tx} G_\mathrm{rx} \tau_\mathrm{p} N_\mathrm{p}}} \\
&= \frac{\sigma_\mathrm{t}}{\sigma_0 \left(\frac{\lambda R}{2 v_p T_d} \cdot \frac{c_0}{2B \sin\theta_i} \right) + \frac{(4\pi)^3 K T_\mathrm{s} F L R^4}{P_\mathrm{t}\lambda^2 G_\mathrm{tx} G_\mathrm{rx} \tau_\mathrm{p} N_\mathrm{p}}} \\
&= \frac{\sigma_\mathrm{t}}{\sigma_0 \cdot \frac{\lambda c_0 R}{4 v_\mathrm{p} T_\mathrm{d} B \sin\theta_i} + \frac{(4\pi)^3 K T_\mathrm{s} F L R^4}{P_\mathrm{t}\lambda^2 G_\mathrm{tx} G_\mathrm{rx} \tau_\mathrm{p} N_\mathrm{p}}} \\
&= \frac{\sigma_\mathrm{t} N_\mathrm{p}}{\frac{\lambda c_0 R \sigma_0 \,\mathrm{PRF}}{4 v_\mathrm{p} \sin\theta_\mathrm{i} B} + \frac{(4\pi)^3 K T_\mathrm{s} F L R^4}{P_\mathrm{t}\lambda^2 G_\mathrm{tx} G_\mathrm{rx} \tau_\mathrm{p}}},
\end{aligned} \tag{2.57}$$

with B the chirp bandwidth.

Minimum Detectable Velocity

The MDV of a target using a single-channel SAR system can be expressed in terms of the Doppler bandwidth B_D as [171]

$$|\mathrm{MDV}| \approx \frac{\lambda}{4} B_\mathrm{D} = \frac{\lambda v_\mathrm{p}}{2 D_\mathrm{l}}, \tag{2.58}$$

by substituting (2.13). For a SAR operating at X-band with $\lambda = 0.03\,\mathrm{m}$, $v_\mathrm{p} = 20\,\mathrm{m/s}$, and $D_\mathrm{l} = 1\,\mathrm{m}$, the minimum detectable velocity of a target is $0.3\,\mathrm{m/s}$.

3 Adaptive Observing SAR Concept

This chapter introduces the concept of the ADaptive OBserving Synthetic Aperture Radar (ADOB-SAR). It starts with its operational concept and application, highlighting its autonomous principle, which differs significantly from state-of-the-art systems in many aspects: ADOB-SAR operates two concurrent modes with different functions. It relies on its own functionality to control the radar acquisition and does not require any interaction with a human operator, neither onboard nor on the ground. The sensor intelligently identifies areas of interest based on the user's a priori requirements and optimizes its configuration in both transmission and reception to focus on these specific areas for detailed observation. This targeted approach enhances performance in areas where it is most needed. Feedback from the environment is crucial for an instrument's self-reconfiguration, especially when multiple modes with different functions are employed. This chapter gives a first overview of this innovative SAR concept. Section 3.1 deals with the operation concept, while Section 3.2 describes the mode concept followed by the system concept in Section 3.3. Parts of this chapter have been previously published in the conference papers [172, 173], and are described in the journal paper [174].

3.1 Operation Concept

This section delves into the operation concept of the proposed ADOB-SAR. It highlights the intended application, which is user-driven, the platform considerations, and the operation principle based on the cognitive radar approach.

3.1.1 User-Driven SAR Application

ADOB-SAR has a different concept of operation compared to state-of-the-art systems. It is intended to serve one specific operational user with small-scale observations for each acquisition rather than offering a global data collection available to many users. The full operation is based on the user's objectives and can be deployed in diverse applications. It can assist maritime surveillance [175, 176], helping to keep the water secure through constant monitoring of ships, illegal activities, overfishing, and water pollution, as well as mapping natural hazards [177]. The environment of these applications is extremely dynamic and fast-evolving, requiring real-time

functionality. In this new concept, the application and the objective are therefore given to the SAR sensor as input before the start of the acquisition. This is different from classical spaceborne SAR observation, where coverage of the complete Earth or a large part of it is achieved and data are made available hours or days after the event of interest happens. The information content extracted from these data using post-processing is sometimes difficult to interpret. Thus, the objective is to improve the quality of the acquired data and maximize the information content of the user's regions of interest while minimizing system resources. In the context of disaster management, ADOB-SAR can offer real-time situational awareness by collecting data in the immediate aftermath of an incident, which can accelerate any necessary rescue operations.

The ADOB-SAR sensor is versatile and can be deployed in various settings based on user preferences: Before the acquisition, the user provides input, such as specific scenarios, regions, or targets, on which the sensor should focus and deliver high-quality quantitative data. Even during flight, the user can adjust these settings remotely. The ADOB-SAR then prioritizes these areas and filters out irrelevant scene components. The user input options and the performance requirements are then translated into radar internal commands, which are utilized to adapt the acquisition, as illustrated in Figure 3.1 describing the different input scenarios.

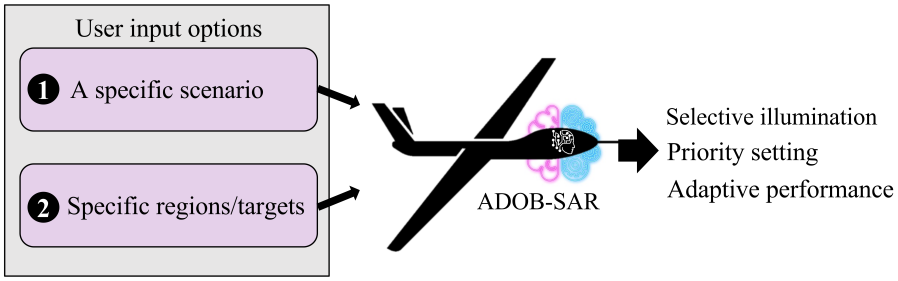

Figure 3.1: The different input scenarios for the ADOB-SAR operation.

3.1.2 Platform Considerations

The platform considered for ADOB-SAR is a high-altitude platform (HAP) fixed-wing aircraft, flying in the stratosphere, as illustrated in Figure 3.2. This selection is based on the following factors. Compared to other platforms, HAP offers constant monitoring of the region of interest not just before and after the occurrence of the event, but also during it, facilitating a more extensive comprehension of the situation. Using spaceborne platforms is challenging as it is strongly dependent on

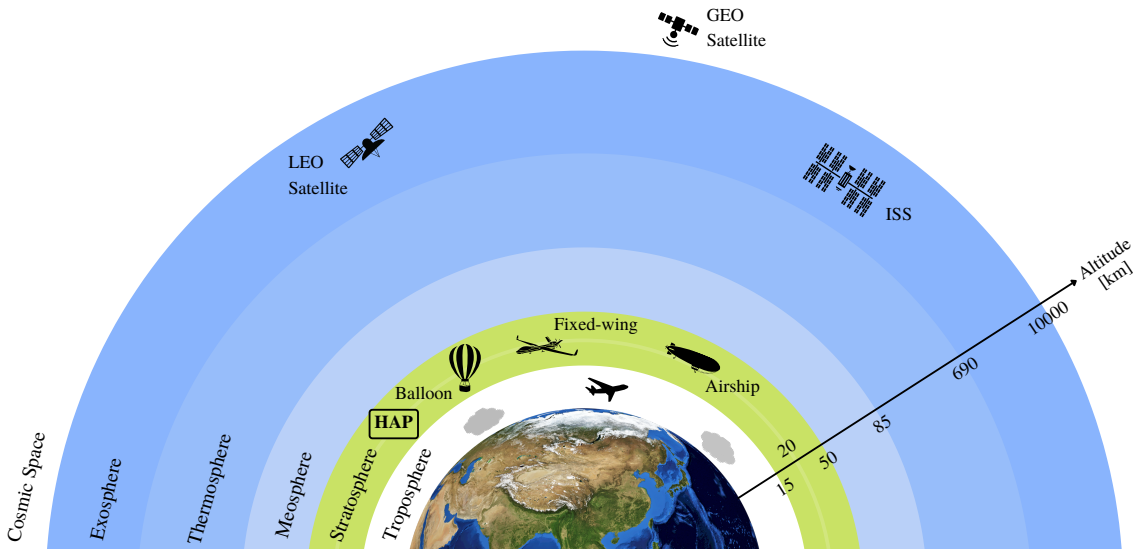

Figure 3.2: Earth's atmosphere layers highlighting the stratosphere, where high-altitude platforms (HAPs) are operated.

their orbital paths and revisit cycles. They might not always be positioned ideally to capture data from a specific area when it is most needed. With extended flight durations ranging from several months to over a year, this platform offers high efficiency in monitoring local areas of interest. Furthermore, it provides the flexibility to switch tasks in just a few minutes, enabling a rapid response to changing user demands. Once launched, HAP travels to the user-defined mission destination and can also relocate to different parts of the Earth for other tasks, thus significantly increasing surveillance capabilities. The platform's endurance offers continuous coverage of specific areas or vast regions over several months, while its reduced sensor distance, compared to spaceborne systems, makes it possible to detect much weaker signals.

The selection of the optimal HAP vehicle depends on the payload capacity, speed, and endurance. A fixed-wing unmanned aircraft has been selected for the ADOB-SAR sensor due to its higher speed, flexibility, and ability to change flight direction and location quickly. The proposed sensor can adapt system performance in real-time through knowledge-aided control and intelligent resource management. As such, it is well-suited for use in a HAP considering the available payload power limitation.

The Earth curvature affects the slant range and the incident angle depending on the platform altitude H and the look angle θ_L. The slant range for a curved Earth with the radius R_e is given by [178, 179]

$$R = \frac{2(R_\mathrm{e}+H)\cos\theta_\mathrm{L} - \sqrt{\left(2(R_\mathrm{e}+H)\cos\theta_\mathrm{L}\right)^2 - 4\left(R_\mathrm{e}^2 - (R_\mathrm{e}+H)^2\right)}}{2}. \tag{3.1}$$

The incident angle deviation caused by the Earth's curvature is given by

$$\theta_{dv} = 2\arcsin\left(\frac{\sqrt{H^2+R^2-2HR\cos\theta_\mathrm{L}}}{2R_\mathrm{e}}\right), \tag{3.2}$$

and plotted in Figure 3.3 for HAP, airborne, and spaceborne platforms with different altitudes.

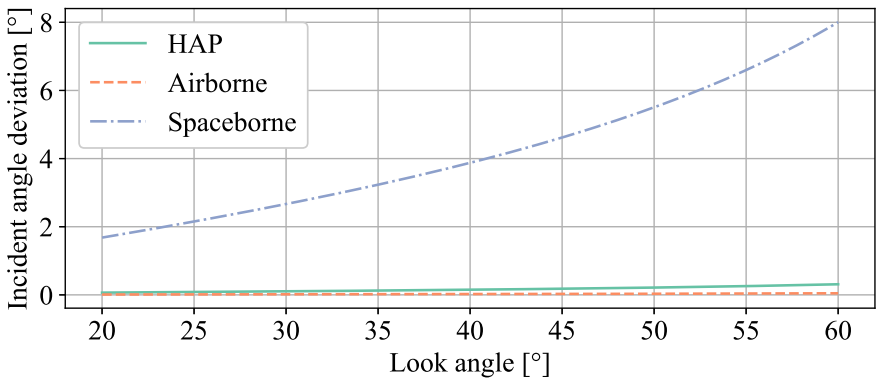

Figure 3.3: Comparison between the incident angle deviations caused by a non-flat Earth for a high-altitude with 20 km, airborne with 3 km, and spaceborne platform with 540 km altitude.

The incident angle deviation for a HAP is very small, as shown in the plotted curve, demonstrating that the curvature of the Earth has a negligible effect on the slant range. A flat Earth is therefore assumed in the design of the ADOB-SAR sensor. This leads to significant simplifications in description and signal processing.

3.1.3 Adaptive Observing SAR Principle

ADOB-SAR selects what to observe and determines the optimal way to do it. Instead of mapping and imaging the entire scene using a predefined configuration, an adaptive setting is employed to image only the regions of high interest with the

desired level of performance. Firstly, it briefly analyzes the environment, and then adapts the acquisition based on the observed data and user requirements. This operation concept adheres to the principle of cognition and is illustrated in Figure 3.4.

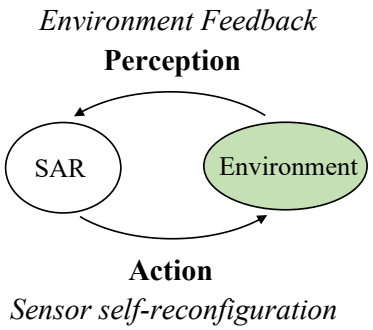

Figure 3.4: The operation principle of the adaptive observing synthetic aperture radar based on cognition.

Cognition is defined as a set of abilities that include knowledge, memory, judgment, and reasoning [180]. They represent the human brain functions. Similar to the eyes and the visual cortex of the brain, radar is a sensor that observes the environment [49]. The goal of cognitive radar is to enhance the functionality and performance of conventional radar systems by emulating certain cognitive abilities of the human brain.

ADOB-SAR is considered a system able to sense the environment and select the appropriate transmit and receive parameters in real-time to optimize its performance. It is seen as an expansion of the adaptive radar, which can process information extracted from target and clutter only at the reception level. This feature is extended by additionally adapting the transmitter on the fly and conceiving a feedback path from the receiver to the transmitter [51]. The sensor creates a perception of its environment and learns relevant information about targets and scenes from it. Then, it takes control over the next transmission, which is the concept of the perception-action cycle introduced by Simon Haykin [50] and shown in Figure 3.5. A perception of the environment is done at the receiver level, which represents the first form of adaptivity. An action is then performed by the transmitter following the feedback from the perception, which transforms the radar into a cognitive sensor.

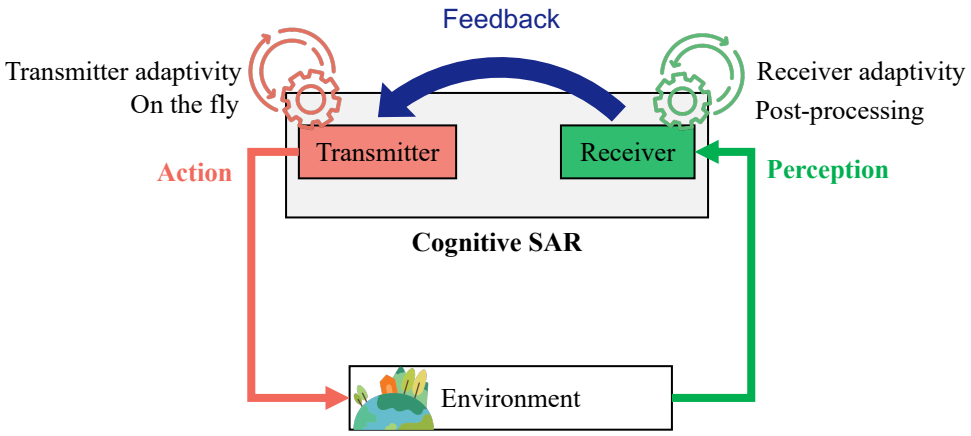

Figure 3.5: Block diagram of a cognitive synthetic aperture radar featuring a feedback loop between the receiver and the transmitter.

The full adaptivity of the SAR system enables the maximization of information content from the observed area. This requires adjustments not only to the received signals after reflection on the Earth's surface but also to the transmitted signal. The quality of the information content depends on the radar backscatter, which is influenced by various radar and surface parameters including frequency, polarization, incident angle, dielectric constant, material, and surface roughness, as described in Section 2.1.4. By adapting these parameters, the backscattering behavior of the signals can be improved, ultimately enhancing the overall quality of the information extracted from the observed scene.

3.2 Mode Concept

The cognitive radar's perception-action cycle is translated into a novel SAR concept that integrates multiple imaging modes. This section introduces the ADOB-SAR operation modes, their unique flow, and the order in which they are executed.

3.2.1 Operational Modes

The ADOB-SAR system interleaves two concurrent imaging modes, which are referred to **MapSearch** and **Tracking** shown schematically in Figure 3.6. Both modes operate simultaneously. The MapSearch mode performs a continuous perception of the surroundings, analogous to the broad observational capability of the human eye. Then, the sensor initiates a reaction by sending an adaptive Tracking mode, which focuses only on areas of interest and maximizes the backscattered information with

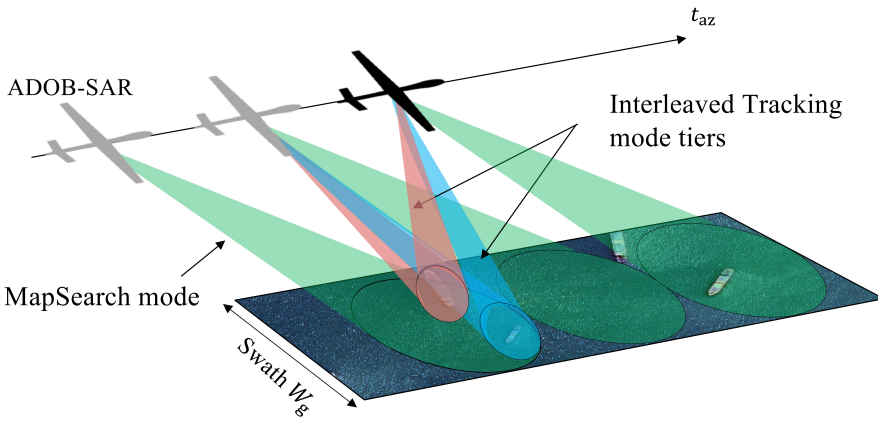

Figure 3.6: Schematic representation illustrating the concurrent imaging modes of the adaptive observing SAR: the MapSearch mode (green beams) and the interleaved Tracking mode tiers (orange and blue beams).

minimal resources. By applying this concept of multiple modes, a knowledge-aided acquisition control is executed that relies on prior observations of the surroundings. Depending on the application and the user's input scenario, the elements of interest in the scene can be individual targets, such as vehicles or houses, as well as regions and larger areas, such as small islands or icebergs. The term *target* is used in the following to refer to both types of elements.

MapSearch Mode

The MapSearch mode is the background imaging mode of the system. It continuously analyzes the echo data from the illuminated swath to extract the information required to reconfigure the sensor. This mode aims to detect and select user-defined targets of interest from a large area using the minimum necessary performance and resources. It operates continuously during flight, with a fixed configuration of beams and instrument parameters. It provides approximate target position and size using low-resolution Stripmap imaging without finer details such as speed and direction in the case of moving targets.

Tracking Mode

The tracking mode is activated automatically once the sensor detects and selects a new target during MapSearch. This mode concurrently tracks and images multiple targets with higher accuracy by generating new beams and adjusting instrument parameters according to the extracted MapSearch information. The reconfigured beams are directed toward the detected objects using a new imaging mode called

Follow Spot or a Circular trajectory SAR, which are detailed in Chapter 4, Sections 4.4.1 and 4.4.2, respectively. The Tracking mode focuses the energy solely on the desired spots using digital beamforming (DBF) and agile two-dimensional beam steering on transmit as well as on receive, enabling precise and high-performance individual imaging of the targets of interest. This mode uses a customized combination of instrument parameters and a scene-matched configuration to optimize the imaging. The Circular SAR is employed exclusively for targets necessitating ultra-high resolution imaging. During the circular platform maneuver, the MapSearch function is temporarily suspended and directly resumed once the platform returns to the linear trajectory

The main Tracking goal is to follow each target individually during transmission and reception, as illustrated in Figure 3.7(a). An exception to this occurs when targets

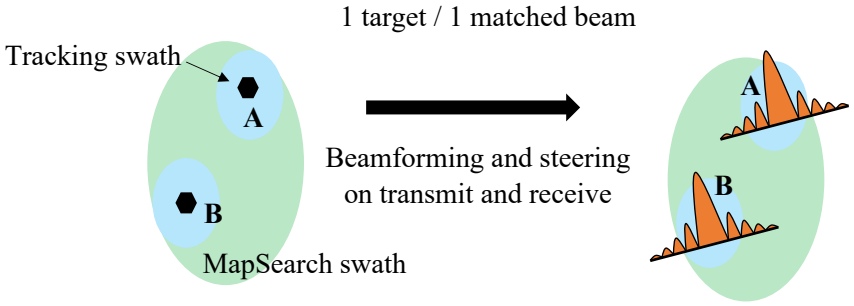

(a) Each target is tracked with a single beam.

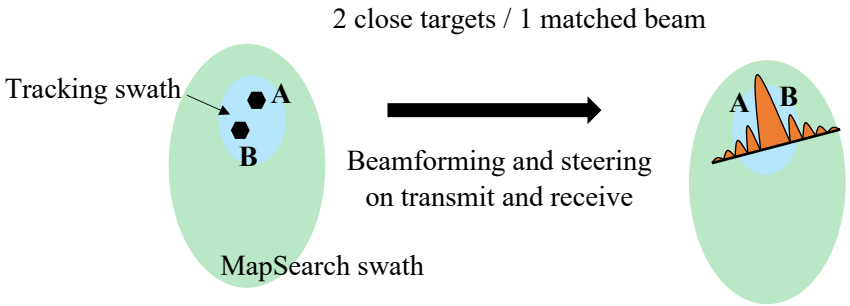

(b) Two targets located closely are tracked with a single beam

Figure 3.7: Target illumination strategy during the Tracking mode.

are located in very close proximity to each other so that individual imaging is no longer possible due to the limited narrowing capabilities of the Tracking beam. This is illustrated in the example shown in Figure 3.7(b), where the distance between target A and B is smaller than the Tracking footprint. In this case, these targets

are illuminated with a single beam adapted to achieve a high performance in terms of spatial resolution.

3.2.2 Mode Rational: from Uncertainty to Certainty

The sensor briefly analyzes the scene by processing the acquired MapSearch mode data in short time intervals onboard. It then sends the extracted target properties, such as imprecise position and size, to a dynamic decision-making processor. The latter uses them to select the targets of interest and adapt the configuration for a new acquisition. The optimized mode parameters are then forwarded to the Tracking mode, which switches on automatically to acquire the desired SAR data and determine precise target information, as shown in Figure 3.8. After being identified

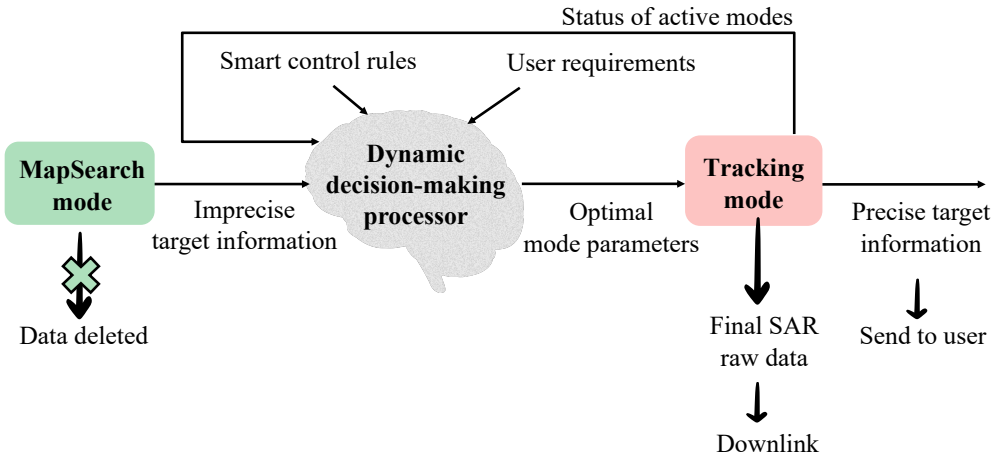

Figure 3.8: The operation loop of the ADOB-SAR system based on the cognitive radar approach.

in MapSearch, each target is either assigned to an already existing Tracking beam or a new beam is specifically generated for it. The MapSearch mode can occasionally give false alarms by mistaking clutter for a target. However, the Tracking mode can efficiently identify and dismiss these invalid targets. This innovative functionality shows the mode flow concept, adeptly transitioning from initial uncertainty to definitive certainty. Even if the MapSearch extracted target position is wrong, it can be corrected during the Tracking by adjusting the beam steering. As new targets need to be detected at regular intervals, the sensor should continually schedule pulses, adjust radar parameters, and reconfigure the beams for optimal performance. This is done automatically by the ADOB-SAR sensor without needing human intervention.

The dynamic processor is capable of selecting the optimal Tracking mode configuration based on a decision-making process with specific adaptive control rules, which are described in Chapter 6.

Once an initial assessment of the targets present in the scene has been conducted, the MapSearch data can be deleted. Only SAR data acquired by the Tracking mode are saved and downlinked directly to Earth. Additionally, the user can request accurate target parameters as a final product. This approach results in a significant reduction of stored and transferred data volume, as only relevant information is retained and data necessary for determining the optimal operation mode can be deleted. Besides, the user has the option to save data collected from the MapSearch mode for offline analysis after the mission has concluded. These data won't be downlinked but will be provided to the user once the platform is back on the ground. This post-mission data retrieval is feasible with high-altitude platforms, like fixed-wing aircraft, which have significant onboard data storage capabilities and frequently return to the ground during the same mission for refueling or battery recharging.

As multiple modes are concurrently operated, the status of all active Tracking modes and their operational SAR parameters and configurations are forwarded back to the dynamic processor to adapt the schedule and verify the sensor's overall duty cycle. Therefore, the operation flow consists of a closed loop between the MapSearch mode, the dynamic decision-making processor, and the Tracking mode, as shown in Figure 3.8. Many operational considerations are addressed when selecting the optimal mode configuration. They are demonstrated in the following chapters.

3.2.3 Multi-Mode Timing Principle

The ADOB-SAR system operates multiple modes concurrently during a single flight via pulse-to-pulse interleaving. The detection of new targets does not disrupt the ongoing MapSearch task, nor does it trigger a transition to another adaptive Tracking mode. Instead, all tasks operate in parallel throughout the acquisition. The adaptive decision-making software uses an adaptive scheduling approach that leverages the available resources and idle time when the sensor is not transmitting nor receiving signals to track more targets. Additionally, multiple Tracking acquisitions, each corresponding to a distinct target, can operate concurrently, as illustrated in Figure 3.9. They are referred to as *Tracking tier*. Hence, interleaving occurs at two levels: multi-mode and multi-target. The duration of the Tracking mode depends on the time needed to observe the target and achieve the desired azimuth resolution. A novel timing strategy, detailed in Chapter 5, has been developed to ensure ambiguity-free pulse-to-pulse interleaving. The concept takes advantage of DBF and multi-dimensional orthogonality techniques to prevent mutual overlap between transmit pulses and/or echoes.

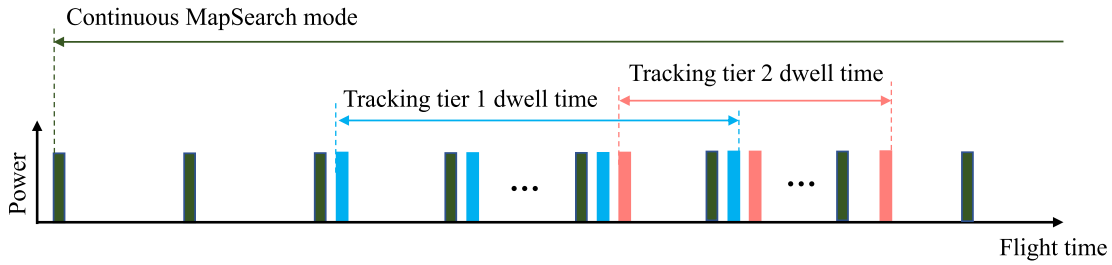

Figure 3.9: Timing example showing the transmit pulses of the interleaved ADOB-SAR modes: the continuous MapSearch and two Tracking tiers with specific dwell times.

3.3 System Concept

As the ADOB-SAR sensor is deployed on a HAP, it requires a compact design that can handle all operational modes. Advanced features are used to implement an adaptive system while taking into consideration the platform's power, size, and weight constraints. The principle involves utilizing minimal but sufficient hardware options

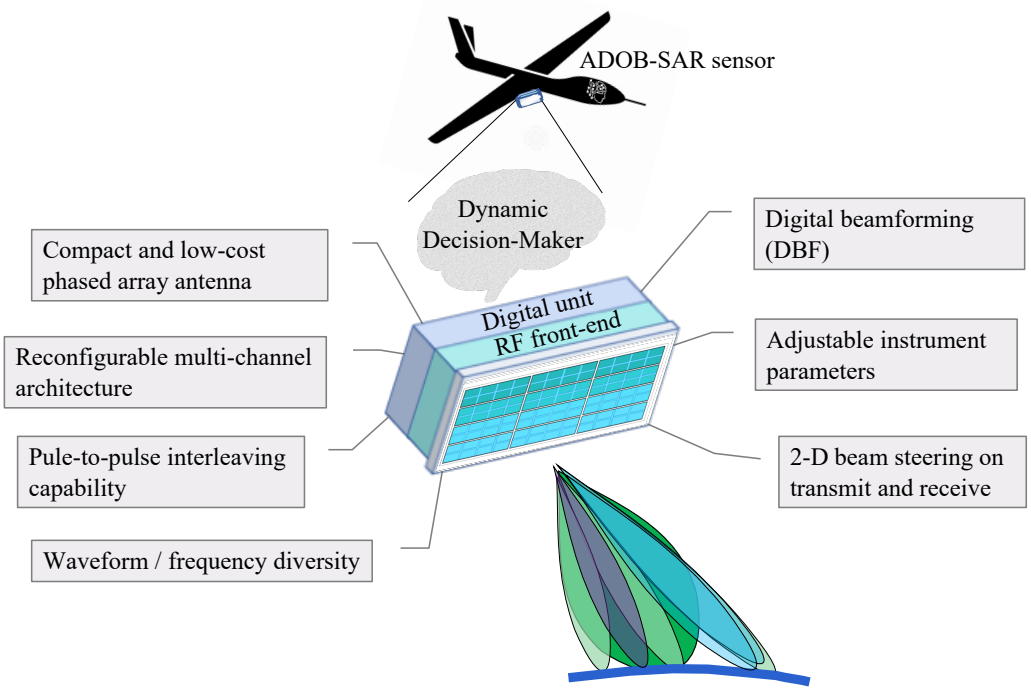

Figure 3.10: ADOB-SAR generic instrument topology and design features.

and resources intelligently. These design features are depicted in Figure 3.10. A reconfigurable multi-channel antenna front-end architecture is used. It is capable of 2-D agile beam steering and supports various adaptive modes. Both the transmit and receive beams can be formed and steered in any direction, allowing flexible and precise imaging of targets located in different areas within the access range. Digital beamforming is deployed and multiple beams can be generated by software on receive. Real-time flexible electronic steering of the beams is therefore achieved, which enhances the detection and tracking accuracy as well as the clutter suppression. The full design guidelines of the ADOB-SAR system are detailed in Chapter 4.

A system's crucial design feature is its capacity to promptly adjust its instrument parameters, adaptively for each scenario, even on a pulse-to-pulse basis. This is achieved by incorporating multiple chirp signal generators, which can be programmed to rapidly switch between diverse waveform parameters, including center frequency, bandwidth, and pulse duration.

Furthermore, the instrument uses waveform agility on the transmit side. It can switch between different waveforms, such as up and down chirps, on the fly to enhance its performance in different scenarios and environmental conditions. Changing the waveform can also suppress interference and ambiguities. The design solutions and features are intended for a future system that would incorporate advancements in HAP technology to support such capabilities.

3.4 ADOB-SAR Concept Summary

ADOB-SAR is a radar system concept designed to adjust its scanning strategy according to real-time information about the environment and observed targets. A target of interest that has been detected and tracked with ADOB-SAR will never be lost during data post-processing. The system can provide more accurate and reliable information to the user, resulting in better decision-making and improved mission operational outcomes.

The concept entails using advanced onboard software and reconfigurable hardware techniques to analyze radar data in real-time and adjust the observation strategy accordingly. Several radar parameters such as center frequency, pulse duration, bandwidth, and antenna pattern are adapted on the fly. By implementing an adaptive observing strategy on a high-altitude platform, enhanced accuracy can be achieved relative to the environment and observed targets, even in adverse circumstances. This approach has significant value in various applications, including disaster response, environmental monitoring, and surveillance. Furthermore, it can tackle the HAP energy challenges by utilizing efficient resource management and multitasking capabilities. The next chapters delve more into the ADOB-SAR features and techniques.

4 Reconfigurable Multi-Mode SAR System Design

The ADaptive OBserving SAR (ADOB-SAR) is a versatile sensor, operating in multiple concurrent modes, each tailored for a specific functionality. Its unique design feature compared to other radar systems is its reconfigurable front-end architecture, employing a single monostatic antenna system for all modes. As each mode has a distinct objective, it requires a different configuration. Therefore, the instrument setup should be able to switch seamlessly during the same acquisition window. A smart beamforming strategy featuring Digital Beamforming (DBF) and SCan-On-Receive (SCORE) is used to cope with the different operational modes. Furthermore, a cost-effective and compact antenna system is designed, prioritizing deployment on high-altitude platforms. Advanced techniques are used to reduce the number of elements while maintaining the desired performance. This chapter provides the full design of the ADOB-SAR instrument, highlighting the developed techniques to achieve exceptional flexibility while maintaining simplicity. It starts with the MapSearch imaging technique in Section 4.1 followed by its corresponding front-end architecture in Section 4.2 and antenna configuration in Section 4.3. The Tracking mode imaging technique is described in Section 4.4 followed by its antenna configuration in Section 4.5 and front-end in Section 4.6. The design methodology provided in this Chapter is described in the journal paper [174].

4.1 MapSearch Mode Imaging Technique

The main task of the MapSearch mode is to acquire information about the environment with minimal performance, focusing solely on target detection and a preliminary qualitative assessment with limited resolution. Wide coverage is preferred for this mode to get a complete view of the entire scene, and hence a Stripmap SAR geometry is applied. The antenna continuously illuminates the maximum achievable swath width denoted by W_{g}, considering the platform height H, as illustrated in Figure 4.1. A mapping-ahead capability is used by squinting the beam slightly ahead of the zero Doppler direction. The beam is thus forward-looking in azimuth. This provides sufficient time for detection processing and Tracking mode activation before potential targets vanish from the field of view.

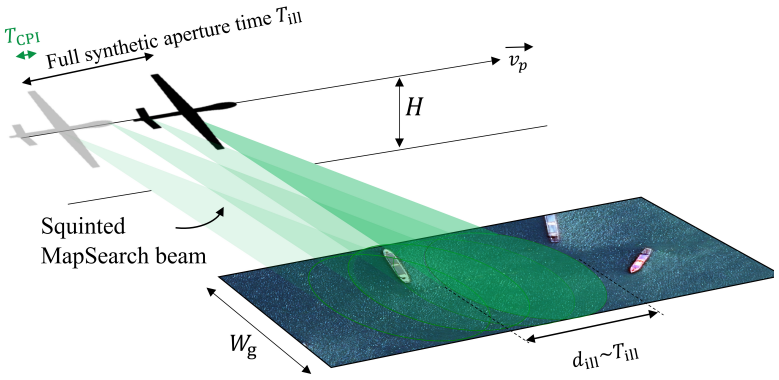

Figure 4.1: Schematic representation of the MapSearch mode imaging strategy. The maximum swath width W_g is illuminated continuously during the flight in a Sripmap geometry. A mapping ahead capability is deployed thanks to a squint in azimuth. The detection is done after each CPI, denoted by T_{CPI}.

A low spatial resolution is sufficient to briefly analyze the scene and ensure real-time onboard processing with a minimal computational load. Therefore, low bandwidth and short integration time are used. The Signal-to-Clutter-plus-Noise Ratio (SCNR) and its resulting probability of detection, defined in (2.57) and (2.50) respectively, are the most relevant performance parameters for the MapSearch mode. The data collected is processed on board using short time intervals known as Coherent Processing Intervals (CPI) [181]. Following the geometry of Figure 4.2, the synthetic aperture denoted by $d_{ill} = T_{ill} v_p$ is typically formed in SAR systems from the point where the target enters the beam footprint, having the beamwidth Θ_{ms} at time t_1 until it leaves it at time t_2. This synthetic aperture is divided into smaller apertures,

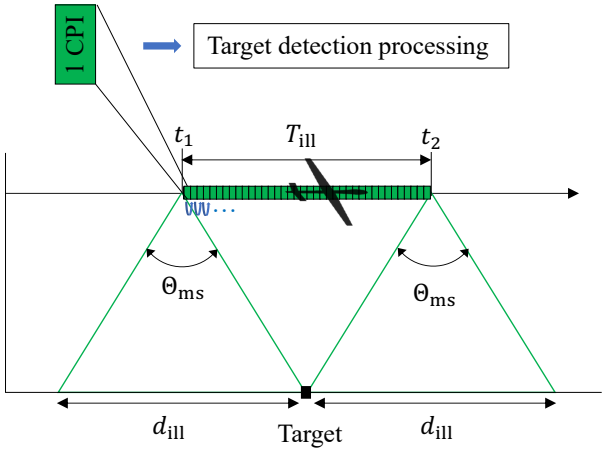

Figure 4.2: MapSearch processing time strategy using small coherent integration intervals, each processed individually.

each processed individually, to achieve a real-time operation but at the expense of a decreased resolution [92, 126, 182]. The acquired CPI data is either deleted upon detection or saved onboard for post-processing of the entire access range on the ground. The MapSearch data is not downlinked from the platform to Earth during the operation.

Therefore, the azimuth resolution $\delta_{\mathrm{a,CPI}}$ used in the detection during MapSearch considers only one CPI, which is denoted by T_{CPI} so that [82]

$$\delta_{\mathrm{a,CPI}} = \frac{\lambda R_{\mathrm{m}}}{2 v_{\mathrm{p}} T_{\mathrm{CPI}}} \tag{4.1}$$

with R_{m} the slant range of the MapSearch beam, and v_{p} the platform velocity. The azimuth resolution can be increased by integrating over the full T_{ill} on the ground after the platform returns to Earth, if desired by the user.

A narrow beam is used in azimuth to ensure a low clutter bandwidth (i.e., (2.15)), and to enhance detection performance by distinguishing between targets moving at different velocities. In SAR imaging, the azimuth beam tends to be wider to achieve a better azimuth resolution by keeping the target within the beam for a longer time. However, as the MapSearch mode does not require fine resolution, a narrow beam is prioritized.

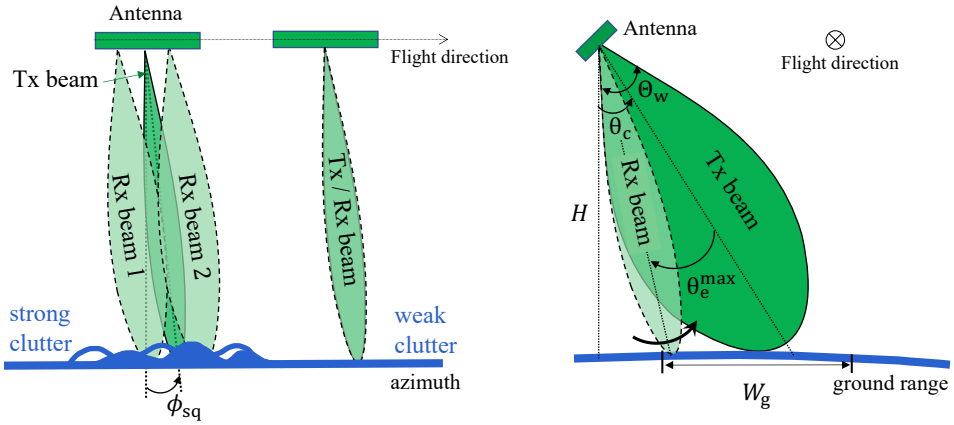

Figure 4.3: Combination of beams for the MapSearch mode on transmit (dark green with solid outline) and on receive(bright green with dashed outline) for the azimuth (left) and elevation direction (right).

The transmit beam is squinted with the angle ϕ_{sq} in azimuth, as shown in Figure 4.3. Depending on the application and the amount of background clutter, the sensor can select between one or two azimuth phase centers on receive as needed to detect the desired targets. In elevation, a wide transmit beam is generated to cover the swath

width W_g based on the platform height H, and a narrow beam is steered within the swath to follow the echo return from near to far range using SCORE [31,112,183,184]. This technique enhances the receive antenna gain, thereby improving the SNR. Its application to the designed sensor is described in more detail in Section 4.1.2.

A summary of the beamforming requirement for the MapSearch mode is outlined in Table 4.1.

	Azimuth	**Elevation**
Tx	narrow beam + fixed squint	wide beam + broadening
Rx	narrow beam + fixed squint	narrow beam + time-variant steering

Table 4.1: MapSearch beamforming requirements for the transmission and reception in the azimuth and elevation direction.

4.1.1 MapSearch Detection Technique

Targets of interest can be stationary or moving, depending on what the user wants to observe. There are different detection techniques depending on the target properties, as illustrated in Figure 4.4.

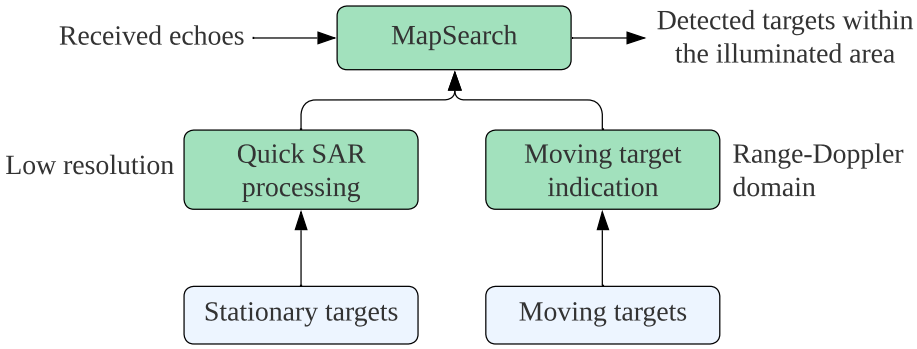

Figure 4.4: The main function of MapSearch mode and the methods used to detect the targets present in the scene.

The easiest and quickest method to identify targets is to verify the signal amplitude from the range profile. It consists of selecting an amplitude threshold that distinguishes the target signal level from the clutter. However, this is only possible when

the target signals exceed the clutter level, which is true for high RCS targets. This method can detect both stationary and moving targets. Unfocused SAR processing can also be used to get a fast SAR image of the surroundings with low resolution without any phase correction or sidelobe suppression. This method is not time-consuming and can provide an initial look at the scene. The relevant components can be then observed with more accuracy during the Tracking mode.

For moving targets, more advanced techniques can be used for detection by taking advantage of their motions relative to the platform. Low RCS moving targets embedded in high clutter can be detected only by using Doppler signal processing, which is the basis of Moving Target Indication (MTI). The detection of moving targets is therefore performed in the Doppler domain, as described in Section 2.3. Only range-compressed SAR data are used to achieve fast processing [128]. Slow-moving targets, which produce Doppler frequencies within the clutter Doppler bandwidth B_{Dc} can not be identified. Only by using a multi-channel receiving antenna system with different azimuth phase centers that the clutter can be suppressed making the detection of slow and low RCS targets possible [28, 134]. The diagram shown in Figure 4.5 represents a design guideline for the SAR instrument. Usually, only one configuration is applied (single or multiple channels). However, both settings can be used during MapSearch, as ADOB-SAR is capable of estimating the clutter behavior on the fly, which will be described in more detail in the following sections.

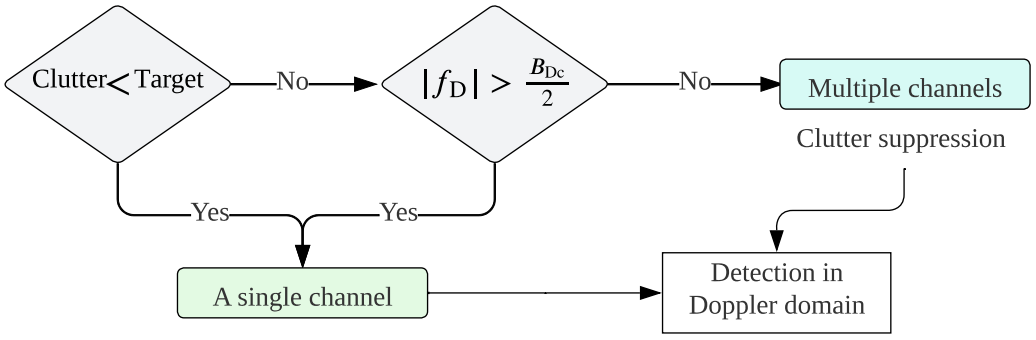

Figure 4.5: Design requirement on the number of azimuth receive channels for target detection depending on the clutter level and motion.

4.1.2 SCORE Imaging Technique

The SCan-On-REceive technique [21, 31, 184] is implemented during the MapSearch mode to increase the SNR while collecting data over a large area with a high receive

antenna gain. A wide elevation beam, with the HPBW denoted by Θ_{ms}, is generated to cover the largest possible range ambiguity-free swath width on transmit. During the reception, DBF is applied in elevation using a multi-channel architecture to digitally steer the receive beam having a narrower HPBW, denoted by Θ_{sc}, as shown in Figure 4.6. The digitized signals are multiplied by time-varying complex-valued weights $w_{\mathrm{i}}(t)$, with $i = 1, 2, \ldots, N_{\mathrm{e}}$, and summed up generating a receive beam that follows the return echo. SCORE can achieve a higher gain despite covering a wide area, as the beam is narrower on receive. The SNR is therefore improved especially at the edges of the swath. The time-varying weighting vector applied to the antenna

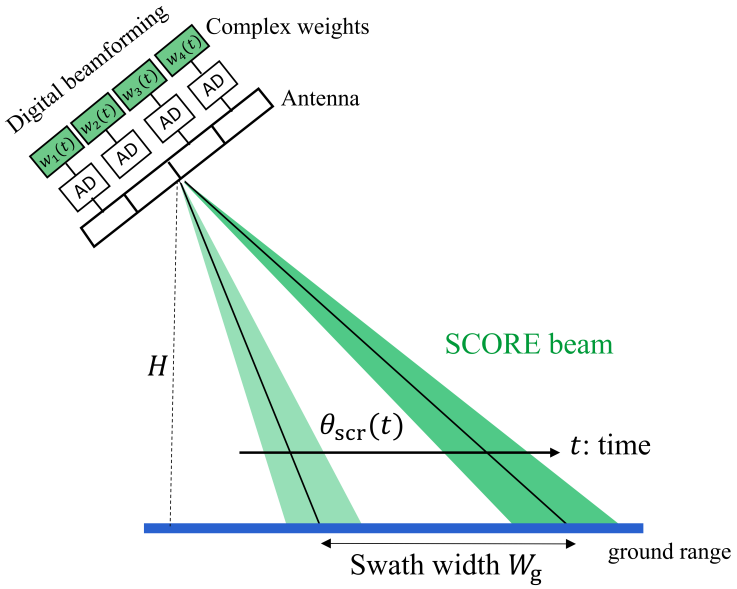

Figure 4.6: SCORE geometry in elevation where the receive beam is steered over time with the angle $\theta_{\mathrm{scr}}(t)$ using the digital channels multiplied by time-varying complex weights, $w_i(t)$ with $i \in [1, N_{\mathrm{e}}]$. $N_{\mathrm{e}} = 4$ in this example.

elements or sub-apertures depends on the steering angle $\theta_{\mathrm{scr}}(t)$ and is given by

$$\mathbf{w}(t) = \begin{pmatrix} 1 \\ e^{\mathrm{j}1kd_{\mathrm{e}} \sin\theta_{\mathrm{scr}}(t)} \\ \cdots \\ e^{\mathrm{j}N_{\mathrm{e}}kd_{\mathrm{e}} \sin\theta_{\mathrm{scr}}(t)} \end{pmatrix}, \tag{4.2}$$

for an array of N_e digitized elements in elevation spaced with d_e. The radiation pattern of the SCORE beam in elevation varies therefore over time and is given by

$$C_\mathrm{scr}(\theta,t) = C_\mathrm{e}(\theta)\mathrm{AF}_\mathrm{scr}(\theta,t) = C_\mathrm{e}(\theta)\sum_{n=1}^{N_\mathrm{e}} A_\mathrm{n} e^{\mathrm{j}k(n-1)\ d_\mathrm{e}\ (\sin\theta - \sin\theta_\mathrm{scr}(t))} \tag{4.3}$$

according to (2.30), where $\theta_\mathrm{scr}(t)$ follows the echo direction of arrival. The switching step of the digital steering follows (2.45).

Precise and agile control over the beam pattern is required for SCORE, where dynamic tracking of echoes is essential. Such control cannot be accomplished solely through analog beamforming methods based on phase shifters as they may not provide the necessary precision due to possible quantization errors and phase resolution limitations. The accuracy of the beam pointing, crucial in this context, is significantly challenged by unknown terrain topography. Digital beamforming, offering advanced adjustments, becomes necessary to ensure precise echo tracking and optimal signal reception. Using the ADOB-SAR principle, it is possible to analyze the topography briefly before starting with the actual acquisition [185–187]. Hence, the digital signal processing can be adjusted to the surroundings in real-time.

To apply the SCORE technique, a large antenna height is needed, which implies a higher gain and results in enhanced MapSearch detection performance. SCORE is also utilized to separate multi-mode echoes received simultaneously from different directions, as described in Chapter 5.

4.2 MapSearch Instrument Design

This section introduces the instrument configuration of the MapSearch mode. It includes the antenna front-end architecture and the different techniques used to minimize the size and cost, considering the Tracking mode requirements, as the same antenna is utilized for both modes. The configuration described in this section is only valid for the MapSearch mode. A different and more advanced configuration is used for Tracking and will be explained in Section 4.6.

4.2.1 Azimuth Front-End Architecture

The ADOB-SAR sensor uses an active phased array antenna. Its MapSearch configuration is shown in Figure 4.7 for the transmit case. The antenna elements are arranged in azimuth into subarrays to minimize the number of control components. This technique is widely used to reduce the mass, power consumption, and cost of

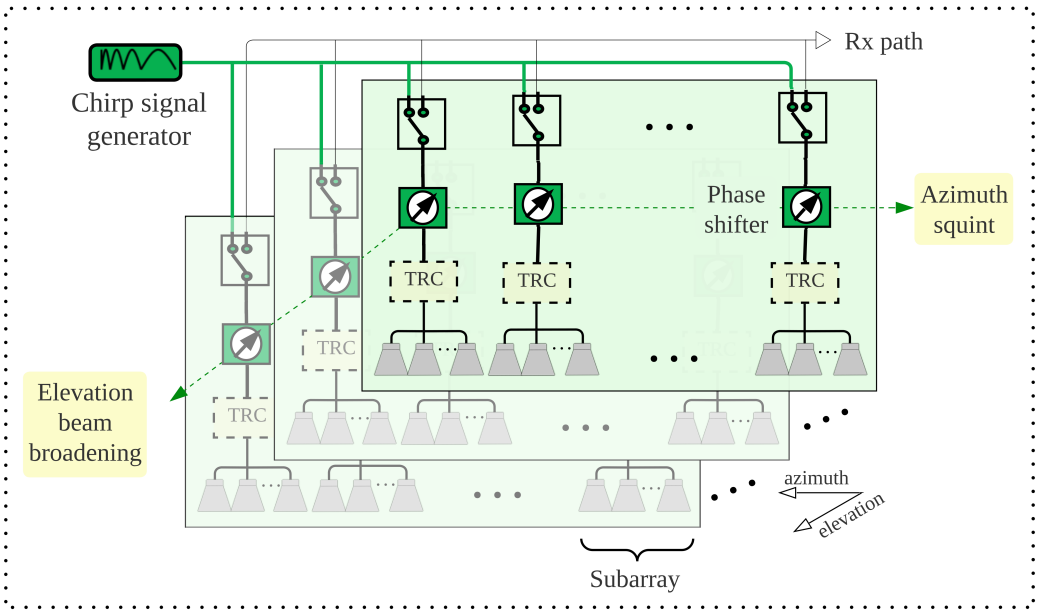

Figure 4.7: A schematic of the MapSearch mode front-end architecture on transmit. Each subarray is connected to a Transmit/Receive Core (TRC).

the phased array front-end. Each subarray is connected to a Transmit/Receive core, denoted by TRC and shown in Figure 4.8, including a circulator to switch between transmission and reception paths, a low-noise amplifier (LNA) to amplify received weak signals with minimal noise, and a high-power amplifier (HPA) to increase the power level before transmission. Using TRCs leads to a compact and integrated solution with minimal losses compared to individual components with external connections. The subarray in azimuth is considered passive as it does not have active control over the individual elements. Phase shifters are used to steer the beam in

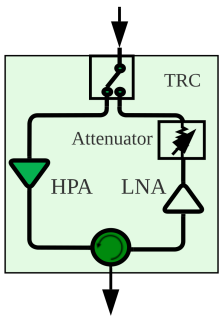

Figure 4.8: Transmit/Receive Core (TRC) during transmission.

azimuth toward the desired squint angle. The customized TRC does not include a

phase shifter, which is typically found in conventional TR modules used for phased arrays. Instead, phase shifters are placed outside of the TRCs to eliminate the need to increase the number of TRCs when multiple beams are desired requiring additional phase shifting stages.

The front-end topology on receive is illustrated in Figure 4.9. The phase shifters are used again to receive the echo from the squinted azimuth direction ϕ_{sq}. The

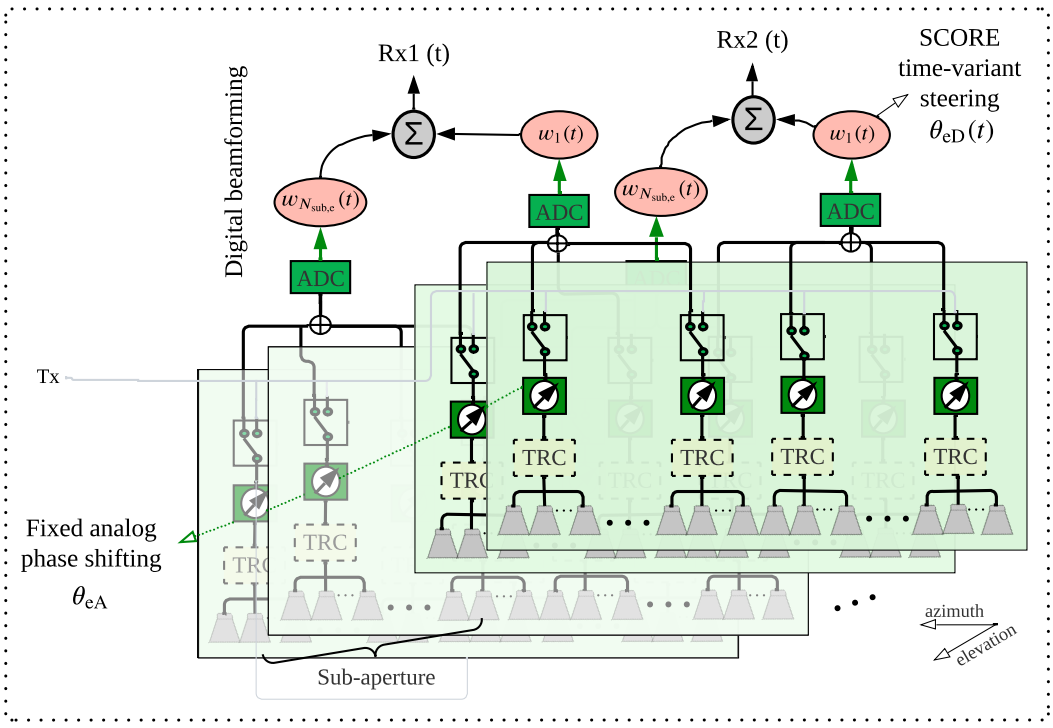

Figure 4.9: MapSearch mode front-end architecture on receive.

number of digital channels is adapted according to the clutter behavior. When the clutter is weak, detection is done using a single phase center, and the full aperture is digitized through one digital channel. In case of strong clutter, the array is divided in azimuth into two sub-apertures that are digitized and processed separately. This creates two phase centers within the antenna array to effectively suppress the clutter and eliminate the irrelevant background. The clutter level can be determined from a priori knowledge or previous MapSearch data by making assumptions about the background statistics, as described in Section 2.3.2 and [152].

4.2.2 Elevation Front-End Architecture

In elevation, the same phase shifters as for azimuth are used, but at the antenna element level to perform analog beam broadening on transmit. It is applied by spoiling the phase distribution of the array while keeping all antenna elements activated [188, 189], as shown in Figure 4.7. This technique is described in more detail in Section 4.3.4.

On receive, a multi-channel digital beamforming configuration is applied. Digitizing each antenna element in the array is the optimal solution in terms of flexibility and performance. However, it is not cost-effective and adds additional complexity and cost to the front-end, mainly due to dynamic range considerations and data processing load. Therefore, sub-apertures of several antenna elements are created and digitized, as illustrated in Figure 4.9. This design employs hybrid SCORE [21, 31, 190] beamforming, which uses a combination of analog and digital beam steering, to minimize the number of required ADCs. Each antenna element in the digital sub-aperture is connected to a phase shifter, similar to the transmit case. The receive beam is first steered in the analog domain to θ_{eA} using the phase shifters. Then, the digitized signals are steered over time with $\theta_{\mathrm{eD}}(t)$ to generate a beam that follows the return echo from near to far range. This hybrid technique is detailed in Section 4.3.5. The steering angles and all antenna parameters are derived in Section 4.3.

4.3 MapSearch Antenna Configuration

The ADOB-SAR 2-D antenna array consists of $N_{\mathrm{e}} \times N_{\mathrm{a}}$ antenna elements separated by d_{e} and d_{a} in elevation and azimuth, respectively. The respective antenna array dimensions $D_{\mathrm{h}} = N_{\mathrm{e}} d_{\mathrm{e}}$ and $D_{\mathrm{l}} = N_{\mathrm{a}} d_{\mathrm{a}}$, shown in Figure 4.10, are determined by a trade-off between the desired beam footprint on the ground and the available payload space on HAP. The antenna radiators are grouped into N_{sa} passive and non-overlapping subarrays in azimuth spaced with d_{sa}. In elevation, the elements are spaced with d_{e}. During reception, sub-apertures are formed and digitized in elevation and azimuth. The digital beamforming on receive is performed using $N_{\mathrm{sub,e}}$ active sub-apertures in elevation having the spacing $d_{\mathrm{sub,e}} = D_{\mathrm{h}}/N_{\mathrm{sub,e}}$. Similarly, the antenna is divided in azimuth into $N_{\mathrm{sub,a}}$ digital sub-apertures separated by $d_{\mathrm{sub,a}} = D_{\mathrm{l}}/N_{\mathrm{sub,a}}$.

The maximum allowable spacing between elements, subarrays, and sub-apertures is primarily determined by the occurrence of grating lobes. This is influenced by the maximum scanning angle, which depends on the system's requirements, geometry, and imaging mode. This section delves into the antenna configuration including

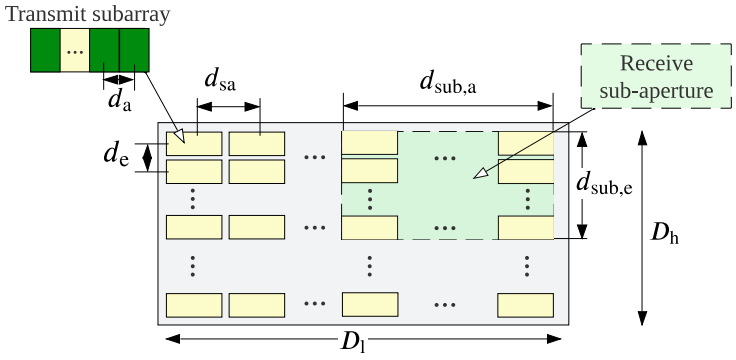

Figure 4.10: The ADOB-SAR 2-D antenna array topology consisting of $N_{\mathrm{e}} \times N_{\mathrm{a}}$ radiators separated by d_{e} and d_{a} and grouped on transmit into $N_{\mathrm{e}} \times N_{\mathrm{sa}}$ subarrays separated in azimuth by d_{sa} and on receive into $N_{\mathrm{sub,e}}$ and $N_{\mathrm{sub,a}}$ active sub-apertures in elevation and azimuth, respectively

the design of all parameters and techniques required to achieve the objective of the MapSearch illumination.

4.3.1 Azimuth Squint Angle

The azimuth squint angle applied to steer the MapSearch beam to the forward-looking direction, denoted by ϕ_{sq}, depends on the imaging geometry and various mode parameters. Having a high squint angle allows for a longer illumination time and transition from MapSearch to Tracking. However, it requires a smaller subarray spacing, which increases the overall number of elements and front-end hardware. Therefore, selecting the appropriate squint angle is crucial, as it strikes a balance between instrument performance, complexity, and cost.

The operation starts with the MapSearch mode, which is registered for every CPI. At $t = t_1$, the target's last echo is collected just when it moves out of the MapSearch transmit beamwidth Φ_{ms}, as depicted in Figure 4.11. The sensor starts tracking the target at $t = t_2 = t_1 + T_{\mathrm{td}}$ after a time delay

$$T_{\mathrm{td}} = T_{\mathrm{proCPI}} + T_{\mathrm{trans}}, \tag{4.4}$$

composed of the detection processing interval T_{proCPI} and the mode transition time T_{trans} from MapSearch to Tracking. At $t = t_3 = t_2 + T_{\mathrm{tr}}$, the Tracking mode ends when the illumination time required for a specific resolution is achieved.

To determine the largest necessary squint angle, ϕ_{sq}, the worst-case scenario is considered. This scenario assumes that the target is at a near range R_{near} and moves in the opposite direction of the platform with the maximum velocity $\max\{|v_{\mathrm{tg}}|\}$ known

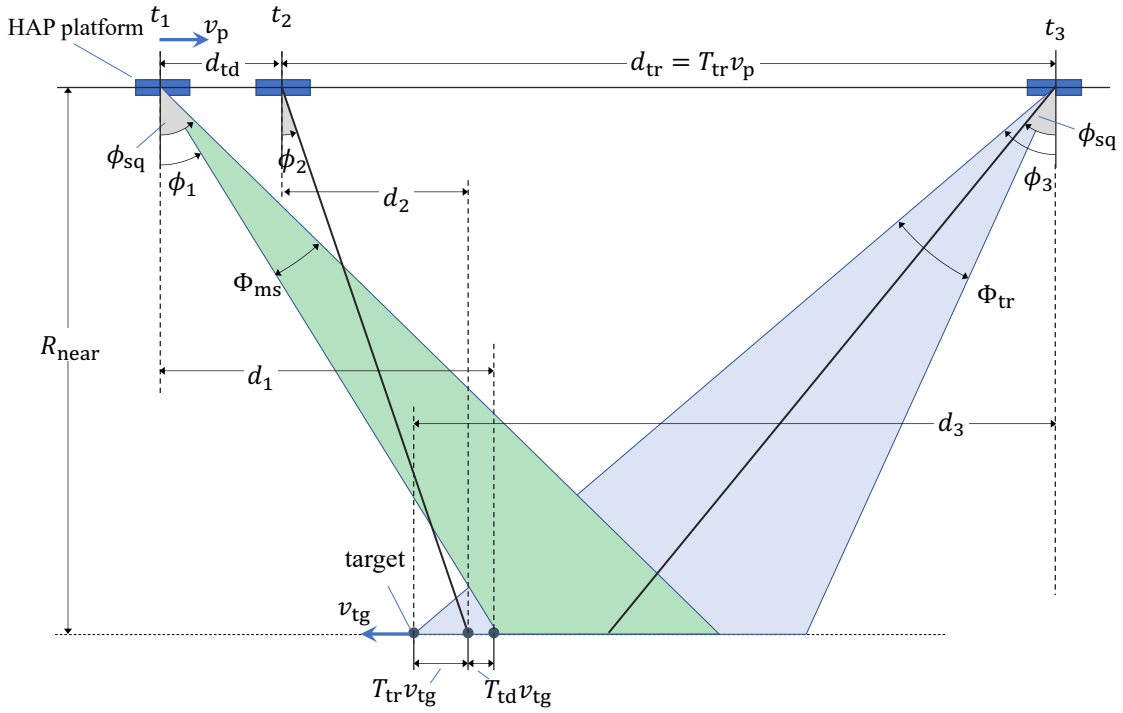

Figure 4.11: Geometry for the HAP and the sent azimuth beams of the two interleaved modes. The left beam in green corresponds to the MapSearch mode, where it is squinted forward with the angle ϕ_{sq}. At the time t_2, the Tracking mode starts imaging the detected target by sending a beam to the direction ϕ_2 and steering it along the flight to the angle ϕ_{tr} at time t_3.

from the requirements. To simplify the analysis, a two-dimensional geometry is considered and illustrated in Figure 4.11, formed by a plane containing the platform track and a target at near range.

The illumination time of the MapSearch mode is given by

$$T_{ill} = R_{near}\left(\tan\left(\phi_{sq} + \frac{\Phi_{ms}}{2}\right) - \tan\left(\phi_{sq} - \frac{\Phi_{ms}}{2}\right)\right). \tag{4.5}$$

It contains more than one CPI with the duration T_{CPI}. The near and far slant ranges R_{near} and R_{near} consider the boresight of the antenna, as depicted in Figure 4.12, and depend only on the platform height H and the elevation looking angles θ_{near} and θ_{far} for near and far ranges, respectively. They are given by

$$R_{near} = \frac{H}{\cos(\theta_{near})}, \qquad R_{far} = \frac{H}{\cos(\theta_{far})}. \tag{4.6}$$

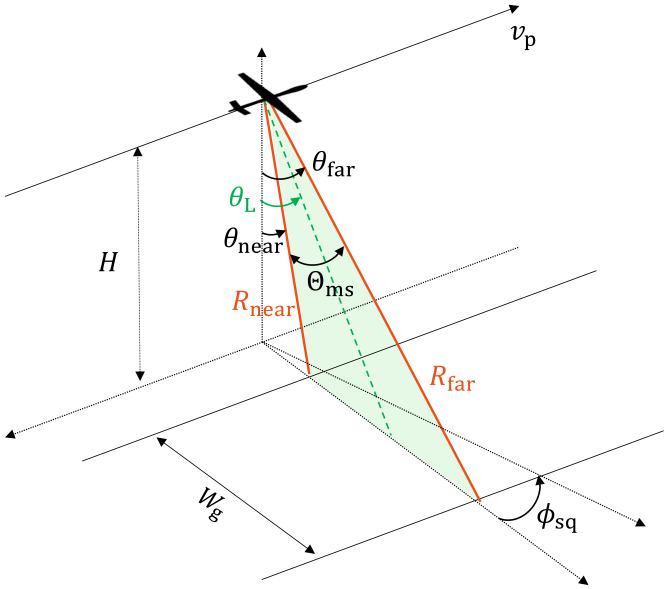

Figure 4.12: 2-D geometry featuring the elevation parameters of the boresight direction, the near and far slant ranges R_{near} and R_{far} and their corresponding looking angles θ_{L}, θ_{near}, and θ_{far} taking into consideration the platform altitude H.

Thus, at t_1 the target is at azimuth angle $\phi_1 = \phi_{\text{sq}} - \Phi_{\text{ms}}/2$. At the time $t_2 = t_1 + T_{\text{td}}$, the platform and target will have moved in opposite directions by a distance of $v_{\text{p}} T_{\text{td}}$ and $v_{\text{tg}} T_{\text{td}}$, respectively. According to Figure 4.11,

$$d_1 = d_2 + d_{\text{td}} + T_{\text{td}} v_{\text{tg}}, \tag{4.7}$$

where $d_i = R_{\text{near}} \tan \phi_i, \forall\ i = 1, 2, 3$. Rewriting the equation in terms of the squint angle and rearranging it to collect the unknown terms on the left side gives

$$\tan\left(\phi_{\text{sq}} - \frac{\Phi_{\text{ms}}}{2}\right) - \tan \phi_2 = \frac{T_{\text{td}}\,(v_{\text{p}} + v_{\text{tg}})}{R_{\text{near}}}. \tag{4.8}$$

This relation proves that the azimuth squint angle depends on the Tracking mode, in particular on its start angle ϕ_2, as well as the distance traveled by the platform and the target during the time delay T_{td}.

If the HAP were to follow a circular flight path in the Tracking mode, the azimuth angle would be $\phi_2 = 0$. However, it is assumed here that the trajectory of the HAP continues along a straight flight path. During this time, the target is imaged with a spotlight geometry, with the beam directed towards its position, for T_{tr} seconds while the platform travels a distance of $d_{\text{tr}} = T_{\text{tr}} v_{\text{p}}$.

The maximum steering angle in the Tracking mode is presumed to be equal to the squint angle, resulting in symmetrical steering with a minimal number of antenna elements. Consequently, when the target exits the tracking beam at $t = t_3$, its

azimuth angle is $\phi_3 = \phi_{\text{sq}} + \Phi_{\text{tr}}/2$, where Φ_{tr} is the transmit beamwidth of the tracking mode. The maximum Tracking illumination time d_{tr} can be be expressed as

$$\begin{aligned} d_{\text{tr}} &= T_{\text{tr}} v_{\text{p}} = d_2 + d_3 - T_{\text{tr}} v_{\text{tg}} \\ &= R_{\text{near}} \tan\phi_2 + R_{\text{near}} \tan\left(\phi_{\text{sq}} + \frac{\Phi_{\text{tr}}}{2}\right) - T_{\text{tr}} v_{\text{tg}}, \end{aligned} \tag{4.9}$$

following the geometry in Figure 4.11.

The distance d_{tr} has a significant impact on the target's azimuth resolution, position accuracy, and velocity accuracy, and is therefore typically determined based on the user requirements and target properties. For example, the azimuth Tracking resolution can be approximated as $\delta_{\text{a}}^{\text{T}} \approx \lambda R_{\text{near}}/2d_{\text{tr}}$, the same way the MapSearch resolution is defined in (4.1) with the only difference that $d_{\text{tr}} \gg d_{\text{CPI}}$. Rearranging the above equation (4.9) gives

$$\tan\phi_2 + \tan\left(\phi_{\text{sq}} + \frac{\Phi_{\text{tr}}}{2}\right) = \frac{d_{\text{tr}}}{R_{\text{near}} v_{\text{p}}}(v_{\text{tg}} + v_{\text{p}}). \tag{4.10}$$

Inserting the expression of $\tan\phi_2$ from (4.8) in (4.10) leads to

$$\tan\left(\phi_{\text{sq}} - \frac{\Phi_{\text{ms}}}{2}\right) + \tan\left(\phi_{\text{sq}} + \frac{\Phi_{\text{tr}}}{2}\right) = \frac{(v_{\text{tg}} + v_{\text{p}})(d_{\text{tr}} + T_{\text{td}} v_{\text{p}})}{R_{\text{near}} v_{\text{p}}}. \tag{4.11}$$

Due to the non-linearity of the obtained equation, the MapSearch squint angle ϕ_{sq} can be calculated by solving (4.11) numerically. The resulting value of ϕ_{sq} is plotted in Figure 4.13 as a function of the Tracking mode illumination time T_{tr} for various mode transition time delays T_{td}. It is shown that a small azimuth squint ϕ_{sq} in the

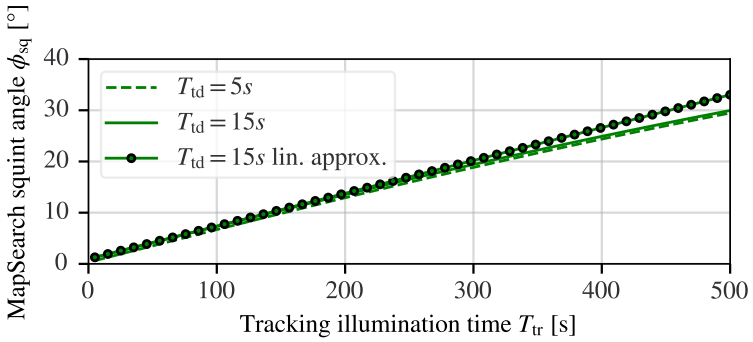

Figure 4.13: MapSearch squint angle ϕ_{sq} versus the Tracking mode illumination time T_{tr} for different mode transition time delays T_{td} considering A HAP with $v_{\text{p}} = 20\,\text{m/s}$. Here equal MapSearch and Tracking mode transmit beamwidths are assumed $\Phi_{\text{ms}} = \Phi_{\text{tr}} = 2°$.

order of some degrees is sufficient to achieve a high resolution. It increases linearly with both transition time T_{tr} and illumination time T_{td}.

When the MapSearch and Tracking beamwidths Φ_{ms} and Φ_{tr} are also small, the tangent terms in (4.11) can be approximated with $\tan x \approx x$ leading to

$$\phi_{\mathrm{sq}} \approx \frac{(v_{\mathrm{tg}} + v_{\mathrm{p}})(d_{\mathrm{tr}} + T_{\mathrm{td}} v_{\mathrm{p}})}{2R_{\mathrm{near}} v_{\mathrm{p}}} + \frac{\Phi_{\mathrm{ms}} - \Phi_{\mathrm{tr}}}{4}, \tag{4.12}$$

which justifies the linear behavior observed in the curve of Figure 4.13. The linear approximation (4.12) may be used for smaller T_{tr} up to 200 s. The longer the time delay between MapSearch and Tracking and the Tracking illumination time, the greater the squint angle should be. This plot can be used later by the system designer to easily select the required MapSearch azimuth squint angle for a specific Tracking resolution requirement.

4.3.2 Azimuth Antenna Parameters

To steer the azimuth beam to the fixed MapSearch squint angle ϕ_{sq} without decreasing the radiation performance, the antenna element spacing should be well-designed. The traditional approach to select this spacing is to apply the classical grating lobe condition (2.43). The spacing directly affects the number of elements required in the array and is a key factor in determining the overall cost and weight of the phased array antenna. Therefore, reducing the number of elements in the array, especially for a HAP, is preferred and can be achieved by carefully balancing the conflicting requirements of element spacing and system performance.

A large azimuth subarray spacing of $d_{\mathrm{as}} > \lambda/2$ is used in this design, resulting in grating lobes in the array factor. As the full array pattern is the multiplication of the subarray pattern and the array factor, $C_{\mathrm{a}} = C_{\mathrm{sub,a}} \cdot \mathrm{AF}_{\mathrm{a}}$, as outlined in equation (2.47), the grating lobes can be suppressed by the subarray pattern. To achieve this, the grating lobe center point ϕ_{GL} should coincide with the first null of the subarray pattern $\phi_{\mathrm{sub}}^{\mathrm{FN}}$, defined in (2.33).

The grating lobes are therefore suppressed when

$$\phi_{\mathrm{GL}} = \phi_{\mathrm{sub}}^{\mathrm{FN}}, \tag{4.13}$$

as shown in Figure 4.14(a).

This condition considers that the grating lobes are symmetric relative to the boresight direction $\phi = 0$. However, the entire array is steered to ϕ_{sq} leading to a phase shift of the grating lobes in the full array factor to ϕ_{sq} as well, as illustrated in Figure 4.14(b).

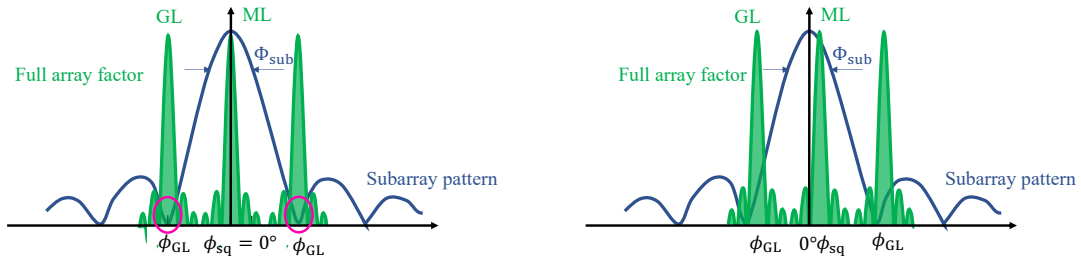

(a) No azimuth squint ($\phi_{sq} = 0$) resulting in symmetric grating lobes.

(b) Azimuth squint ($\phi_{sq} \neq 0$) resulting in non-symmetric grating lobes.

Figure 4.14: Representation of the azimuth transmit subarray pattern with the HPBW Φ_{sub} and the array factor of the full aperture highlighting the effect of the main lobe (ML) steering on the symmetry of the grating lobes (GL) relative to the subarray boresight direction and first nulls.

The full array pattern in azimuth, with N_{sa} subarrays separated by d_{sa}, is the multiplication of the subarray pattern $C_{sub}(\phi)$ with the full array factor $AF_{array}(\phi)$ and is expressed as

$$C_{array}(\phi) = \underbrace{C_e(\phi)\frac{\sin\left(\frac{N_{as}}{2}kd_{as}(\sin\phi)\right)}{N_{as}\sin\left(\frac{1}{2}kd_{as}(\sin\phi)\right)}}_{\text{Subarray pattern } C_{sub}(\phi)} \underbrace{\frac{\sin\left(\frac{N_{sa}}{2}kd_{sa}(\sin\phi-\sin\phi_{sq})\right)}{N_{sa}\sin\left(\frac{1}{2}kd_{sa}(\sin\phi-\sin\phi_{sq})\right)}}_{\text{Full array factor } AF_{array}(\phi)}, \tag{4.14}$$

for an azimuth subarray consisting of N_{as} antenna elements separated by d_{as}. The subarray pattern is fixed to the boresight direction without additional steering. When the array factor is steered to ϕ_{sq}, the grating lobes are no longer symmetric relative to the subarray pattern. The left grating lobe is at $\phi_{GL}^{-} = -\phi_{sub}^{FN}$ and the right grating lobe is at

$$\phi_{GL}^{+} = \mid \phi_{GL}^{-} \mid + \phi_{sq}. \tag{4.15}$$

Thus, the intersection between the subarray first nulls and the grating lobes is no longer possible for both left and right lobes simultaneously, as shown in Figure 4.14(b). The average value between the right and left is therefore used to force the grating lobes to be at

$$\phi_{GL} = \phi_{sub}^{FN} - \frac{\phi_{sq}}{2}. \tag{4.16}$$

Using this approach, the grating lobes are not fully suppressed by the subarray pattern but are typically attenuated by better than $-20\,\text{dB}$. With respect to the specifications of the proposed ADOB-SAR system, this is an acceptable level.

The azimuth subarray spacing is then given by

$$d_{sa} = \frac{\lambda}{\sin\mid \phi_{sub}^{FN} - \frac{\phi_{sq}}{2} \mid + \sin\mid \phi_{sq} \mid}, \tag{4.17}$$

by inserting ϕ_{GL} from (4.16) in equation (2.42) as long as $\phi_{\mathrm{sq}} < \Phi_{\mathrm{sub}}/2$.

To achieve a better suppression of the grating lobes when the full array is steered to the maximum squint angle, the subarray pattern should also be steered to ϕ_{sq} so that the grating lobes become symmetric relative to the subarray boresight direction and thus coincide with its first nulls. In this case, equation (4.13) is valid. Nevertheless, this requires the phase control of all elements in the subarray level on azimuth, which is not suitable for the subarray deployment goal to reduce the hardware complexity and cost, especially for small squint requirements. As described in (4.14), the azimuth squint is generated by changing the phase of each subarray, which is considered a single stacked antenna element.

4.3.3 Staggered Array Configuration

Another way to prevent grating lobes and increase the spacing between elements is to use the triangular lattice [104, 191]. In an antenna array, a lattice refers to the physical distribution of the elements. The most commonly used lattice is rectangular with uniformly distributed elements. A triangular lattice is a special type where the elements are arranged in a repeating pattern of equilateral triangles, as illustrated in Figure 4.15. This configuration can also be referred to as staggered since the elements are nearly interleaved in distinct planes. The triangular grid can be seen as a rectangular grid with alternate elements removed. The geometry of the equilateral triangle lattice creates a smaller virtual spacing between the elements.

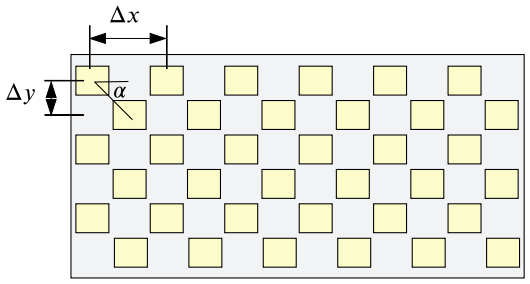

Figure 4.15: A triangular lattice antenna array with Δx the spacing between elements in a row (x-axis) and Δy the spacing between elements in every column (y-axis) distributed with the cell angle α.

The coordinates of the (n, m) element in a triangular grid array are given by

$$x_n = n\Delta x + \frac{m\Delta y}{\tan\alpha}, \qquad y_m = m\Delta y, \tag{4.18}$$

where Δx is the element spacing in each row and Δy the element spacing in each column shown in Figure 4.15. The angle α represents the cell angle and has a direct influence on the lattice geometry. An $\alpha = 90°$ results in a rectangular lattice. In the case of an equilateral triangular grid with $\alpha = 60°$ the element spacing in the y-axis is given by

$$\Delta y = \Delta x \sin \alpha = \Delta x \frac{\sqrt{3}}{2}. \tag{4.19}$$

Grating lobes also occur in a triangular grid array. Therefore, the element spacing should be optimized as well. However, the main advantage of this technique is that the element area is larger compared to the rectangular grid, resulting in fewer antenna elements with the same grating lobe performance.

For the same maximum steering angle θ_e in elevation and θ_a in azimuth , the distance between the elements should satisfy

$$\Delta y \leq \frac{\lambda}{1 + \sin \theta_{\mathrm{e}}}, \tag{4.20}$$

$$\Delta x \leq \frac{\lambda}{\frac{1 + \sin \theta_{\mathrm{a}}}{\sin \alpha}}, \tag{4.21}$$

where Δx is larger than the regular rectangular element spacing d_{rec}. For the example of $\alpha = 60°$, $\Delta x \approx 1.155\ d_{\mathrm{rec}}$, as shown in Figure 4.16. This results in approximately 15% fewer antenna elements for the same steering angle. Hence, the number of reduced elements is determined by the solid angle in which the main beam is positioned [192].

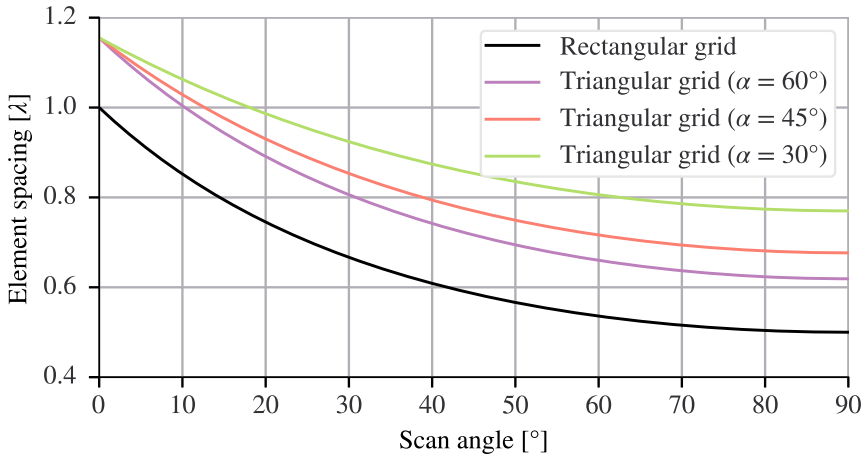

Figure 4.16: Required element spacing variation with the scan angle using the rectangular and the triangular lattices for different cell angles α.

The 2-D array factor of a triangular grid array is given by [104]

$$\mathrm{AF}_{\mathrm{tri}}(\theta,\phi) = \sum_{n=1}^{N_\mathrm{a}} \sum_{m=1}^{N_\mathrm{e}} A_{nm} e^{\mathrm{j}k(n\Delta x + \frac{m\Delta y}{\tan\alpha})(u-u_\mathrm{s}) + m\Delta y(v-v_\mathrm{s})}, \tag{4.22}$$

with $u = \sin\theta\cos\phi$, $v = \sin\theta\sin\phi$, $u_\mathrm{s} = \sin\theta_\mathrm{e}\cos\phi_\mathrm{a}$, and $v_\mathrm{s} = \sin\theta_\mathrm{e}\sin\phi_\mathrm{a}$. It can also be expressed as the multiplication of two array factors, each in one direction such as

$$\mathrm{AF}_{\mathrm{tri}}(\theta,\phi) = \sum_{n=1}^{N_\mathrm{a}} A_n e^{\mathrm{j}kn\Delta x(u-u_\mathrm{s})} \sum_{m=1}^{N_\mathrm{e}} A_m e^{\mathrm{j}km\Delta y((v-v_\mathrm{s}) + \frac{u-u_\mathrm{s}}{\tan\alpha})}. \tag{4.23}$$

Figure 4.17 shows a simulated 2-D array factor comparison between the triangular and the regular rectangular lattice configurations for the same element spacing. A

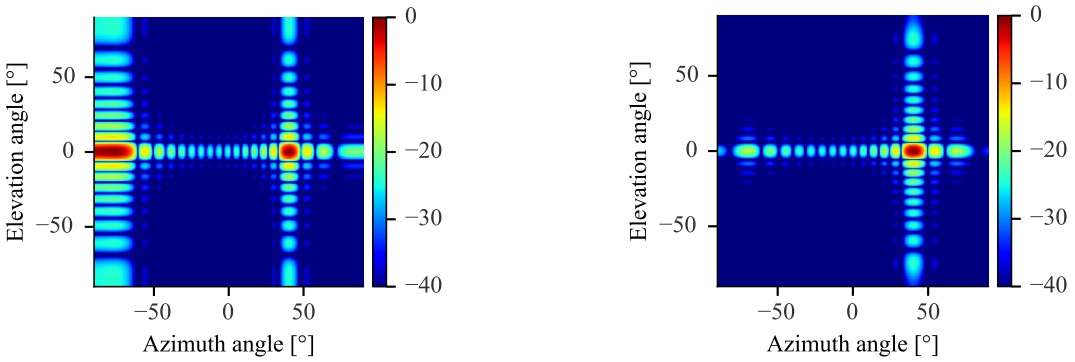

(a) Rectangular lattice.

(b) Triangular lattice.

Figure 4.17: 2-D array factors for rectangular and triangular lattices of an array of 16 elements spaced with $\Delta x = d_\mathrm{rec} = 0.6\lambda$ and steered to 40° in azimuth.

grating lobe is evident in the rectangular lattice configuration, as the element spacing exceeds the threshold specified by (2.43) for a steering angle of 60°. In contrast, the triangular lattice array factor is free from any grating lobes, demonstrating the effectiveness of this configuration in suppressing unwanted signal interference. Ultimately, the lattice choice depends on the beamforming requirements and application constraints, balancing cost, gain performance, and design complexity.

4.3.4 Elevation Transmit Beam Broadening

During MapSearch, a wide elevation beam is generated to illuminate the desired swath. The antenna configuration in elevation is provided in the following, and all the required parameters are derived. The required illumination beamwidth in elevation, denoted by Θ_{w}, depends on the platform altitude H and the swath width W_{g}, which is defined as

$$W_{\mathrm{g}} = \frac{R_{\mathrm{far}} - R_{\mathrm{near}}}{\sin\theta_{\mathrm{far}}}, \tag{4.24}$$

where the subscripts $_{\mathrm{near}}$ and $_{\mathrm{far}}$ relate the quantity to the near and far range, respectively, as illustrated in Figure 4.12. The antenna illumination beamwidth is therefore expressed through geometry and using (4.24) as

$$\sin\Theta_{\mathrm{w}} = \frac{W_{\mathrm{g}}\cos\theta_{\mathrm{far}}}{R_{\mathrm{near}}} = \frac{W_{\mathrm{g}}H}{R_{\mathrm{near}}R_{\mathrm{far}}}. \tag{4.25}$$

It corresponds to the required MapSearch azimuth HPBW Θ_{ms}.

The antenna height D_{h} is usually designed considering the beamwidth Θ_{w} illuminating the entire swath. However, the receive beam is narrower in this concept, as described in the MapSearch imaging strategy illustrated in Figure 4.3. Therefore, the antenna height is larger and the transmit beam is broadened using beamforming techniques. There are different techniques to broaden the antenna beam. The first consists of applying amplitude tapering. The second is phase tapering, which involves adjusting the phase excitation of the antenna elements. These two techniques are described in this section followed by a novel beam broadening technique using the superposition of steered sub-apertures.

Amplitude Tapering with a Rectangular Window

For a linear antenna array with N_{e} elements uniformly distributed in the elevation direction with the spacing d, the half power beamwidth is given by

$$\Theta = 0.886\frac{\lambda}{N_{\mathrm{e}}d} \tag{4.26}$$

when all elements are activated, as defined in (2.35) for $\theta_0 = 0$. To increase the beamwidth Θ, the number of elements should be decreased. Hence, some elements of the antenna aperture are deactivated by setting their amplitude excitation to $A_{\mathrm{n}} = 0$, as illustrated in Figure 4.18.

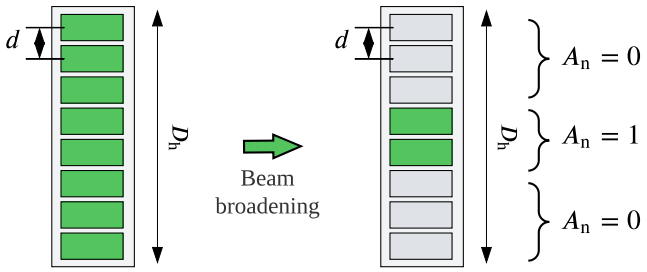

Figure 4.18: The antenna array configuration used to broaden the beam by changing the amplitude excitation and in consequence the number of active elements.

The number of required elements N_e^b for the larger beamwidth Θ^b depends on the desired beam broadening factor γ_b with

$$N_e^b = \frac{\Theta}{\Theta^b} N_e = \frac{N_e}{\gamma_b}. \tag{4.27}$$

One advantage of this method is that it produces an antenna pattern, with no increase in sidelobe level and minimal irregularities or ripples in the main beam. However, deactivating elements in the array can lead to a significant decrease in the overall gain of the antenna expressed by

$$G_{Tx}^b = \mu_{ant} \left(\frac{4\pi N_e^b d}{\lambda^2} \right) = \frac{G_{Tx}}{\gamma_b}, \tag{4.28}$$

where μ_{ant} is the antenna efficiency and G_{Tx} is the gain when using all elements in the array. The resulting gain of the broadened array can be better expressed in decibels as

$$G_{Tx}^b/\mathrm{dB} = 10 \log_{10}(N_e^b) + G_e/\mathrm{dB} = 10(\log_{10}(N_e) - \log_{10}(\gamma_b)) + G_e/\mathrm{dB}, \tag{4.29}$$

with G_e/dB the element gain. This means that reducing the number of elements with the factor γ_b results in a gain reduction of the order of $10 \log_{10}(\gamma_b)$, as shown by the plotted antenna patterns in Figure 4.19, which correspond to the configuration of Figure 4.18. In this example, only two adjacent elements $N_e^b = 2$ are used to generate the transmit beam out of $N_e = 8$ elements, which results in a broadening factor of $\gamma_b = 8/2 = 4$. The resulting beam has therefore the beamwidth $\Theta^b = 4\Theta$, while the antenna gain is only (1/4) of the total array gain following (4.28). This corresponds to a gain decrease of $-6\,\mathrm{dB}$, which aligns with (4.29), as demonstrated in the simulated antenna pattern of Figure 4.19.

Nevertheless, the available peak power is divided among all TR cores during the design. Given that only a few elements are used in the array, only the corresponding

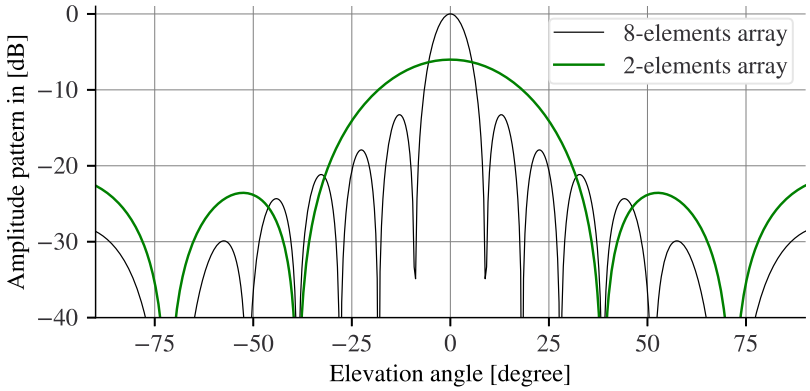

Figure 4.19: Normalized antenna pattern of an array of 2 and 8 adjacent elements separated by 0.8λ with a beamwidth of 31° and 7.75°, respectively.

power is radiated through those elements, which leads to an additional decrease in the overall radiated power with

$$P_{\text{avg,out}} = \frac{P_{\text{t}} d_{\text{c}}}{\gamma_{\text{b}}}, \tag{4.30}$$

where P_{t} is the available peak power and d_{c} is the duty cycle. It is important to note that the decrease in gain and radiated power can be offset by increasing the peak power. However, this approach may not always be practical due to the power constraints of the platform and the input signal specifications of the HPA. Therefore, careful consideration must be given to the trade-offs between beam broadening and radiated power when using this method.

Quadratic Phase Spoiling

In this method, beam broadening is achieved by using a quadratic phase distribution along the antenna elements while maintaining a constant amplitude. Quadratic phase tapering is a common phase spoiling technique used in antenna array design to control the beamwidth and shape of the radiation pattern [100, 193]. It involves applying a phase excitation that varies quadratically across the elements of the antenna array, given by

$$\vartheta_n(x_n) = 4\vartheta_{\max} \left(\frac{x_n}{D_{\text{h}}} \right)^2, \tag{4.31}$$

with x_n the position of the element n in the array, $\vartheta_{\max}$ the maximum phase value at the edge elements. This phase tapering is applied to the antenna weighting vector. During the MapSearch mode, the transmit beam is not steered in elevation.

Therefore, only this phase excitation is applied to the array, leading to the array factor given by

$$\mathrm{AF}(\theta) = \frac{1}{N}\sum_{n=1}^{N} e^{\mathrm{j}(n-1)\frac{2\pi}{\lambda}d\sin\theta+\mathrm{j}\vartheta_n}, \tag{4.32}$$

by substituting the phase excitation (4.31) in (2.27) with N the total number of elements and d their relative spacing. An example of a phase spoiled beam using

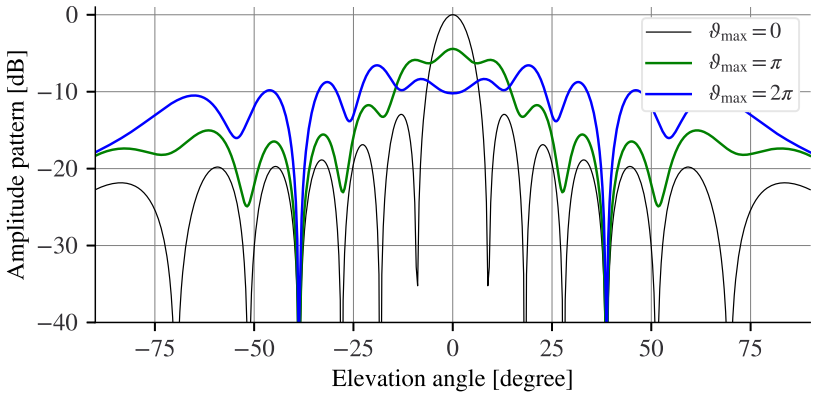

Figure 4.20: Normalized antenna pattern of an array of 8 elements separated by 0.8λ using the quadratic phase spoiling defined in (4.31).

quadratic tapering is plotted in Figure 4.20. It can be seen that the beam shaping results in a decrease in the directivity by −6 dB. The broadening in the boresight has a symmetric pattern and depends solely on the maximum edge tapering of the quadratic function. To generate a specific beamwidth, it is necessary to have prior knowledge of the corresponding maximum quadratic phase distribution.

The quadratic phase tapering can however result in higher sidelobes. Some ripples in the main direction of the beam can also occur, which affects the 3 dB beamwidth property of the pattern. Therefore, it is important to carefully design and optimize the phase tapering coefficients using processing compensations to achieve the desired performance [102, 122].

Superposition of Steered Sub-Apertures

In this method, the full antenna array is partitioned into two sub-apertures, each with its own set of phase shifters and amplifiers. Each subarray is designed to generate a beam in a specific direction. By steering the two subarrays in opposite directions, two broadened beams are formed, each with distinct beamwidth and

sidelobe level. The two steered beams are then combined by summing their patterns, resulting in a much wider beam with a lower sidelobe level. Each sub-aperture

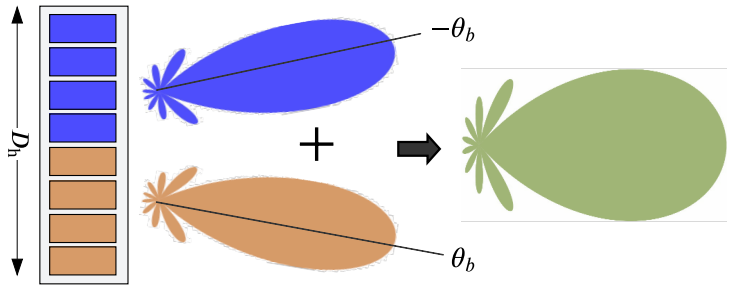

Figure 4.21: The superposition of two sub-apertures steered to opposite elevation directions results in a broadened beam. The sub-apertures are steered in this example symmetrically to $\pm\theta_b$.

generates a wider beam with a half-power beamwidth Θ_s pointed to a distinct direction, as illustrated in Figure 4.21. This method is considered a dual-beamforming approach.

The collective sum of the two beams is expressed in terms of the array factor as

$$\mathrm{AF}(\theta) = \frac{2}{N}\sum_{n=1}^{N/2} e^{\mathrm{j}(n-1)\frac{2\pi}{\lambda}d\sin(\theta-\theta_{b1})} + \frac{2}{N}\sum_{n=1}^{N/2} e^{\mathrm{j}(n-1)\frac{2\pi}{\lambda}d\sin(\theta-\theta_{b2})}, \tag{4.33}$$

with θ_{b1} and θ_{b2} the steering angles of the first and second subarrays, respectively. The resulting array factor can be multiplied with the element factor to get the total radiation pattern out of the two sub-apertures.

The beam broadening factor increases with the steering angles of the sub-apertures, as shown in Figure 4.22 illustrating the broadened antenna pattern using symmetric steering angles according to (4.33). The resulting beamwidth Θ^{b} depends on the beamwidth of sub-aperture Θ_s and their symmetric steering angles θ_b and is derived as

$$\Theta^{\mathrm{b}} = \begin{cases} 2\left(\frac{\Theta_s}{2} + \theta_b - \left(\frac{\Theta_s}{2} - \theta_b\right)\right) & \text{for } \theta_b \leq \frac{\Theta_s}{2} \\ 2\left(\frac{\Theta_s}{2} + \theta_b + 2(\theta_b - \frac{\Theta_s}{2})\right) & \text{for } \theta_b > \frac{\Theta_s}{2} \end{cases}, \tag{4.34}$$

leading to

$$\Theta^{\mathrm{b}} = \begin{cases} 4\theta_b & \text{for } \theta_b \leq \frac{\Theta_s}{2} \\ 6\theta_b - \Theta_s & \text{for } \theta_b > \frac{\Theta_s}{2}. \end{cases} \tag{4.35}$$

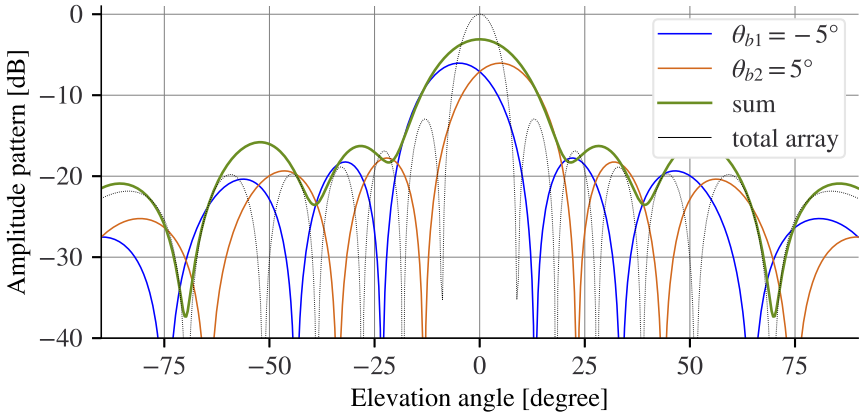

Figure 4.22: Normalized radiation pattern of the broadened beam (in green) using the sum of two sub-aperture patterns steered symmetrically in opposite directions. The resulting broadened beamwidth is $\Theta^{\mathrm{b}} = 20°$ and the gain decrease is in the order of $-3\,\mathrm{dB}$. A array of 8 elements separated by 0.8λ is used.

Ripples can occur in the resulting pattern when the main lobes of the two sub-apertures no longer overlap due to a large steering. Those ripples in the summation pattern can be reduced by steering the sub-apertures non-symmetrically so that $\mid \theta_{b1} \mid \neq \mid \theta_{b2} \mid$. However, this results in a small steering of the broadened beam to the angle

$$\theta^{\mathrm{b}}_{\mathrm{steer}} = \theta_{b1} + \theta_{b2}. \tag{4.36}$$

An example of this configuration using non-symmetric steering angles is shown in Figure 4.23. The first subarray steered to $\theta_{b1} = -6°$ and the second to $\theta_{b2} = 9°$,

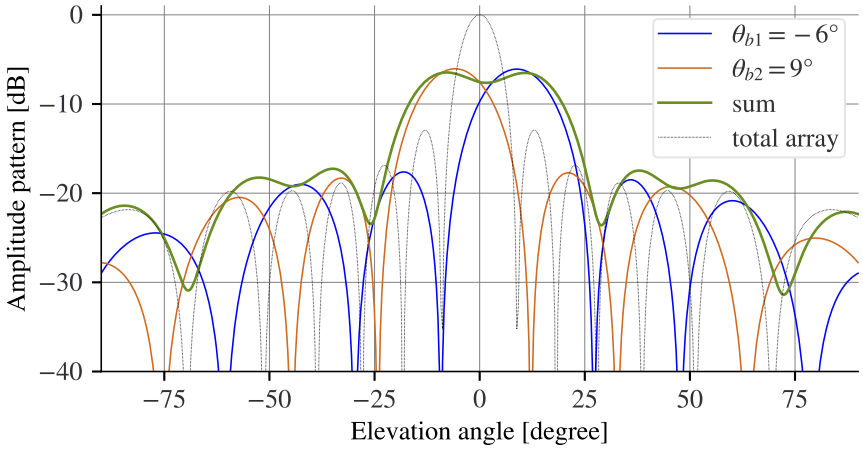

Figure 4.23: Normalized radiation pattern of two superimposed sub-apertures with opposite and non-symmetric steering angles. A array of 8 elements separated by 0.8λ is used.

resulting in a broadened beamwidth of $\Theta^{\mathrm{b}}_{\mathrm{steer}} = 35°$ with a ripple of $\approx 1\,\mathrm{dB}$ and a slight steering to $\theta^{\mathrm{b}}_{\mathrm{steer}} = 3°$, as defined in (4.36). This additional steering is relevant if an antenna tilt different from the center swath is used. This method can be useful to achieve a wider coverage area while maintaining a sufficient antenna gain.

The resulting broadened beamwidth in this case of non-symmetric steering is given by

$$\Theta^{\mathrm{b}}_{\mathrm{steer}} = \Theta^{\mathrm{b}} - \theta^{\mathrm{b}}_{\mathrm{steer}}, \tag{4.37}$$

with Θ^{b} defined in (4.35) and $\theta^{\mathrm{b}}_{\mathrm{steer}}$ in (4.36).

This beam broadening method can also be considered another form of phase tapering, with a triangular linear distribution, as shown in Figure 4.24 illustrating the resulting phase excitation of the symmetric and non-symmetric steering.

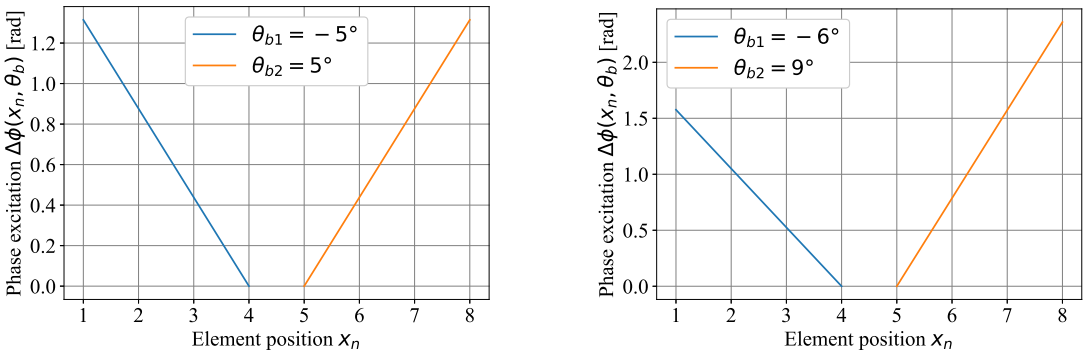

(a) Symmetrical phase excitation

(b) Non-symmetrical phase excitation

Figure 4.24: The different phase excitations applied to the sub-apertures to direct their beams toward symmetrical and non-symmetrical steering angles θ_{b1} and θ_{b2}.

Comparison of Beam Broadening Techniques

The subarray superposition method offers greater control over the sidelobe levels and beamwidth than the other two described beam broadening techniques. Amplitude tapering is not suitable for the ADOB-SAR concept because it inefficiently reduces the amount of power emitted, ultimately worsening the SNR. In contrast, phase tapering can broaden the beam without causing power dissipation issues. Overall, the decision to employ the dual-beamforming approach to create two widened beams and subsequently combine their steered patterns to generate a wider beam is determined by the particular needs and limitations of the application. When selecting the optimal beam broadening technique, a trade-off between gain, loss, and

other performance metrics such as beamwidth and sidelobe level needs to be considered. A performance comparison between the three described methods for the same broadened beamwidth is listed in Table 4.2. More advanced array pattern synthesis techniques can be additionally used by applying suitable optimization processes. They involve automatically determining the amplitude and phase excitation of the antenna array to meet specific performance criteria [122, 194]. Combining different broadening techniques can also result in an enhanced performance [195].

	Amplitude tapering with rectangular window	**Quadratic phase spoiling**	**Superposition of steered sub-apertures**
Gain loss [dB]	-6	-6	-6
Power loss [dB]	-6	0	0
Beam ripples [dB]	0	-1.5	-1
Sidelobe level [dB]	16	13	13

Table 4.2: Comparison between the three beam broadening techniques for the same beam broadening factor of $\gamma_\mathrm{b} = 4$

4.3.5 Elevation SCORE Hybrid Beamforming

The receive aperture in elevation D_h is divided into $N_\mathrm{sub,e}$ non-overlapping sub-apertures capable of steering the received beam digitally over time to perform the SCORE technique. The elevation beam is steered within the illumination beamwidth Θ_w covered by the transmit beam, defined in (4.25) and shown in Figure 4.25, up to the maximum steering angle ${\theta_\mathrm{e}}^{\max}$ defined as

$${\theta_\mathrm{e}}^{\max} = \max\left(\theta_\mathrm{tilt} - \theta_\mathrm{near}, \theta_\mathrm{far} - \theta_\mathrm{tilt}\right), \tag{4.38}$$

considering the side-looking geometry of the SAR instrument where the antenna is mechanically tilted to θ_tilt. If the antenna tilt is directed toward the swath center, the maximum elevation angle becomes

$${\theta_\mathrm{e}}^{\max} = \frac{\Theta_\mathrm{w}}{2}, \tag{4.39}$$

which is assumed in the following to arrive at the antenna beamforming constraints.

The spacing between the digital channels $d_\mathrm{sub,e}$ in elevation is an important design parameter as it affects both performance and the number of required ADCs.

Typically, this spacing is determined by balancing the required beam steering performance against available resources such as cost, power consumption, and system complexity. It depends on both the maximum steering angle of the SCORE beam ${\theta_e}^{max}$ and the required grating lobe-free region. As shown in Section 4.2.2, an ingenious hybrid beamforming is used for SCORE. Two methods are described in this section. The first approach involves analog pre-steering to the first half of ${\theta_e}^{max}$, followed by time-varying digital steering of the remaining half. The second method combines time-varying digital steering of the complete array and analog beamforming and steering at the sub-aperture level.

Hybrid 1) Half Analog – Half Digital Steering

In this method, the maximal SCORE beam steering is equally divided between analog and digital domains. The field of view of the entire antenna array is electronically shifted from the boresight direction, assumed in the swath center, to the two halves of the maximum elevation steering angle ${\theta_e}^{max}$, as depicted in Figure 4.25. The angular swath width Θ_w is divided into two equal segments, $\Theta_w/2$. Analog beamforming is utilized to generate a beam pointing to the center of each segment in a two-step approach, i.e., first to $-\theta_{eA}$ then to θ_{eA}, with

$$\theta_{eA} = \frac{1}{2}\,{\theta_e}^{max} = \frac{1}{4}\,\Theta_w. \tag{4.40}$$

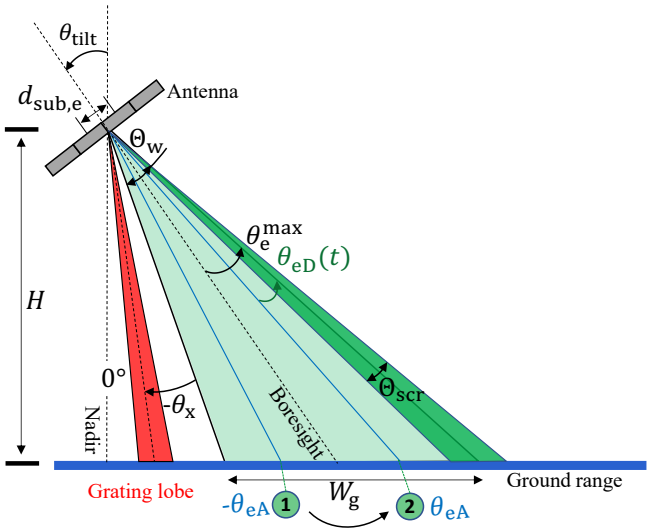

Figure 4.25: The elevation geometry featuring the MapSearch SCORE beamforming where the beam is steered first to $-\theta_{eA}$ then to θ_{eA} on the analog domain and digitally over time with $\theta_{eD}(t)$ to reach the maximum elevation steering ${\theta_e}^{max}$ within the swath W_g.

The SCORE time-variant steering is done digitally up to the maximum steering angle $\theta_{\mathrm{eD}}^{\max}$ given by

$$\theta_{\mathrm{eD}}^{\max} = \frac{1}{2}\,\theta_{\mathrm{e}}^{\max} = \frac{1}{4}\,\Theta_{\mathrm{w}} = \theta_{\mathrm{eA}}. \tag{4.41}$$

This approach reduces the digital steering range and results in fewer digital channels while having the same performance and beam precision, leading to a simpler and more cost-effective system.

To obtain the optimal spacing between the sub-apertures, the angular position of potential grating lobes should be considered. Grating lobes are allowed on receive only if they appear outside of the swath angular segment, defined as the transmit illumination beamwidth Θ_{w}. When the SCORE beam is steered to the nearest swath edge, which corresponds to the maximal digital steering $-\theta_{\mathrm{eD}}^{\max}$ defined in (4.41), a grating lobe is accepted only if its angular position is beyond the farthest swath edge including an angle margin θ_{x}. When the SCORE beam is digitally steered to the antenna tilt angle in the opposite direction with $\theta_{\mathrm{eD}}^{\max}$, a grating lobe is accepted beyond the nearest swath edge. This ensures that grating lobes appear outside of the swath wherever the SCORE beam is steered and given by:

$$\theta_{\mathrm{GL}} = \left(\left| \theta_{\mathrm{eA}} + \frac{\Theta_{\mathrm{w}}}{2} + \theta_{\mathrm{x}}, -\frac{\Theta_{\mathrm{w}}}{4} - \theta_{\mathrm{x}} \right| \right). \tag{4.42}$$

The same conditions apply for the second sub-swath in far range, where the beam is pre-steered to θ_{eA} in the analog domain. θ_{x} is an angle margin defined as the half of the SCORE beamwidth

$$\theta_{\mathrm{x}} = \frac{\Theta_{\mathrm{scr}}}{2}, \tag{4.43}$$

to avoid any cross-overlapping between the grating lobe and the SCORE beam at the swath edge and to prevent receiving echoes from a strong transmit sidelobe region.

A conservative element spacing is thus determined by averaging θ_{GL} in (4.42) and the distance between the digital sub-apertures is thus derived as

$$d_{\mathrm{sub,e}} \leq \frac{\lambda}{\sin\left|\overline{\theta_{\mathrm{GL}}}\right| + \sin\left|\theta_{\mathrm{eD}}^{\max}\right|} = \frac{\lambda}{\sin\left|\dfrac{\Theta_{\mathrm{w}}}{2} + \theta_{\mathrm{x}}\right| + \sin\left|\theta_{\mathrm{eD}}^{\max}\right|}, \tag{4.44}$$

by substituting the maximum digital steering $\theta_{\mathrm{eD}}^{\max}$ in (2.42). This spacing can also be expressed in terms of the illumination beamwidth Θ_{w} by substituting (4.40) and (4.41) in (4.44). It thus becomes

$$d_{\mathrm{sub,e}} \leq \frac{\lambda}{\sin\left|\dfrac{\Theta_{\mathrm{w}}}{2} + \dfrac{\Theta_{\mathrm{scr}}}{2}\right| + \sin\left|\dfrac{\Theta_{\mathrm{w}}}{4}\right|}. \tag{4.45}$$

Compared to the full digital approach, a larger spacing between the digital sub-apertures can be used with the described hybrid method, as depicted in Figure 4.26. This spacing can be further increased if more discrete analog phase shifting steps are added or time-variant analog steering is combined with the time-variant digital steering instead of a two-step analog switching. This depends strongly on the switching speed capabilities of the used phase shifters.

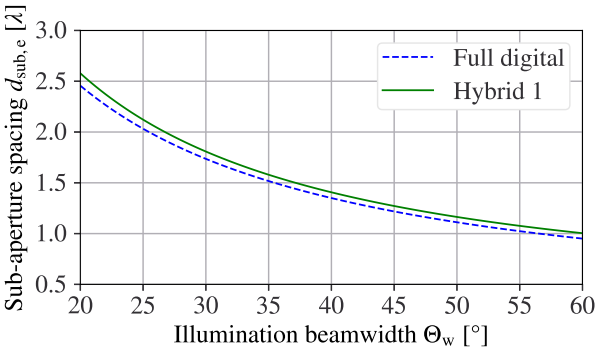

Figure 4.26: Comparison of the sub-aperture spacing in elevation $d_{\mathrm{sub,e}}$ between the hybrid 1 method and the fully digital approach as a function of the MapSearch beamwidth, which illuminates the swath width W_{g} on transmit.

The resulting antenna pattern of the hybrid-formed receive beam, when applying half analog steering and then half time-variant digital steering, is thus given by

$$C(\theta,t) = C_{\mathrm{e}}(\theta) \sum_{n=1}^{N_{\mathrm{e}}} \underbrace{A_n e^{\mathrm{j}knd_{\mathrm{e}}\ (\sin\theta - \sin\theta_{\mathrm{eA}})}}_{\substack{\text{Array factor term} \\ \text{analog}}} \underbrace{A_{\lfloor \frac{n+(N_{\mathrm{es}}-1)}{2} \rfloor} e^{-\mathrm{j}k\lfloor \frac{n+(N_{\mathrm{es}}-1)}{2} \rfloor d_{\mathrm{sub,e}}\ \sin\theta_{\mathrm{eD}}(t)}}_{\substack{\text{Array factor term} \\ \text{digital}}}, \tag{4.46}$$

with N_{e} the number of antenna elements in elevation, N_{es} the number of elements per sub-aperture, and $\lfloor \cdot \rfloor$ the floor function. An example of a radiation pattern following (4.46) is shown in Figure 4.27. The grating lobe appears on the receive outside of the area illuminated during transmission when the SCORE beam is steered to the swath edge. This grating lobe can be attenuated in the final two-way pattern.

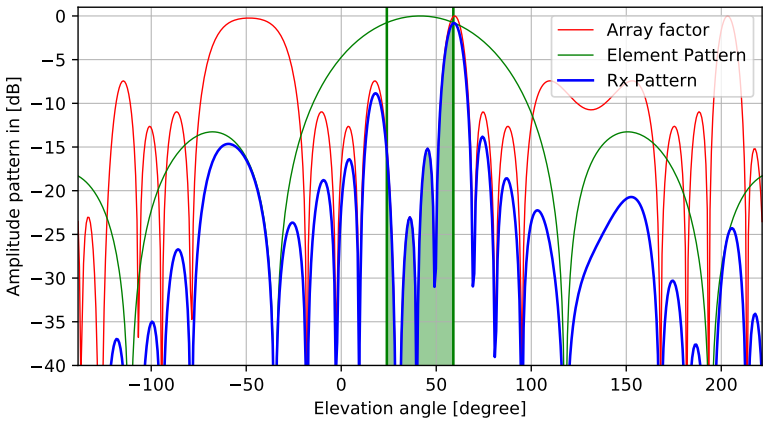

Figure 4.27: Normalized radiation pattern of the MapSearch receive beam in elevation following (4.46). The beam is steered analog to $\theta_{\mathrm{eA}} = \theta_{\mathrm{e}}^{\max}/2 = 8.75°$, then digitally to the swath extremity up to $\theta_{\mathrm{eD}}^{\max} = 8.75°$ with digitized sub-apertures spaced with $d_{\mathrm{sub,e}} = 1.5\lambda$. The antenna array tilt angle is $\theta_{\mathrm{tilt}} = 41.5°$ and the green highlighted area is the area illuminated on transmit.

Hybrid 2) Full Digital – Sub-Aperture Analog Steering

The second proposed SCORE hybrid beamforming method is to steer the receive beam digitally up to maximum elevation angle $\theta_{\mathrm{e}}^{\max}$ and perform analog steering at the sub-aperture level to eliminate any grating lobe appearing in the illuminated sector. A large spacing between the digitized sub-apertures is desired, leading to grating lobes. Given that each antenna element within the sub-aperture is connected to a phase shifter, the look angle of the sub-aperture pattern is changed in the analog domain to force a null at the grating lobe location when the SCORE beam is digitally steered, as shown in Figure 4.28. The difference from the previous method is that the digital steering is not halved to get a larger spacing, but kept at the maximum.

This hybrid method is based on the assumption that the sub-aperture pattern illuminates the swath width W_{g} with the half-power beamwidth

$$\Theta_{\mathrm{HPBW}}^{\mathrm{sub}} = \Theta_{\mathrm{w}} = 2\theta_{\mathrm{e}}^{\max}, \tag{4.47}$$

directly proportional to the maximum elevation steering angle, as defined (4.38). The SCORE beam is digitally steered up to the swath edges corresponding to an echo coming from the nearest and farthest range, considering the tilted boresight direction assumed at the swath center. In this hybrid method, the spacing between the digital sub-apertures is designed such that the first grating lobe can be received

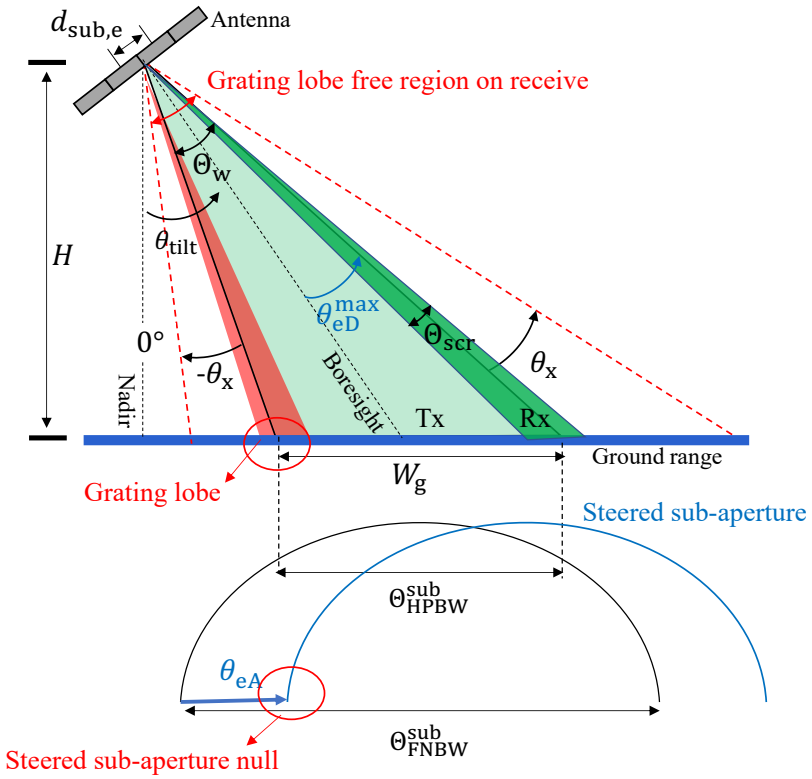

Figure 4.28: Elevation geometry of the SCORE Hybrid Beamforming method 2, where the sub-aperture pattern with the beamwidth $\Theta_{\mathrm{HPBW}}^{\mathrm{sub}} = \Theta_{\mathrm{w}}$ is steered to $\theta_{\mathrm{e}}^{\mathrm{max}}$ to place its first null at the grating lobe caused by the digital SCORE steering.

at the swath edge while being completely suppressed by the sub-array pattern. The grating lobe appears at the swath edge defined as

$$\theta_{\mathrm{GL}} = \pm\frac{\Theta_{\mathrm{w}}}{2}. \tag{4.48}$$

when the SCORE beam is digitally steered in the opposite direction with $\theta_{\mathrm{eD}} = \theta_{\mathrm{e}}^{\mathrm{max}}$. To eliminate it, the sub-aperture beam is steered to the same digital steering angle so that its first null coincides with the grating lobe, as depicted in Figure 4.29 illustrating this suppression technique.

The spacing between digital sub-apertures $d_{\mathrm{sub,e}}$ is then determined by

$$d_{\mathrm{sub,e}} = \frac{\lambda}{\sin\left|\pm\frac{\Theta_{\mathrm{w}}}{2}\right| + \sin\left|\theta_{\mathrm{eD}}^{\mathrm{max}}\right|}, \tag{4.49}$$

by substituting (4.48) in (2.43). Therefore, the analog steering required to suppress the swath edge grating lobes is given by

$$\theta_{\mathrm{eA}} = \pm\theta_{\mathrm{e}}^{\max} = \pm\theta_{\mathrm{eD}}^{\max} = \pm\frac{\Theta_{\mathrm{w}}}{2}, \tag{4.50}$$

which is directly proportional to the transmit illumination beamwidth Θ_{w}. Unlike the SCORE beam steering, it does not vary over time. But it starts first by directing the sub-aperture pattern to the nearest swath edge with $-\theta_{\mathrm{e}}^{\max}$, then switches to the farthest edge with $+\theta_{\mathrm{e}}^{\max}$ once the SCORE beam crosses the boresight. Only one analog change occurs during a swath reception period. After substituting (4.50) in (4.49), the spacing between the sub-apertures becomes

$$d_{\mathrm{sub,e}} = \frac{\lambda}{2\sin|\frac{\Theta_{\mathrm{w}}}{2}|} = \frac{\lambda}{2\sin|\theta_{\mathrm{eD}}^{\max}|}. \tag{4.51}$$

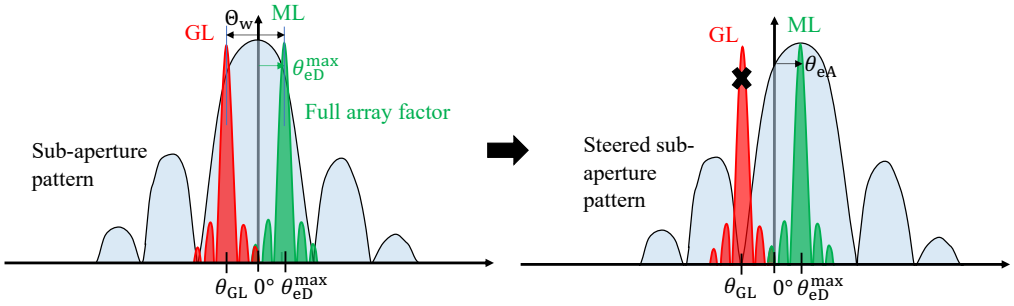

Figure 4.29: Representation of hybrid beamforming strategy where the beam is steered digitally to $\theta_{\mathrm{eD}}^{\max}$ represented by the main lobe (ML) in green and the sub-aperture pattern is steered in the analog domain to $\theta_{\mathrm{eA}} = \theta_{\mathrm{eD}}^{\max}$ to create a null at the grating lobe (GL) location highlighted in red.

This second hybrid beamforming method results in larger spacing between the sub-apertures and better reduction of grating lobes in the field of view compared to the full digital approach, as depicted in Figure 4.30.

The resulting array pattern is the multiplication of the sub-aperture pattern with the full array factor and is expressed as

$$C(\theta,t) = \underbrace{C_{\mathrm{e}}(\theta)\sum_{n=1}^{N_{\mathrm{es}}} A_{\mathrm{n}} e^{[\mathrm{j}k(n-1)d_{\mathrm{e}}(\sin\theta-\sin\theta_{\mathrm{eA}})]}}_{\text{Sub-aperture pattern } C_{\mathrm{sub}}(\theta)} \underbrace{\sum_{m=1}^{N_{\mathrm{sub,e}}} A_{\mathrm{m}} e^{[\mathrm{j}k(m-1)d_{\mathrm{sub,e}}(\sin\theta-\theta_{\mathrm{eD}}(t)))]}}_{\text{Full array factor } \mathrm{AF}_{\mathrm{array}}(\theta,t)}, \tag{4.52}$$

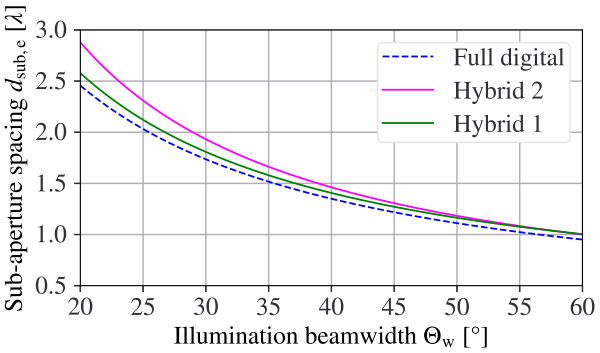

Figure 4.30: Comparison of the sub-aperture spacing in elevation $d_{\mathrm{sub,e}}$ between the hybrid 1, hybrid 2, and fully digital approaches as a function of the MapSearch beamwidth, which illuminates the swath width W_{g} on transmit.

with N_{es} antenna elements in a receive sub-aperture, separated by d_{e} and $N_{\mathrm{sub,e}}$ subarrays placed in elevation with the distance $d_{\mathrm{sub,e}}$. The sub-aperture pattern $C_{\mathrm{sub}}(\theta)$ is the product of the single element pattern $C_{\mathrm{e}}(\theta)$ with the sub-aperture factor, as shown by the simulated receive antenna patterns with and without analog sub-aperture steering in Figure 4.31. In this example, the beam is steered digitally

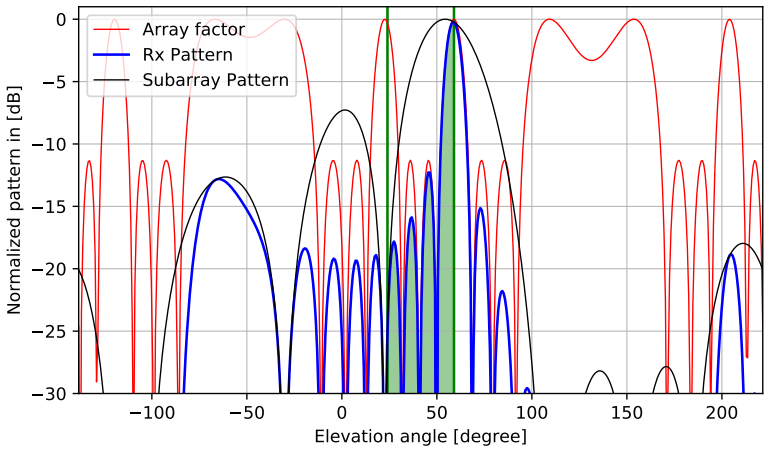

Figure 4.31: Normalized radiation pattern of the MapSearch receive beam in elevation applying the hybrid method 2 and following (4.52). A subarray spacing of $d_{\mathrm{sub,e}} = 1.6\lambda$ is used and the antenna array is tilted to $\theta_{\mathrm{tilt}} = 41.5°$. The highlighted area in green corresponds to the transmit HPBW.

to $\theta_{\mathrm{eD}}(t) = \theta_{\mathrm{e}}^{\max} = 17.5°$ while the subarray pattern is steered to the same direction $\theta_{\mathrm{eA}} = 17.5°$, resulting in a suppression of the grating lobe.

4.3.6 MapSearch Antenna Gain

The transmit gain is a measure of the antenna's ability to amplify and direct the transmitted signal toward the target and maintain a consistent level of SNR. In MapSearch mode, the transmit gain is given by [104]

$$G_{\text{ms}}^{\text{Tx}} = \mu_{\text{ant}}\mu_{\text{b}} \left(\frac{4\pi A_{\text{t}}}{\lambda^2} \right) \cos \phi_{\text{sq}}^{1.5}, \tag{4.53}$$

where μ_{ant} represents the antenna efficiency, A_{t} is the antenna area defined by the product of the antenna height D_{h} and length D_{l}, and $\mu_{\text{b}} = 1/\gamma_{\text{b}} < 1$ is the beam broadening gain loss factor defined in (4.27). The last cosine term accounts for the azimuth squint loss factor. A higher antenna gain improves the probability of detection, especially in scenarios where the received signal is weak.

The MapSearch receive gain is determined by the full array aperture, and can be expressed as:

$$G_{\text{ms}}^{\text{Rx}} = \mu_{\text{ant}} \left(\frac{4\pi A_{\text{t}}}{\lambda^2} \right) \cos \theta_{\text{e}}(t)^{1.5} \cos \phi_{\text{sq}}^{1.5}. \tag{4.54}$$

The receive gain is higher than the transmit gain in (4.53) due to the utilization of SCORE. There is no broadening loss factor on receive. The first cosine term in the equation corresponds to the elevation steering loss, which varies with time based on the SCORE echo timing. The second cosine term accounts for the azimuth squint loss factor. A higher receive gain improves the probability of detecting weak echoes from targets, while balancing the power level when two azimuth channels are activated.

4.4 Tracking Imaging Techniques

The MapSearch and Tracking modes are concurrent and share the same instrument hardware and antenna. However, different configurations are used and each mode utilizes its unique imaging technique. This section highlights the different Tracking mode imaging techniques.

The Tracking mode is activated only for targets of interest that are detected during the MapSearch mode. It images a smaller spot using adaptive performance with the goal of:

1. identifying targets and obtaining more accurate information, such as velocity, size, and direction.
2. confirming interesting targets and mitigating any false alarms detected during MapSearch.

The transmit antenna beamwidth is narrowed in elevation to point all the energy around the target area, maximize the antenna gain, and follow targets individually for longer periods with adapted system parameters, as described by the ADOB-SAR Tracking mode concept in Section 3.2.

The beamforming, instrument configuration, and timing are adaptively set so that multiple targets can be followed individually but simultaneously while still providing continuous MapSearch functionality, as described in the ADOB-SAR timing concept in Section 3.2.3. Depending on the scenario, multiple beams can be generated simultaneously during transmission to illuminate different areas, as illustrated in Figure 4.32 showcasing the deployed imaging techniques. A new imaging mode called Follow Spot SAR steers pencil beams toward targets over time in both dimensions; azimuth and elevation. It images the target as it moves across the antenna's field of view. This technique enables the antenna to gather a great number of data points on the target, which enhances the estimation of important parameters. Alternatively, a circular trajectory SAR is deployed to enhance the spatial resolution, which is described in more detail in Section 4.4.2. Targets can be imaged from different azimuth aspect angles, which has been demonstrated to mitigate possible SNR losses [196].

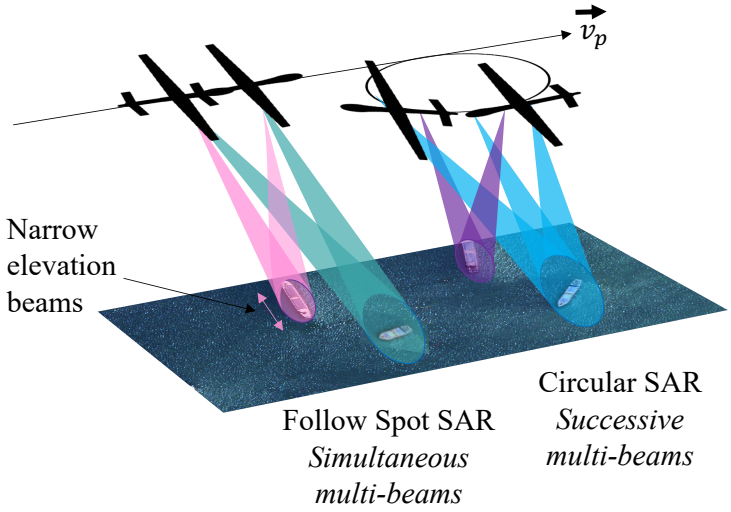

Figure 4.32: Schematic representation of the Tracking mode imaging techniques: Follow Spot SAR and Circular SAR with simultaneous or successive multi-beams.

4.4.1 Follow Spot SAR

The Follow Spot SAR mode aims to maximize the information content of the backscattered signals during tracking. Its geometry is illustrated in Figure 4.33. This mode involves pointing the transmit beam toward the target in elevation and then steering it over time in azimuth to observe the target from different aspect angles until the desired azimuth resolution are achieved by forming the required synthetic aperture. The beams are steered on transmit to keep up with the motion

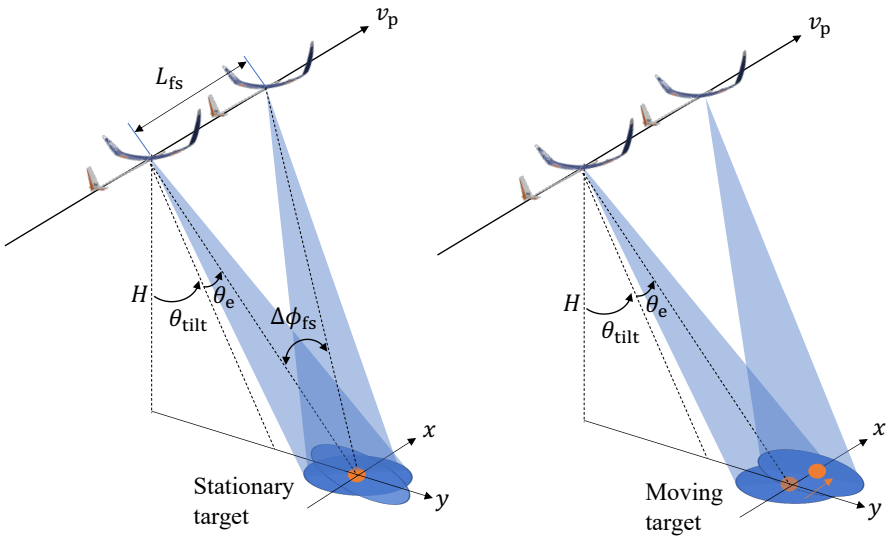

Figure 4.33: Follow Spot SAR imaging of a stationary target on the left and a moving target on the right.

of moving targets. Real-time tracking of the new position is necessary to point the next beam at the moving target's new location if it has left the initial beam footprint. In the case of a stationary or slow-moving target, the transmit beam remains pointing at the same azimuth position on the ground, while steering the beam over time to compensate for the flight pointing. Follow Spot SAR shares the same geometry as the Spotlight SAR imaging, in which the beam is continually steered in azimuth to illuminate the same spot on the ground from all positions of the synthetic aperture [197]. However, the two modes differ in concept and objective. Spotlight SAR is typically used to achieve a finer azimuth resolution while avoiding range ambiguities. By retrieving a larger range of Doppler frequencies from the constant illumination of the same area, more pulses can be combined without increasing the PRF, compared to the Stripmap imaging mode. The proposed Follow Spot mode, however, does not rely on a specific resolution and PRF requirements. Instead, it

has adaptive parameters that adjust to the target scenario. A high PRF may be required for some targets, regardless of the scanning geometry. The physical following of targets with different aspect angles, coupled with the agile switching of array weights for a 2-D steering capability, as depicted in Figure 4.33, can achieve high-quality imaging with minimal SNR losses, thereby providing better accuracy in tracking scenarios.

The azimuth antenna beamwidth remains the same for all modes. After the target is detected, the platform travels the distance d_{td} defined in (4.4), then starts the Tracking mode, as illustrated in Figure 4.11. Given that the MapSearch and Tracking azimuth beams have the same beamwidth, which is larger than the target size, the first Follow Spot beam is directed to the same azimuth direction as the MapSearch mode, but with a slight steering ϕ_2. Considering the platform movement and the geometry, this start steering angle is given by

$$\phi_2 = \phi_{\mathrm{a}}(t=0) = -\arcsin\left(\frac{2d_{\mathrm{td}}^2 - 2d_{\mathrm{td}}R_{\mathrm{m}}\sin\phi_{\mathrm{sq}}}{2d_{\mathrm{td}}\sqrt{d_{\mathrm{td}}^2 + R_{\mathrm{m}}^2 - 2d_{\mathrm{td}}R_{\mathrm{m}}\sin\phi_{\mathrm{sq}}}}\right), \tag{4.55}$$

with R_{m} the slant range distance of the last MapSearch beam center and ϕ_{sq} the MapSearch squint angle defined in (4.11). In elevation, the transmit beam is steered to a fixed angle θ_{e} in the direction of the target having the incident angle θ_{it}

$$\theta_{\mathrm{e}} = \theta_{\mathrm{it}} - \theta_{\mathrm{tilt}}, \tag{4.56}$$

taking into consideration the antenna tilt angle θ_{tilt}, as shown in Figure 4.33. The azimuth resolution of the Follow Spot SAR depends on the illuminated angular segment $\Delta\phi_{\mathrm{fs}}$ and the time spent on target t_{fs} corresponding to the synthetic aperture L_{fs}, and is given by

$$\delta_{\mathrm{a,fs}} = \frac{\lambda}{2\Delta\phi_{\mathrm{fs}}} \approx \frac{\lambda R}{2L_{\mathrm{fs}}\cos\phi_2} = \frac{\lambda R}{2v_{\mathrm{p}}t_{\mathrm{fs}}\cos\phi_2}, \tag{4.57}$$

with R the slant range and ϕ_2 the start squint angle of the Tracking beam, defined in (4.55). The range varies over the synthetic aperture, which can cause a change in the received power due to the signal attenuation. However, this variation can be negligible as the spot angle segment $\Delta\phi_{\mathrm{fs}}$ is not large even for high resolutions, as shown in Figure 4.34.

The beam combinations during the Follow Spot SAR imaging technique are depicted in Figure 4.35. In the azimuth case (left scheme), the beam is steered on transmit with the angle $\phi_{\mathrm{a}}(t)$ varying over time. In elevation (right scheme), the beam is steered within the MapSearch swath width W_{g} toward the target position with the angle θ_{e}. To achieve accurate target tracking in cluttered environments, it is recommended to operate the receiver with a minimum of three azimuth phase centers. One of these phase centers is used for clutter suppression, while the other

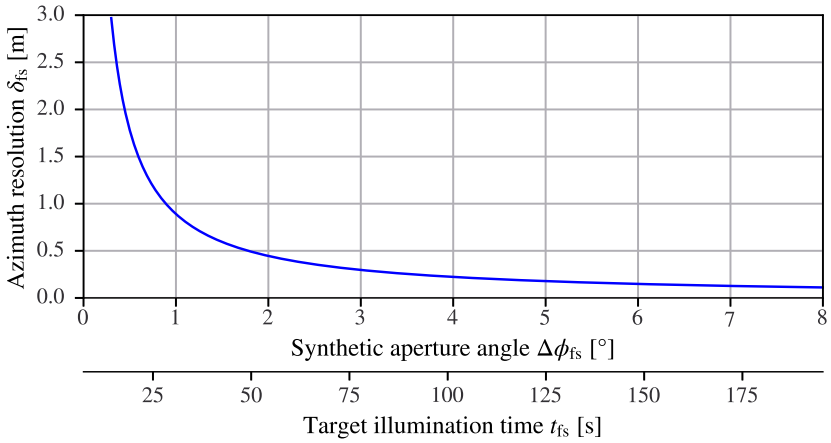

Figure 4.34: Azimuth resolution of the Follow Spot SAR imaging mode plotted versus the synthetic aperture angle $\Delta\phi_{fs}$ and illumination time t_{fs}.

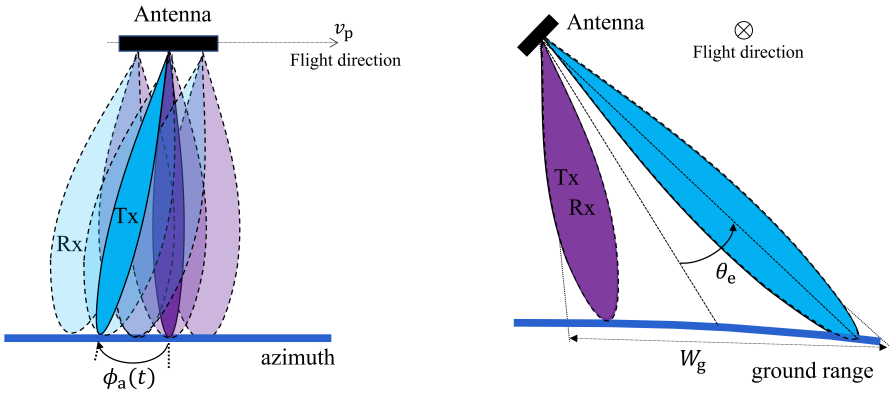

Figure 4.35: Combination of beams for the Tracking mode on transmit (dark shades with solid outline) and receive (bright shades with dashed outline) for two targets, each represented by a distinct color.

two channels are used for precise moving target parameter estimation [127]. A summary of the Tracking Follow Spot SAR beamforming requirements is listed in Table 4.3.

	Azimuth	**Elevation**
Tx	narrow beam + time-variant steering	narrow beam + steering toward a fixed point
Rx	multiple beams + different phase centers	narrow beam + steering toward a fixed point

Table 4.3: Tracking Follow Spot SAR beamforming requirements for the transmission and reception in the azimuth and elevation directions.

4.4.2 Circular Trajectory SAR

ADOB-SAR can enhance resolution and observe targets from different aspect angles by operating under a Circular trajectory during the Tracking mode. The spatial resolution for this circular imaging depends only on the wavelength λ and the target depression angle θ_{d} such as [198]

$$\delta_{\mathrm{x,cir}} = \delta_{\mathrm{y,cir}} = \frac{4.8\lambda}{2\cos\theta_{\mathrm{d}}}, \tag{4.58}$$

with $\theta_{\mathrm{d}} = \arcsin(H/\sqrt{H^2 + R_{xy}^2})$. When the target is located exactly at the center of the formed circle, the finest resolution is achieved, which is $\delta_{\mathrm{cir}} \approx \lambda/4$. While the azimuth and range resolutions in linear trajectory SAR can be different, the circular SAR resolution is the same for the x and y directions defined in Figure 4.36 so that $\delta_{\mathrm{x,cir}} = \delta_{\mathrm{y,cir}}$, as expressed in (4.58).

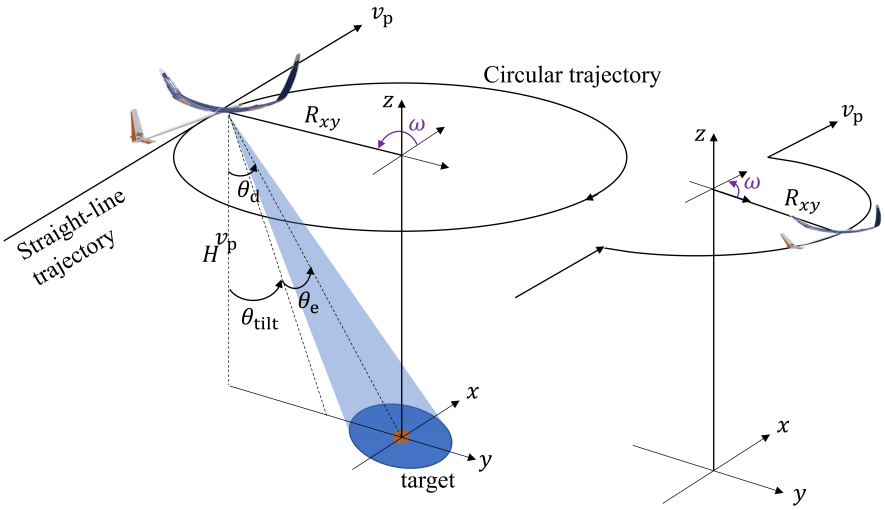

Figure 4.36: Adaptive Observing Circular and Half Circular SAR geometry for very high-resolution imaging during the Tracking mode. The platform follows a circular trajectory with the radius R_{xy} and rotation angle ω.

The platform switches from a linear trajectory to a circular path by forming a circle at the top of the target to be imaged with high resolution, as illustrated in Figure 4.36. Then it returns to its standard straight-line trajectory to continue the operation from the same point. During the circular flight, the coordinates of the platform are given by

$$R(t) = (R_{xy}\cos\omega(t), R_{xy}\sin\omega(t), R_z), \tag{4.59}$$

with R_{xy} the radius of the formed circle and ω the time-variant flight rotation angle with respect to the coordinate system (x, y, z) shown in Figure 4.36. The size of the circular platform trajectory corresponds to the synthetic aperture length defined as $L_{\text{saCir}} = 2\pi R_{xy}$, which can be in the order of kilometers. Following the multi-mode interleaving strategy described in Section 3.2.3, multiple targets can be imaged simultaneously during one circular flight. The only steering used in this mode is therefore in elevation and defined in (4.56), while no azimuth steering is required (i.e., $\phi_{\text{a}} = 0$) because of the circular trajectory. This imaging technique offers a 360° viewing angle, thereby enhancing the backscattering properties of targets and facilitating their identification. Additionally, circular SAR systems provide information about the height of the targets in the scene, which is used to produce a 3-D image. The metric for evaluating accuracy is defined as the height resolution, which refers to the ability to resolve the height difference between the target and the background and is expressed by [198, 199]

$$\delta_{\text{z,cir}} = \frac{2\sqrt{2\pi}}{\sin\theta_{\text{d}}}\frac{c_0}{B}, \tag{4.60}$$

with B the chirp signal bandwidth.

In time-sensitive situations, ADOB-SAR follows another flight pattern, shown in Figure 4.36, which consists of only half a circle with the radius R_{xy}. The platform starts in a straight-line trajectory. Once targets requiring very high resolutions are detected, the platform executes a rightward rotation and forms a half-circle so that the target falls within the center of the trajectory. In this particular half circular path, the mechanical tilt of the antenna should be changed to the opposite direction. This flight pattern is referred to as Half Circular SAR (HCSAR). The platform continues after this with the linear trajectory. In this imaging path, the synthetic aperture length is halved to $L_{\text{sahCir}} = \pi R_{xy}$, resulting in reduced resolution compared to the full circular SAR imaging mode, which is given by

$$\delta_{\text{x,hcir}} = \delta_{\text{y,hcir}} = \frac{9.6\lambda}{2\cos\theta_{\text{d}}}, \tag{4.61}$$

which is the double of (4.58).

A summary of the Tracking mode Circular SAR beamforming requirements is listed in Table 4.3.

In many practical scenarios, the target of interest may not be located precisely at the center of the circular flight path, particularly if it is a moving target. To follow the physical movements of the targets within the observed spot on the ground, an extra azimuth steering of the transmit beam is needed. This can be important for tracking fast-moving targets or imaging complex scenes with multiple moving targets over time.

	Azimuth	**Elevation**
Tx	narrow beam	narrow beam + steering toward a fixed point
Rx	multiple beams + different phase centers	narrow beam + steering toward a fixed point

Table 4.4: Tracking Circular SAR beamforming requirements for the transmission and reception in the azimuth and elevation directions.

4.5 Tracking Antenna Configuration

The Tracking mode shares the same antenna as the MapSearch mode, depicted in Figure 4.10. However, an advanced configuration is used for tracking to achieve the beamforming requirements for the Follow Spot SAR imaging of Table 4.3 and the Circular SAR of Table 4.4, and to acquire more precise target information. As mentioned in Section 4.3, the maximum size of the antenna is obtained from the desired Tracking footprint on the ground, as the beam is narrower. The antenna element spacing in elevation is also determined by the transmit steering during the Tracking mode. This section delves into the overall instrument topology and derives its remaining parameters.

4.5.1 Elevation Antenna Parameters

During the Tracking mode, the full height of the antenna is used to generate a narrow transmit beam and steer it within the swath width W_{g}, as depicted in Figure 4.37. The elevation steering depends on the target range location inside the swath, which is estimated a priori from MapSearch mode real-time data. The maximum elevation steering angle corresponds to the farthest and nearest range where a target can be located. It also specifies the instrument requirements necessary to generate a transmit beam in the desired direction without the antenna pattern performance being degraded by grating lobes. This maximum elevation steering depends on the angular swath width Θ_{w} and is defined similarly to the maximum elevation SCORE steering during MapSearch derived in (4.38) and (4.39).

The only difference with the MapSearch SCORE steering is that the Tracking beam is not steered in elevation over time, but instead has a fixed steering angle θ_{e} that only changes from one target-based Tracking tier to the next.

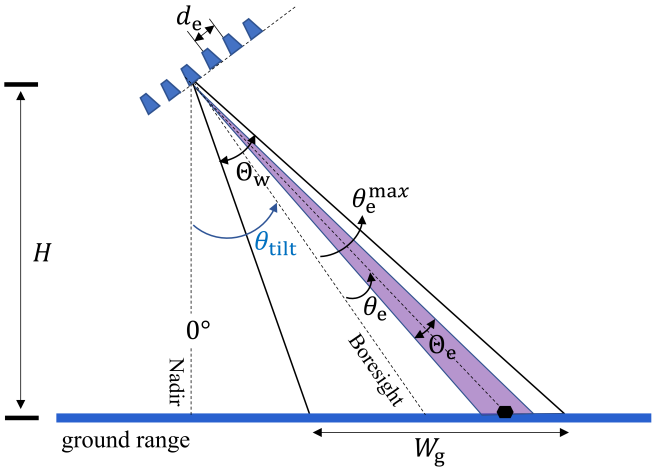

Figure 4.37: Elevation geometry for the Tracking mode where the narrow transmit beam is steered inside the MapSearch swath with the angle θ_e depending on the target location up to ${\theta_e}^{max}$ defined in (4.39).

Considering the side-looking geometry and the antenna tilt θ_{tilt} shown in Figure 4.37, no grating lobes should appear within the field of view during transmission leading to an antenna element spacing in elevation d_e equal to

$$d_e \leq \frac{\lambda}{1 + \sin|\,{\theta_e}^{max}\,|}. \tag{4.62}$$

This ensures that the grating lobes appear in the array factor at $\theta_{GL} = \pm\pi/2$ when steering to ${\theta_e}^{max}$ following (2.43). Multiplying it with the element pattern having a beamwidth of 90° results in a total elimination of the grating lobes on transmit. The number of elements in each digital sub-aperture is then given by

$$N_{es} = \frac{d_{sub,e}}{d_e}. \tag{4.63}$$

The antenna height D_h is given by the desired beam footprint in elevation, which is defined as

$$A_{fe} = \frac{R\,\Theta_{tr}}{\cos\theta_e}, \tag{4.64}$$

leading to

$$D_h \approx \frac{\lambda R}{A_{fe}\cos\theta_e}, \tag{4.65}$$

by setting the Tracking half-power beamwidth equal to $\Theta_{tr} \approx \lambda/D_g$.

4.5.2 Azimuth Antenna Parameters

For the Follow Spot SAR mode, the azimuth steering on transmit varies over time with the angle $\phi_{\mathrm{a}}(t)$. It depends on the target location as well as the desired azimuth resolution and its corresponding angular segment $\Delta\phi_{\mathrm{fs}}$ defined in (4.57). Starting at the azimuth angle $\phi_{\mathrm{a}}(t=0)$, defined in (4.55), the maximum azimuth beam steering is given by

$$\phi_{\mathrm{a}}^{\max} = \Delta\phi_{\mathrm{fs}} + \phi_{\mathrm{a}}(t=0). \tag{4.66}$$

This azimuth steering limit is set to the MapSearch azimuth squint angle given by

$$\phi_{\mathrm{a}}^{\max} = \phi_3 = \phi_{\mathrm{sq}}, \tag{4.67}$$

as described in Section 4.2 and illustrated in Figure 4.11. This leads to the same MapSearch subarray spacing in azimuth d_{sa} defined in (4.17).

The antenna length D_{l} is given by the desired azimuth footprint A_{fa} of the transmit beam so that

$$D_{\mathrm{l}} \approx \frac{\lambda R}{A_{\mathrm{fa}} \cos\phi_{\mathrm{sq}}}. \tag{4.68}$$

4.6 Tracking Mode Instrument Design

Each antenna subarray separated by d_{e} in elevation, defined in (4.62), and by d_{sa} in azimuth, defined in (4.17) requires a dedicated phase shifter during transmission to apply the required steering weighting vector and hence point the beam to the location of the target. The phased array front-end is designed so that multiple simultaneous transmit beams can be generated to track different targets simultaneously with distinct instrument parameters, as shown by the Tracking imaging beams in Figure 4.32. The simultaneous beams should be steered in different directions. Therefore, different weights are applied.

The schematic front-end configuration of the Tracking mode during transmission is shown in Figure 4.38. The multi-beam hardware configuration is described in more detail in the next subsections followed by the receive configuration.

4.6.1 Multi-Beam Transmit Configuration

The antenna array is capable of generating two transmit beams simultaneously in different directions. This is done by connecting each subarray with passive elements to two phase shifters. The first beam is steered to θ_{e1}. The MapSearch front-end configuration is enhanced with an additional phase shifting stage for each subarray

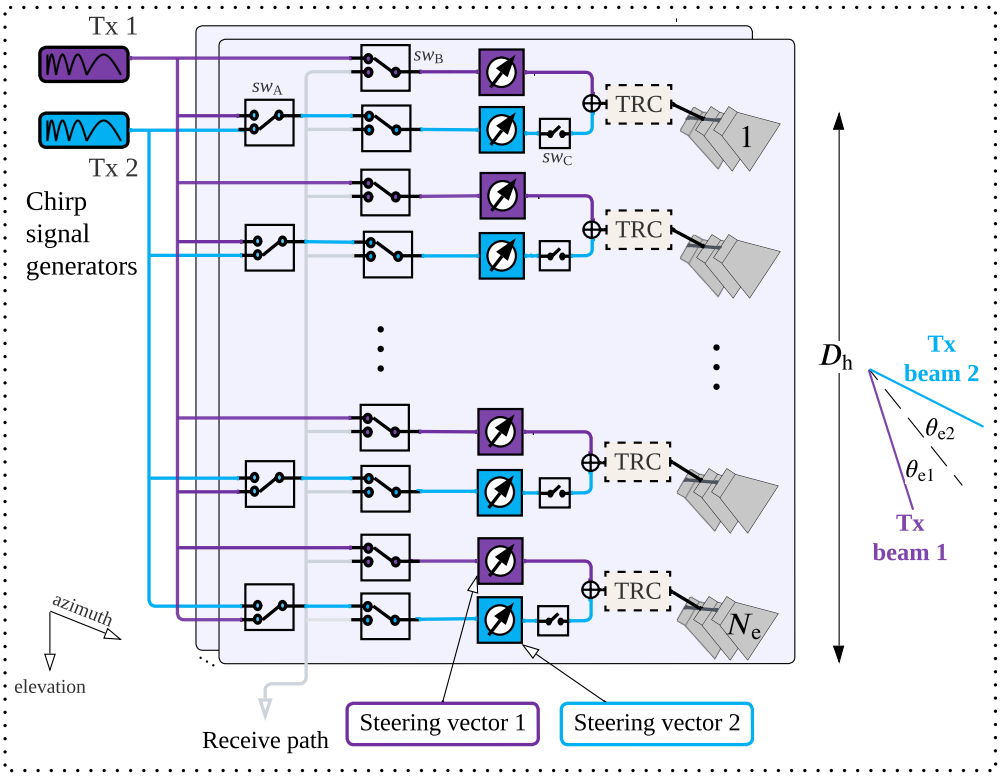

Figure 4.38: Schematic of the front-end architecture in elevation during transmission capable of generating two independent beams in different directions.

to steer a second beam to a different steering angle θ_{e2}. The second phase shifting stage can be activated and deactivated when needed using the digital switches sw_c, as shown in Figure 4.38. The two resulting beams are then used to track two targets located in different positions on the ground. Each beam uses the full antenna height D_h to ensure that the narrow elevation beamwidth is maintained regardless of the number of transmit beams. The antenna gain remains the same for both simultaneous beams. More transmit beams can be generated with the same principle by adding additional phase shifting stages, depending on the application requirements, as the antenna system is considered modular. The two simultaneous beams can be generated by a single chirp signal generator. If they are operated with different waveform parameters following different performance criteria, each beam is generated with a distinct generator using the digital switch sw_A, as is the case in the front-end architecture of Figure 4.38. The available transmit peak power P_t is divided equally between the two networks such as

$$P_{t1} = P_{t2} = \frac{P_t}{2}, \tag{4.69}$$

where P_{t1} and P_{t2} are the peak power of the first and second beam respectively. This reduction in peak power is compensated by adjusting other adaptive instrument parameters to maintain a consistent level of SNR. The two phase-shifted transmit

signals are summed and fed into a single TR core including a HPA connected to one antenna element, as depicted in Figure 4.38. This ensures minimizing the number of TR cores, which influences the overall phased array cost and power consumption. However, this requires operating the HPA in the linear region, which may reduce efficiency. This efficiency loss can be also compensated by optimizing other SAR parameters, as the Tracking mode is adaptive.

Applying this configuration for an array of N_e antenna elements in elevation results in the following number of required phase shifters

$$N_\mathrm{shifter} = 2N_\mathrm{e}. \tag{4.70}$$

The grating lobe free scan region for the two beams is given by the maximum elevation steering angle $\theta_\mathrm{e}^\mathrm{max}$ defined in (4.39)

$$\theta_{\mathrm{e}1,2} \in [-\theta_\mathrm{e}^\mathrm{max}, \theta_\mathrm{e}^\mathrm{max}]\,. \tag{4.71}$$

When generating two beams in different directions with the same antenna array, the total array factor $\mathrm{AF}_\mathrm{total}$ in elevation is the sum of the array factors for each beam and is given by

$$\begin{aligned}\mathrm{AF}_\mathrm{total}(\theta) &= \mathrm{AF}_1(\theta) + \mathrm{AF}_2(\theta) \\ &= \sum_{n=0}^{N_\mathrm{e}-1} A_n \left(e^{\mathrm{j}kd_\mathrm{e}n\left(\sin(\theta)-\sin(\theta_{\mathrm{e}1})\right)} + e^{\mathrm{j}kd_\mathrm{e}n\left(\sin(\theta)-\sin(\theta_{\mathrm{e}2})\right)} \right).\end{aligned} \tag{4.72}$$

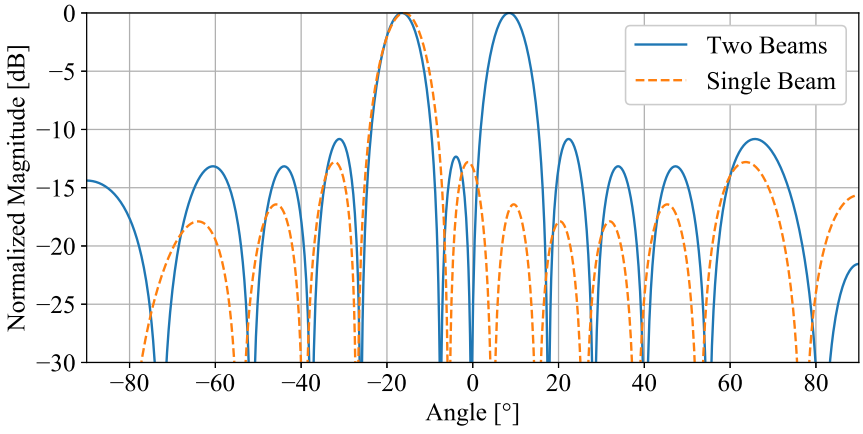

Figure 4.39: Normalized array factor of the two simultaneous beams in different directions compared to the array factor of the single beam for an antenna array of $N_\mathrm{e} = 8$ elements with a spacing of $d_\mathrm{e} = 0.7\lambda$.

The minimum angular difference between the two simultaneous beams is described in Chapter 6 Section 4.6.1.

Alternative Multi-Beam Configuration

An alternative hardware configuration to generate the two simultaneous beams is described in this subsection. This configuration requires only one phase shifter per antenna element in elevation. It involves grouping two antenna elements into a passive subarray on transmit and connecting it to two beamforming networks, each including a different phase shifter and a TR core, as depicted in Figure 4.40. It is like

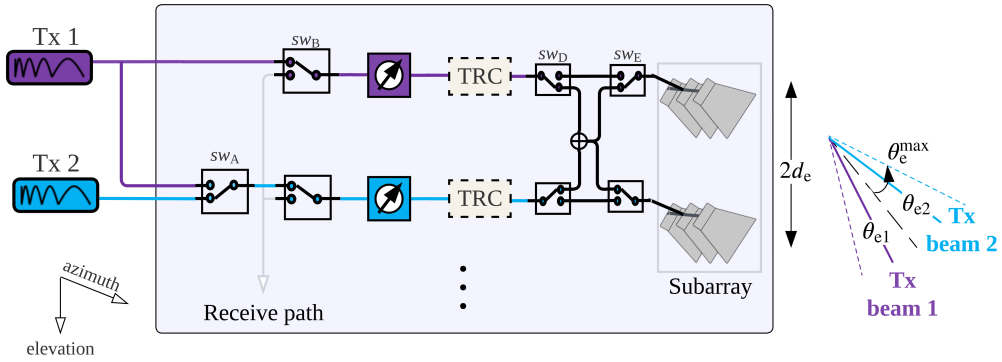

Figure 4.40: Schematic of the alternative front-end architecture **II** in elevation during transmission to generate two independent beams. The full antenna aperture transmits and the beams are steered using one phase shifter connected to each antenna element in elevation by forming subarrays.

each second phase shifter is used for the second steering vector. This configuration requires a higher signal routing complexity but almost the same number of switches as the previous configuration. This technique can degrade the signal strength due the combining and splitting of losses after the HPA, which should be considered in the pre-analysis of the overall system performance with compensation through other instrument parameters. The number of required phase shifters for an array of N_e elements is given by

$$N_{\text{shifterII}} = N_e, \tag{4.73}$$

which is half the number of phase shifters required for the previous configuration. Each transmit signal undergoes phase shifting and then amplification within the TRC, and the resulting signals are then summed up and fed to the subarray. The full aperture D_h is then used to generate the two final beams by multiplying the subarray pattern with the array factors. The subarray is created in elevation to generate a narrow subarray pattern and avoid having grating lobes caused by the

multiplication with a wide antenna element pattern. This configuration doubles, however, the spacing between antenna elements in elevation due to the subarray formation so that

$$d_{\mathrm{e,2txII}} = 2d_{\mathrm{e}} \tag{4.74}$$

Consequently, the grating lobe free scan range in elevation is reduced for both beams to

$$\theta_{\mathrm{e1,2}} \in \left[\frac{-\theta_{\mathrm{e}}^{\max}}{2}, \frac{\theta_{\mathrm{e}}^{\max}}{2}\right]. \tag{4.75}$$

When cost savings are prioritized over the steering capabilities of two simultaneous beams, it is recommended to use this configuration.

The same principle can be applied in the azimuth direction by combining two azimuth subarrays and using the second set of phase shifters to create an additional beam pointed at the second direction θ_{e2}. In this case, the initial elevation element spacing d_{e} and steering range (4.71) remain unchanged and can be applied without grating lobes. However, the azimuth steering ϕ_{a} becomes limited due to the larger subarray spacing. Hence, this configuration is more useful for Circular Trajectory SAR imaging as it does not require azimuth steering.

4.6.2 Elevation Receive Configuration

During reception, the beam is steered to the same transmit direction either in the analog domain by using the phase shifters or digitally using the available digital channels or a combination of both. The same number of beams generated simultaneously on transmit is maintained on receive using DBF, as illustrated in Figure 4.41. Additionally, echoes from different directions can be received simultaneously, given that their beams can be separated in the digital domain using DoA information. This is important because it enables the radar system to track multiple targets simultaneously without ambiguities. If more beams are required, up to $N_{\mathrm{sub,e}}$ beams can be formed using the digital channels with different weights, as depicted in Figure 4.41. The same number of phase shifters used on transmit, shown in Figure 4.38, are used on receive by activating both paths as presets for the digital channels. Alternatively, only one path with one phase-shifting stage can be activated, and the different receive beams can be digitally generated if the second steering angle is smaller than $\theta_{\mathrm{e}}^{\max}/2$.

As the same antenna system is used for both MapSearch and Tracking, the subaperture spacing is set to $d_{\mathrm{sub,e}}$ defined in (4.44), and the element spacing is (4.62). The difference between the two modes is that the digital receive steering in elevation is no longer time-variant during Tracking. Unlike SCORE, where the digital receive steering varies depending on the time delay of the wide transmit beam echo, the Tracking mode directs the digital receive steering toward the target location within

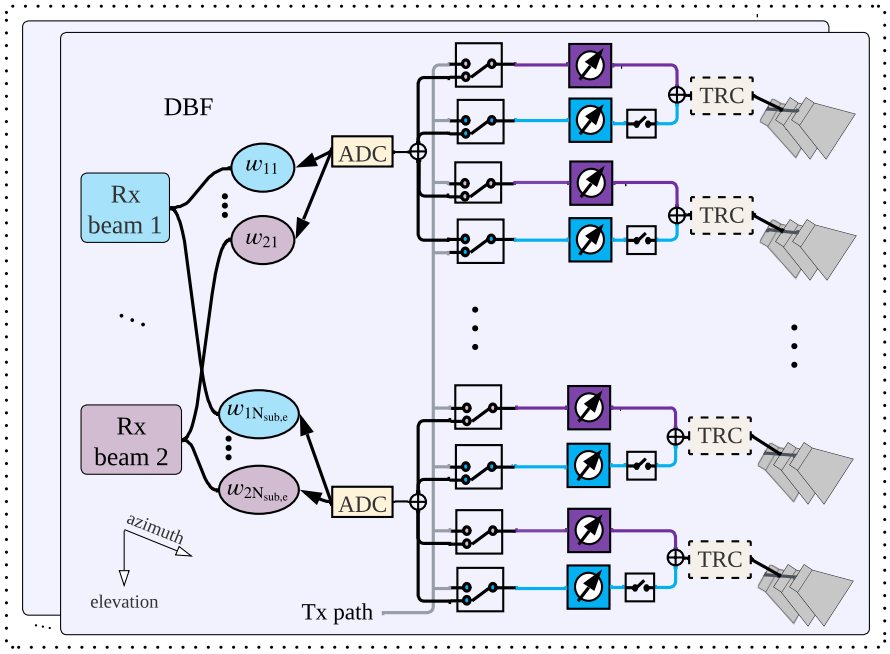

Figure 4.41: The front-end architecture of the Tracking mode configuration on receive employing DBF to generate two receive beams according to transmit configuration of Figure 4.38.

the swath. No SCORE is used during Tracking, given that a narrow transmit beam is used. This feature enables the radar system to constantly focus on multiple targets, track their movements, and update their positions in real-time.

4.6.3 Azimuth Receive Configuration

In azimuth, the aperture is split into $N_{\text{sub,a}}$ digital channels, according to the user requirements for the moving target indication. The number of azimuth phase centers is higher than during the MapSearch mode. Therefore, the front-end architecture should be reconfigurable to cope with the different channel settings from pulse-to-pulse. For each mode, the antenna elements are reconnected differently to construct one, two, or three azimuth sub-arrays using adaptive digital switches, as illustrated in Figure 4.42. Hybrid beamforming is thus used to generate different numbers of receive beams according to the mode requirement even though the design has three ADCs:

1. One beam with $N_{\text{sub,a}} = 1$: the output of the three digitized channels is summed up. This configuration is intended for the MapSearch mode in weak-clutter scenarios.

2. Two beams $N_{\text{sub,a}} = 2$: the antenna aperture is split into subarrays leading to two beams by connecting the middle elements to different subarrays

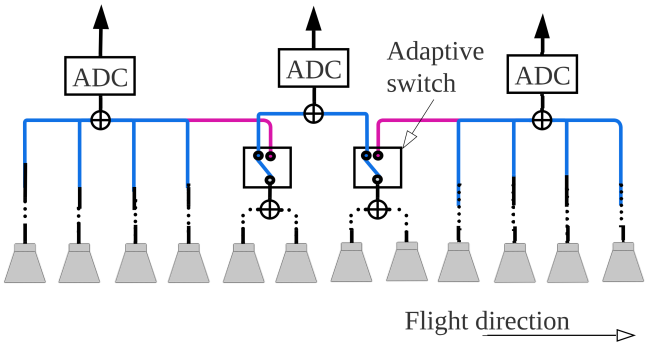

Figure 4.42: A schematic of the reconfigurable antenna array architecture on receive. The number of channels can be changed adaptively depending on the mode.

using adaptive digital switches. Only two ADCs are therefore used for this combination, which is used for the MapSearch mode in case of strong clutter.

3. Three beams with $N_{\text{sub,a}} = 3$: the connection of the middle elements is rearranged to form three subarrays. Three ADCs are activated. This configuration is special for the Tracking mode.

The spacing between the azimuth phase centers affects the performance of the Displaced Phase Center Antenna (DPCA) method in clutter suppression and GMTI. A smaller spacing between azimuth phase centers results in better clutter performance, as it allows the radar to better resolve small targets and distinguish them from clutter. The PRF determines the rate at which pulses are received by the different azimuth phase centers and, as a result, affects the along-track sampling rate such as [200]

$$\text{PRF}_{\text{DPCA}} = \frac{2v_{\text{p}}}{d_{\text{sub,a}}}. \tag{4.76}$$

However, a small azimuth channel spacing worsens the minimum detectable velocity, defined in (2.58). This condition should be considered when selecting the optimal PRF and the spacing $d_{\text{sub,a}}$ between the azimuth channels.

4.6.4 Tracking Antenna Gain

Due to the narrower beam in elevation, the transmit antenna gain during the Tracking mode is higher than that of the MapSearch mode. Specifically, the gain is given by

$$G_{\text{tr}}^{\text{Tx}} = \mu_{\text{ant}}\left(\frac{4\pi A_{\text{t}}}{\lambda^2}\right)\cos\theta_{\text{e}}^{1.5}\cos\phi_{\text{a}}(t)^{1.5}, \tag{4.77}$$

where the beam broadening factor in (4.53) is $\mu_{\text{b}} = 1$. The azimuth steering loss factor varies with time due to the Follow Spot imaging technique while the elevation steering loss factor is fixed according to the target location. By focusing the energy

in a narrower beam, the high-gain antenna can enhance the performance of the radar system, leading to accurate tracking of targets.

The Tracking receive gain depends on the number of digital channels, and can be expressed as

$$G_{\mathrm{tr}}^{\mathrm{1Rx}} = \mu_{\mathrm{ant}} \left(\frac{4\pi A_{\mathrm{s}}}{\lambda^2} \right) \cos \theta_{\mathrm{e}}(t)^{1.5} \tag{4.78}$$

for a single azimuth channel with the aperture A_{s}. The azimuth steering loss is dropped as the receive beam is wider when splitting the antenna into the three required digitized sub-apertures for GMTI parameter estimation so that no steering is needed on receive.

As the designed front-end has a multichannel architecture with more than one configuration, the total noise figure, defined in Section 2.2.8, changes with the setting depending on the signal path and the active components during each acquisition.

5 Multi-Mode SAR: Signal Space Orthogonality

The ADoptive OBserving Synthetic Aperture Radar (ADOB-SAR) adds unprecedented flexibility and precision to radar applications through its capability for simultaneous interleaved mode operation. The focus of this chapter lies in the derivation of the multi-mode timing and the associated considerations for the interleaving design and scheduling strategy. Starting with the MapSearch mode, which forms the initial stage of operation, the chapter explores the variation of the adaptive Tracking mode depending on the scenario while being strongly influenced by the continuous MapSearch operation. ADOB-SAR is capable of handling complex target environments with multiple echoes by employing adaptive techniques that leverage temporal, angular, frequency, and waveform orthogonality. Together, these multi-dimensional techniques allow for a flexible scheduling strategy enabling individual target tracking with instrument parameters adapted to their properties.

This chapter starts with the timing of the MapSearch mode and its features. Section 5.2 delves into the Tracking mode timing, delineating its adaptive characteristics in various scenarios and covering the multi-mode timing strategy, and the corresponding scheduling algorithm. Section 5.3 addresses the suppression of overlapping tracking echoes with transmitted pulses. A thorough analysis of the orthogonality techniques is presented in Sections 5.4, 5.5, 5.6, and 5.7 highlighting their integral role in resolving overlapping echoes, and deriving all related equations. Finally, a simulation example of an interleaved multi-mode schedule is provided in Section 5.8. Parts of this chapter are described in the journal paper [201].

5.1 MapSearch Mode Timing

The MapSearch mode operates in the background throughout the entire data take, continuously searching for potential targets in the scene. The waveform parameters, such as pulse duration $\tau_{\mathrm{p}}^{\mathrm{M}}$, center frequency $f_{\mathrm{c}}^{\mathrm{M}}$, and bandwidth B^{M}, are fixed during MapSearch.

5.1.1 Transmit and Receive Timing

The SAR instrument successively transmits pulses at a rate of $\mathrm{PRF}^{\mathrm{M}} = 1/\mathrm{PRI}^{\mathrm{M}}$ starting at a time t_0. The radar echo duration $T_{\mathrm{echo}}^{\mathrm{M}}$ due to a transmitted MapSearch pulse is given by

$$T_{\mathrm{echo}}^{\mathrm{M}} = \frac{2\,(R_{\max} - R_{\min})}{c_0} + \tau_{\mathrm{p}}^{\mathrm{M}}, \tag{5.1}$$

with $\tau_{\mathrm{p}}^{\mathrm{M}}$ the duration of the MapSearch pulse. $R_{\min}$ and $R_{\max}$ are the minimum and maximum slant ranges of the illuminated scene, respectively, which depend on the near and far ranges of the beam, as well as the azimuth squint angle ϕ_{sq} and are given by [1]

$$\begin{aligned} R_{\min} &= \frac{R_{\mathrm{near}}}{\cos(\phi_{\mathrm{sq}} - \Phi_{\mathrm{ms}}/2)} = \frac{H}{\cos(\theta_{\mathrm{near}})\cos(\phi_{\mathrm{sq}} - \Phi_{\mathrm{ms}}/2)}, \\ R_{\max} &= \frac{R_{\mathrm{far}}}{\cos(\phi_{\mathrm{sq}} + \Phi_{\mathrm{ms}}/2)} = \frac{H}{\cos(\theta_{\mathrm{far}})\cos(\phi_{\mathrm{sq}} + \Phi_{\mathrm{ms}}/2)}, \end{aligned} \tag{5.2}$$

respectively, with Φ_{ms} the azimuth pattern's half-power beamwidth, which is defined in Figure 5.1. R_{near} and R_{far} are the zero Doppler near and far slant ranges, which

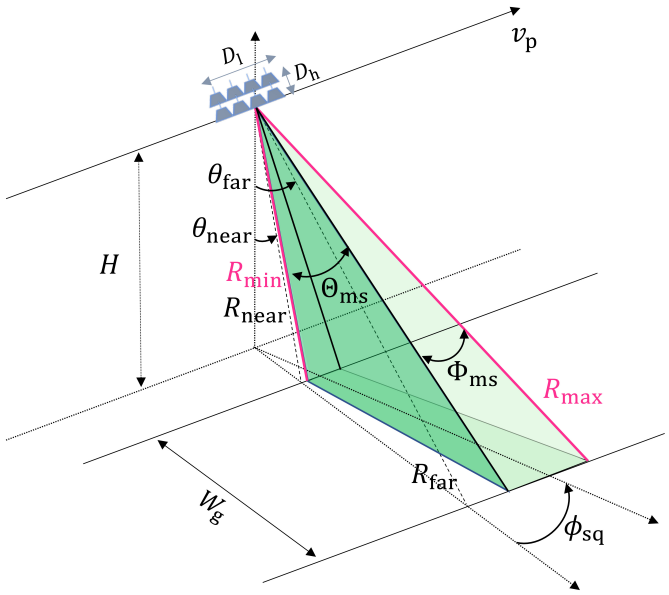

Figure 5.1: The minimum and maximum slant ranges of the illuminated scene on the 2-D geometry in azimuth and elevation considering the squinted azimuth geometry.

[1] The topography variation is very low for the application considered here and can be neglected in the calculation of the minimum and maximum slant ranges.

are defined in (4.6).

Figure 5.2 shows the time distribution of the transmitted pulses and received echoes for a given $\mathrm{PRF}^{\mathrm{M}}$. The radar return echo timing is from near to far range, as illustrated by the range plot. Given that SCORE is used, a time-variant beam is steered digitally to the echo direction of arrival.

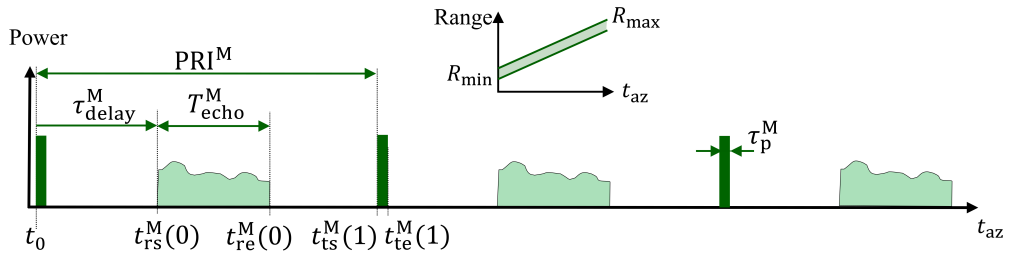

Figure 5.2: Timing schedule snapshot of the MapSearch transmit pulses and received echoes showing the relevant parameters. The range variation of the echoes is plotted over time.

The time delay of the MapSearch echo is expressed by

$$\tau_{\mathrm{delay}}^{\mathrm{M}} = \frac{2R_{\mathrm{min}}}{c_0} = \frac{2H}{c_0 \cos(\theta_{\mathrm{near}}) \cos(\phi_{\mathrm{sq}} - \Phi_{\mathrm{ms}}/2)}. \tag{5.3}$$

The pulse transmission interval is defined as

$$\mathcal{T}_{\mathrm{t}}^{\mathrm{M}}(m) = \left[t_{\mathrm{ts}}^{\mathrm{M}}(m), t_{\mathrm{te}}^{\mathrm{M}}(m)\right] = \left[t_0 + m\,\mathrm{PRI}^{\mathrm{M}}\ ,\ t_0 + \tau_{\mathrm{p}}^{\mathrm{M}} + m\,\mathrm{PRI}^{\mathrm{M}}\right], \tag{5.4}$$

with the pulse start $t_{\mathrm{ts}}^{\mathrm{M}}(m)$ and end time $t_{\mathrm{te}}^{\mathrm{M}}(m)$, c.f. Figure 5.2, where $m \in \mathbb{Z}^+$ is the pulse index. By incrementing m, the timings of all MapSearch pulses along the flight can be determined.

Given the echo delay time and duration defined in (5.3) and (5.1) respectively, the echo start and end time interval is given by

$$\begin{aligned} \mathcal{T}_{\mathrm{r}}^{\mathrm{M}}(m) &= \left[t_{\mathrm{rs}}^{\mathrm{M}}(m), t_{\mathrm{re}}^{\mathrm{M}}(m)\right] \\ &= \left[t_0 + \tau_{\mathrm{delay}}^{\mathrm{M}} + m\,\mathrm{PRI}^{\mathrm{M}}\ ,\ t_0 + \tau_{\mathrm{delay}}^{\mathrm{M}} + T_{\mathrm{echo}}^{\mathrm{M}} + m\,\mathrm{PRI}^{\mathrm{M}}\right] \\ &= \left[t_{\mathrm{ts}}^{\mathrm{M}}(m) + \tau_{\mathrm{delay}}^{\mathrm{M}}\ ,\ t_{\mathrm{rs}}^{\mathrm{M}}(m) + T_{\mathrm{echo}}^{\mathrm{M}}\right]. \end{aligned} \tag{5.5}$$

5.1.2 SCORE Timing

The SCORE technique used in MapSearch generates a pencil beam following the echo time of the wide transmit beam as it travels from near to far range. The number of registered SCORE beams depends on the switch steps of the receiver, as described in (2.45). Assuming a continuous registration of the echo return, the range $R(\theta, \psi)$ is considered variable with the incident angle θ and the angular azimuth squint term $\psi = \cos(\phi_{\text{sq}} \pm \Phi_{\text{ms}}/2)$, as defined in (5.2).

The MapSearch delay, defined as the time when the echo arrives from a certain incident angle $\theta \in [\theta_{\text{near}}, \theta_{\text{far}}]$, is given by

$$t_{\text{rs}}^{\text{M}}(\theta) = t_0 + \frac{2}{c} R(\theta, \psi). \tag{5.6}$$

The MapSearch echo lasts until

$$t_{\text{re}}^{\text{M}}(\theta) = t_0 + \frac{2}{c} R(\theta, \psi) + \tau_{\text{p}}^{\text{M}}. \tag{5.7}$$

This variation of the MapSearch return echo time depending on the incident angle is plotted in Figure 5.3 using an angle-time diagram. The echo span starts from

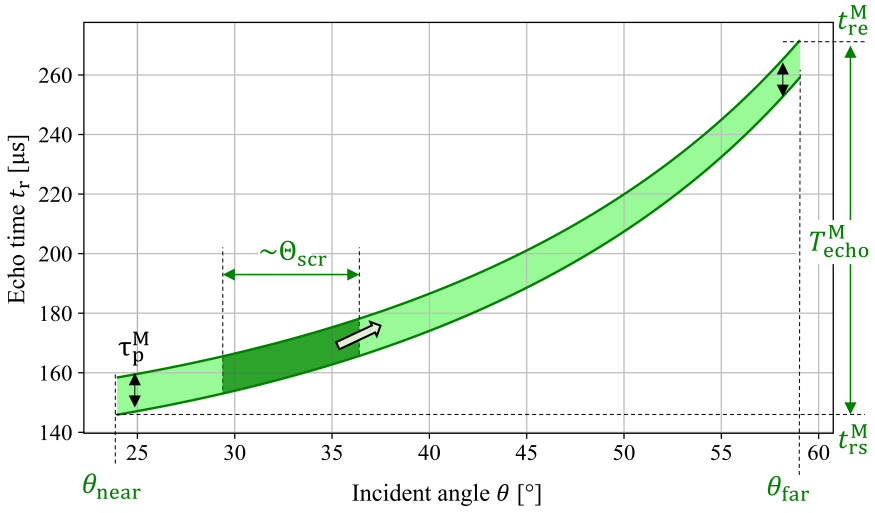

Figure 5.3: Angle-time diagram illustrating the echo timing diagram versus incident angle during MapSearch. The light green colored area corresponds to the echo span of the entire swath, while the dark green portion of it corresponds to the SCORE beam with the beamwidth Θ_{scr}.

$t_{\text{rs}}^{\text{M}}(\theta_{\text{near}})$ to $t_{\text{re}}^{\text{M}}(\theta_{\text{far}})$, which corresponds to the echo duration $T_{\text{echo}}^{\text{M}}$ and the illumi-

nation beamwidth during transmission $\Theta_{\mathrm{ms}} = \theta_{\mathrm{far}} - \theta_{\mathrm{near}}$. In this example, a pulse duration of $\tau_{\mathrm{p}}^{\mathrm{M}} = 12.5\,\mu\mathrm{s}$ and a platform height of 20 km are used.

The echo time of a single SCORE beam increases obviously with the range and depends on its beamwidth Θ_{scr}, as it is steered digitally inside the swath over time. The SCORE beam echo depends on the incident angle it is received from θ_{scr} and varies from the nearest to the farthest range limited by the SCORE beamwidth Θ_{scr}, as shown in Figure 5.3. Its time interval is given by

$$\mathcal{T}_{\mathrm{r}}^{\mathrm{Mscr}}(\theta_{\mathrm{scr}}) = \left[t_{\mathrm{rs}}^{\mathrm{M}} \left(\theta_{\mathrm{scr}} - \frac{\Theta_{\mathrm{scr}}}{2} \right), t_{\mathrm{re}}^{\mathrm{M}} \left(\theta_{\mathrm{scr}} + \frac{\Theta_{\mathrm{scr}}}{2} \right) \right], \tag{5.8}$$

by substituting $\theta = \theta_{\mathrm{scr}} \pm \Theta_{\mathrm{scr}}/2$ in (5.6) and (5.7) and considering the SCORE beam extremities.

5.1.3 Pulse Repetition Frequency Timing Considerations

In most SAR systems, ambiguities play a crucial role in determining the optimal swath width, the suitable pulse repetition frequency, as well as the sensor parameters [130, 202]. Therefore, checking the timing of transmit and receive events and determining the best combination become crucial to strike a trade-off between target signal strength, ambiguities, and timing constraints.

PRF Constraints due to Range Ambiguities

The first step in selecting the MapSearch $\mathrm{PRF}^{\mathrm{M}}$ is to investigate its upper limit through echo return timing to avoid range ambiguities. Pulse $m+1$ should be transmitted after the echo of pulse m has been fully received to avoid any ambiguity in the range direction

$$t_{\mathrm{ts}}^{\mathrm{M}}(m+1) = t_0 + \mathrm{PRI}^{\mathrm{M}} \geq t_{\mathrm{re}}^{\mathrm{M}}(m) + \tau_{\mathrm{g}}, \tag{5.9}$$

taking into account a guard time τ_{g} to ensure sufficient separation between the echo and the subsequent transmit pulse. The upper limit of the PRF is therefore given by substituting (5.3) and (5.1) in (5.5) and solving for $\mathrm{PRF}^{\mathrm{M}} = 1/\,\mathrm{PRI}^{\mathrm{M}}$

$$\begin{aligned} \mathrm{PRF}^{\mathrm{M}} \leq \frac{1}{t_{\mathrm{re}}^{\mathrm{M}}(0) + \tau_{\mathrm{g}}} &= \frac{1}{\tau_{\mathrm{delay}}^{\mathrm{M}} + T_{\mathrm{echo}}^{\mathrm{M}} + \tau_{\mathrm{g}}} \\ &= \frac{1}{\frac{2}{c_0} R_{\max} + \tau_{\mathrm{p}}^{\mathrm{M}} + \tau_{\mathrm{g}}}, \end{aligned} \tag{5.10}$$

while setting $t_0 = 0$ and $m = 0$ in (5.9). The maximum $\mathrm{PRF}^{\mathrm{M}}$ to image a swath of 25 km with a HAP is 3600 Hz using a pulse duration of $\tau_{\mathrm{p}}^{\mathrm{M}} = 12.5\,\mu\mathrm{s}$ and a guard time of $\tau_{\mathrm{g}} = 2\,\mu\mathrm{s}$.

PRF Constraints due to Nadir Return

The return signal from nadir can be particularly strong due to minimal path loss, potentially causing receiver saturation if not properly attenuated through the control of the antenna pattern. To mitigate this, the nadir return should be avoided during the reception of the echo from the illuminated swath through timing. Hence, the selection of $\mathrm{PRF}^{\mathrm{M}}$ should satisfy [87, 178, 203]

$$\frac{m-1}{\frac{2}{c}R_{\min} - \tau_{\mathrm{p}}^{\mathrm{M}} - \tau_{\mathrm{g}} - \frac{2}{c}H} \leq \mathrm{PRF}^{\mathrm{M}} \leq \frac{m}{\frac{2}{c}R_{\max} + \tau_{\mathrm{p}}^{\mathrm{M}} + \tau_{\mathrm{g}} - \frac{2}{c}H}. \tag{5.11}$$

The nadir return echo is received in this case while the radar is transmitting.

PRF Constraints due to Velocity Ambiguities

Velocity ambiguities can arise in radar systems when the Doppler frequencies produced by moving targets, defined in (2.10), are equal to integer multiples of the PRF. These ambiguities are known as blind velocities and are given by [92, 204]

$$v_{\mathrm{blind}} = n\frac{\lambda\,\mathrm{PRF}}{2}, \tag{5.12}$$

where $n \in N$ is an integer and λ is the wavelength. Targets moving at these speeds cannot be detected by the radar due to the lack of variation in the phase-detector output. To avoid blind velocities, or more precisely, to ensure that the first blind velocity is as high as possible, a high PRF is typically used.

Additionally, as described in Section 2.3.1, the PRF should be more than twice as high as the target Doppler frequency to ensure accurate representation based on the Nyquist Theorem. For Doppler frequencies above the Nyquist limit (PRF /2), a Doppler aliasing occurs, folding these frequencies back into the observable range. This results in higher velocities being misrepresented as lower velocities, making them indistinguishable. To avoid these ambiguities, the minimum PRF for a target moving towards or away from the radar with the maximum ground radial velocity $v_{\mathrm{tg}}^{\max}$ should be therefore set to

$$\mathrm{PRF}^{\mathrm{M}} \geq 2f_{\mathrm{D}}^{\max} = \frac{4}{\lambda}|v_{\mathrm{tg}}^{\max}|\sin\theta_{\mathrm{i}}, \tag{5.13}$$

by substituting (2.10). For example, if $v_{\mathrm{tg}}^{\max} = 25\,\mathrm{m/s}$, the minimum required PRF would be 1600 Hz for an incident angle of $\theta_{\mathrm{i}} = 30°$ and a wavelength of $\lambda = 3.125\,\mathrm{cm}$. Figure 5.4 shows the influence of the target incident angle on the PRF required to avoid velocity ambiguities. Higher incident angles require higher PRF values to accurately measure the target's velocity.

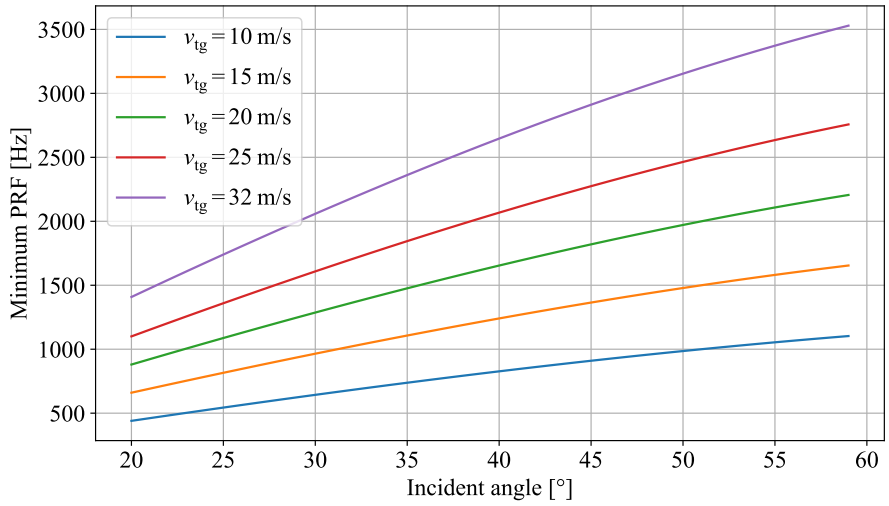

Figure 5.4: Minimum PRF versus incident angle for different target ground velocities required for unambiguous velocity estimation.

PRF Constraints due to Azimuth Sampling

The PRF should be equal to or greater than the Doppler bandwidth of the scene to ensure adequate sampling and avoid azimuth ambiguities [87]

$$\mathrm{PRF}^{\mathrm{M}} \geq B_{\mathrm{d}} = \frac{2v_{\mathrm{p}}}{\lambda}\Theta_{\mathrm{a}} \tag{5.14}$$

This requirement is based on the Nyquist sampling theorem. If the PRF is less than this threshold, aliasing effects occur, resulting in targets being folded back to incorrect positions. This condition is relaxed for HAPs, as their slow movement results in a lower Doppler bandwidth. Consequently, the minimum required PRF does not conflict with the unambiguous range constraint.

Considering the azimuth squint geometry during MapSearch, a high squint angle ϕ_{sq} influences the Doppler behavior with [205, 206]

$$B_{\mathrm{d,sq}} = \frac{2v_{\mathrm{p}}}{\lambda}\Theta_{\mathrm{a}} \cos\phi_{\mathrm{sq}}. \tag{5.15}$$

Hence, this effect should be taken into account when selecting the minimum PRF if the MapSearch is operated with a high azimuth squint.

5.1.4 MapSearch Burst Mode with Alternating PRF

To resolve velocity ambiguities without increasing the PRF, the MapSearch mode switches to burst mode, which alternates between two distinct pulse repetition frequencies, $\mathrm{PRF}_1^{\mathrm{M}}$ and $\mathrm{PRF}_2^{\mathrm{M}}$, across successive CPI intervals with

$$\mathrm{PRF}_2^{\mathrm{M}} = \gamma\,\mathrm{PRF}_1^{\mathrm{M}}, \tag{5.16}$$

where $\gamma < 1$. Different blind velocities are registered in each burst, and targets that were not detectable in the first burst can be detected in the second burst [207]. In Figure 5.5, the SCNR, defined in (2.57), is plotted over the line-of-sight velocity for different PRFs [138]. The resulting blind velocities are different. A lower PRF

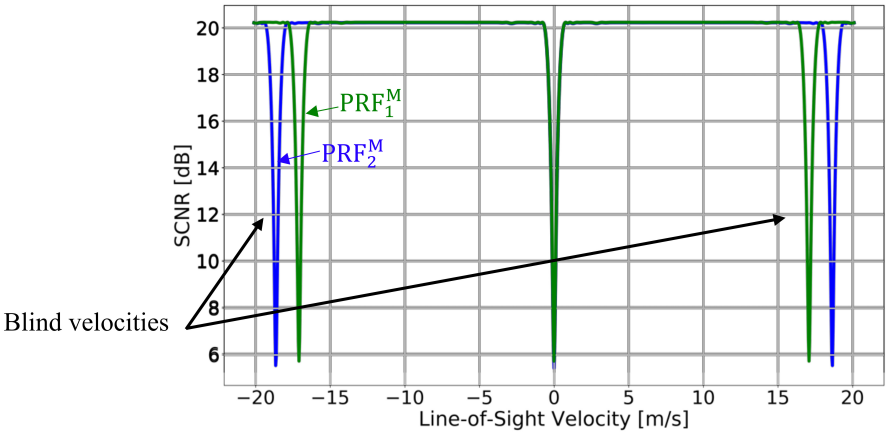

Figure 5.5: SCNR versus line of sight velocity of the target for two different MapSearch PRFs smaller than (5.13). Different blind velocities occur, which can be eliminated by the PRF alternating burst mode.

than (5.13) can therefore be used without ambiguities. Given that the platform is moving very slowly and the integration time of one MapSearch burst is considered short (less than one second), corresponding to a flight distance of approximately 12 m given a platform velocity of $v_{\mathrm{p}} = 20\,\mathrm{m/s}$, almost the same area on the ground is illuminated during the second burst with a slightly different PRF, as shown in Figure 5.6.

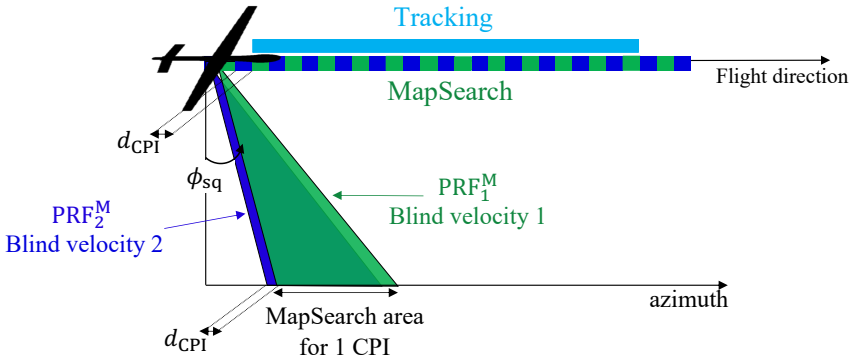

Figure 5.6: Velocity ambiguities resulting from the use of a low MapSearch PRF are resolved by operating in burst mode with two looks with slightly different PRFs.

5.1.5 Scenario-Based Adaptation of MapSearch PRF

Although the imaging parameters of the MapSearch mode remain fixed while data is being collected, two exceptions occur when:

1. the clutter behavior changes requiring a clutter-based PRF adaptation.
2. the number of targets to track individually increases requiring a target-based PRF adaptation.

Clutter-Based PRF Adaptation

The scene clutter depends on the application [28, 160]. For maritime applications, it may further be time-dependent changing with the sea state and wind [148, 152, 153], as described in Section 2.3.2. ADOB-SAR measures the clutter behavior and uses it to set the PRF to the minimum values that ensure satisfactory detection probability. During the MapSearch mode, a higher false alarm rate is tolerated compared to conventional GMTI systems, as it is the task of the Tracking mode to investigate adaptively those false alarms and enhance the overall detection and tracking performance. This approach enables the system to effectively respond to changing conditions, improving performance in detecting the intended targets that emerge in clutter.

When dealing with sea clutter, the radar detection performance is significantly influenced by the roughness and dynamic of the sea surface. In case of strong sea clutter, a high PRF is generally required to expand the range of visible target velocities [130], as described in Section 2.3.1.

Target-Based PRF Adaptation

An increase in the number of detected targets can cause timing conflicts between MapSearch and Tracking. To relax the timing such that all required targets can be tracked, the MapSearch PRF is temporarily decreased to accommodate an additional time interval for the new targets. Hence, the PRF is adapted according to the target scenario and reduced by half with

$$\mathrm{PRF}_1^{\mathrm{M}} = \frac{\mathrm{PRF}_0^{\mathrm{M}}}{2}, \tag{5.17}$$

where $\mathrm{PRF}_0^{\mathrm{M}}$ is the initial optimal PRF, determined after the clutter analysis, shown previously. The timings of all other operating Tracking tiers remain the same when the MapSearch PRF is halved. Figure 5.7 illustrates a flow chart, which describes the

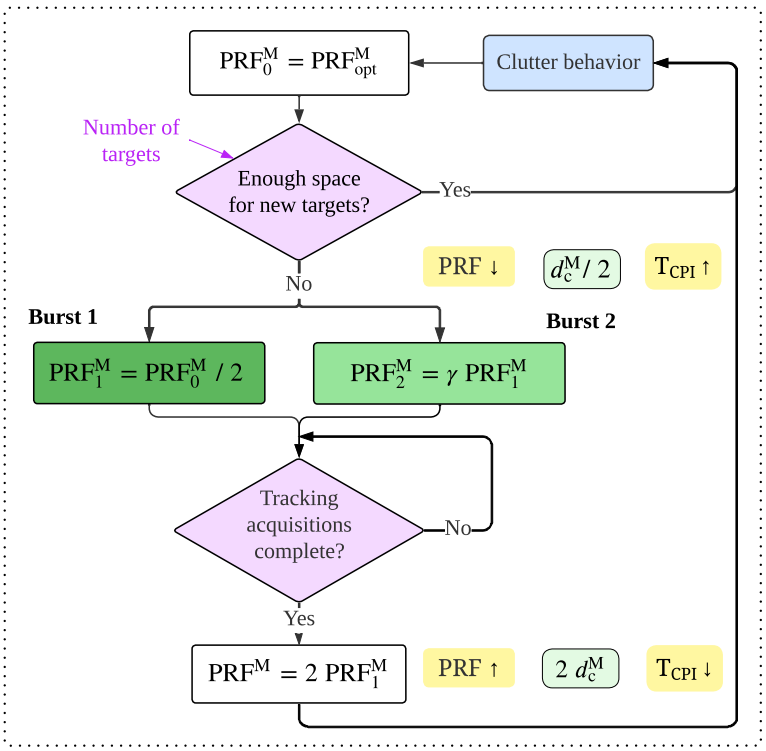

Figure 5.7: Flow chart describing the MapSearch PRF adaptation with the scenario.

procedure for adapting the MapSearch PRF. The operation starts with the optimal $\mathrm{PRF}_{\mathrm{opt}}^{\mathrm{M}}$ determined after the clutter analysis. When the number of targets causes a time conflict, the PRF is reduced by half (5.17). Decreasing the MapSearch PRF during the operation can however lead to velocity ambiguities if (5.13) is no longer

satisfied. Therefore the burst mode, described in Section 5.1.4, is activated in this case by alternating slightly different PRFs.

The pulse duration $\tau_{\mathrm{p}}^{\mathrm{M}}$ is kept constant, as the goal of decreasing the PRF is to gain time for other tasks. This results in halving the duty cycle. To keep the same received MapSearch energy level, the same initial number of integrated pulses is maintained by doubling the integration time T_{CPI}.

When the Tracking acquisitions of targets are complete, and enough space for additional Tracking tiers is available, $\mathrm{PRF}^{\mathrm{M}}$ is increased step-wise back to the initial operation value.

The increase in the integration time can result in target fluctuations especially when dealing with moving targets, leading to a lower detection performance. The decrease in PRF can also lead to velocity ambiguities. The highest priority should be given to tracking targets of interest. Therefore, brief periods of MapSearch performance reduction are acceptable, as the accuracy and ambiguities will be resolved during the Tracking mode. Additional techniques can be applied to the low performance MapSearch to tackle these drawbacks, as described in the following.

5.1.6 MapSearch Burst Mode with Alternating Frequency

For a distributed target that exhibits fluctuating behavior due to a long integrating time, its scattering points produce various amplitudes. When averaged over time, these diverse amplitudes can nullify each other, complicating the target's detection. The spatial distribution of these scattering points is tied to the radar's operating wavelength, which in turn is frequency-dependent. By using two distinct center frequencies, these fluctuations can be effectively averaged out, leading to a more reliable and strong return signal from the target [208, 209].

Figure 5.8 illustrates a simulated RCS of a complex target over frequency. A theoretical model is used in the simulation that considers the target as a composition of discrete scatterers, each contributing to the overall RCS based on geometric and electromagnetic characteristics [210]. The plot shows the expected variation of RCS with frequency, which demonstrates the constructive and destructive interference effects among the scatterers.

When the integration time is long, especially if the PRF is halved (c.f. Section 5.1.5), the MapSearch is operated with two bursts, each having the same integration time T_{CPI}. Using different center frequencies for the two bursts can introduce diversity in the way the target scatters the emitted signal. If a target is not visible with the first frequency burst, it may potentially be detectable when combining the second burst, given that the target has a distinct wavelength-dependent backscattering profile at that frequency [211].

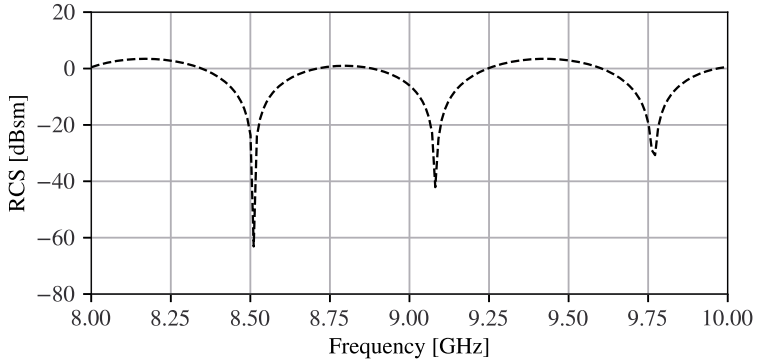

Figure 5.8: Simulated RCS of a complex target as a function of frequency.

The MapSearch mode operates with a low bandwidth B_{M} compared to the total available ADOB-SAR system bandwidth. Therefore, another segment of the spectrum is used for the second burst. Given that two successive CPIs illuminate approximately the same ground area, this technique is nearly equivalent to sending simultaneous MapSearch beams at different carrier frequencies.

The difference between the two distinct chirp center frequencies Δf should ensure a decorrelation of the received echoes. The frequency correlation function of a target with more than one reflecting point can be expressed by [211, 212]

$$\chi(\Delta f) = \cos\left(4\pi \frac{\Delta f L_{\mathrm{t}} \sin\theta_{\mathrm{i}}}{c_0}\right), \tag{5.18}$$

with L_{t} the target length, and θ_i its incident angle. The required frequency shift to ensure sufficient decorrelation is therefore given by

$$\Delta f = |f_{\mathrm{c1}} - f_{\mathrm{c2}}| \geq \frac{c_0}{8 L_{\mathrm{t}} \sin\theta_{\mathrm{i}}} \approx \frac{37.5 \times 10^6 \text{ m/s}}{\min\{L_{\mathrm{t}}\} \sin\theta_i}, \tag{5.19}$$

by setting $\chi(\Delta f) = 0$ in (5.18) and taking the minimum value of a target length. For a minimum target length of 10 m, the frequency shift should be greater than approximately $\Delta f = \mid f_{\mathrm{c2}} - f_{\mathrm{c1}} \mid = 90\,\mathrm{MHz}$.

This dual-frequency approach is demonstrated by simulating a fluctuating target response, shown in Figure 5.9. The upper plot represents the backscattered signal observed at a single center frequency of 9.6 GHz, where the fluctuating nature of the target makes it difficult to detect. The lower plot shows the signal when alternating between two center frequencies with a difference of $\Delta f = 90\,\mathrm{MHz}$. The target is located around 30 km and is visible only with the latter method. Frequency diversity can avoid signal fading and improve the probability of target detection, which is illustrated by the difference in signal intensity shown in the plots.

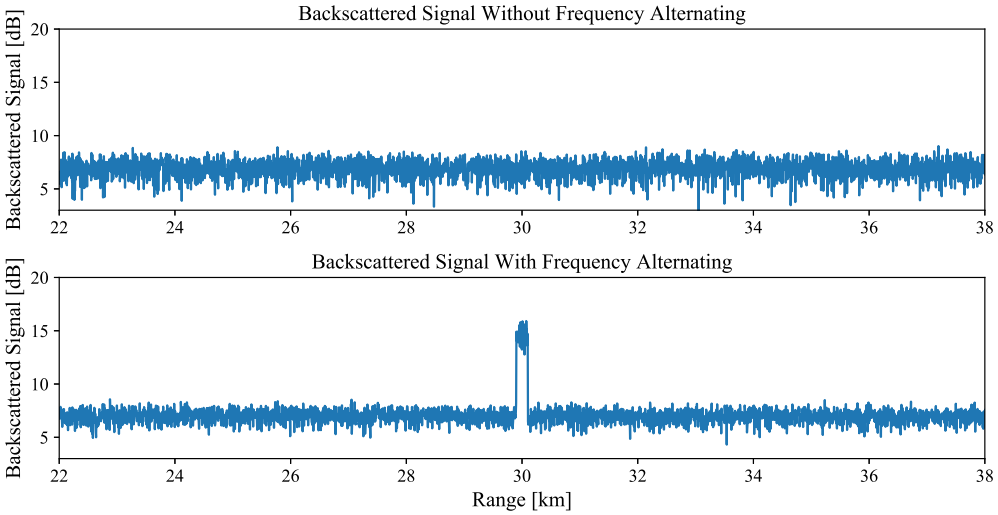

Figure 5.9: Comparison of simulated backscattered radar signals with and without frequency diversity.

5.2 Interleaved Tracking Mode Timing

The Tracking mode consists of several tiers, each imaging a single target with instrument parameters adapted according to its properties. The timing of the Tracking mode signal echo depends on the used elevation beamwidth, the pulse duration, and the steering angle, which corresponds to the target's location within the swath. The waveform transmitted during a Tracking tier may have a different pulse duration, PRF, and bandwidth than the MapSearch waveform and can also differ from one Tracking tier to the other, while being further adapted during operation. A careful timing design is implemented to manage these changing mode parameters.

5.2.1 Transmit and Receive Timing

The antenna transmit beam is steered toward the target location, which is given by its incident and azimuth angle, θ_{it} and ϕ_{at}, respectively. The minimum and maximum slant ranges of the illuminated target area during Tracking depend on the 2-D beamwidth in elevation and azimuth given by Θ_{tr} and Φ_{tr}, respectively. They also depend on the 2-D steering and are derived, based on the geometry of Figure 5.10, as

$$\begin{aligned} R^{\mathrm{T}}_{\mathrm{min}} &= \frac{H}{\cos(\theta_{\mathrm{it}} - \Theta_{\mathrm{tr}}/2)} \frac{1}{\cos(|\phi_{\mathrm{at}}| - \Phi_{\mathrm{tr}}/2)}, \\ R^{\mathrm{T}}_{\mathrm{max}} &= \frac{H}{\cos(\theta_{\mathrm{it}} + \Theta_{\mathrm{tr}}/2)} \frac{1}{\cos(|\phi_{\mathrm{at}}| + \Phi_{\mathrm{tr}}/2)}, \end{aligned} \tag{5.20}$$

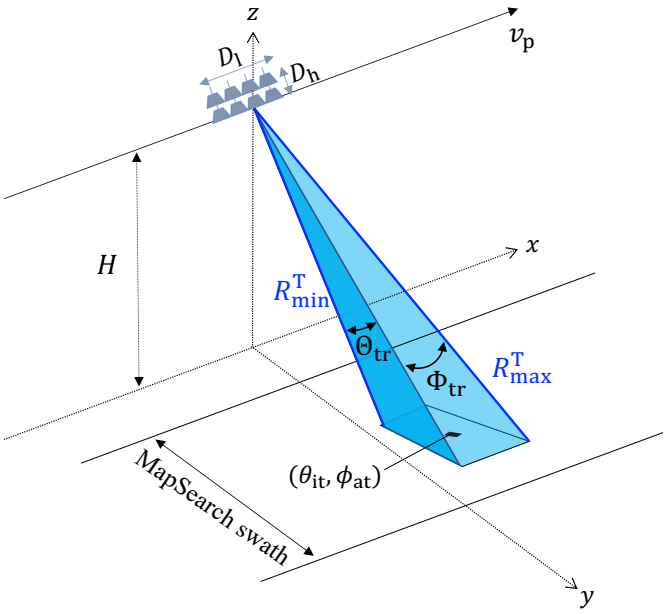

Figure 5.10: Tracking mode geometry highlighting the relation between the minimum and maximum slant ranges $R^{\mathrm{T}}_{\mathrm{min}}$ and $R^{\mathrm{T}}_{\mathrm{max}}$ defined in (5.20), the antenna dimensions, and target incident and azimuth angles.

similar to (5.2). Different zero Doppler near and far slant ranges are used here according to the elevation steering.

The time delay of the Tracking echo plays a crucial role in the pulse scheduling strategy because it determines the exact time instance when the echo return is received by the antenna. It depends on the target location (roughly extracted from the MapSearch detection) and is given by

$$\tau^{\mathrm{T}}_{\mathrm{delay}} = \frac{2R^{\mathrm{T}}_{\mathrm{min}}}{c_0} = \frac{2H}{c_0 \cos(\theta_{\mathrm{it}} - \Theta_{\mathrm{tr}}/2)\cos(|\phi_{\mathrm{at}}| - \Phi_{\mathrm{tr}}/2)}, \tag{5.21}$$

with $R^{\mathrm{T}}_{\mathrm{min}}$ substituted from (5.20). According to the design, the elevation steering range is much larger than the azimuth steering, resulting in the delay being mostly dependent on the incident angle. The minimum delay is achieved when the beam is steered to the nearest swath area defined with θ_{near} and increases with incident angle. It may vary between 143 µs and 235 µs for the designed ADOB-SAR reference system provided in Chapter 7.

The Tracking echo signal duration is given by

$$T^{\mathrm{T}}_{\mathrm{echo}} = \frac{2\left(R^{\mathrm{T}}_{\mathrm{max}} - R^{\mathrm{T}}_{\mathrm{min}}\right)}{c_0} + \tau^{\mathrm{T}}_{\mathrm{p}}, \tag{5.22}$$

with $\tau^{\mathrm{T}}_{\mathrm{p}}$ the Tracking pulse duration.

For the same look angle $\theta_{\mathrm{Lt}} = \theta_{\mathrm{it}}$, the echo duration is typically constant. However, as the platform is moving the echo timing can change according to the distance between the target and the receiver. The term *echo span* is used to refer to the total

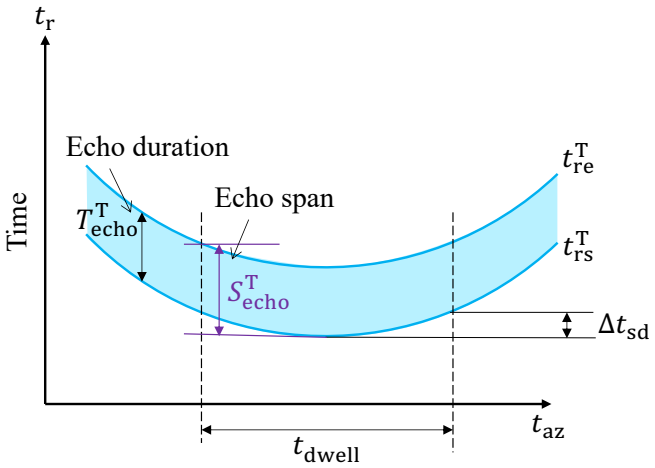

Figure 5.11: Tracking echo variation over the flight time t_{az} and comparison between echo duration and span.

time range when the echo is received over time, as illustrated in Figure 5.11, and is given by

$$S^{\mathrm{T}}_{\mathrm{echo}} = T^{\mathrm{T}}_{\mathrm{echo}} + \Delta t_{\mathrm{sd}} = T^{\mathrm{T}}_{\mathrm{echo}} + \left(\max\{\tau^{\mathrm{T}}_{\mathrm{delay}}\} - \min\{\tau^{\mathrm{T}}_{\mathrm{delay}}\}\right) \tag{5.23}$$

where Δt_{sd} is the range variation caused by the platform movement when considering the Follow Spot imaging mode. It depends on the Tracking dwell time and the synthetic aperture angular sector $\Delta\phi_{\mathrm{fs}}$ defined in Section 4.4.1. If $\Delta t_{\mathrm{sd}} << \tau_{\mathrm{g}}$, this variation can be neglected, and only the echo duration is considered. For instance, for a maximum azimuth steering of $\max\{\phi_{\mathrm{at}}\} = 3°$ and a pulse duration of $\tau^{\mathrm{T}}_{\mathrm{p}} = 12.5\,\mu\mathrm{s}$, the echo span is $S^{\mathrm{T}}_{\mathrm{echo}} = 66.5\,\mu\mathrm{s}$, while the maximum echo duration is $T^{\mathrm{T}}_{\mathrm{echo}} = 66\,\mu\mathrm{s}$ considering the far range. Hence, $\Delta t_{\mathrm{sd}} \leq 0.5\,\mu\mathrm{s} \leq \tau_{\mathrm{g}} \approx 2\,\mu\mathrm{s}$, which demonstrates that the major contribution to the echo span comes from the echo duration.

The echo duration can vary from one Tracking tier to the other depending on the used parameters and the target location within the swath, as depicted in Figure 5.12. The Tracking echo has the shortest duration when the minimum pulse duration is used and the Tracking beam is steered to the nearest range when $\theta_{\mathrm{e}} = \theta_{\mathrm{near}}$. It increases with the look angle and pulse duration. For the designed ADOB-SAR reference system, the Tracking echo varies from 19 µs up to 66 µs for a maximum pulse duration of $\tau^{\mathrm{T}}_{\mathrm{p}} = 12.5\,\mu\mathrm{s}$.

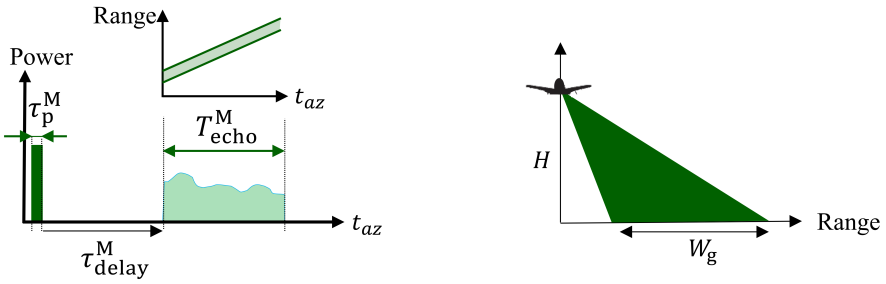

(a) MapSearch mode.

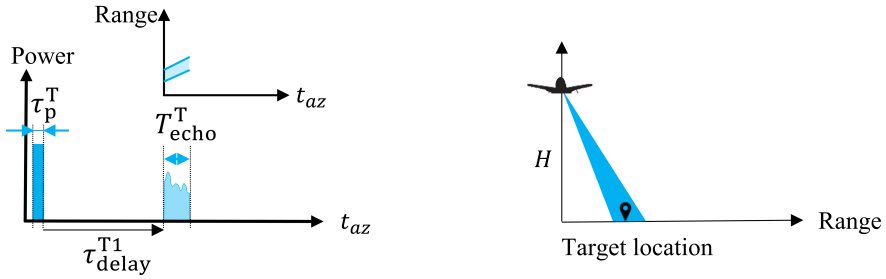

(b) Tracking mode tier with a target in near range.

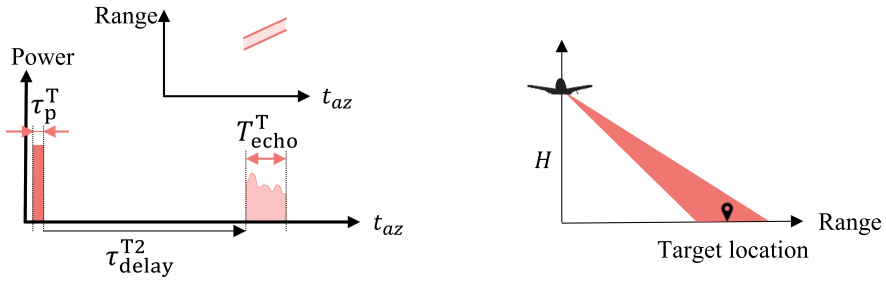

(c) Tracking mode tier with a target in far range.

Figure 5.12: Echo signal duration and time delay for the different ADOB-SAR modes and scenarios. In this example, the same pulse duration is used.

When the first pulse of the Tracking mode tier i is transmitted at t_0^i, the start and end times of all successive pulses are given by the interval

$$\mathcal{T}_{\mathrm{t}}^{\mathrm{T}i}(n) = \left[t_{\mathrm{ts}}^{\mathrm{T}i}(n), t_{\mathrm{te}}^{\mathrm{T}i}(n)\right] = \left[t_0^i + n\ \mathrm{PRI}^{\mathrm{T}i}\ ,\ t_0^i + \tau_{\mathrm{p}}^{\mathrm{T}i} + n\ \mathrm{PRI}^{\mathrm{T}i}\right], \tag{5.24}$$

$\forall\ n \in [0, N_{\mathrm{p}}^{\mathrm{T}i}]$ the pulse index, and $N_{\mathrm{p}}^{\mathrm{T}i}$ the number of pulses used for Tracking tier i. The corresponding echoes arrive at every interval

$$\begin{aligned}\mathcal{T}_{\mathrm{r}}^{\mathrm{T}i}(n) &= \left[t_{\mathrm{rs}}^{\mathrm{T}i}(n), t_{\mathrm{re}}^{\mathrm{T}i}(n)\right] \\ &= \left[t_0^i + \tau_{\mathrm{delay}}^{\mathrm{T}i} + n\ \mathrm{PRI}^{\mathrm{T}i}\ ,\ t_0^i + \tau_{\mathrm{delay}}^{\mathrm{T}i} + T_{\mathrm{echo}}^{\mathrm{T}i} + n\ \mathrm{PRI}^{\mathrm{T}i}\right].\end{aligned} \tag{5.25}$$

Since the timing of the Tracking mode has been calculated, the scheduling strategy of the multiple interleaved modes can now be initiated.

5.2.2 Interleaved Multi-Mode PRF Condition

To avoid any overlap between transmit and receive events of the concurrent modes, the PRI of any new mode should be either an integer multiple or divisor of the PRI of all other n_{op} modes already in operation. By applying this to the ADOB-SAR operation, the selection of the $\text{PRI}^{\text{T}i}$ for the Tracking mode with the tier index i, should satisfy the following interleaving condition namely,

$$\text{PRI}^{\text{T}i} = \begin{cases} n\ \text{PRI}^{\text{M}} \\ \frac{1}{n}\ \text{PRI}^{\text{M}} \end{cases} \quad n \in \mathbb{N}, \tag{5.26}$$

$\forall\ i \in [1, n_{\text{op}}]$. Figure 5.13 illustrates two cases of timing showing the interleaving of a MapSearch with a Tracking mode tier. A random PRI is used in the first example (a), leading to an overlap between a Tracking pulse and a MapSearch return echo. Applying (5.26) results in a smooth multi-mode interleaving, as demonstrated in the second example (b).

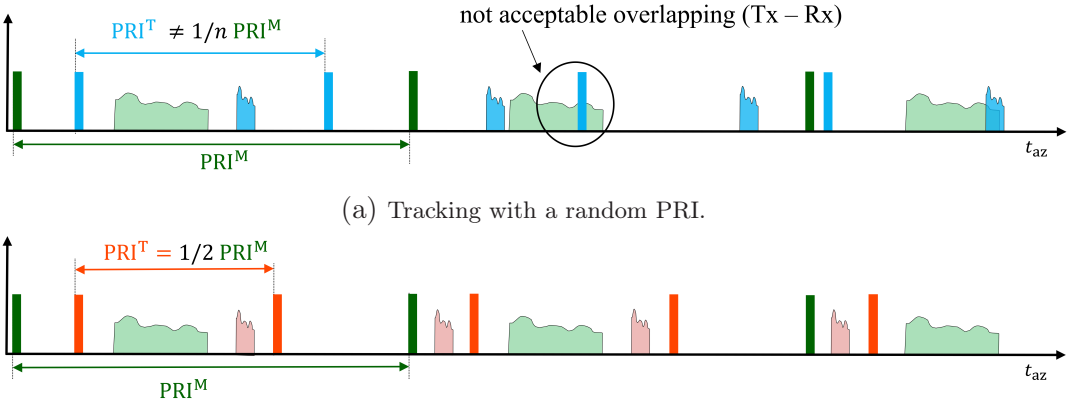

(a) Tracking with a random PRI.

(b) Tracking with the double MapSearch PRI.

Figure 5.13: Timing schedule snapshots showcasing the pulse repetition intervals used for the interleaving of a Tracking tier with the MapSearch mode. (a) represents the case where (5.26) is not satisfied, while (b) shows an example without overlap by applying the interleaving condition.

The dynamic decision-making processor, described later in Chapter 6, automatically selects the appropriate PRF for each Tracking mode. However, the interleaving condition (5.26) transforms the variable Tracking PRF into discrete values that depend on the timing of MapSearch and other Tracking tiers. The decrease in MapSearch PRF during the operation, as described in Section 5.1.5 and (5.17), satisfies the same interleaving condition (5.26), considering the Tracking tiers in operation.

Tracking PRF Update for Burst Mode

When using the burst mode with PRF alternating during MapSearch, described in Section 5.1.4, the PRFs of all Tracking tiers should be updated in the second burst with

$$\mathrm{PRF}_2^{\mathrm{T}i} = \gamma\,\mathrm{PRF}_1^{\mathrm{T}i}, \tag{5.27}$$

with the same γ used in (5.27), based on the interleaving condition (5.26). This ensures that no overlap occurs when a mode changes its PRF, as illustrated in Figure 5.14.

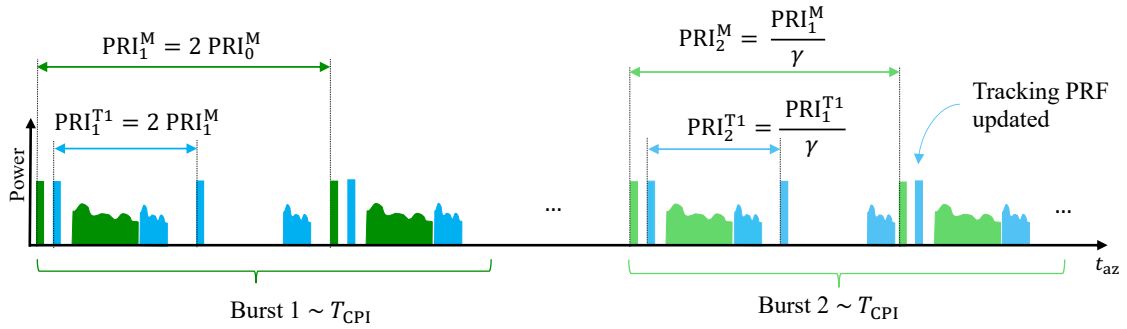

Figure 5.14: Tracking PRF update when the burst mode with PRF alternating is activated according to Section 5.1.4. In burst 2, the Tracking PRF of tier 1 is changed according to the condition (5.26).

5.2.3 Tracking Mode Transmit Timing Strategy

New Tracking transmit pulses are scheduled whenever new targets are detected or when two or more targets within one illumination spot are separated. The transmit pulse and timing parameters are then further adapted to track these targets individually using different beams. The Tracking pulses are transmitted interleaved with the MapSearch pulses, enabling concurrent operation of both modes. When the target is no longer tracked, its corresponding tier is removed from the schedule. The first interleaving degree underlies multiple modes (MapSearch – Tracking), while the second degree emphasizes multiple targets, each is imaged with a distinct Tracking tier.

The first step in scheduling a new Tracking acquisition of a target j is to figure out a suitable pulse transmit time, thus determining t_0^j and then all following pulses $t_{\mathrm{ts}}^{\mathrm{T}j}$ in (5.24). Typically, a pulsed radar system cannot transmit and receive simultaneously

using a single antenna due to the potential to damage the receiver with the high transmit power. Furthermore, transmitting different pulses simultaneously is not preferred because it would decrease the power available for each pulse. The main requirement consists therefore of transmitting the Tracking pulse within the available time margin, defined as

1. The echo free time interval: The time when no other MapSearch or Tracking echoes are arriving

$$\mathcal{T}_{\mathrm{t}}^{\mathrm{T}j} = \left[t_{\mathrm{ts}}^{\mathrm{T}j}(n), t_{\mathrm{te}}^{\mathrm{T}j}(n)\right] \not\subset \left[t_{\mathrm{rs}}^{\mathrm{M}}(m), t_{\mathrm{re}}^{\mathrm{M}}(m)\right] \cup \left[t_{\mathrm{rs}}^{\mathrm{T}i}(t), t_{\mathrm{re}}^{\mathrm{T}i}(t)\right], \tag{5.28}$$

2. The transmit free time interval: The time when no other MapSearch or Tracking pulses are transmitted

$$\mathcal{T}_{\mathrm{t}}^{\mathrm{T}j} = \left[t_{\mathrm{ts}}^{\mathrm{T}j}(n), t_{\mathrm{te}}^{\mathrm{T}j}(n)\right] \not\subset \left[t_{\mathrm{ts}}^{\mathrm{M}}(m), t_{\mathrm{te}}^{\mathrm{M}}(m)\right] \cup \left[t_{\mathrm{ts}}^{\mathrm{T}i}(t), t_{\mathrm{te}}^{\mathrm{T}i}(t)\right], \tag{5.29}$$

while considering only the new Tracking tier j pulses with the index

$$n \in \left[0, \frac{\mathrm{PRF}^{\mathrm{T}j}}{\mathrm{PRF}_{\min}} - 1\right], \tag{5.30}$$

as illustrated in Figure 5.15. Due to the periodicity of the pulses, only the MapSearch pulses and echoes with the index $m \in \left[m^*, m^* + \frac{\mathrm{PRF}^{\mathrm{M}}}{\mathrm{PRF}_{\min}} - 1\right]$ are considered. m^* refers to the actual $\mathrm{PRI}^{\mathrm{M}}$ index, where the first tier j pulse will be scheduled. The same applies for the Tracking tiers i already in operation, with $t \in \left[t^*, t^* + \frac{\mathrm{PRF}^{\mathrm{T}i}}{\mathrm{PRF}_{\min}} - 1\right]$.

The first pulse of Tracking tier j is transmitted in the idle time interval between the MapSearch pulse end time $t_{\mathrm{te}}^{\mathrm{M}}(m^*)$ and its echo start time $t_{\mathrm{rs}}^{\mathrm{M}}(m^*)$, as shown in Figure 5.15(a). This idle time interval is given by

$$\mathcal{T}_{\mathrm{idle}}^{\mathrm{M}} = \left[t_{\mathrm{te}}^{\mathrm{M}}(m^*) + \tau_{\mathrm{g}}, t_{\mathrm{rs}}^{\mathrm{M}}(m^*) - \tau_{\mathrm{g}}\right], \tag{5.31}$$

excluding a guard time τ_{g} after the pulse and before the echo. The pulse start and end time of the Tracking mode j should be within

$$\mathcal{T}_{\mathrm{t}}^{\mathrm{T}j}(0) \subset \mathcal{T}_{\mathrm{idle}}^{\mathrm{M}}(m^*), \tag{5.32}$$

leading to

$$\left[t_{\mathrm{ts}}^{\mathrm{T}j}(0), t_{\mathrm{te}}^{\mathrm{T}j}(0)\right] \subset \left[t_{\mathrm{te}}^{\mathrm{M}}(m^*) + \tau_{\mathrm{g}}, t_{\mathrm{rs}}^{\mathrm{M}}(m^*) - \tau_{\mathrm{g}}\right], \tag{5.33}$$

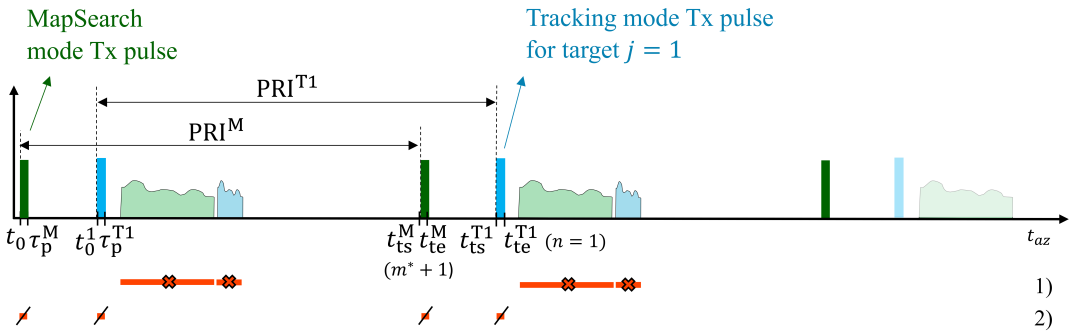

(a) First degree of pulse interleaving: Multi-mode.

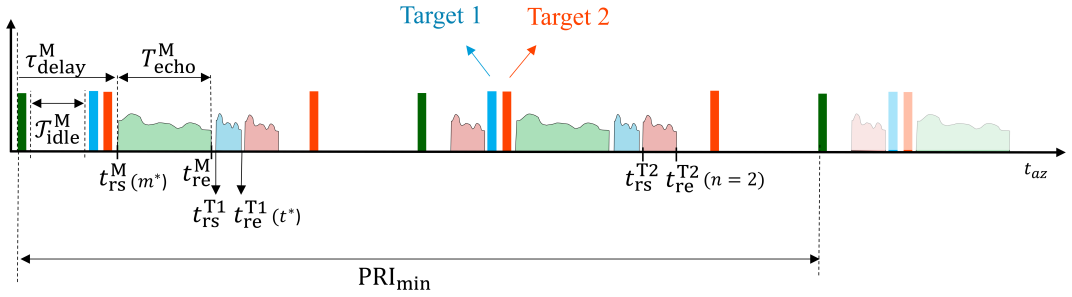

(b) Second degree of pulse interleaving: Multi-target.

Figure 5.15: Timing schedule snapshots featuring the (a) multi-mode and (b) multi-target pulse-to-pulse interleaving techniques. The areas highlighted in orange in (a) represent the timing of the pulses and echoes of operational modes that should be avoided when scheduling a new Tracking Tier, such as 2 in (b).

by substituting (5.31) in (5.32). Hence, the radar idle time interval, during which it is neither transmitting nor receiving, is exploited to send pulses consecutively using an intra-pulse principle. Therefore, a high PRF can be used for the concurrent modes without creating any ambiguity. Subsequent interleaved Tracking tiers are added in the same way. Their optimal timing depends on all operating modes and their corresponding timings. Their first pulse transmit time is preferred to occur within the MapSearch idle time interval defined in (5.31) and illustrated in Figure 5.15(b).

The scheduling algorithm begins by calculating the anticipated timing of a new Tracking mode tier j when its pulse is transmitted immediately after the MapSearch pulse with

$$t_0^j = t_{\mathrm{te}}^{\mathrm{M}}(m^*) + \tau_{\mathrm{g}}. \tag{5.34}$$

The transmit interval $\mathcal{T}_{\mathrm{t}}^{\mathrm{T}j}$ is then calculated and compared to all other Tx pulses and Rx echoes of MapSearch and other Tracking tiers by evaluating the conditions (5.28) and (5.29). If one of them is not maintained, the transmit time t_0^j is shifted and the new pulse location is saved, as illustrated in Figure 5.16. t_0^j is then updated until the pulse can be placed within a free time interval.

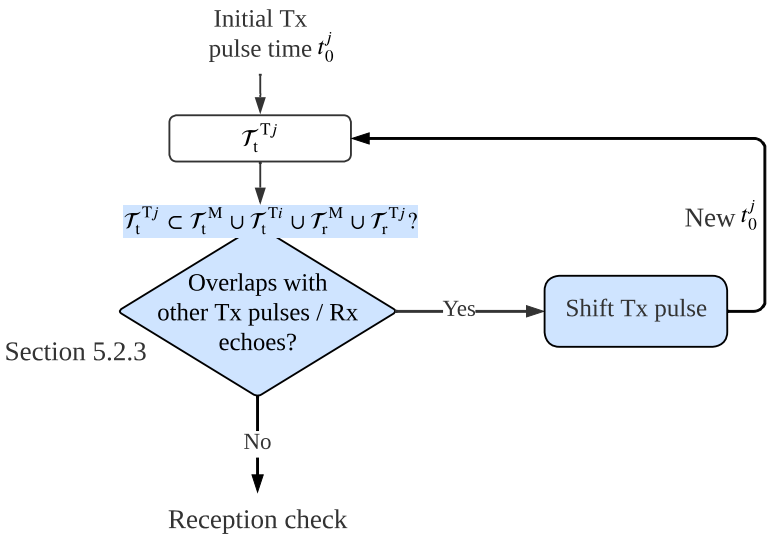

Figure 5.16: Initial transmit time scheduling flow of a new Tracking tier j.

The influence of the echo return time on the pulse transmission time is also taken into consideration in the scheduling process. Given the known target position through information obtained from MapSearch, it is possible to predict the echo timing for a new Tracking tier. An adaptive scheduling model is then used to prevent potential ambiguity in the schedule, which is described in more detail in the following sections.

5.2.4 Adaptive Tracking Scheduling Algorithm

Careful scheduling for each new scenario is required to prevent interference when interleaving pulses and echoes of other modes. The objective here is to adjust the scheduling of pulses so that the sensor can unambiguously receive the corresponding echo as well. The adaptive scheduling algorithm begins by calculating the anticipated echo signal timing based on the target's position when the pulse is transmitted at t_0^j, as illustrated in the flow chart of Figure 5.17. It then subsequently checks whether its anticipated echo will overlap with the transmitted pulses of other operating modes, which will be described in Section 5.3. In this case, the transmit pulse time of the new Tracking tier j is shifted to avoid any potential time conflict. The second stage looks into whether the new Tracking echo temporally overlaps with any echoes of other Tracking tiers or the MapSearch mode. If no temporal overlap is detected, the initial transmit time t_0^j of Tracking tier j is maintained. However, if echoes are received simultaneously, additional techniques are employed to address the overlap.

The techniques used to separate the echoes of different targets are:

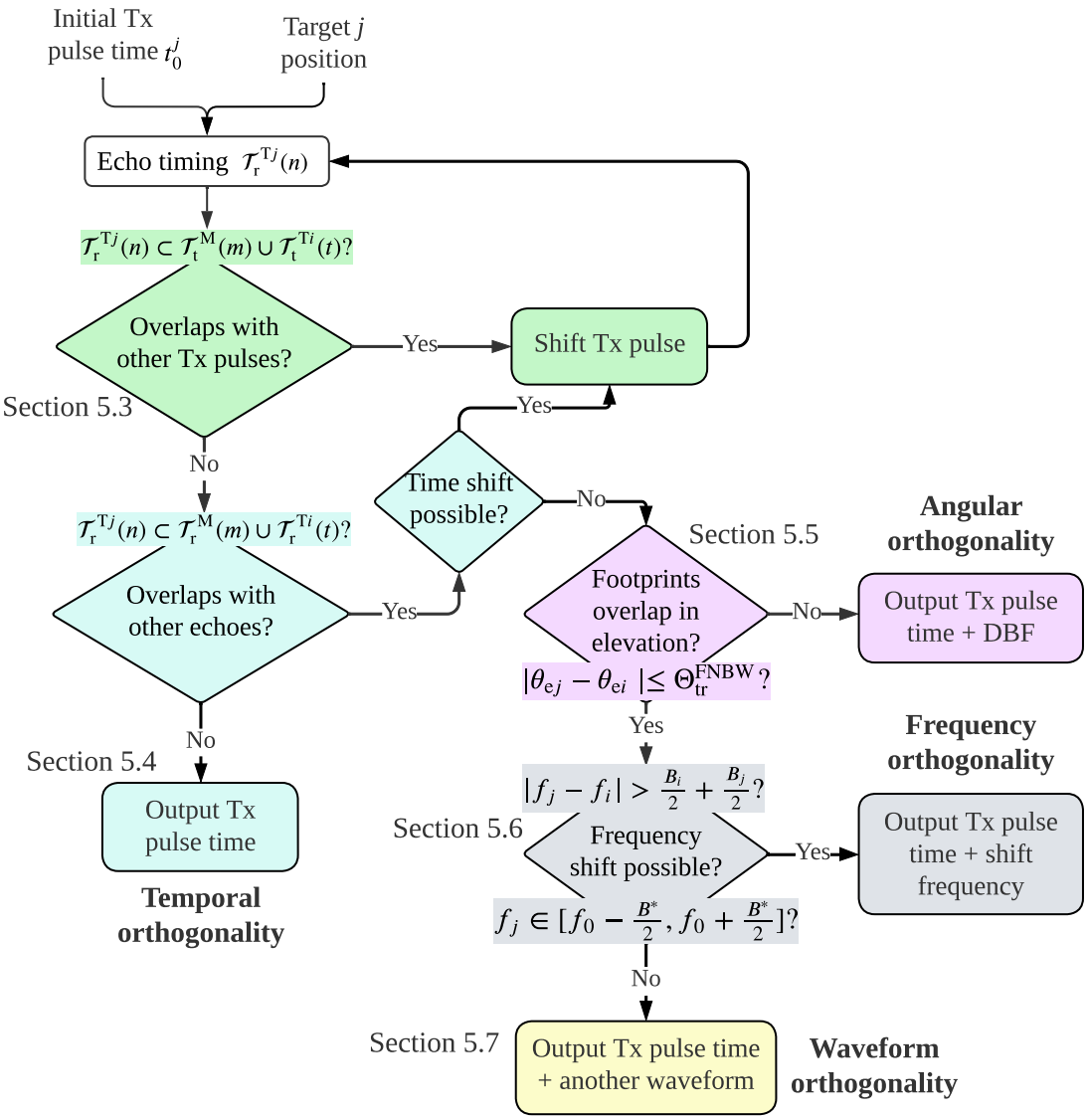

Figure 5.17: Flow chart of the adaptive scheduling process to check the echo reception timing of a newly detected target j.

- **Temporal Orthogonality:** The new Tracking echo arrives in the free-echo time without any overlap.
- **Angular Orthogonality:** The new Tracking echo overlaps with an echo of another mode but is arriving from a different direction.
- **Frequency Orthogonality:** The new Tracking echo overlaps with an echo of another mode, but its pulse has a distinct frequency.
- **Waveform Orthogonality:** The new Tracking echo overlaps with an echo of another mode but its pulse has a different waveform.

The adaptive scheduling algorithm is used to decide on the timing and operation technique depending on the scenario, as depicted in Figure 5.17. If superimposed echos originate from distinct range spots on the ground, angular orthogonality is applied and DBF is used to separate the different targets. Conversely, when targets are at the same range, the only solution to separate them is to send the new pulse j with a frequency shift or another waveform.

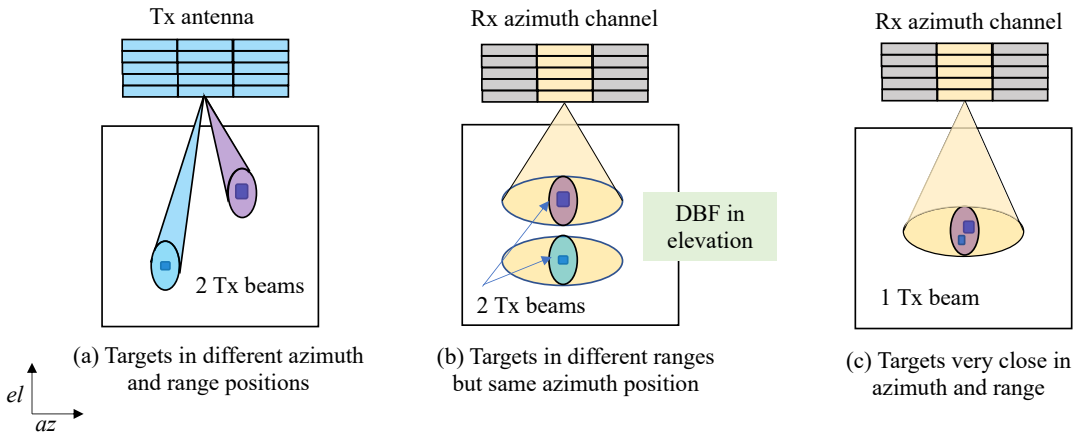

Figure 5.18: Target scenarios illustrating the transmit and receive beam footprints and the echo separation technique, assuming simultaneous reception. The blue and purple beams represent the illuminated footprint during transmission, while the yellow beams depict the footprint on receive, corresponding to a single channel.

The ADOB-SAR operation goal is to individually track each target using a distinct transmit beam and adapt the instrument parameters to the target properties, such as position, RCS, and size. Figure 5.18 illustrates different target scenarios and their corresponding illuminated transmit and receive footprints. The ADOB-SAR concept is based on making the illumination spots of targets on the ground as spatially

distinct as possible, as demonstrated in scenarios (a) and (b). The only exception occurs when the targets are very close to each other, with a distance smaller than the beam footprint on the ground, as illustrated in scenario (c). In this case, the targets are imaged within the same Tx footprint during a single Tracking tier. They are then separated through SAR imaging using azimuth and range compression at the finest spatial resolution. When the simultaneous echoes are received from different ranges, such as scenarios (a) and (b), the corresponding targets are separated through their directions of arrival using angular orthogonality and DBF in the elevation direction.

The receive azimuth beam is wider than the transmit beam according to the digital front-end design. It is therefore not possible to employ angular orthogonality in azimuth. Assuming two targets i and j are located in the same range line and are moving with the same velocity, a separation in the Doppler domain is not possible. When they are tracked with individual Tx beams and their echoes are received simultaneously from two Rx beams that are spatially overlapping, the resolution is the only criterion for separation. If the CPI azimuth resolution of one of the adaptive Tracking tiers corresponding to targets i and j, defined in (4.1), is smaller than their physical separation d_{ij}

$$\delta_{\mathrm{a,CPI}}^{\mathrm{T}i,j} \leq d_{\mathrm{ij}}, \tag{5.35}$$

then the two targets can be distinguished through SAR processing later during azimuth compression. If the resolution is not enough to separate them, other forms

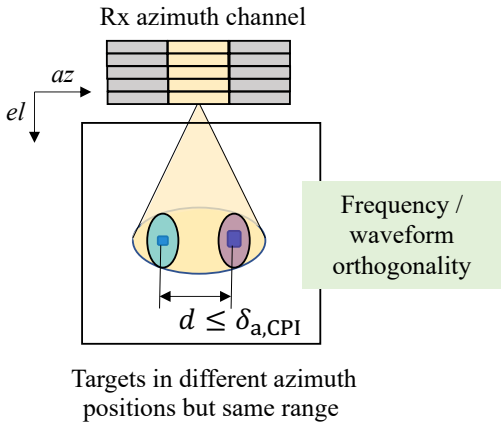

Figure 5.19: Scenario demonstrating the limitations of echo separation using angular orthogonality or chirp compression, assuming simultaneous reception. The blue and purple beams represent the illuminated footprint during transmission, while the yellow beams depict the footprint on receive, corresponding to a single channel.

of orthogonality techniques are utilized. This case is shown in Figure 5.19. One of the two Tracking tiers i or j is operated with a different waveform or carrier frequency to ensure the two received echoes are orthogonal and distinct. Their corresponding methodologies are delineated in the subsequent subsections, as indicated in Figure 5.17.

5.3 Suppression of Tracking Echo Overlapping with Multi-Mode Transmit Pulses

The scheduling process for a newly detected target j starts by checking if the predicted echo will overlap with the transmit pulses of other modes that are currently in operation when its pulse is sent immediately after the pulse of the previous mode, as defined in (5.34).

The number of Tracking tiers in operation is n_{op} and the newly detected target is assigned a Tracking tier with the index $j = n_{\mathrm{op}} + 1$. The foreseen timing of the echo from the new target j, is compared to all other transmitted pulses to check for potential overlap. An unacceptable receive-transmit overlap occurs when the echo interval of the new target, defined in (5.22), coincides with the pulse of the MapSearch or another Tracking tier i so that

$$\mathcal{T}_{\mathrm{r}}^{\mathrm{T}j}(n) \subset \mathcal{T}_{\mathrm{t}}^{\mathrm{M}}(m) \cup \mathcal{T}_{\mathrm{t}}^{\mathrm{T}i}(t), \tag{5.36}$$

which can also be written as

$$\left[t_{\mathrm{rs}}^{\mathrm{T}j}(n), t_{\mathrm{re}}^{\mathrm{T}j}(n)\right] \subset \left[t_{\mathrm{ts}}^{\mathrm{M}}(m), t_{\mathrm{te}}^{\mathrm{M}}(m)\right] \cup \left[t_{\mathrm{ts}}^{\mathrm{T}i}(t), t_{\mathrm{te}}^{\mathrm{T}i}(t)\right], \tag{5.37}$$

$\forall\, n \in [0, N_{\mathrm{p}}^{\mathrm{T}j}], m \in [0, N_{\mathrm{p}}^{\mathrm{M}}]$ and $t \in [0, N_{\mathrm{p}}^{\mathrm{T}i}]$ with N_{p} the number of pulses.

In this case, the new Tracking tier j should be sent with a time shift given by

$$\Delta_{\mathrm{sh}} = \begin{cases} t_{\mathrm{te}}^{\mathrm{M}}(m_{\mathrm{ov}}) - t_{\mathrm{rs}}^{\mathrm{T}j}(n_{\mathrm{ov}}) + \tau_{\mathrm{g}} & \text{overlap with the MapSearch pulse } m_{\mathrm{ov}} \\ t_{\mathrm{te}}^{\mathrm{T}k}(t_{\mathrm{ov}}) - t_{\mathrm{rs}}^{\mathrm{T}j}(n_{\mathrm{ov}}) + \tau_{\mathrm{g}} & \text{overlap with the Tracking pulse } t_{\mathrm{ov}}, \end{cases} \tag{5.38}$$

with k the index of the Tracking tier causing the overlapping, m_{ov} the index of the overlapping MapSearch pulse, t_{ov} the index of the overlapping Tracking pulse, and n_{ov} the echo index of the new Tracking tier j under scheduling.

Figure 5.20(a) shows an example of a receive-transmit overlap situation, where the echo n_{ov} of the new target $j = 2$ (in coral) is received at the same time as the transmit pulse of Tracking tier $k = 1$ (in blue), at exactly the pulse t_{ov}. This situation is avoided by shifting the pulse transmit time of the new mode using $j = 2$ based on (5.38), as illustrated in the second timing diagram.

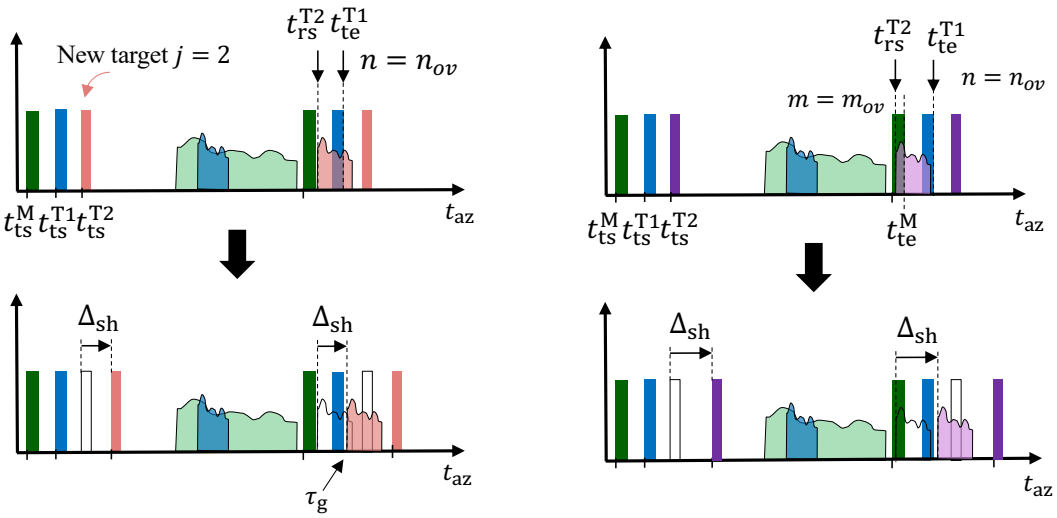

(a) Tracking echo overlap with a single transmit pulse.

(b) Tracking echo overlap with more than one transmit pulse.

Figure 5.20: Examples of Tracking echo overlap with pulses of other interleaved modes. A time shift of the new Tracking pulse of tier 2 is automatically applied according to (5.38) so that the echo arrives after overlapping pulses to avoid the unacceptable Rx-Tx overlap.

The new Tracking echo can overlap with multiple transmit pulses of different modes at the same time, as shown in Figure 5.20(b). In this example, the echo overlaps with the MapSearch transmit pulse (in green) and the Tracking tier 1 transmit pulse (in blue). The time shift is carried out in two steps, and the condition (5.37) is checked for all operating modes. The applied time shift can also cause the echo to overlap with another pulse of a different mode or Tracking tier. Therefore, a repeat loop is executed to reassess the condition (5.37) after each pulse time shift, as shown in the flow chart of Figure 5.17.

5.4 Temporal Orthogonality of Interleaved Multi-Mode Echoes

The duration of the MapSearch echo is relatively long due to its broad swath width, as illustrated in Figure 5.12 and defined by (5.1). Conversely, the echo duration for different Tracking mode tiers varies based on the position of the tracked target, as indicated in (5.22).

The most straightforward and efficient method to interleave the Tracking mode is to use the available MapSearch idle time window $\mathcal{T}_{\text{idle}}^{\text{M}}$ and ensure there is no temporal overlap between Tracking and MapSearch echoes, as demonstrated in Figure 5.21. This method is referred to as cross-mode temporal orthogonality.

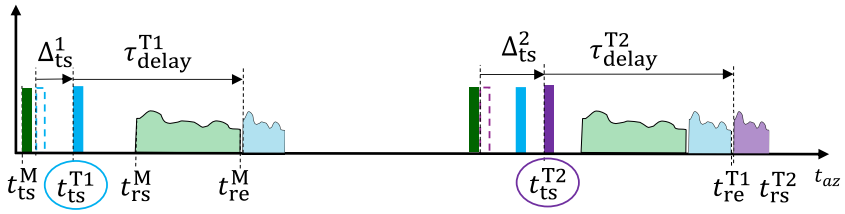

Figure 5.21: Timing schedule snapshot showing the temporal orthogonality of the interleaved MapSearch and Tracking modes. The pulse is timely shifted for target $j = 1$ to avoid the echo overlapping with MapSearch in the first PRI. A second Tracking tier is also shifted so that its echo is received after all previous echoes.

For a new Tracking tier j, cross-mode temporal orthogonality is achieved when

$$\left[t_{\mathrm{rs}}^{\mathrm{T}j}(n), t_{\mathrm{re}}^{\mathrm{T}j}(n)\right] \not\subset \left[t_{\mathrm{rs}}^{\mathrm{M}}(m), t_{\mathrm{re}}^{\mathrm{M}}(m)\right]. \tag{5.39}$$

Auto-mode temporal echo overlapping can also be avoided between Tracking tiers by ensuring that

$$\left[t_{\mathrm{rs}}^{\mathrm{T}j}(n), t_{\mathrm{re}}^{\mathrm{T}j}(n)\right] \not\subset \left[t_{\mathrm{rs}}^{\mathrm{T}i}(t), t_{\mathrm{re}}^{\mathrm{T}i}(t)\right], \tag{5.40}$$

with i the index of the operating Tracking tiers. The Tracking echo start time $t_{\mathrm{rs}}^{\mathrm{T}j}$ of a target j should be, therefore, be greater than the end time of MapSearch echo $t_{\mathrm{re}}^{\mathrm{M}}$

$$t_{\mathrm{rs}}^{\mathrm{T}j}(n) \geq t_{\mathrm{re}}^{\mathrm{M}}(m) + \tau_{\mathrm{g}}, \tag{5.41}$$

$\forall\ n \in [0, N_{\mathrm{p}}^{\mathrm{T}j}]$ and $m \in [m^*, N_{\mathrm{p}}^{\mathrm{T}j}]$ with $N_{\mathrm{p}}^{\mathrm{T}j}$ the number of Tracking pulses and m^* the index of the MapSearch PRI where the new Tracking tier j is added. Given the time delay $\tau_{\mathrm{delay}}^{\mathrm{T}j}$ of the echo defined in (5.21), the corresponding Tracking pulse should then be sent at

$$t_{\mathrm{ts}}^{\mathrm{T}j}(n) = t_{\mathrm{rs}}^{\mathrm{T}j}(n) - \tau_{\mathrm{delay}}^{\mathrm{T}j}. \tag{5.42}$$

Substituting (5.41) in (5.42) leads to

$$t_{\mathrm{ts}}^{\mathrm{T}j}(n) \geq t_{\mathrm{re}}^{\mathrm{M}}(m) + \tau_{\mathrm{g}} - \tau_{\mathrm{delay}}^{\mathrm{T}j}. \tag{5.43}$$

Sending pulses of different modes successively causes the cross-mode echoes to overlap. Therefore, a transmit time shift is necessary for the Tracking tier j to achieve the temporal orthogonality. It is therefore given by

$$\Delta_{\mathrm{ts}}^{j} \geq t_{\mathrm{re}}^{\mathrm{M}}(m) + \tau_{\mathrm{g}} - \tau_{\mathrm{delay}}^{\mathrm{T}j} - \left(t_{\mathrm{te}}^{\mathrm{M}}(m) + \tau_{\mathrm{g}}\right). \tag{5.44}$$

This time shift of the new Tracking pulse is however limited as it should not overlap with the MapSearch echo. Therefore the end time of the shifted pulse should be shorter than the start time of the MapSearch echo

$$t_{\mathrm{te}}^{\mathrm{T}j}(n) \leq t_{\mathrm{rs}}^{\mathrm{M}}(m) + \tau_{\mathrm{g}}. \tag{5.45}$$

The echo of an additional Tracking mode $j+1$ can easily overlap with the first Tracking mode j. To avoid this and ensure an auto-mode temporal orthogonality, the new Tracking mode should be also sent with a time shift relative to the previous echoes, as illustrated in the second PRI of Figure 5.21. If

$$\left[t_{\mathrm{rs}}^{\mathrm{T}j+1}(n), t_{\mathrm{re}}^{\mathrm{T}j+1}(n)\right] \subset \left[t_{\mathrm{rs}}^{\mathrm{T}j}(t), t_{\mathrm{re}}^{\mathrm{T}j}(t)\right], \tag{5.46}$$

the pulse of the Tracking mode $j+1$ is transmitted at

$$t_{\mathrm{ts}}^{\mathrm{T}j+1}(n) \geq t_{\mathrm{re}}^{\mathrm{T}j}(t) + \tau_{\mathrm{g}} - \tau_{\mathrm{delay}}^{\mathrm{T}j+1}. \tag{5.47}$$

Complete Temporal Orthogonality

The number of targets that can be tracked individually while maintaining temporal orthogonality in both cross-mode and auto-mode is given by

$$N_{\mathrm{t0}} \leq \left\lfloor \frac{t_{\mathrm{ts}}^{\mathrm{M}}(m+1) - t_{\mathrm{re}}^{\mathrm{M}}(m)}{\max\{T_{\mathrm{echo}}^{\mathrm{T}j}\}} \right\rfloor, \qquad N_{\mathrm{t0}} \in \mathbb{N}, \tag{5.48}$$

where $\lfloor \cdot \rfloor$ denotes the floor function to ensure N_{t0} is an integer. While temporal orthogonality offers efficiency, it also imposes certain constraints on the system. Its primary limitation is the capacity, particularly when considering a tight schedule. This limitation reduces the ability to track multiple targets across different tiers concurrently, as there is not sufficient time to ensure non-overlapping echoes. Furthermore, adhering strictly to this orthogonality curtails the system's adaptability to introduce additional Tracking tiers. As a consequence, the MapSearch idle time $\mathcal{T}_{\mathrm{idle}}^{\mathrm{M}}$ can not be optimally utilized. To tackle these constraints, the ADOB-SAR system accepts temporal overlapping of multi-mode echoes. To manage the resulting overlap, additional techniques, described in the next sections, are adopted to differentiate between echoes originating from distinct targets.

MapSearch-Tracking Cross Echo Orthogonality

The basic idea of the cross-mode orthogonality is to shorten the cumulative return echo duration by enforcing temporal overlapping of Tracking echoes while keeping

the MapSearch echo free of overlapping. The Tracking echoes received simultaneously are then separated using angular, frequency, or waveform orthogonality. To avoid the cross-mode temporal echo overlapping with MapSearch, the Tracking pulses are transmitted with a time shift according to (5.44), as depicted in Figure 5.22. A gap is created after the MapSearch pulse and the earliest Tracking pulse

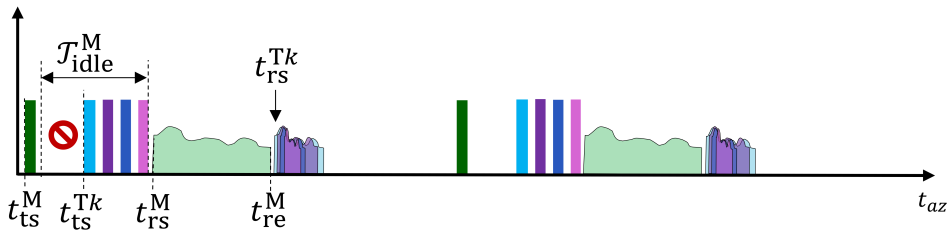

Figure 5.22: Timing diagram for the case that echo overlap between the different Tracking tiers is accepted.

is transmitted at $t^{\mathrm{T}k}_{\mathrm{ts}}(0)$, which corresponds to the farthest target k located at the maximum incident angle $\max\{\theta_{\mathrm{it}}\}$ and is given by (5.42) while setting the time delay $\tau^{\mathrm{T}k}_{\mathrm{delay}}$ to the maximum. The maximum number of Tracking tiers becomes dependent on the number of pulses that can be sent in the MapSearch idle time interval excluding the gap and is given by

$$N_{\mathrm{t1}} \leq \left\lfloor \frac{\mathcal{T}^{\mathrm{M}}_{\mathrm{idle}} - t^{\mathrm{T}k}_{\mathrm{ts}}(0) + t^{\mathrm{M}}_{\mathrm{te}}(m^*)}{\max\{\tau^{\mathrm{T}}_{\mathrm{p}}\}} \right\rfloor, \qquad N_{\mathrm{t1}} \in \mathbb{N}, \tag{5.49}$$

with $t^{\mathrm{T}k}_{\mathrm{rs}}$ satisfying the cross-mode temporal orthogonality defined in (5.41).

As it is possible that Tracking tiers are operated with different PRFs, more targets can be tracked by taking into consideration the use of a low PRF. Therefore, the maximum number takes into consideration the various Tracking PRFs and is updated to

$$N_{\mathrm{t1}} \leq \left\lfloor \underbrace{\frac{\mathcal{T}^{\mathrm{M}}_{\mathrm{idle}} - t^{\mathrm{T}k}_{\mathrm{ts}}(0) + t^{\mathrm{M}}_{\mathrm{te}}(m^*)}{\max\{\tau^{\mathrm{T}}_{\mathrm{p}}\}}}_{n_{\mathrm{p}}} + \sum_{i=1}^{n_{\mathrm{p}}} \left(\frac{\max\{\mathrm{PRF}^{\mathrm{T}}\}}{\mathrm{PRF}^{\mathrm{T}i}} - 1 \right) \right\rfloor, \tag{5.50}$$

which can also be written as

$$N_{\mathrm{t1}} \leq \left\lfloor \frac{\mathcal{T}^{\mathrm{M}}_{\mathrm{idle}} - (t^{\mathrm{M}}_{\mathrm{re}}(m^*) + \tau_{\mathrm{g}} - \max\{\tau^{\mathrm{T}k}_{\mathrm{delay}}\}) + t^{\mathrm{M}}_{\mathrm{te}}(m^*)}{\max\{\tau^{\mathrm{T}}_{\mathrm{p}}\}} + \sum_{i=1}^{n_{\mathrm{p}}} \left(\frac{\max\{\mathrm{PRF}^{\mathrm{T}}\}}{\mathrm{PRF}^{\mathrm{T}i}} - 1 \right) \right\rfloor, \tag{5.51}$$

by substituting (5.43) in (5.50).

Multi-mode Full Echo Overlap

The second level of temporal overlap involves various modes, including MapSearch and Tracking. Here, the overlap of the MapSearch echo with the Tracking echoes of different tiers is accepted. The pulses of the Tracking tiers are transmitted during the MapSearch idle time interval $\mathcal{T}_{\text{idle}}^{\text{M}}$ with respect to a short guard time τ_{g}, immediately after the MapSearch transmit pulse, when the cross-mode temporal overlapping of echoes is applied, as illustrated in Figure 5.23.

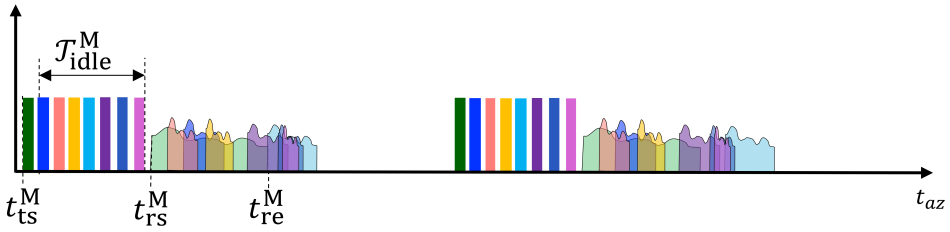

Figure 5.23: Timing diagram showing the maximum number of interleaved Tracking modes when the echo overlap between the MapSearch and the Tracking modes is accepted.

Referring to Figure 5.23, the upper limit on the number of targets that can be tracked individually is expressed as

$$N_{\text{t2}} \leq \left\lfloor \underbrace{\frac{\mathcal{T}_{\text{idle}}^{\text{M}}}{\max\{\tau_{\text{p}}^{\text{T}}\}}}_{n_{\text{p}}} + \sum_{i=1}^{n_{\text{p}}} \left(\frac{\max\{\text{PRF}^{\text{T}}\}}{\text{PRF}^{\text{T}i}} - 1 \right) \right\rfloor > N_{\text{t1}}, \tag{5.52}$$

which increases when a lower Tracking PRF is used, as defined in N_{t1} with (5.51). The only difference here is that the total MapSearch idle time $\mathcal{T}_{\text{idle}}^{\text{M}}$ is available for the Tracking tiers.

To manage the resulting temporal overlap, additional techniques, described in the next sections, are adopted to differentiate between echoes originating from distinct targets.

5.5 Angular Orthogonality of Multi-Mode Temporal Overlapped Echoes

Temporal overlapping of echoes is sometimes inevitable, especially as the number of targets within a scene grows and the need to include additional Tracking tiers surpasses the system's time constraints. This section delves into the concept of angular orthogonality, which can resolve ambiguities that arise from temporal overlaps.

5.5.1 Angular Diversity of Overlapped Echoes via DBF

Temporally overlapping echoes can be separated in the spatial domain if they arrive from different directions. Hence, two targets located at the incident angle θ_{e1} and θ_{e2}, can still be distinctly recognized and separated during post-processing if their respective receive elevation beams do not overlap, i.e., if the following orthogonality condition is fulfilled

$$| \theta_{e1} - \theta_{e2} | > \Theta_{tr}^{FN}. \tag{5.53}$$

The first-null-power beamwidth Θ_{tr}^{FN} is considered in this condition to avoid any space overlapping between the two signals, as illustrated in Figure 5.24(a). This condition indicates that while the two echoes may be received simultaneously due to differences in their respective pulse transmission times, their footprints on the ground must be distinctly separate. The difference between these footprints ensures that the two signals will not spatially interfere with each other, even if they do so temporally, as illustrated by the incident angle-time diagram in Figure 5.24(b). The higher the angular separation between the beams, the lower the spatial interference.

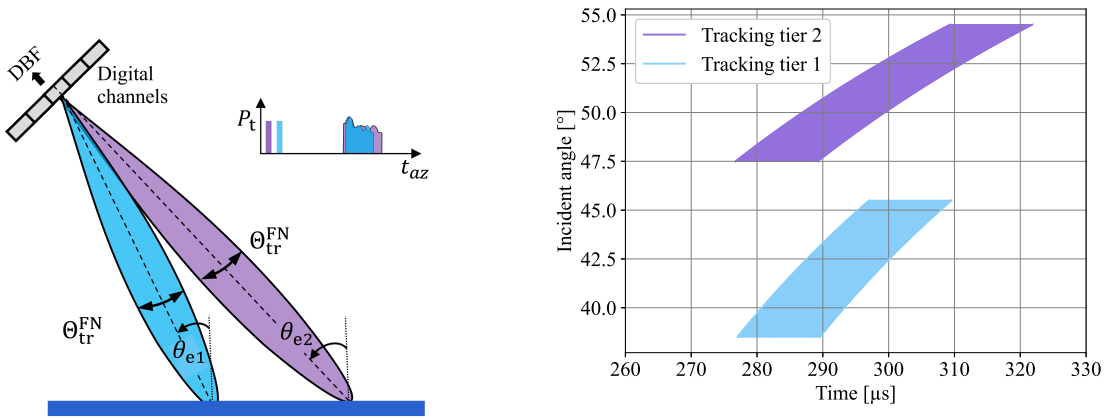

(a) Angular beam separation.

(b) Incident angle-time diagram of the return echoes.

Figure 5.24: Angular orthogonality between two temporal overlapped echoes from two beams steered to θ_{e1} and θ_{e2} while they have the same null beamwidth Θ_{tr}^{FN}.

The ADOB-SAR system can use the angular orthogonality via DBF only in the elevation direction due to the narrow receive beam. Conversely, the receive beam in the azimuth direction is broader than the transmit beam. The antenna array, equipped with several digital receive channels in elevation, can separate two simultaneous echoes originating from different range locations by analyzing their angles of arrival and reducing sidelobe interference. This capability is demonstrated in target scenarios (a) and (b) in Figure 5.18. The maximum number of separable echoes, assuming sufficient spacing, i.e. (5.53) applies for all targets, depends on the number of digital beams corresponding to the number of receive channels $N_{\mathrm{sub,e}}$. Advanced algorithms can be used such as spatial filtering and adaptive nulling to reconstruct the two distinct beams [118, 122, 213–217]. When a target is illuminated by the main lobe while the sidelobes cover another target on receive, range ambiguities can occur. The a priori knowledge of the targets' positions through the ADOB-SAR concept allows for managing the sidelobe echoes during post-processing. The Cross Elevation Beam Range Ambiguity Suppression (CEBRAS) method effectively suppresses range ambiguities by applying ground-based processing of multiple elevation beams and accounting for local topography and satellite errors [115]. Another technique involves employing a higher-order Blind Source Separation (BSS) method, which considers the 2-D dependence of the antenna radiation pattern to analytically model and resolve the range-ambiguity issue using a range-time and Doppler-frequency dependent mixing matrix [114, 218].

An example of the angular distribution of the temporally overlapped echoes across various Tracking Tiers is shown in Figure 5.25. They correspond to the scenario illustrated in the timing diagram of Figure 5.22. The corresponding incident angle

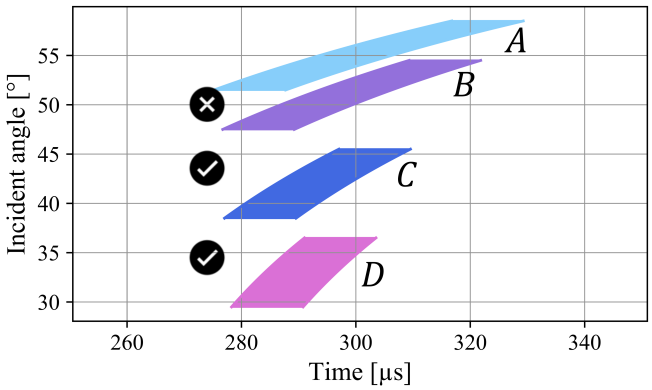

Figure 5.25: Incident angle-time diagram of temporally overlapped echoes originated from different Tracking tiers. The black circle indicates whether the echoes are angularly orthogonal or not.

of each received echo is plotted over time. The angular orthogonality condition

(5.53) is fulfilled for all Tracking tiers in operation except between A and B, as their echoes originate from the same far-range direction. Because they are tracked with different beams, the fact that their corresponding targets are located in the same range location indicates that they are in different azimuth positions. Therefore, an additional ambiguity suppression technique is needed for those two spatially overlapped echoes.

5.5.2 SCORE Angular Orthogonality

Transmitting Tracking pulses immediately after the MapSearch pulse increases the capability to simultaneously track multiple targets individually. However, due to the difference in echo timing between modes, Tracking beams often overlap temporally with the long green-colored MapSearch echo spanning the entire swath, as illustrated in Figure 5.26. Some echoes are received simultaneously from the same direction,

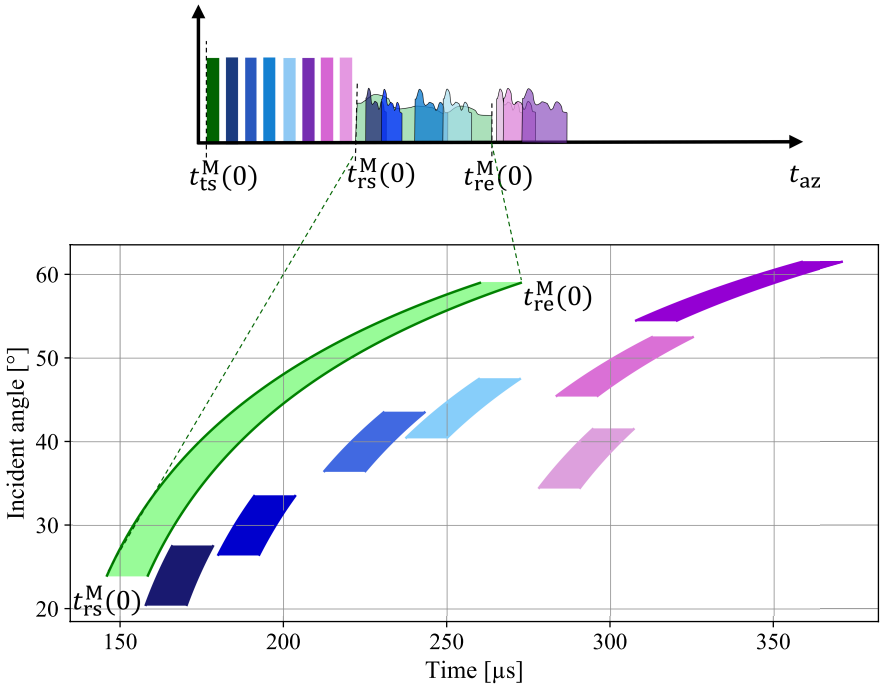

Figure 5.26: Timing diagram showing the cross-mode interleaving with temporal overlapping echoes. The incident angle of each echo is plotted over time in the second plot corresponding to different target locations.

such as the MapSearch and the first Tracking tier (in dark blue). Hence (5.53) is not fulfilled in this case. To mitigate this overlap and achieve precise angular

differentiation, the multichannel SCORE technique is employed. The idea of using SCORE to separate the cross-mode temporal overlapped echoes consists of taking advantage of the time-variant digital steering of the MapSearch beam on receive to ensure that the Tracking echo arrives with a SCORE beam from an entirely different direction. This angular difference creates a clear separation between the MapSearch and Tracking echoes, despite their temporal proximity.

Assuming that a target i is detected at the incident angle θ_i, its Tracking starts then with the beamwidth $\Theta_{\mathrm{tr}} = \Theta_{\mathrm{scr}}$, the same during transmission and reception. The Target i Tracking pulse is sent directly after the MapSearch pulse with a guard time τ_{g}, as depicted in Figure 5.27. The reception interval of its echo return is written as a function of $\theta \in \left[\theta_{\mathrm{i}} - \Theta_{\mathrm{tr}}/2\ ,\ \theta_{\mathrm{i}} - \Theta_{\mathrm{tr}}/2\right]$ as

$$\begin{aligned}\mathcal{T}_{\mathrm{r}}^{\mathrm{T}i}(\theta) &= \left[t_{\mathrm{rs}}^{\mathrm{T}i}(\theta), t_{\mathrm{re}}^{\mathrm{T}i}(\theta)\right] \\ &= \left[t_0 + \frac{2}{c}R_{\mathrm{min}}^{\mathrm{T}}(\theta) + \tau_{\mathrm{p}}^{\mathrm{M}} + \tau_{\mathrm{g}}\ ,\ t_0 + \frac{2}{c}R_{\mathrm{max}}^{\mathrm{T}}(\theta) + \tau_{\mathrm{p}}^{\mathrm{M}} + \tau_{\mathrm{g}} + \tau_{\mathrm{p}}^{\mathrm{T}i}\right],\end{aligned} \tag{5.54}$$

with $R_{\mathrm{min}}^{\mathrm{T}i}(\theta)$ and $R_{\mathrm{max}}^{\mathrm{T}i}(\theta)$ the near and far range limits of the Tracking beam defined in (5.20).

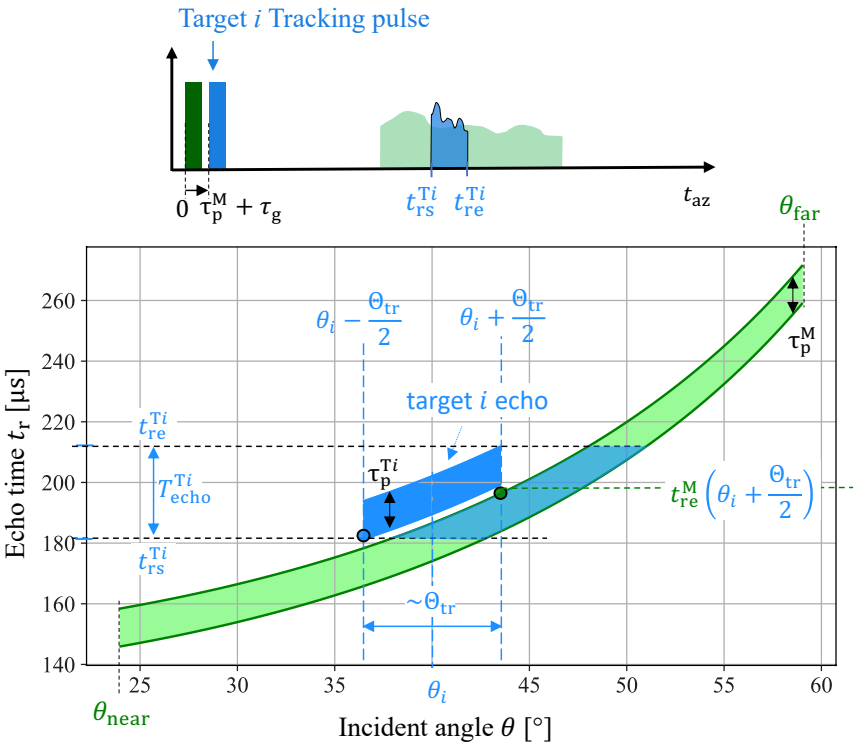

Figure 5.27: Incident angle-time diagram of the MapSearch echo (in green) and the Tracking mode of the target i echo return (in blue).

The Tracking echo timing is plotted over the incident angle in Figure 5.27. Depending on where the target is located, the echo is calculated following (5.54) and the Tracking beamwidth Θ_{tr}. In this example, $\tau_{\mathrm{p}}^{\mathrm{T}i} = \tau_{\mathrm{p}}^{\mathrm{M}}$. It can be seen that the projection of the Tracking echo overlaps with the SCORE beam coming from the same direction as the target i. Given that the Tracking pulse of target i is only offset from the MapSearch pulse by the guard time τ_{g}, its echo overlaps with the MapSearch SCORE beam coming from the same direction. This is primarily because the pulse duration's ground extension is smaller than the Tracking and SCORE beamwidth. When projecting the target echo timing onto the MapSearch echo by setting $\mathcal{T}_{\mathrm{r}}^{\mathrm{Mscr}}(\theta)$ (5.8) equal to $\mathcal{T}_{\mathrm{r}}^{\mathrm{T}i}(\theta)$ (5.54), the angular interval of their overlap becomes evident, as shown in the simulated plot of Figure 5.27.

The strategy behind using the SCORE configuration detailed here is to guarantee an adequate time shift between the target echo and the SCORE beam that originates from the same direction to create angular orthogonality. This shift is directly proportional to the Tracking mode beamwidth Θ_{tr}. Hence, it becomes possible to receive echoes simultaneously from different directions of arrival without physical footprint overlap. Distinguishing between these different beams becomes straightforward during post-processing.

An additional time shift is necessary if the earliest arrival of the target echo $t_{\mathrm{rs}}^{\mathrm{T}i}$ happens before the latest arrival of a SCORE beam having the Tracking beam farthest extremity $\theta_i + \Theta_{\mathrm{tr}}/2$, which after inserting it in (5.8) gives

$$t_{\mathrm{rs}}^{\mathrm{T}i}\left(\theta_i - \frac{\Theta_{\mathrm{tr}}}{2}\right) < t_{\mathrm{re}}^{\mathrm{M}}\left(\theta_i + \frac{\Theta_{\mathrm{tr}}}{2}\right), \tag{5.55}$$

as illustrated by the blue and green dots in Figure 5.27. The time shift necessary for the echo separation with respect to the previous pulse position is thus

$$\Delta t_{\mathrm{scr}} = t_{\mathrm{re}}^{\mathrm{Msc}}\left(\theta_i + \frac{\Theta_{\mathrm{tr}}}{2}\right) - t_{\mathrm{rs}}^{\mathrm{T}i}\left(\theta_i - \frac{\Theta_{\mathrm{tr}}}{2}\right) + \tau_{\mathrm{g}}. \tag{5.56}$$

This shift ensures that the Tracking echo arrives later than the virtual SCORE beam from the same direction and footprint as the target i, leading to angular orthogonality. As shown in Figure 5.28, the Tracking echo is shifted in time, and its projection on the MapSearch echo no longer overlaps with the echo coming from the incident θ_i. It still overlaps with the MapSearch echo but at different incident angles, which is the goal. The timing diagram highlighting this necessary shift is also provided. Achieving a positive SCORE time shift becomes more challenging when the number of targets increases. The final expression for the SCORE shift used to distinguish the echoes reduces to $\Delta t_{\mathrm{scr}} = 0$ if condition (5.55) is not met. This scenario arises when additional Tracking pulses are scheduled after the MapSearch pulse, implying

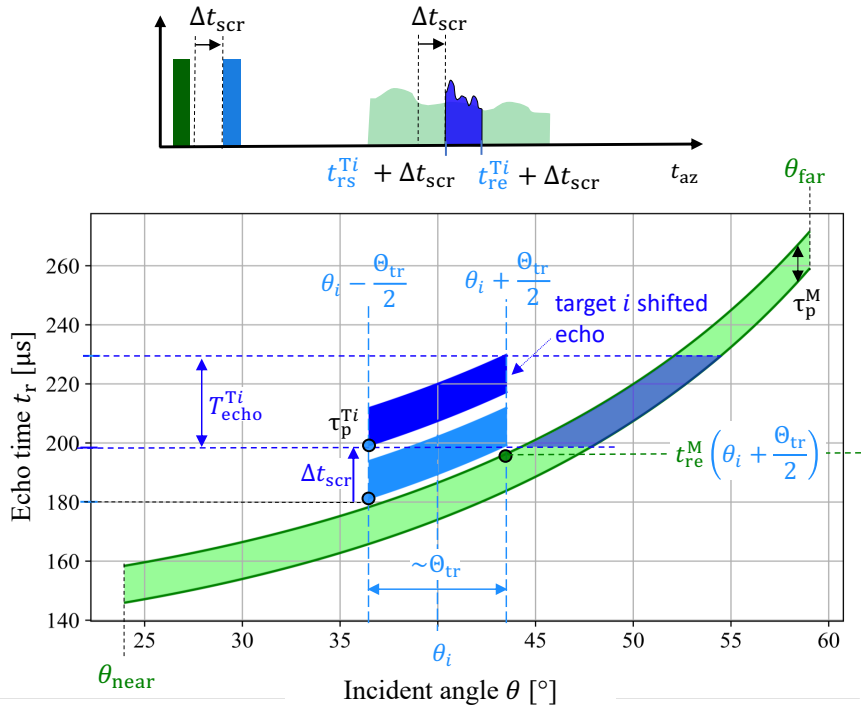

Figure 5.28: Incident angle-time diagram of the MapSearch echo (in green) and the Tracking mode of the target i echo return without time shift (in blue) and with time shift (in dark blue) according to (5.56).

that the requisite shift has already been applied. Such is the situation for the third and fourth Tracking echoes, depicted in blue, in Figure (5.26).

5.6 Multi-Mode Frequency Orthogonality

While the first two techniques leveraging temporal and angular orthogonality are efficient in mitigating ambiguities arising from inevitable echo overlaps, they might not always be applicable due to other constraints. In such cases, the third strategy comes into play, which is frequency orthogonality, following the scheduling algorithm shown in the flow chart of Figure 5.17. The main idea behind it is to ensure disjoint, i.e. non-overlapping, frequency spectra of the radar return echoes.

For a mode i operating with a transmit pulse of carrier frequency f_i and bandwidth B_i, the frequency spectrum of its return echo is defined as

$$\mathcal{R}_{fi} = \left[f_i - \frac{B_i}{2} - \varepsilon, f_i + \frac{B_i}{2} + \varepsilon \right], \tag{5.57}$$

where ε is a margin accounting for the sidelobes and Doppler frequency shift at the edges of the interval.

If the echo of mode j is temporally overlapping with the echo of mode j, frequency orthogonality can be applied when their respective frequency spectra are disjoint, namely when $\mathcal{R}_{\mathrm{f}i} \not\subset \mathcal{R}_{\mathrm{f}j}$. Figure 5.29 shows an example of the utilization of the frequency orthogonality, where $\mathcal{R}_{\mathrm{f}i}$ and $\mathcal{R}_{\mathrm{f}j}$ indicate disjoint frequency spectra of the MapSearch and Tracking acquisitions.

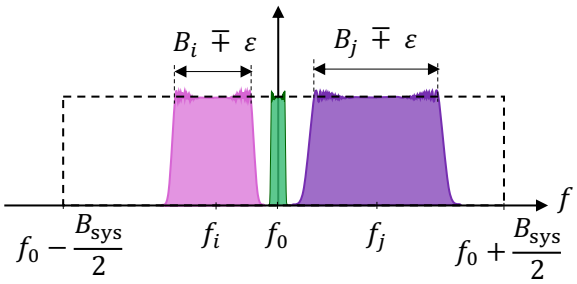

Figure 5.29: Frequency orthogonality to separate temporal and angular overlapping echoes. The green spectrum at f_0 corresponds to MapSearch, while the pink at f_i and the purple at f_j to Tracking tier i and j, respectively.

The maximum Doppler shift is considered for the spectra separation, which is given by

$$f_{\mathrm{D}}^{\max} = -\frac{2}{c_0} f^{\max} v^{\max} \sin\left(\theta_i^{\max}\right), \tag{5.58}$$

A HAP having a velocity of $v_{\mathrm{p}} = 20\,\mathrm{m/s}$ or a target moving on ground with maximally $v_{\mathrm{tg}} = 25\,\mathrm{m/s}$ leads to a Doppler shift of approximately $f_{\mathrm{D}} = -1500\,\mathrm{Hz}$, which is negligible compared to the chirp bandwidth B_i.

The ADOB-SAR decision-maker defines each Tracking tier by a unique chirp bandwidth, which is adapted based on the range resolution requirements and target characteristics. It can vary up to the maximum sensor bandwidth B_{sys}. As this maximum bandwidth is not always fully utilized, it is possible to select different portions of the frequency spectrum when scheduling subsequent Tracking tiers. The maximum sensor bandwidth B_{sys} is preset during the design phase and corresponds to the finest desired range resolution for the Tracking mode. A system bandwidth $B_{\mathrm{sys}} = 600\,\mathrm{MHz}$ is set for the designed ADOB-SAR reference system. The number of orthogonal spectra that can be used within B_{sys} depends strongly on the Tracking bandwidths, as they vary from one tier to the other. Considering the minimum bandwidth in the order of $\min\{B_i\} = 20\,\mathrm{MHz}$, up to 30 orthogonal spectra can be used simultaneously.

Figure 5.30 shows the incident angle and the timing of the temporal and angular overlapping echoes MapSearch and Tracking tiers i and j.

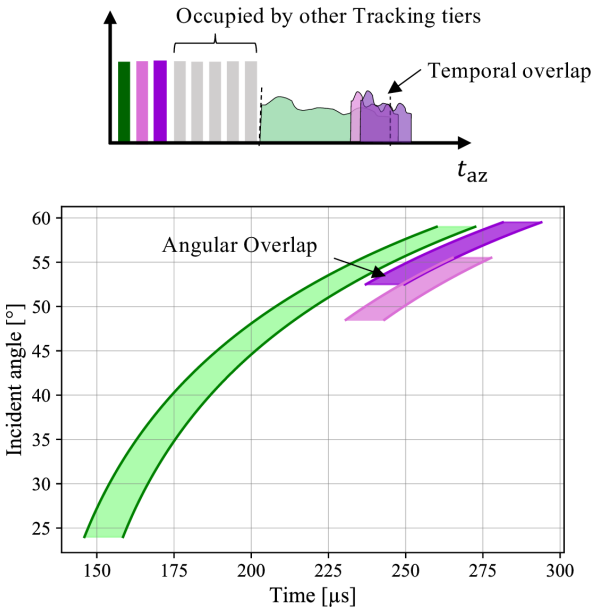

Figure 5.30: Incident time-angle diagram showing the angular and temporal overlap between MapSearch and Tracking return echoes of tiers i and j.

The MapSearch mode is operated with a low bandwidth at the center frequency f_0 within the frequency spectrum $\mathcal{R}_{\mathrm{f}_0}$. The target i is tracked with a higher bandwidth $B_i > B^{\mathrm{M}}$, and its center frequency is shifted to f_i to ensure frequency orthogonality with MapSearch. The elevation footprint of the beam illuminating a new target j overlaps with the footprint of the beam corresponding to target i, therefore (5.53) does not apply and angular orthogonality cannot be used. Their echoes temporarily overlap as well. Therefore, to separate the two echoes, target j should be tracked with a different center frequency $f_j \neq f_i \neq f_0$ according to the condition

$$|f_j - f_i| > \frac{B_i}{2} + \frac{B_j}{2} + 2\varepsilon. \tag{5.59}$$

This ensures that the frequency spectra of both tiers are not superimposed.

However, the frequency shift has a limit as the new Tracking chirp j should stay within the total sensor bandwidth following

$$\mathcal{R}_{\mathrm{f}j} \subset \left[f_0 - \frac{B_{\mathrm{sys}}}{2}, f_0 + \frac{B_{\mathrm{sys}}}{2} \right]. \tag{5.60}$$

5.7 Multi-Mode Waveform Diversity

As frequency shifting is limited by the maximum sensor bandwidth, waveform diversity is used as an alternative strategy to separate superimposed echoes and resulting ambiguities [179, 219–221]. This approach uses different waveforms to create a distinct signature for each target, thus resolving the temporal, angular, and frequency spectrum overlapping issues. Assuming a target i is being tracked with an up-chirp signal defined in (2.5). A second target j can be tracked separately using a different waveform, such as a down-chirp defined in (2.6). The separation of their two return echoes based on their waveforms is done during range compression through cross-correlation with both the transmitted up-chirp and down-chirp reference signals.

The two Tracking tiers can be operated with different bandwidths and pulse durations, hence different chirp rates k_i and k_j, as the waveform parameters for each target are selected by the adaptive decision-maker according to its properties.

The corresponding echoes, when considered independent, are represented with a time delay proportional to the chirp reflection on the ground as

$$r_{\text{up}}(t) = s_{\text{up}}\big(t - \tau_{\text{delay}}^{\text{T}i}\big), \tag{5.61}$$

and

$$r_{\text{down}}(t) = s_{\text{down}}\big(t - \tau_{\text{delay}}^{\text{T}j}\big), \tag{5.62}$$

for the up- and down-chirp, respectively.

The total received signal, when sending both chirp types, is the summation of the two superimposed echoes including cross-reflections, and is given by

$$r(t) = r_{\text{up}}(t) + r_{\text{down}}(t) + s_{\text{up}}\big(t - \tau_{\text{delay}}^{\text{T}j}\big) + s_{\text{down}}\big(t - \tau_{\text{delay}}^{\text{T}i}\big). \tag{5.63}$$

To separate these overlapping echoes, a range compression is conducted with the two different waveforms, first with the complex conjugate of the time-reversed up-chirp reference signal (2.5), then with the down-chirp (2.6) as follows

$$\begin{aligned} R_{\text{up}}(t) &= r(t) \otimes s_{\text{up}}^{*}(-t), \\ R_{\text{down}}(t) &= r(t) \otimes s_{\text{down}}^{*}(-t). \end{aligned} \tag{5.64}$$

Figure 5.31 shows a simulated example of superimposed echoes and the range compression with waveform diversity. The total received signal is the summation of the two return echoes over time, as shown in the first plot. The range compression gives as output a peak at the target range location when the reference signal is the same as the transmitted waveform. The resulting peaks designate the two targets, each imaged with a distinct Tracking tier. Different bandwidths are used in the illustrated example. Therefore, the peak of target i is wider than that of target j. By

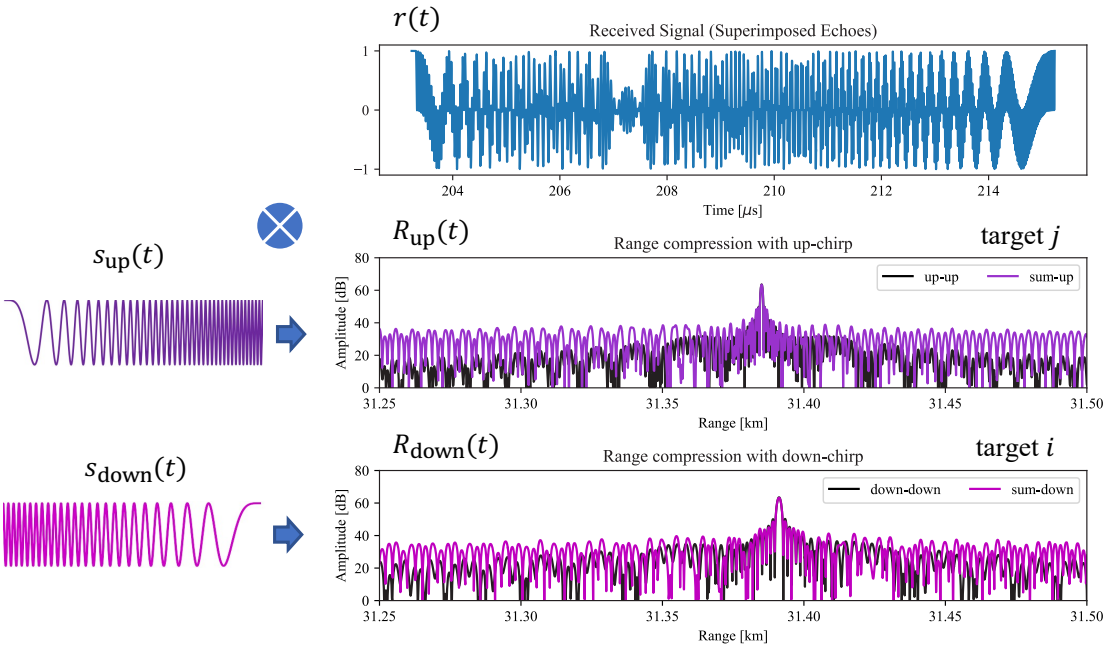

Figure 5.31: Range compression with two different orthogonal waveforms to separate two echoes of different Tracking tiers arriving simultaneously from close range positions. The bandwidth used for the up-chirp is $B_{\text{up}} = 50\,\text{MHz}$ for the down-chirp is $B_{\text{down}} = 25\,\text{MHz}$ with a pulse duration of $\tau_{\text{p}} = 12\,\mu\text{s}$.

employing the waveform orthogonality technique, the radar can effectively separate the simultaneously returning echoes. The suppression of target i from the range compressed data of target j indicated how well the system can distinguish between the two different return echoes. It is a measure of what remains from the undesired signal (target i) after the desired signal (target j) has been processed, and vice versa. The analysis showed a suppression of 25.5 dB for the up-chirp target in down-chirp data and 26 dB for the down-chirp target in up-chirp data, indicating effective differentiation and interference reduction between the two targets.

However, it is crucial to acknowledge that the orthogonality of transmitted signals, including up-chirps and down-chirps, is not inherently guaranteed, especially in the case of distributed targets, as demonstrated in [222–224]. This lack of precise orthogonality may lead to the misalignment of energy from the two echoes after range compression, potentially resulting in smeared or inaccurately positioned echo signals. When the backscattering of the targets exceeds that of the background, which is considered in this ADOB-SAR concept by a homogeneous clutter, the energy leakage spreads over an extended range and the two targets can be individually tracked, as depicted in Figure 5.31.

5.8 Multi-Mode Interleaving Simulation

Depending on the real-time target scenario, the ADOB-SAR processor follows the time scheduling strategy of the multi-mode interleaving, illustrated in Figure 5.17. Each new Tracking tier is sequentially added to the acquisition after checking all ambiguity constraints. The most suitable orthogonality technique is selected based on the available radar resources. In this section, a scenario with eight targets is simulated, and the resulting automatic scheduling plan is depicted in Figure 5.32. It includes a first subplot showing the time flow of all transmitted pulses and received echoes of the MapSearch mode, as well as the different operating tracking tiers. To highlight the spatial overlapping of echoes, the incident angle and the frequency variation for each mode are plotted over time in the second and third subplots.

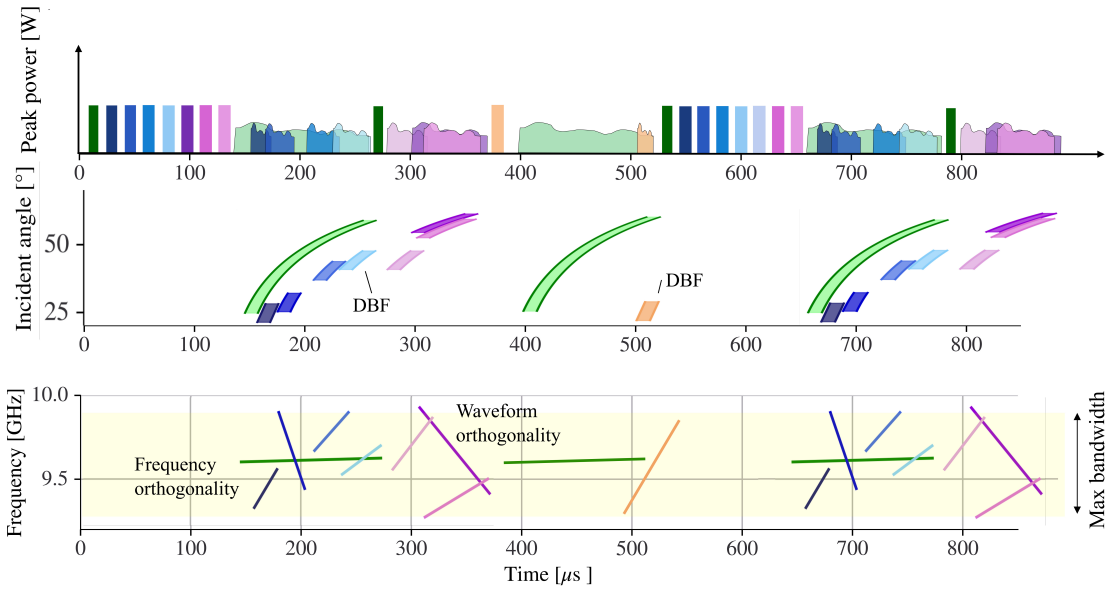

Figure 5.32: Simulated example of a cross-mode echo overlapping suppression using temporal, angular, frequency, and waveform orthogonality.

In this example, a scenario with a high level of clutter is considered. Thus, the MapSearch is operated with a high $\mathrm{PRF}^{\mathrm{M}}$, following the clutter-based PRF adaptation approach in Section 5.1.5. The instrument parameters of the designed reference system listed in Chapter 7, Table 7.2 with a center frequency of $f_{\mathrm{c}} = 9.65\,\mathrm{GHz}$ and a bandwidth of $B^{\mathrm{M}} = 20\,\mathrm{MHz}$ are applied, as illustrated by the frequency variation of the echoes in the third plot. The tracking tiers have higher resolutions than MapSearch, resulting in higher bandwidths and frequency variations. Each target is imaged with a distinct bandwidth, which is determined by the decision-making

processor. This simulation demonstrates how the adaptive bandwidth adjustment facilitates the shifting of the waveform frequency between the interleaved modes.

The echoes of the first four Tracking tiers are received simultaneously as the MapSearch echo. The following techniques are used to separate them:

1. As the first target is located in the near range, its echo overlaps with the SCORE beam arriving from the same direction. This overlap is evident in the incident angle plot. Therefore, frequency orthogonality is used in this case, and the Tracking Tier 1 operates with a shifted frequency, as depicted in the third plot. This target requires a moderate resolution, therefore its bandwidth remains below the maximum sensor bandwidth $B^{\mathrm{T1}} < B_{\mathrm{sys}}$, and the frequency shift can be applied following (5.59).

2. The echo from the second Tracking tier temporally intersects with both the MapSearch and the first Tracking tier. A frequency shift is not possible due to the high-resolution requirement of target 2. This Tracking tier is operated with a high bandwidth, so that condition (5.60) cannot be fulfilled. Therefore, waveform orthogonality is applied in this case, and a down-chirp is sent to track target 2 individually.

3. The third Tracking tier temporally and angularly overlaps with MapSearch. Frequency orthogonality is applied here, given that it operates with a moderate bandwidth, similar to the first tier.

4. The fourth Tracking tier has an echo that is superimposed with the MapSearch echo. Nevertheless, there exists an angular difference between the two beams, as illustrated in the incident angle plot in the middle. Therefore, DBF is used to separate the two overlapping echoes by using their respective directions of arrival. The same center frequency f_{c} can be then used, as demonstrated in the frequency plot.

Subsequent Tracking tiers follow the same scheduling principle. The next chapter delves into the selection criteria for the optimal parameters tailored for each Tracking acquisition.

6 Adaptive Observing SAR Decision-Making

This chapter delves into the innovative Adaptive Observing SAR system, spotlighting its smart algorithm: the dynamic decision-maker. As an advanced control unit, it intelligently adapts the system's operational parameters according to the given scenario by considering both the scene properties and the operation constraints. A standout feature is its adaptive rule-based resource management, which facilitates a rapid reconfiguration of various interleaved modes, adapting to distinct scenario requirements. The selection of the optimal configuration is based on the dynamic optimization model, which adjusts the system's performance in response to the changing conditions of the scenario. Specific control decision rules based on user requirements and target properties are implemented. The dynamic decision-maker is based on adaptive forcing models, which consider time and hardware constraints. Drawing on the foundational principles outlined in the reconfigurable instrument design of Chapter 4 and the interleaving techniques and signal orthogonality detailed in Chapter 5, the processor's objective is to select the optimal instrument operation technique and configuration for each target scenario. One feature of the ADOB-SAR concept is leveraging the required performance parameters to achieve specific operational objectives. The implemented control model achieves data reduction and efficient use of the radar resources including power consumption.

The chapter is organized as follows. Section 6.1 introduces the used decision rules for selecting the optimal instrument configuration, followed by the mathematical derivation of the adaptive forcing models, considering the entire scenario and modes in operation, in Section 6.2. Then in Section 6.4, the dynamic optimization model, which combines all the previous models, is derived. The decision-making methodology described in this chapter is presented in the journal paper [174].

6.1 Smart Control Decision Rules

The performance of the Adaptive Observing SAR system depends significantly on the underlying decision-making process. While the MapSearch mode facilitates the extraction of target and scene properties, the decision rules ensure efficient Tracking and imaging, conserving SAR resources and achieving precise object recognition. The rules dictate how operational instrument parameters are adjusted and how

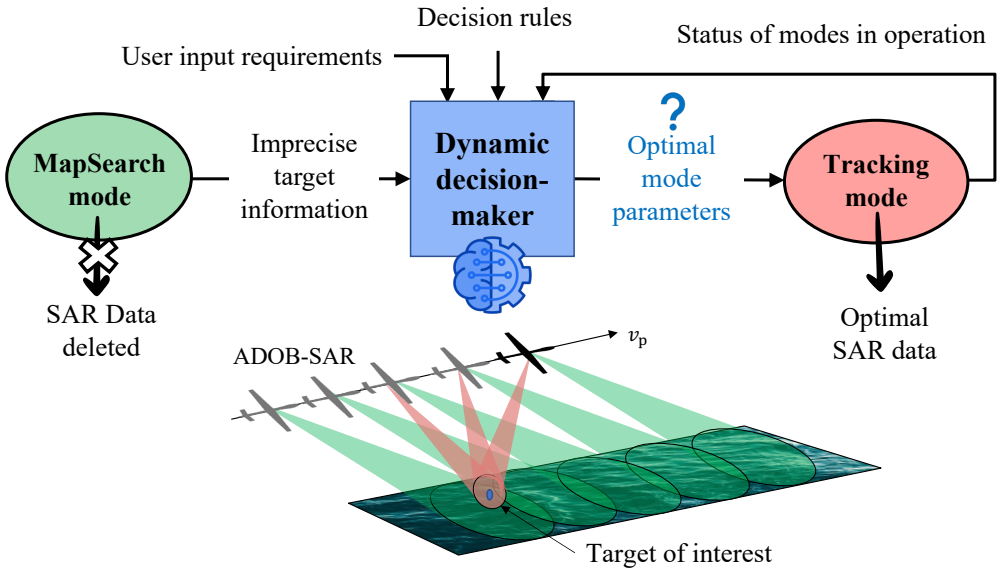

Figure 6.1: The dynamic decision-maker of the ADOB-SAR operation, which selects the optimal configuration and runs an adaptive Tracking according to the target and scene information provided by the continuous MapSearch mode.

beam combinations are selected for each acquisition, as illustrated in Figure 6.1. The decision-maker should have an overview of previous decisions of modes in operation, as depicted by the feedback arrow from the Tracking mode. User requirements also play a vital role in influencing the decision-making. It is important to note that, while MapSearch offers initial insights into the target properties, it is not sufficient in terms of accuracy and precision. The preliminary estimation serves as the basis for further investigations conducted by the adaptive Tracking mode. This acquisition, which is focused on the target, substantiates the initial findings with a higher degree of accuracy and certainty, thereby providing a more reliable assessment of the target parameters. This Section outlines the different control decision rules applied to the ADOB-SAR system.

6.1.1 Adaptive Spatial Resolution Control

During the Tracking mode, a synthetic aperture is formed throughout the flight leading to a SAR image after processing. The image quality required for object recognition depends on its spatial resolution and the size of the tracked object. It is, thus, evident that a finer resolution is necessary for the recognition of smaller targets compared to larger ones. To effectively recognize and classify objects in SAR images, it is generally recommended to have a minimum of 50 to 100 pixels on the target [142]. This criterion forms the basis of the first control decision rule, which sets the spatial resolution dependent on the target size. This approach ensures that only the necessary resources are used to achieve the required pixel density. Adapting

the resolution based on the target size and goals of the operation can help focus the radar's capabilities where they are most needed. Hence, the system operates more intelligently, making the entire operation more efficient.

The spatial resolution varies across different Tracking mode tiers based on the properties of the observed targets. The required azimuth δ_a and ground range resolution δ_r are linked to the size of the target area, denoted by A_t, so that

$$\frac{A_\mathrm{t}}{N_\mathrm{px1}} \leq \delta_\mathrm{a}\delta_\mathrm{r} \leq \frac{A_\mathrm{t}}{N_\mathrm{px2}}, \tag{6.1}$$

with

$$\delta_\mathrm{a} = \beta\, \delta_\mathrm{r}, \tag{6.2}$$

and $A_\mathrm{t} = W_\mathrm{t} L_\mathrm{t}$ the product of the target width and length, as shown in Figure 6.2. The target area size is assumed rectangular, based on the bounding box principle of irregular target shapes. N_px1 is the desired maximum and N_px2 minimum number of pixels (azimuth and range resolution cells) on target, respectively. β represents a factor describing the desired ratio between azimuth and range resolutions.

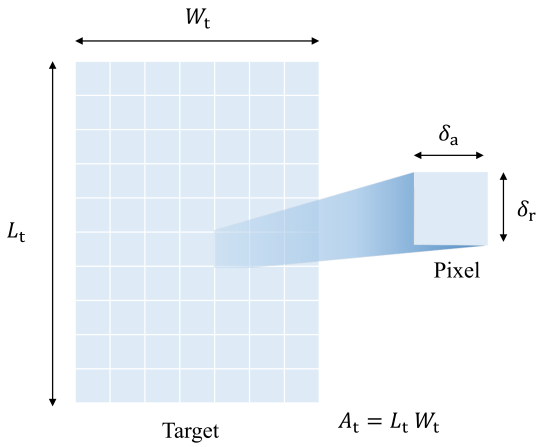

Figure 6.2: The pixel size corresponding to the azimuth δ_a and range resolution δ_a depending on the total required number of pixels, target width W_t and length L_t.

While the number of pixels contributes to the SAR image quality, the fundamental resolution depends more on the radar system's design parameters, such as bandwidth, wavelength, and synthetic aperture length. Hence, increasing the number of pixels using interpolation is not considered, as it does not improve the actual resolution of the SAR image.

The number of pixels on target is set as a range for more flexibility. It can be defined by the user, according to specific performance requirements.

The target size is initially estimated in the MapSearch mode, described in Section 4.1. It is done by analyzing the signal strength, which is directly proportional to the target radar cross Section [141, 225]. Supplementary sources, such as the Automatic Identification System (AIS) signal information for maritime applications, can also be used, if available.

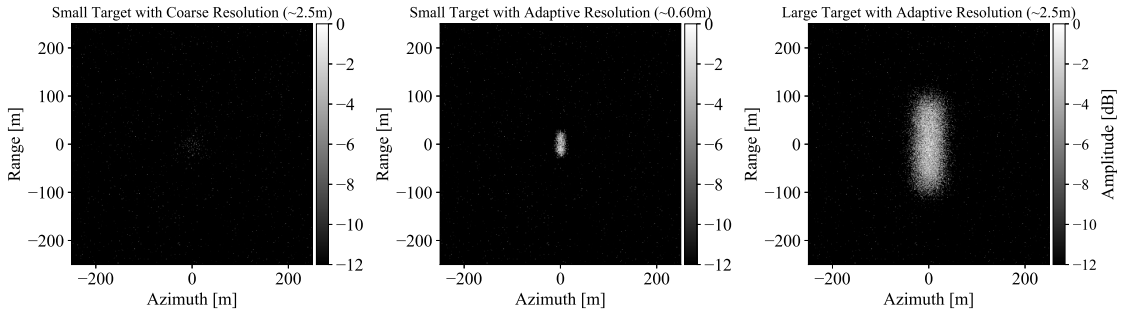

Figure 6.3: SAR simulated images of different targets (small: $20\,\mathrm{m}^2$ and large: $400\,\mathrm{m}^2$) with various adaptive resolutions based on their sizes.

Simulated targets having different sizes are shown in Figure 6.3. The left image represents a small target with an area of $20\,\mathrm{m}^2$ imaged with a coarse resolution of approximately 2.5 m, causing the target features to appear blurred and making it difficult to recognize. The middle image shows the same small target but with a fine resolution of approximately 0.6 m, which is adapted to its size. Its features are much clearer, which emphasizes the need for a higher resolution when imaging smaller objects. The image on the right represents a larger target with an area of $400\,\mathrm{m}^2$ with an adaptive resolution of approximately 2.5 m. Despite the coarser resolution, its features remain clear, demonstrating that it doesn't require a high resolution to be recognizable. These visuals reinforce the idea of adaptive spatial resolution in SAR imaging. Larger targets can be effectively recognized even with coarser resolutions, while smaller targets may require finer resolutions to distinguish their features.

Resolution Control Parameters

To achieve a specific azimuth resolution δ_a, the target should be observed for a defined period, called the SAR dwell time and denoted by T_D. It is, therefore, the

first control parameter that adapts the azimuth resolution for each Tracking mode tier and is expressed by [87]

$$T_{\mathrm{D}} = \underbrace{\frac{\lambda}{2v_{\mathrm{p}}}}_{\substack{\text{constant}\\ \text{term}}} \underbrace{\frac{R_{\mathrm{t}}}{\delta_{\mathrm{a}}}}_{\substack{\text{input}\\ \text{variables}}}, \tag{6.3}$$

where R_{t} is the slant range of the target. The azimuth resolution δ_{a} depends on the target area size A_{t} according to (6.1). These two parameters, extracted from the initial MapSearch mode analysis, are set as the input variables in determining the optimal dwell time for each target.

A proportional relationship exists between the dwell time and the resolution, where an enhancement in resolution needs a longer dwell time. Furthermore, targets in the far range need a longer observation period than targets in the near range to achieve the same resolution, as illustrated by the simulated plot in Figure 6.4(a). The dwell time is therefore reduced for larger targets in near range, thereby conserving time and resources to image new targets.

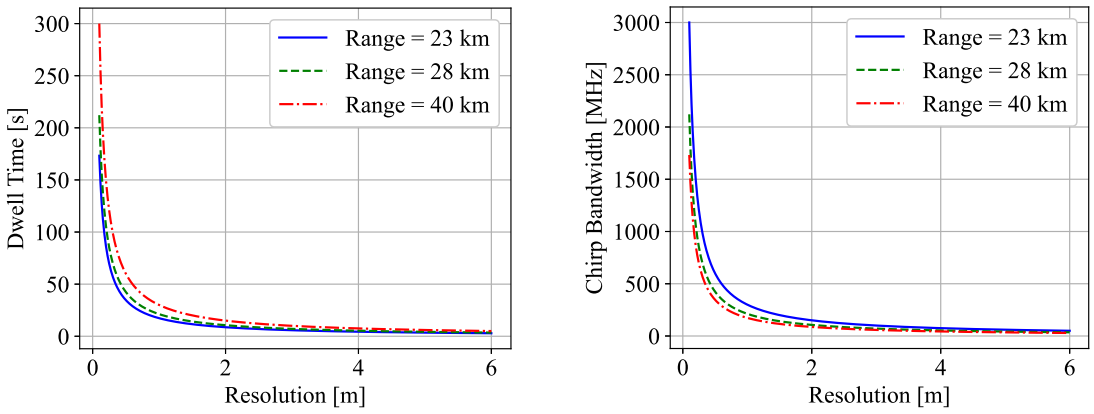

(a) Dwell time versus azimuth resolution.

(b) Chirp bandwidth versus range resolution.

Figure 6.4: Spatial resolution control highlighting the influence of the dwell time and chirp bandwidth for different slant ranges. A platform height of $H = 20\,\mathrm{km}$ at X-band is used in the simulation.

To achieve a specified ground range resolution, the chirp bandwidth B should be controlled according to

$$B = \underbrace{\frac{c_0}{2}}_{\substack{\text{constant}\\ \text{term}}} \underbrace{\frac{1}{\delta_{\mathrm{r}} \sin\theta_{\mathrm{it}}}}_{\substack{\text{input}\\ \text{variables}}}, \tag{6.4}$$

where θ_{it} is the incident angle of the target, serving as the third input variable in consequence as shown in Figure 6.5. In conventional SAR systems, the ground range resolution typically improves with increasing range, as shown in Figure 6.4(b). Using the proposed approach, targets having similar characteristics will retain uniform range resolution, regardless of their range location. The transmit signal bandwidth is therefore increased for targets in near range and decreased for large sizes.

The spatial resolution control rule applied to the ADOB-SAR system is summarized by the process depicted in Figure 6.5. It is based on adjusting two key parameters: the bandwidth and the SAR dwell time. These adaptations are carried out for each target, according to its unique properties, which are the slant range, size, and incident angle. The adaptive resolution control rule can be expressed as a function f_{res} given by

$$\Big(T_{\mathrm{D}}, B\Big) = f_{\mathrm{res}}\Big(R_{\mathrm{t}}, A_{\mathrm{t}}, \theta_{\mathrm{it}}\Big), \tag{6.5}$$

according to (6.3) and (6.4).

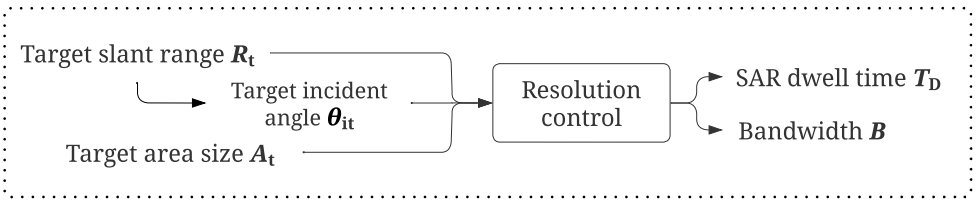

Figure 6.5: Schematic representation of the resolution control process, where the bandwidth and the SAR dwell time are adapted for each target depending on its slant range, size, and incident angle, as given in (6.3) and (6.4).

By adapting the bandwidth and dwell time based on these variables, the system can maintain an optimized resolution control strategy that ensures uniform image quality and efficient target recognition throughout the swath. This innovative approach overcomes the limitations of a fixed resolution, thereby paving the way for more effective target analysis, as demonstrated by the simulation in Chapter 7.

6.1.2 Adaptive Energy Control

Targets can be located in different positions within the swath and exhibit different backscattering behaviors that depend on their size, material, and orientation. Therefore, the radar equation becomes a key tool in the resource control strategy. The second control decision rule consists of adapting the transmitted energy depending on the following factors:

- The target range position.
- The target backscatter characteristics/RCS.
- The clutter reflectivity.
- The number of targets in the scene.

During the Tracking mode, each detected target is assigned to a distinct narrow beam, that is automatically directed toward its respective position on the ground. The backscattering behavior of targets varies across ranges, as shown in Figure 6.6. Signals are typically less attenuated in near range compared to far range, due to

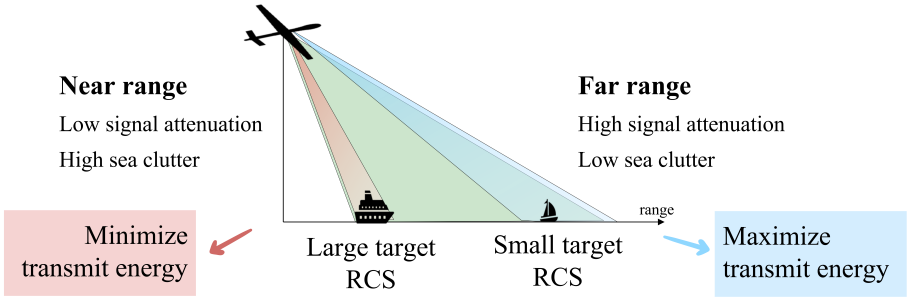

Figure 6.6: Adaptive energy control strategy. The wide green beam corresponds to the MapSearch mode, which illuminates the entire swath. The narrower red and blue beams correspond to two Tracking mode tiers for targets at different range locations.

the free-space loss. Furthermore, the clutter reflectivity decreases with the incident angle, enhancing the visibility of targets at far range [155]. Consequently, the target range position is considered a critical input parameter to adapt the energy level for each Tracking tier.

The goal is to achieve only the required performance for all targets, regardless of their varying characteristics. Consequently, the strategy is based on adapting the transmitted energy for each target to ensure that the received power is within the limits derived from the required performance. This conserves instrument resources, which can then be reallocated to more demanding scenarios and targets.

A consistent Signal to Clutter plus Noise Ratio (SCNR) is maintained across all target ranges and RCS values so that

$$\mathrm{SCNR} = \frac{\sigma_\mathrm{t} N_\mathrm{p}}{\dfrac{\lambda c_0 R_\mathrm{t} \sigma_0 \mathrm{PRF}}{4 v_\mathrm{p} \sin\theta_\mathrm{it} B} + \dfrac{(4\pi)^3 K T_\mathrm{s} F L R_\mathrm{t}^4}{P_\mathrm{t} \lambda^2 G_\mathrm{tx} G_\mathrm{rx} \tau_\mathrm{p}}} \stackrel{!}{=} \mathrm{SCNR}_\mathrm{D}, \tag{6.6}$$

according to (2.57). Its expression depends on many parameters, as defined in (6.6). To elaborate on this, the parameters are categorized into three distinct groups:

1. **Target and clutter variables**: These variables are extracted from the MapSearch mode and change with the observed scenario. They serve as the input parameters to the energy control function, including the target cross section σ_t, the target slant range R_t and corresponding incident angle θ_it, and the clutter reflectivity σ_0.
2. **Instrument operational parameters**: These are the control parameters adapted to achieve the desired performance, including the number of pulses N_p, the PRF, the pulse duration τ_p, the bandwidth B, the peak power P_t, and the transmit and receive antenna gains $G_\mathrm{tx,rx}$. They are highlighted in blue in equation (6.6).
3. **Fixed instrument parameters and constants**: These parameters are specific characteristics of the radar platform and the frequency of the radar signals being used. They may include the wavelength λ, the platform velocity v_p, the Boltzmann's constant K, the system temperature T_s, the noise Figure F, and the losses L.

The user can set the desired SCNR value, $\mathrm{SCNR_D}$, according to the required observation performance. A typical value is between 15 dB to 20 dB.

The stated SAR parameters are dynamically adjusted on the fly for each target scenario. The transmit power, namely the average power P_avg plays a major role in the energy control of the system. It is given by

$$P_\mathrm{avg} = P_\mathrm{t}\, d_\mathrm{c} = P_\mathrm{t}\ \mathrm{PRF}\ \tau_\mathrm{p}. \tag{6.7}$$

To control the average power, the duty cycle d_c is adjusted for each detected target. The decision-making processor needs to select the optimal PRF and pulse duration τ_p to achieve the desired energy performance, which is quantified by the SCNR (6.6). The average power can be expressed as a function of the target slant range R_t and its RCS σ_t for a desired Signal to Noise Ratio $\mathrm{SNR_D}$. Inserting (6.7) into (2.57) and solving for the average power yield to

$$P_\mathrm{avg} = \underbrace{\frac{\mathrm{SNR_D}(4\pi)^3 K T_\mathrm{s} F L}{\lambda}}_{\text{constants}} \quad \underbrace{\frac{R_\mathrm{t}^4}{\sigma_\mathrm{t}}}_{\text{input variables}} \quad \underbrace{\frac{\mathrm{PRF}}{G_\mathrm{tx} G_\mathrm{rx} N_\mathrm{p}}}_{\substack{\text{other control}\\ \text{parameters}}}. \tag{6.8}$$

As illustrated in Figure 6.7, the average power is increased for targets in far range or having smaller target RCS until it reaches a threshold defined by the predetermined maximum duty cycle $d_\mathrm{c,max}$. Beyond this point, the system can no longer increase

the average power, but it can adjust other radar parameters, such as N_p, to achieve the requisite transmit energy necessary to obtain the desired SNR.

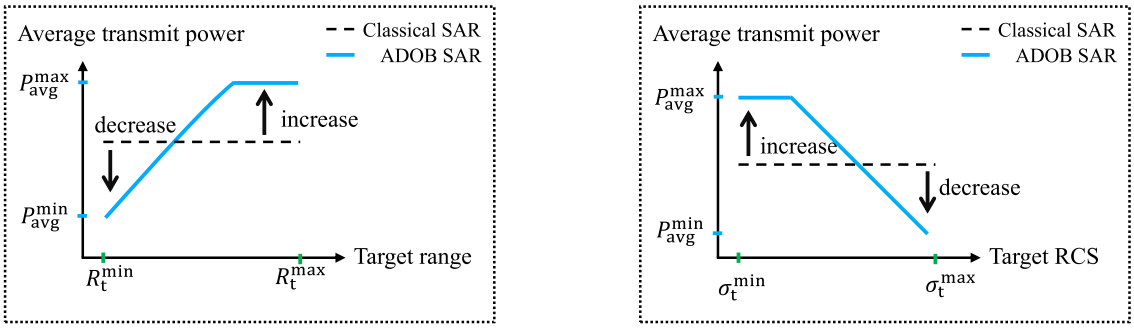

(a) Average transmit power vs target range

(b) Average transmit power vs target RCS

Figure 6.7: Illustration of the Average power control behavior according to the target's range position and RCS.

A small CPI is typically applied in Moving Target Indication (MTI) processing, as described in Section 4.1.1. This involves dividing the registered data along the formed synthetic aperture into small bursts to determine the parameters of the moving target. Therefore, it is important to have sufficient SNR in each CPI since the SNR is directly proportional to SCNR, as defined in (2.56).

The required number of transmit pulses for the desired SCNR is considered a control parameter and can be expressed in terms of the target properties as

$$N_\mathrm{p} = \underbrace{\frac{\mathrm{SCNR}}{\sigma_\mathrm{t}}}_{\text{input}} \left[\underbrace{\frac{\lambda c_0}{4 v_\mathrm{p}}}_{\text{const}} \overbrace{\frac{\sigma_0 R}{\sin\theta_\mathrm{it}}}^{\text{input}} \underbrace{\frac{\mathrm{PRF}}{B}}_{\text{control}} + \underbrace{\frac{(4\pi)^3 K T_\mathrm{s} F L}{\lambda^2}}_{\text{const}} \underbrace{\frac{\overbrace{R_\mathrm{t}^4}^{\text{input}}}{P_\mathrm{t}\tau_\mathrm{p} G_\mathrm{tx} G_\mathrm{rx}}}_{\text{control}} \right], \tag{6.9}$$

by solving (2.57) for the number of pulses. It is plotted in Figure 6.8 highlighting its adaptive control rule applied. For targets in near range, the sensor needs to integrate over a smaller number of pulses to maintain comparable performance to that of targets located at farther distances. Therefore, N_p exhibits an increase with range and shows a decrease with RCS, thereby optimizing the system's performance across varying target conditions.

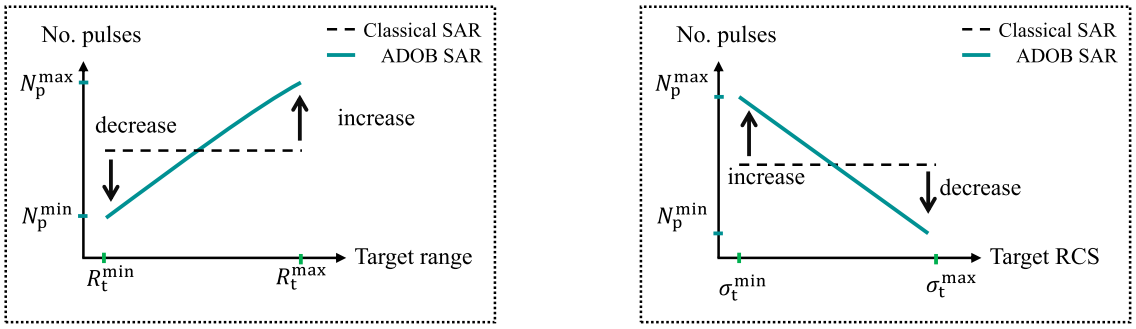

(a) Number of pulses vs target range

(b) Number of pulses vs target RCS

Figure 6.8: Illustration of the number of pulses adaptation behavior according to the target's range position and RCS.

The target image quality is also considered in the energy control decision rule through the Noise-Equivalent Sigma Zero (NESZ) given by [87]

$$\mathrm{NESZ} = \underbrace{\frac{4(4\pi)^3 K T_\mathrm{s} F L v_\mathrm{p}}{\lambda^3 c_0}}_{\text{constants}} \underbrace{\sin\theta_\mathrm{it} R_\mathrm{t}^3}_{\text{input variables}} \underbrace{\frac{B}{P_\mathrm{t} G_\mathrm{tx} G_\mathrm{rx} \tau_\mathrm{p}\,\mathrm{PRF}}}_{\text{control parameters}} \overset{!}{=} \mathrm{NESZ}_\mathrm{D}\,. \tag{6.10}$$

The NESZ depends on several control parameters, some of which have different variations compared to SCNR. The selection of the optimal configuration and parameters is based on multiple interdependent objectives. Therefore, adjusting a single SAR parameter independently is not feasible due to the necessity of considering the collective influence of all other parameters as well as the resolution control decision rule. To address this, an optimization model will be introduced in the subsequent sections, designed to automate the selection process for the optimal combination of control parameters, while effectively managing the inherent trade-offs.

The overall energy control strategy is expressed as

$$\Big(\mathrm{PRF}, \tau_\mathrm{p}, B, N_\mathrm{CPI}, P_\mathrm{t}, G_\mathrm{tx}, G_\mathrm{rx}\Big) = f_\mathrm{energy}\Big(R_\mathrm{t}, \sigma_\mathrm{t}, \sigma_0, \theta_\mathrm{it}\Big), \tag{6.11}$$

where the vector on the left represents the instrument's operational parameters, which are adapted according to the target input parameters designated by the vector on the right, through the function f_energy. This relationship is illustrated in Figure 6.9. A comparison between the energy consumption of state-of-the-art SAR sensors intended for HAP and a system with adaptive energy is shown in Chapter 7.

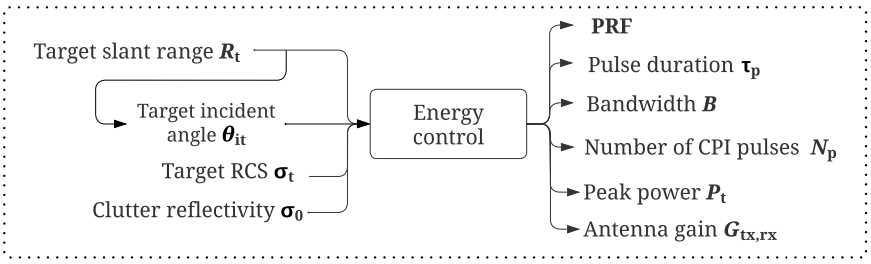

Figure 6.9: Diagram describing the energy control process where the different control parameters are adapted according to the desired energy performance in terms of SCNR and NESZ for each target depending on the information extracted from MapSearch.

6.2 Adaptive Forcing Models

The control parameters obtained from the resolution and energy control decision rules consider only one target independently of others. However, the control processor should consider all the scenario variables, especially the number of Tracking tiers in operation and the number of newly detected targets along with their properties. Therefore, the control processor is enhanced with derived adaptive forcing functions to ensure that the selection of the optimal parameters is based on an analysis of the entire scenario rather than isolated cases. They are designed to modify the control inputs and dynamically force certain conditions on the operation to ensure the system follows the desired behavior within the operating hardware limits. This approach improves the selection of the instrument configuration, making it more efficient and accurate, and enabling it to address a wider range of situations and unexpected events. Adaptive forcing functions are widely used in control theory for changing the behavior of a system by dynamically adapting the input using feedback [226,227]. Adaptive control deals with systems that can adjust their parameters in response to changes in system dynamics or the environment. The derived models in this section are adaptive and are used to enforce specific parameter values and instrument configurations on the decision-maker depending on the scenario, hence their name.

The number of newly detected targets significantly influences the time scheduling of their acquisitions, considering their priorities and properties. For each detection, the processor starts by determining if the detected target is both new and of interest. The flow diagram of the dynamic decision-making processor is depicted in Figure 6.10. If the target has been previously detected, it is already assigned to a Tracking mode, and the new detection is disregarded. When a new target of interest emerges, adaptive forcing models are activated. Firstly, a multi-target single-beam model checks if it is possible to include a newly detected target in an ongoing Tracking tier by imaging it with the same transmit beam. Then, a time

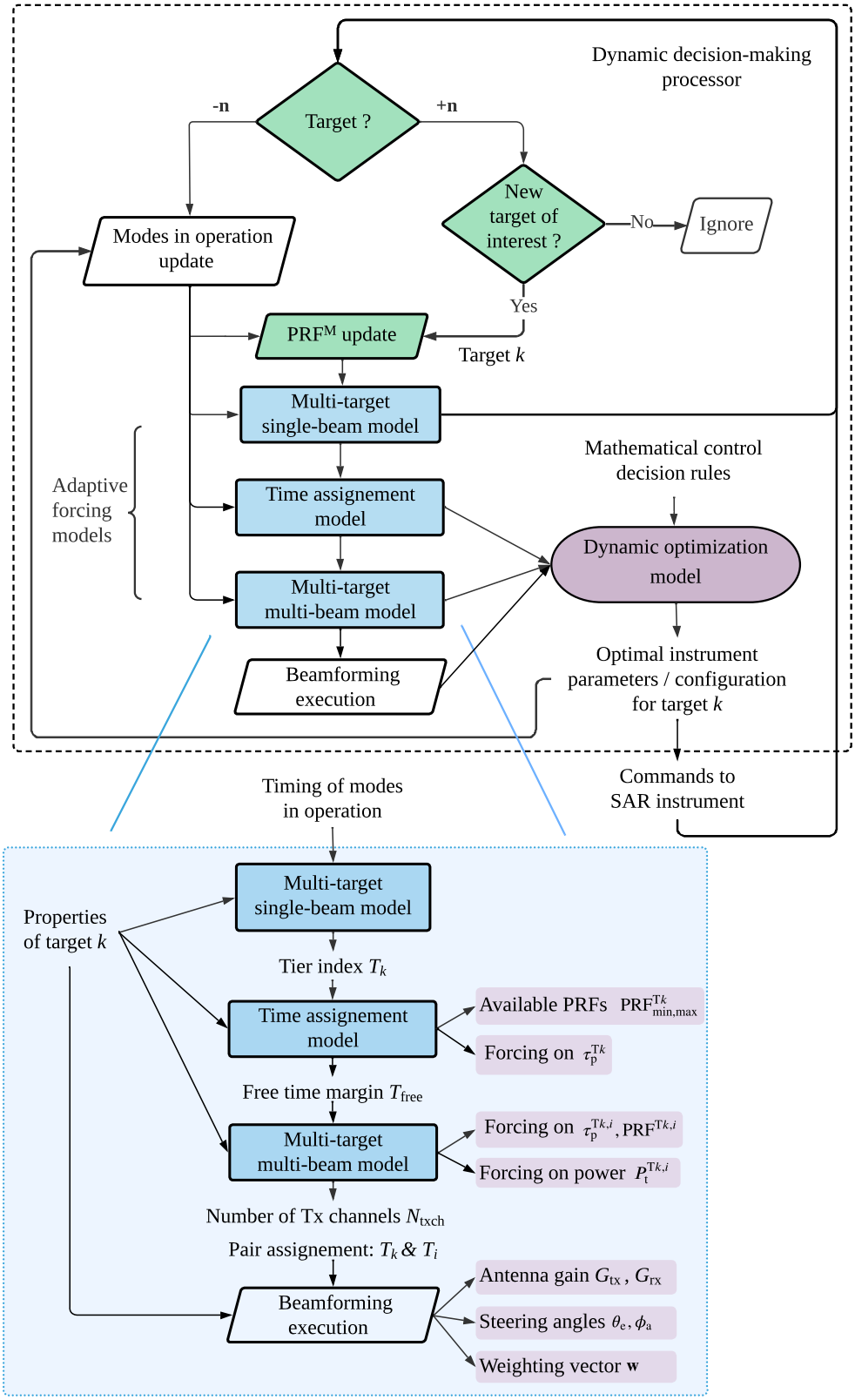

Figure 6.10: Flow diagram of the dynamic decision-maker illustrating the step-by-step process initiated upon target detection.

assignment model is activated to assess the feasibility of integrating new interleaved pulses into the ongoing schedule while considering the parameters of the currently operational Tracking mode tiers. The output from this model guides the selection of the channel configuration for transmission and reception, which includes assessing the necessity of generating simultaneous beams through the multi-target multi-beam model. Then, the beam is formed, and the steering weighting vector is generated during the beamforming execution. All these adaptive models are interconnected and some of their outputs serve as inputs for the subsequent model, as shown in the inset box featuring their different parameters and interconnections in Figure 6.10. The number of Tracking tiers is also updated whenever an acquisition is complete and the MapSearch PRF is updated accordingly.

Once all these adaptive forcing models are completed, a dynamic optimization model starts resolving the various objectives based on the resolution and energy decision rules. This model selects the optimal instrument parameters and configuration for each target and its corresponding new Tracking tier. This section covers the adaptive forcing models required to dynamically optimize the Tracking mode.

6.2.1 Multi-Target Single-Beam Model

The objective of the multi-target single-beam model is to assign a newly detected target k to an old ongoing Tracking tier $i \in [1, n_{\text{op}}]$, when the following conditions are met:

- The angular difference between their respective incident angles lies within the HPBW of the Tracking transmit beam in elevation, Θ_{tr}, such as

$$\mid \theta_k - \theta_i \mid < \Theta_{\text{tr}}. \tag{6.12}$$

- The time difference between their respective detection times is smaller than the time extent of the Tracking azimuth footprint A_{fa}, such as

$$t_{\text{det},k} - t_{\text{det},i} < \frac{A_{\text{fa}}(\Phi_{\text{tr}})}{v_{\text{p}}}. \tag{6.13}$$

- The two targets are moving in the same direction.
- The new target k is larger than the target i, $A_{\text{t},k} \geq A_{\text{t},i}$, to ensure the optimized resolution used to image target i is enough for target k.

If these conditions are satisfied, it means that the targets k and i are close enough to share the same footprint on the ground. In such scenarios, the radar system forces the illumination of both targets using the same transmit beam, denoted by

the index i. The Tracking tier of the new target k becomes $T_k = T_i$. This strategy is visually demonstrated in Figure 6.11, which depicts the assignment of transmit beams and pulses for closely located targets.

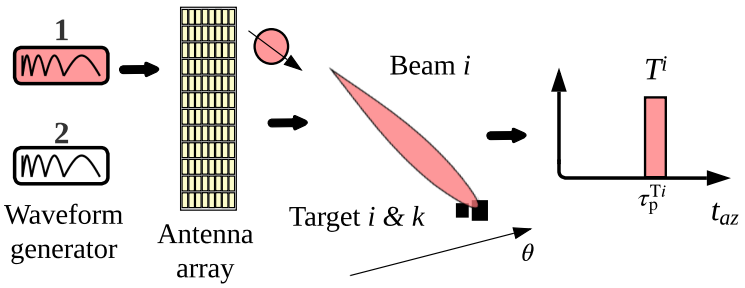

Figure 6.11: The transmit beam and pulse allocation for closely located targets k and i. A single transmit beam effectively caters to both targets within a single Tracking tier, utilizing just one Tx antenna channel.

In azimuth, the precise location of the targets is not a concern. This is because the Tracking transmit beam has the same azimuth beamwidth as the MapSearch, the mode in which the targets were originally detected. Consequently, the azimuth beam footprint can illuminate the detected target if condition (6.13) is met, irrespective of their exact placements. In case any of the conditions are not satisfied, a new Tracking tier T_k is activated with a dedicated transmit beam.

6.2.2 Time Assignment Model

The objective of the timing model is to analyze the timing parameters based on the number of targets present throughout the entire scenario while considering the coordination of the interleaved modes. As depicted in Figure 6.10, the outputs of this model are as follows:

- **Free Time Margin:** Determining the available time gaps within which new interleaving pulses for emerging targets can be scheduled.
- **Available PRFs:** Identifying the range of Tracking PRFs that can be used from a set of predefined discrete values.

Free Time Margin

The first step of the adaptive timing model involves determining the feasibility of incorporating a new Tracking tier for a new target within the existing schedule.

This is assessed using the free time margin, denoted by T_{free}, which is defined as the period or gap during which the sensor is neither transmitting nor receiving. It depends on the start and end times of all transmitted pulses and return echoes of operating modes, including MapSearch and Tracking mode tiers n_{op}.

The time interval T_{int} considered in the calculation of the free time margin depends on the smallest operating PRF throughout the MapSearch mode and the n_{op} Tracking tiers and is given by

$$T_{\text{int}} = \max\left\{ \text{PRI}^{i} \right\}, \tag{6.14}$$

with $i \in [0, n_{\text{op}}]$. The interval T_{int} comprises all distinct MapSearch and Tracking events required, as illustrated in Figure 6.12. The MapSearch is the initial mode and is therefore represented by $i = 0$.

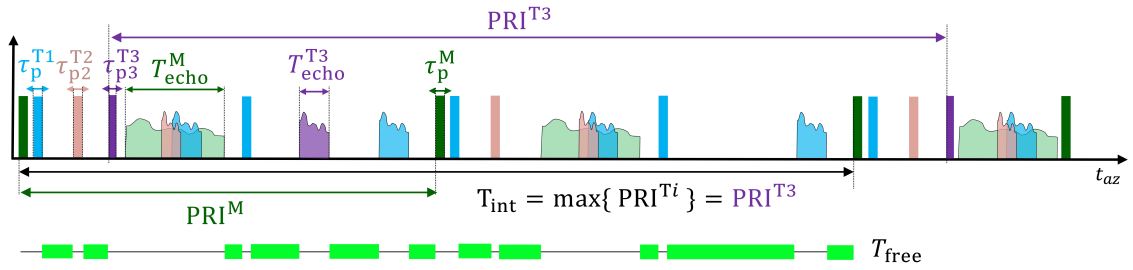

Figure 6.12: Timing schedule snapshot showcasing the free time margins (highlighted in green) for a scenario with $n_{\text{op}} = 3$ Tracking tiers interleaved with the MapSearch mode.

The number of pulses used for the mode/tier i within the considered time interval T_{int} is defined as

$$p^{i} = \frac{T_{\text{int}}}{\text{PRI}^{i}}. \tag{6.15}$$

In the example of Figure 6.12, the Tracking tiers have different numbers of pulses within T_{int} as they are operated with different PRFs. Tracking tier $i = 1$ has $p^1 = 4$ pulses due to the high PRF, while tier $i = 3$ has only one $p^3 = 1$.

A set of start and end time event intervals, denoted by E, is defined in the following as

$$E = \bigcup_{i=0}^{n_{\text{op}}} \bigcup_{l=0}^{p^{i}-1} \left\{ \left(t^{i}_{\text{ts}}(l), t^{i}_{\text{te}}(l)\right), \left(t^{i}_{\text{rs}}(l), t^{i}_{\text{re}}(l)\right) \right\}, \tag{6.16}$$

where t^{i}_{ts} and t^{i}_{te} represent the transmit pulse start and end time of the i-th mode, respectively, defined in (5.4), (5.24). t^{i}_{rs} and t^{i}_{re} represent the echo start and end time of the i-th mode, respectively, defined in (5.5), (5.25). The union notation

indicates that the set E includes all p^i transmit and receive intervals across each mode and tier i, combining them into a single set of time intervals.

To determine the gap between the different pulses and echoes, the set E, defined in (6.16), is sorted by arranging the intervals in an increasing order based on their lower bounds (start time) with

$$E_{\text{sorted}} = \left\{(t_{\text{s}}^j, t_{\text{e}}^j)\right\}_{j=0}^{n_j}, \text{ where } t_{\text{s}}^j \leq t_{\text{s}}^{j+1}, \tag{6.17}$$

for the combined number of time intervals n_j defined as

$$n_j = \sum_{i=0}^{n_{\text{op}}} 2p^i. \tag{6.18}$$

The start and end times of the transmit and receive events are represented by the same parameters t_{s} and t_{e}, respectively.

The free temporal gap T_{free} between the events is then given by

$$T_{\text{free}}^j = t_{\text{s}}^{j+1} - t_{\text{e}}^j \quad \forall\, 0 \leq j \leq n_j. \tag{6.19}$$

Target Assignment Using Free Time Margin

The time assignment procedure is conducted on a target-by-target basis. It starts with the first target, as illustrated in the flow chart of Figure 6.13, and checks if there is enough time to transmit a new Tracking pulse. For a newly detected target k, a pulse can be placed in the free time gap j if

$$T_{\text{free}}^j - 2\tau_{\text{g}} \geq \tau_{\text{p}_{\text{max}}}^{\text{T}}, \tag{6.20}$$

where τ_{g} is the guard time required between events, and $\tau_{\text{p}_{\text{max}}}^{\text{T}}$ the maximum pulse duration of the Tracking transmitted pulse. This approach guarantees that the worst-case scenario is always accounted for when scheduling a new Tracking tier by accounting for the longest pulse duration. The actual pulse duration is subsequently determined through the dynamic optimization model. The free time margins T_{free} are continuously updated using the actual timing of the modes in operation after. Hence, the time assignment model operates on a feedback loop, where the schedule is updated before assigning any new target, as illustrated in the flow chart of Figure 6.13.

The model begins by evaluating condition (6.20) for $j = 0$, which corresponds to the first available time gap. If this gap does not meet the condition to accommodate a new pulse, the next gap is evaluated by incrementing j by 1, i.e., $j = j + 1$. This

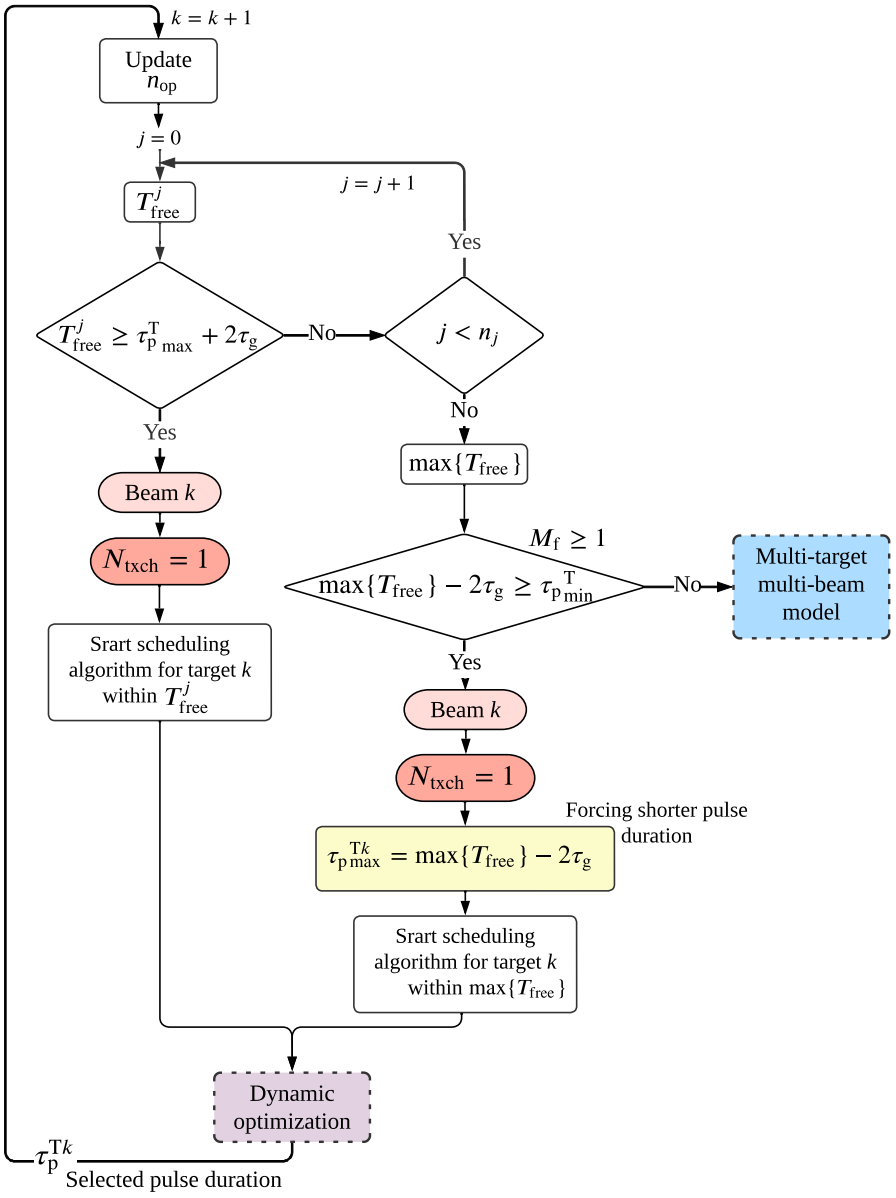

Figure 6.13: Time assignment flow diagram of a newly detected target k.

process is repeated iteratively until a suitable time gap is found that satisfies the condition (6.20), as illustrated by the flow diagram of Figure 6.13.

In the scenario where there is sufficient free time to accommodate a new pulse, i.e., (6.20), the system starts the scheduling algorithm, for the new Tracking tier k within the corresponding free time gap, while also considering the return echo timing and the ambiguity-free interleaving, as described in Chapter 5. The model generates a single transmit beam, which is assigned the same index k as the detected target. This beam is adapted specifically to the individual Tracking of target k. A single transmit channel is therefore activated with $N_{\mathrm{txch}}^{\mathrm{T}k} = 1$, as illustrated in Figure 6.14 and Figure 6.13.

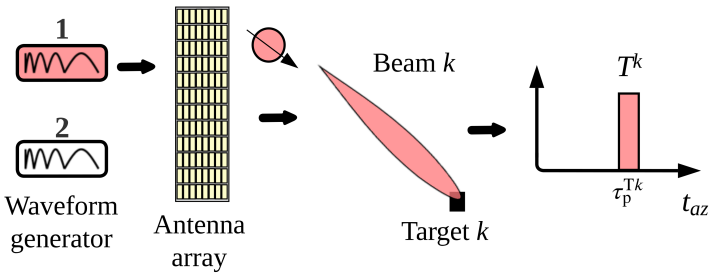

Figure 6.14: The transmit beam and pulse allocation for a target k using a single Tx antenna channel.

Target Assignment with Constrained Pulse Duration

If none of the free time margins can accommodate a pulse of maximum duration, yet the longest time gap is enough to fit a pulse of duration $\tau_{\mathrm{p1}} \geq \tau_{\mathrm{p}_{\mathrm{min}}}^{\mathrm{T}}$, the model employs a forcing criterion that modifies the predefined upper bound of the pulse duration for the new target k, as depicted in the flow chart of Figure 6.13.

The longest free time gap is defined as

$$T_{\mathrm{free}}^{\mathrm{max}} = \max_{j=0}^{n_j} T_{\mathrm{free}}^{j}. \tag{6.21}$$

Hence, when the condition (6.20) is not met for all $j < n_j$, and $T_{\mathrm{free}}^{\mathrm{max}} - 2\tau_{\mathrm{g}} \geq \tau_{\mathrm{p}_{\mathrm{min}}}^{\mathrm{T}}$, the maximum allowable pulse duration for the new Tracking tier k is set to

$$\tau_{\mathrm{p}_{\mathrm{max}}}^{\mathrm{T}k} = T_{\mathrm{free}}^{\mathrm{max}} - 2\tau_{\mathrm{g}}, \quad \text{for} \quad M_{\mathrm{f}} < 1, \tag{6.22}$$

where M_{f} is a free-time metric, defined to simplify the scheduling algorithm, and is given by

$$M_{\mathrm{f}} = \frac{T_{\mathrm{free}}^{\max}}{\tau_{\mathrm{p}_{\min}}^{\mathrm{T}} + 2\tau_{\mathrm{g}}}. \tag{6.23}$$

The adjusted maximum pulse duration is then sent to the dynamic optimization model.

Forced Refining of PRF Interval

The second step of the timing model involves updating the interval of feasible PRFs available for selection during the optimization process. Based on the energy control rule described in Section 6.1.2, the PRF is a critical control parameter, as it allows the duty cycle adjustment. Before the processor selects the optimal PRF for a certain energy level, it is essential to assess its feasibility through timing considerations. Hence, the selection of the optimal Tracking PRF for each target depends on:

- The energy control rule.
- The number of detected targets.
- The current MapSearch PRF.
- The number and timing properties of active Tracking tiers.

The selection of the PRF for an individual target is constrained to predefined discrete values. It cannot be arbitrarily or linearly chosen. This limitation is based on the multi-mode interleaving condition, defined in equation (5.13). According to this condition, the PRFs of different modes must be either integer multiples or divisors of one another.

The first step in updating the PRF interval for a new Tracking tier k involves evaluating the feasibility of using the maximum $\mathrm{PRF}_{\max}^{\mathrm{T}} = \mathrm{PRF}_{\max}^{\mathrm{M}}$, shown in Figure 6.15. This is determined based on the capacity of the MapSearch idle time interval $\mathcal{T}_{\mathrm{idle}}^{\mathrm{M}}$

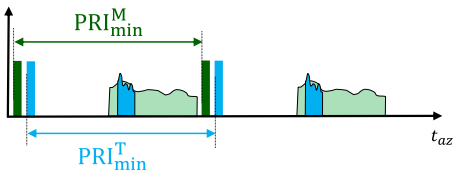

Figure 6.15: The maximum Tracking PRF, which is defined as the maximum MapSearch PRF that satisfies the range ambiguity-free timing within the swath, defined in (5.10).

to accommodate new Tracking pulses. In the following, only the time interval T_{int}, defined in (6.14) is investigated, as depicted in Figure 6.16.

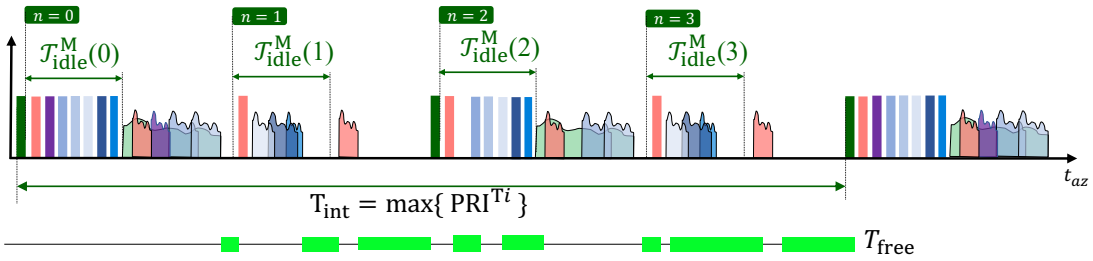

Figure 6.16: Timing schedule snapshot highlighting the condition on using the maximum Tracking PRF for a new target. The free time margins are highlighted in green.

The MapSearch idle time intervals within T_{int} are defined as

$$\mathcal{T}^{\text{M}}_{\text{idle}}(n) = \left[t_0 + \tau^{\text{M}}_{\text{p}} + \tau_{\text{g}} \ + n\,\text{PRI}^{\text{M}},\ t_0 + \tau^{\text{M}}_{\text{delay}} + n\,\text{PRI}^{\text{M}} \right], \tag{6.24}$$

for all $n \in [0, p^0]$ with p^0 defined in (6.15). In the example shown in Figure 6.16, 4 idle time intervals are within T_{int}.

The maximum PRF cannot be used for the new Tracking tier k if any idle time intervals $\mathcal{T}^{\text{M}}_{\text{idle}}(n)$ when setting $\text{PRI}^{\text{M}} = \text{PRI}^{\text{M}}_{\text{min}}$ in (6.24) cannot accommodate an additional pulse. The free time margin T^j_{free}, defined in (6.19), is therefore calculated slowly for the pulses and echoes occurring within those idle time intervals, which are given by

$$\mathcal{T}^j_{\text{t}}, \mathcal{T}^j_{\text{r}} \subset \mathcal{T}^{\text{M}}_{\text{idle}}(n), \quad \forall\, 0 \leq j \leq n_j. \tag{6.25}$$

If condition (6.20) is not fulfilled for any $n \in [0, p^0]$, the upper bound of the Tracking PRF is halved

$$\text{PRF}^{\text{T}}_{\text{max}} = \frac{1}{2}\,\text{PRF}_{\text{max}} \quad \text{if} \ \ T^j_{\text{free}} - 2\tau_{\text{g}} \leq \tau^{\text{T}}_{\text{pmax}}. \tag{6.26}$$

For instance, referring to Figure 6.16, the first idle time interval (with $n = 0$) is fully occupied. Although the free time gap within the subsequent idle time interval retains a vacant time slot, $\text{PRF}^{\text{T}}_{\text{max}}$ cannot be used.

Assuming that the first pulse of a new Tracking tier k is sent at $t^{\text{T}k}_0$, as illustrated in the example of Figure 6.17, all subsequent pulses within T_{int} with the index

$n = [1, p^k = T_{\text{int}}/\,\text{PRI}^k]$ should not intersect with any other pulses or echoes corresponding to the n_{op} operating Tracking tiers. This condition is already maintained by the adaptive scheduling algorithm described in Chapter 5. The maximum PRF can be used for the new Tracking tier k if

$$\mathcal{T}_{\text{t}}^{\text{Tnew}}(n) \not\subset \mathcal{T}_{\text{t}}^{\text{T}i}(t) \not\subset \mathcal{T}_{\text{r}}^{\text{T}i}(t), \tag{6.27}$$

with $t = [0, p^{\text{T}i}]$ the index of transmit pulse and echo of the i-th Tracking tier in operation.

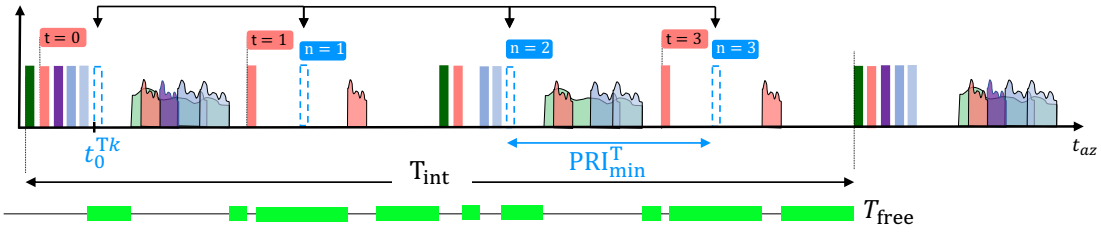

Figure 6.17: Timing schedule snapshot highlighting the condition on using the maximum Tracking PRF for a new target k, given the start time of its first transmitted pulse $t_0^{\text{T}k}$.

The interval of Tracking PRF values predetermined during the design phase is adjusted based on the scenario and synchronized with the timing of other modes before being used as input for the ultimate performance optimization, as illustrated in the flowchart of Figure 6.18. The timing model checks if all the Tracking PRF values can be used for each specific new Tracking tier. First, the maximum Tracking PRF is verified using the conditions (6.26) and (6.27). If it is not feasible, half of the maximum PRF is forwarded, and the interval is updated. When a smaller value of the PRF upper bound is enforced, the corresponding duty cycle decreases. However, this can be compensated automatically by tuning the pulse duration or the number of pulses, depending on the target requirements.

Due to potential nadir echo overlapping at low pulse repetition frequencies, the timing model also updates the minimum allowable tracking $\text{PRF}_{\text{min}}^{\text{T}}$ value. The nadir conditions (5.11) should be fulfilled while considering the maximum pulse duration as a worst-case scenario. If this condition is not met, indicating that the nadir echo coincides with the target echo, the time assignment model enforces a higher PRF value, the double, as illustrated in the flow chart of Figure 6.18. If doubling the PRF is not temporally feasible, $\text{PRF}_{\text{min}}^{\text{T}}$ can still be used, though with the additional requirement of employing different waveforms from pulse to pulse to

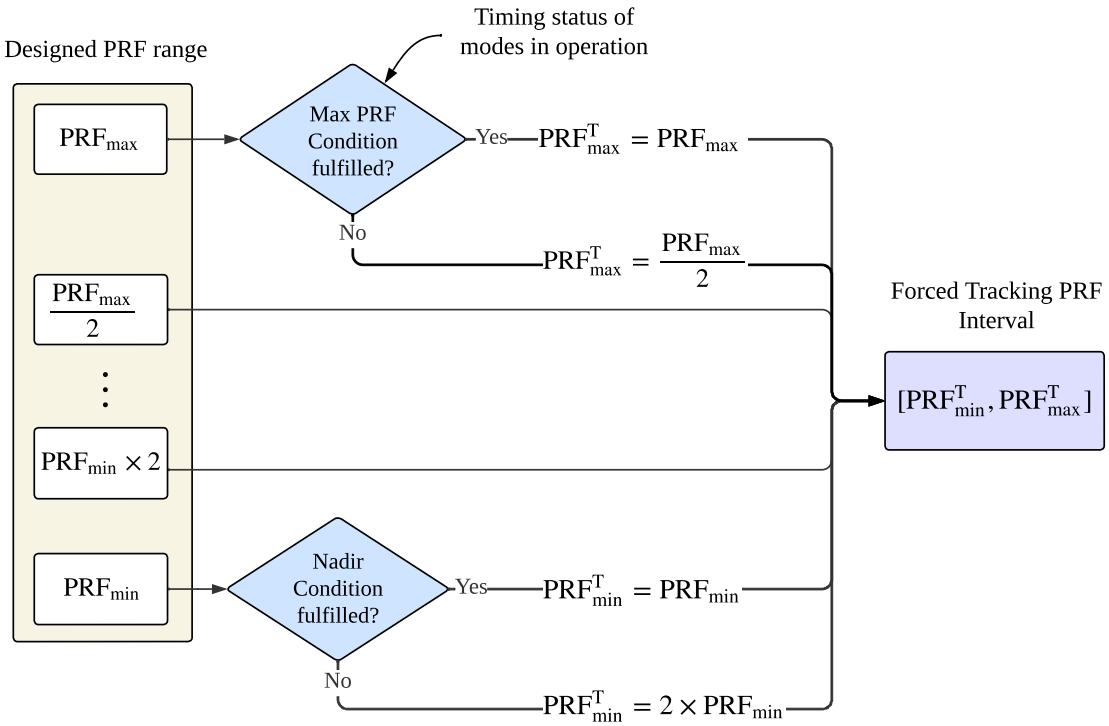

Figure 6.18: Flow chart describing the forcing criteria for the PRF selection conducted for each newly detected target and corresponding Tracking tier. The final interval of all applicable PRFs is updated and then sent to the optimization function.

suppress the nadir echoes during processing [228]. After executing these conditions, the disposable tracking PRF interval is updated and sent to the optimization control model.

6.2.3 Multi-Target Multi-Beam Model

The primary objective of the multi-target multi-model is to reconfigure the transmit and receive channels when the time assignment model, described in Section 6.2.2, cannot schedule the newly detected target. Based on the free time gaps, the model decides whether there is a need and feasibility to activate multiple transmit networks to generate several simultaneous beams. Hence, this model updates the number of transmit channels, N_{txch}, and adjusts the associated peak power P_{t} for each channel. It also forces specific values on some chirp signal parameters.

The multi-target multi-model, illustrated in the flow chart of Figure 6.19, is activated if there is no sufficient time available to transmit a new Tracking pulse for a new target k, namely when condition (6.20) is not met and $M_{\mathrm{f}} < 1$, defined in (6.23).

The process begins by searching for the optimal tracking tier $i \in [1, n_{\mathrm{op}}]$ that is currently in operation, to which the new target tier k will be added. The primary

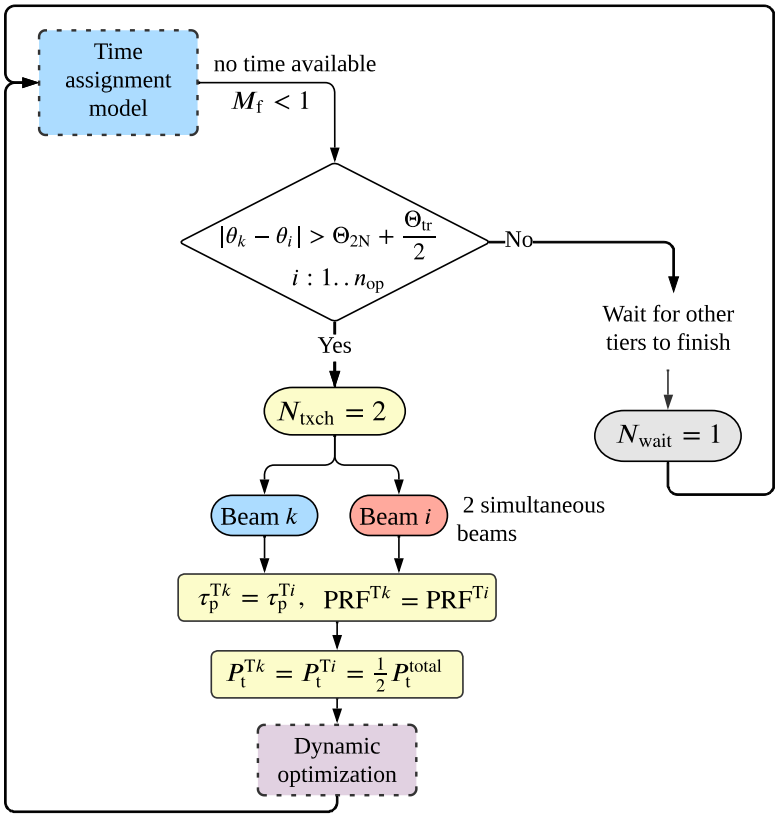

Figure 6.19: Flow chart describing the multi-target multi-beam model model for a newly detected target k.

condition is that the two targets must have sufficient spatial separation to ensure non-overlapping beam footprints. This strategy allows both targets to be simultaneously illuminated by separate beams, as illustrated in Figure 6.20. The Tracking mode, as designed, can produce two simultaneous beams by doubling the phase-shifting stage for each antenna element and using two chirp generators. This design flexibility enables independent modulation of the parameters for each beam. A detailed discussion on the relevant instrument configuration can be found in Chapter 4.

Simultaneous Multi-Beam Angular Separation

Ensuring adequate separation is imperative to avoid sidelobe interference during transmission. As such, the channel model verifies that the targets are not just positioned apart to prevent main lobe overlap, but also guarantees that the first sidelobe of one beam doesn't interfere with the main lobe of the other. The spatial condition for this decision is given by

$$|\theta_k - \theta_i| > \Theta_{2N} + \frac{\Theta_{tr}}{2}, \tag{6.28}$$

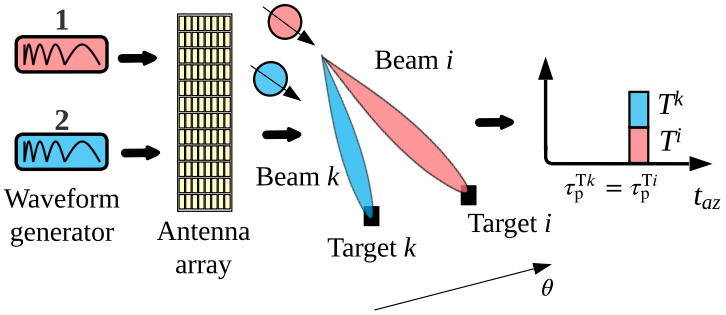

Figure 6.20: The transmit beam and pulse allocation for spatially separated targets k and i. Each target is assigned a transmit beam, resulting in two simultaneous Tracking tiers generated with two transmit antenna channels in different directions with two distinct phase shifting stages.

where θ_k and θ_i denote the spatial centers of the beams tracking targets k and i, respectively, while Θ_{2N} stands for the second null angle of the elevation pattern looking at boresight. The multi-target multi-beam model continuously checks the criterion in (6.28) across all operating tiers $i \in [1, n_{op}]$, selecting the target pair with the most significant angular separation. Only Tracking tiers i operating with a single beam, $N_{txch}^{Ti} = 1$, are considered, as the designed hardware can generate only two simultaneous Tracking beams on transmit. The number of transmit channels becomes

$$N_{txch}^{Tk} = 2, \quad \text{if (6.28) and } N_{txch}^{Ti} = 1, \tag{6.29}$$

in this case, as illustrated in the flow chart of Figure 6.19.

When a large target k is tracked with the first beam and located at the sidelobe of the second beam imaging target i, amplitude tapering, which is detailed in Section 2.2.7, is used on receive to attenuate the level of sidelobes and suppress the unwanted target k from the acquisition of target i.

Figure 6.21 illustrates the antenna patterns in elevation for two possible target separations. In the scenario depicted in Figure 6.21(a), only the HPBW is considered in the beam separation. Hence, the first sidelobe of one pattern falls within the main lobe of the other one. Such a scenario can lead to potential interference, complicating the desired individual Tracking of each target. On the other hand, Figure 6.21(b) showcases the patterns when adhering to the necessary angular separation given in (6.28). The sidelobes are positioned outside the main lobes, hence avoiding interference.

The echo delays of target pairs illuminated simultaneously differ because they are at different range locations. This simplifies the separation of the beams during the reception using temporal orthogonality, detailed in Chapter 5 Section 5.4.

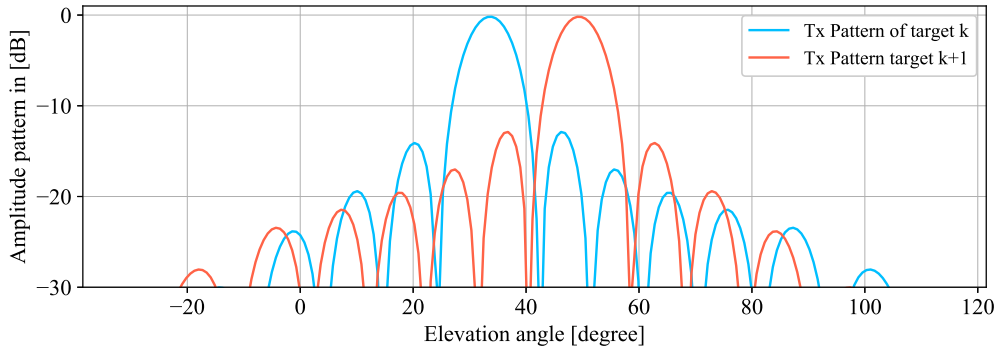

(a) Without the necessary target separation.

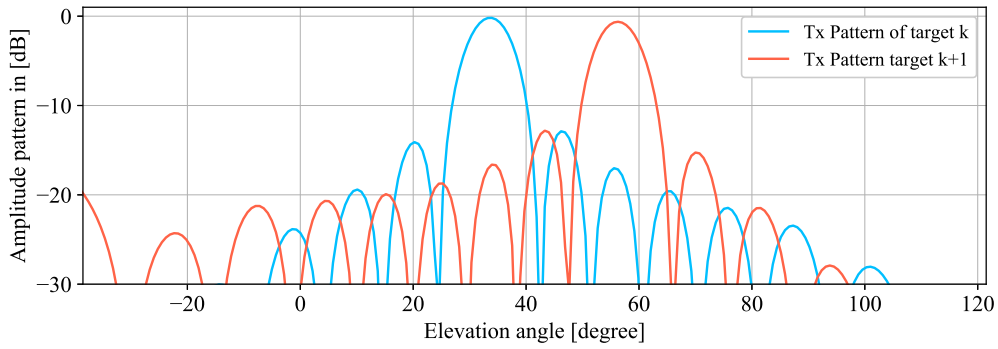

(b) With the necessary target separation.

Figure 6.21: Normalized elevation antenna patterns of two Tracking tiers observing two targets k and $k+1$ highlighting their beam angular separation.

Forced Adjustment of Operational Parameters

When two beams are activated simultaneously in different directions, the peak power gets divided over the two transmission paths based on the corresponding target energy need. The old Tracking tier i was optimized using the maximum available peak power before adding the new tier tracking k. Therefore, the decision-maker accounts for the power reduction and reruns the dynamic mode optimization for the old Tracking tier i, as depicted in the flow chart of Figure 6.19. The reduced power for both tiers can be compensated by other control parameters, like increasing the number of pulses or the integration time. Ideally, simultaneous tracking of two targets with reduced power is most effective if both have high RCS values, according to the energy control rule described in Section 6.1.2.

Hence, the peak power is equally divided between the two beams, where each beam receives half of the total peak power for hardware simplicity.[1] The power variation

[1] Dynamically adjusting the peak power for each beam based on the varying target conditions would add more complexity in terms of power amplification, calibration, and thermal management.

is therefore activated and the following peak powers of the Tracking tier k and i are enforced:

$$P_{\mathrm{t}}^{\mathrm{T}k} = P_{\mathrm{t}}^{\mathrm{T}i} = \frac{1}{2} P_{\mathrm{t}}^{\mathrm{total}} \text{ for } N_{\mathrm{txch}}^{\mathrm{T}k} = 2, \tag{6.30}$$

which are forwarded to the optimization model, as illustrated in the flow chart of Figure 6.19.

Simultaneous beams should share similar chirp signal properties since the different transmit channels are merged at the end through a single high-power amplifier according to the designed front-end architecture. This includes having the same pulse duration and PRF for the two simultaneous tiers. As a result, a forcing criterion is applied to the Tracking tier pair k and i, to ensure they have the same pulse duration $\tau_{\mathrm{p}}^{\mathrm{T}k} = \tau_{\mathrm{p}}^{\mathrm{T}k}$ and bandwidth $\mathrm{PRF}^{\mathrm{T}k} = \mathrm{PRF}^{\mathrm{T}k}$.

Forced Waiting

When the multi-target multi-beam model cannot find a Tracking tier i to which the new target k can be added with an additional beam, target k is placed on a waiting list until an active Tracking tier acquisition is finalized. This condition is given by

$$N_{\mathrm{wait}}^{k} = 1 \text{ if } |\theta_k - \theta_i| < \Theta_{\mathrm{2N}} + \frac{\Theta_{\mathrm{tr}}}{2}, \tag{6.31}$$

$\forall\ i \in [1.n_{\mathrm{op}}]$ and $N_{\mathrm{txch}}^{\mathrm{T}i} = 1$. The beam steering mechanism can be dynamically adjusted in azimuth to concentrate on a designated target after a predefined time interval using the beamforming model. For optimal tracking accuracy, it is, however, essential that the target continuously remains within the operational field of view of the steerable antenna system. If this is not feasible, especially when the target is moving faster than the platform in the opposite direction, the decision-maker will abort an active Tracking tier based on target priority and dwell time status.

6.2.4 Target Assignment Examples

In Figure 6.22, several scenarios demonstrate the system's adaptability to different target situations and time availability. Scenario (a) highlights the simplest case, where the first target $k = 1$ is detected. In this case, sufficient time is available to interleave a Tracking tier, as $M_{\mathrm{f}} \geq 1$. This leads to the activation of a single Tx channel with $N_{\mathrm{txch}}^{\mathrm{T1}} = 1$, as described in Section 6.2.2.

Scenario (b) presents a more complex situation, where the multi-target single-beam model, described in Section 6.2.1 is activated. A second target with $k = 2$ is detected while only one Tracking tier of target $k = 1$ is in operation. As target 2 is very close to target 1 and all required conditions apply, i.e. (6.12) and (6.13), target 2 is

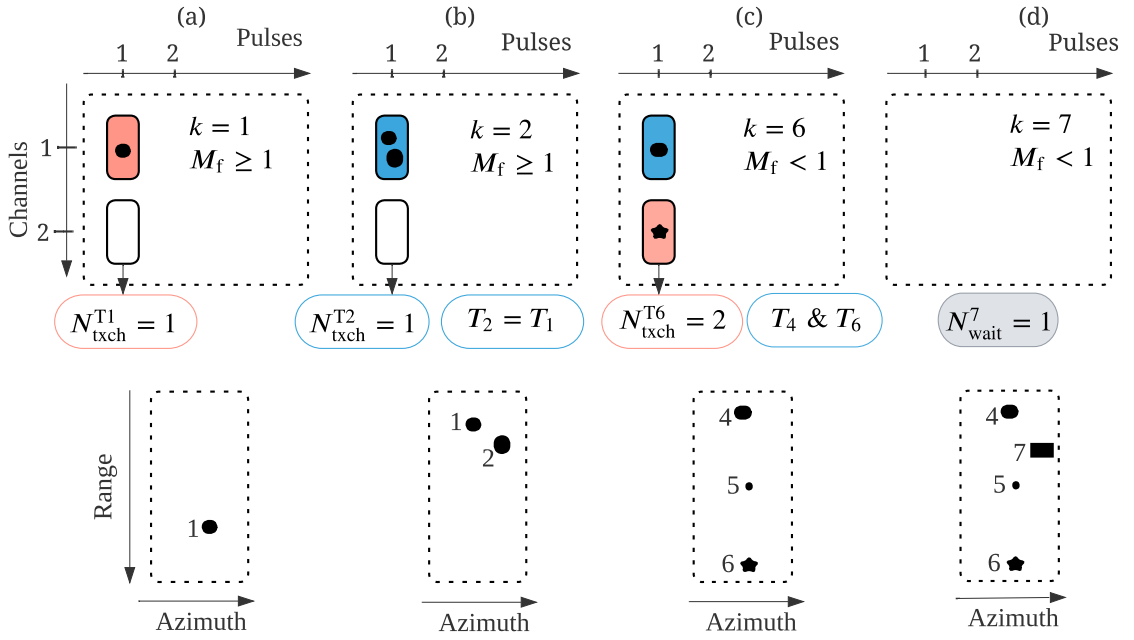

Figure 6.22: Examples of transmit channel configurations for different target scenarios and free time margins based on the three beam assignment conditions.

added to Tracking tier $k = 1$ within the same antenna beam. The Tracking tier 2 is therefore operated with tier 1, i.e. $T_2 = T_1$.

In scenario (c), 5 Tracking tiers are already active, and the new target is assigned the index $k = 6$. Based on the interleaving schedule and the free time intervals, there is not sufficient time available to add a pulse for the newly detected target, and hence $M_f < 1$. The multi-target multi-beam model, described in Section 6.2.3, is activated in this case. It searches for the active Tracking tier, which is observing a target that satisfies the simultaneous multi-beam angular separation described in (6.28) with the new target 6. The new Tracking tier 6 is hence added to tier 4 with a second beam, as target 4 is located at a different range location. This leads to the activation of two simultaneous beams with $N^{T6}_{txch} = N^{T4}_{txch} = 2$, and the new pair is identified T_4 and T_6.

Finally, scenario (d) demonstrates the system's ability to handle resource constraints by assigning the newly detected target $k = 7$ to the waiting list because of limited availability of free time with $M_f < 1$ and the inability to activate a second beam concurrently with an active Tracking tier, as all options fail to meet the multi-beam angular separation requirement, and tiers T_4 and T_6 are already operating with two simultaneous beams according to scenario (c).

6.3 Beamforming Execution

The beamforming model adapts the beams assigned for each Tracking tier based on target properties and the outputs of the adaptive forcing models, described in the previous section. Thus, the beam is steered toward the target and shaped to enhance the gain in that direction by reducing the sidelobe level or applying pattern nulling to suppress unwanted sources or objects. The antenna gain varies depending on beamforming, which affects the energy control performed during the final selection step of the operational parameters. Therefore, the resulting antenna gain is included as an input to the optimization model, as shown in Figure 6.10.

The beamforming model aims to update the complex antenna weights, which determine the steering direction in azimuth and elevation. They also define the pattern shape (such as sidelobes and beamwidth), and the resulting antenna gain. The antenna gain varies with the steering angle. Steering the beam away from the boresight direction induces a scan loss [105], which should be considered in the final selection of the instrument parameters. The antenna gain is therefore adjusted to the scenario according to the Tracking transmit and receive gain expressions (4.77) and (4.54) derived in Section 4.6.4. It is then forwarded to the dynamic optimizer. Activating both transmit channels with double networks does not influence the antenna gain, as the full aperture is used for each beam.

The Tracking tier k steering angle in elevation, denoted by $\theta_{\mathrm{e}}^{\mathrm{T}k}$, is defined as a function of the target incident angle θ_{it} (known from MapSearch), and is given by

$$\theta_{\mathrm{e}}^{\mathrm{T}k} = \theta_{\mathrm{it}}^{k} - \theta_{\mathrm{tilt}}, \tag{6.32}$$

considering the mechanical antenna tilt angle, and assuming flat Earth geometry. The elevation steering angle is fixed during Tracking, as the footprint size on the ground accounts for any target movement.

The azimuth beam is also steered toward the target considering the platform travel time d_{s} between the MapSearch detection and the activation of the Tracking tier, as described in Chapter 4 and Figure 6.23. The azimuth steering angle is required to keep the antenna beam focused on the moving target. Therefore, the steering angle varies over time and is always pointing toward the target's ground position given by

$$x_k(t) = x_{k_0} + \kappa v_{\mathrm{t}k} t, \tag{6.33}$$

with x_{k_0} the initial target azimuth position when the Tracking starts and κ a factor taking $\kappa = 1$ when the target is moving with the velocity v_{tg} in the same direction as the platform and $\kappa = -1$ for the opposite direction. Following the geometry of

Figure 6.23, the azimuth steering angle, denoted by $\phi_{\mathrm{a}}^{\mathrm{T}k}$, of the Tracking tier k is given by

$$\phi_{\mathrm{a}}^{\mathrm{T}k}(t) = \arctan\left(\frac{x_k(t) - v_{\mathrm{p}}t}{H}\right). \tag{6.34}$$

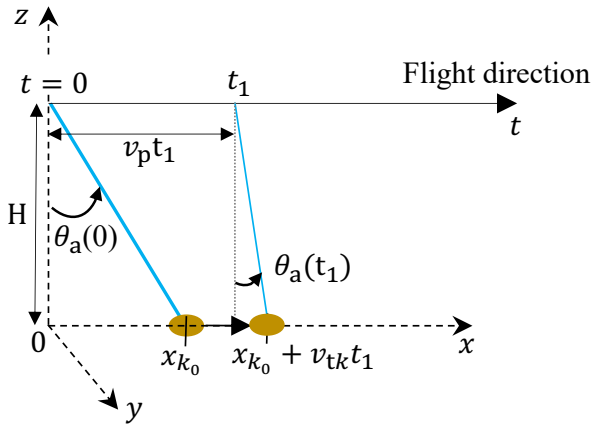

Figure 6.23: Schematic representation of the azimuth steering angle $\phi_{\mathrm{a}}^{\mathrm{T}k}(t)$ of a new Tracking tier k, starting at $t = 0$. The target is located at x_{k_0} and moves with the velocity $v_{\mathrm{t}k}$.

Substituting (6.33) in (6.34) gives

$$\phi_{\mathrm{a}}^{\mathrm{T}k}(t) = \arctan\left(\frac{x_{k_0} + \kappa v_{\mathrm{t}k}t - v_{\mathrm{p}}t}{H}\right). \tag{6.35}$$

The complex-valued weighting matrix applied to the planar phased array antenna depends on the 2-D steering angles (6.32) and (6.35). It is given by

$$\mathbf{w}(n_{\mathrm{a}}, n_{\mathrm{e}})^{\mathrm{T}k}(t) = \begin{bmatrix} e^{j\Delta\phi(1,1)}(t) & e^{j\Delta\phi(1,2)}(t) & \cdots & e^{j\Delta\phi(1,N_{\mathrm{a}})}(t) \\ e^{j\Delta\phi(2,1)}(t) & e^{j\Delta\phi(2,2)}(t) & \cdots & e^{j\Delta\phi(2,N_{\mathrm{a}})}(t) \\ \vdots & \vdots & \ddots & \vdots \\ e^{j\Delta\phi(N_{\mathrm{e}},1)}(t) & e^{j\Delta\phi(N_{\mathrm{e}},2)}(t) & \cdots & e^{j\Delta\phi(N_{\mathrm{e}},N_{\mathrm{a}})}(t) \end{bmatrix}, \tag{6.36}$$

where $\Delta\phi(n_{\mathrm{a}}, n_{\mathrm{e}})(t)$ is the phase shift applied to each antenna element at row n_{a} and column n_{e}

$$\Delta\phi(n_{\mathrm{a}}, n_{\mathrm{e}})(t) = -\left(kd_{\mathrm{a}}n_{\mathrm{a}}\sin\left(\phi_{\mathrm{a}}^{\mathrm{T}k}(t)\right) + kd_{\mathrm{e}}n_{\mathrm{e}}\sin\left(\theta_{\mathrm{e}}^{\mathrm{T}k}\right)\right), \tag{6.37}$$

where d_{a} and d_{e} are the element separation in azimuth and elevation, respectively.

Additional antenna weight adjustments are used on receive to reduce the sidelobe level and to perform pattern nulling in the direction of potential interference, as detailed in Chapter 2 Section 2.2.7. The transmit antenna weights don't include amplitude tapering to avoid any potential decrease in gain.

6.4 Dynamic ADOB-SAR Optimization Model

Once the adaptive forcing models have been executed, the next step is to finalize the selection of the operational parameters for each Tracking tier acquisition. This is accomplished through the optimization model based on the decision-making rules described in Section 6.1. The primary objective of this model is to determine the optimal combination of the control parameters that will ensure the desired performance.

6.4.1 Input and Output Vectors

Each detected target with the index k is assigned a vector of input parameters obtained from the MapSearch mode and denoted by

$$Y_k = \left[A_\mathrm{t}, R_\mathrm{t}, \sigma_\mathrm{t}, \theta_\mathrm{it}, \theta_\mathrm{at}\right], \tag{6.38}$$

with A_t the target size, R_t its slant range, σ_t its RCS, θ_it its incident angle, and θ_at its azimuth angle. The index k considers the total number of active Tracking tiers n_op with $k = n_\mathrm{op} + 1$, The total number of detected targets in a single CPI, denoted by N_t, is a crucial parameter for pre-assessing tracking capability and timing.

Using an optimization model function $\mathcal{F}$, as depicted in Figure 6.24, the optimal control vector of the target k is obtained and expressed by

$$X_k = \mathcal{F}\left(Y_k, N_\mathrm{t}\right) = \left[P_\mathrm{t}, B, T_\mathrm{D}, N_\mathrm{CPI}, \mathrm{PRF}, \tau_\mathrm{p}\right]. \tag{6.39}$$

These parameters of the control vector X_k include the peak power P_t, system bandwidth B, SAR dwell time T_D, number of pulses for one coherent integration time N_CPI, pulse repetition frequency PRF, and pulse duration τ_p. The selection is guided by the control decision rules from Section 6.1 and the adaptive forcing models from Section 6.2. The model dynamically optimizes X_k, which is considered the decision vector, based on the target input vector, Y_k. A unique feature of this model is its feedback mechanism, which takes into account previously chosen parameters from different operational tiers, represented by X_i with $i \in [1, n_\mathrm{op}]$. The control vector is denoted in the following by $X_k = \left[x_{k_1}, ..., x_{k_M}\right]$ in the optimization model with $M = 6$ the total number of the control parameters.

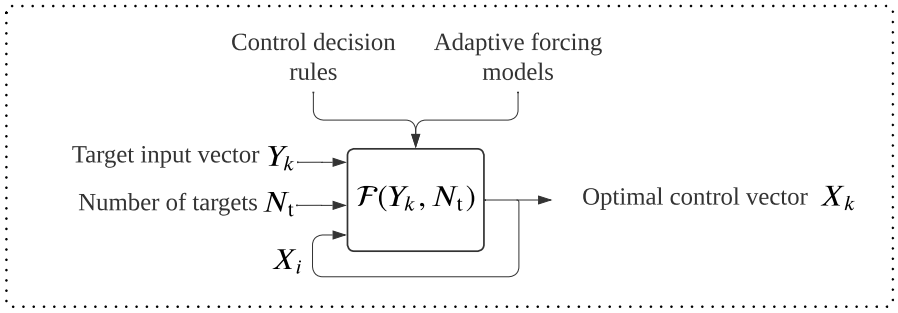

Figure 6.24: Schematic of the optimization model process for the target k. A feedback loop is established to gather input on the operational parameters X_i previously selected for different operational tiers.

6.4.2 Adaptive Multi-Objective Function

To select the optimal combination between the SAR parameters, many trade-offs with different objectives should be made. Therefore, the problem is considered a multiple-criteria decision-making process. The model uses, for each scenario, the results of the adaptive forcing models, which set new limits and capabilities for the selection.

Considering a model with m objective functions denoted by $f_m(x)$, such as f_{res} in (6.5) and f_{energy} in (6.11), its optimization can yield multiple solutions. To avoid this issue and to achieve a single valid solution, the multi-objectives are converted into a single-objective optimization problem, denoted as $\mathcal{F}(x)$. One of the commonly used methods is the weighted sum method given by [229]

$$\mathcal{F}(x) = \sum_{m=1}^{M} w_m \, f_m(x). \tag{6.40}$$

This method uses a scalarization technique that involves multiplying each objective by a weight w_m and summing them up. The weights are proportional to the relative importance of their objectives and are based on the user preferences. The weights are normalized with $w_m \in [0, 1]$ such that

$$\sum_{m=1}^{M} w_m = 1. \tag{6.41}$$

In scenarios where objectives might conflict or a comprehensive perspective is necessary for optimization, like in ADOB-SAR decision-making, a more nuanced approach is required. Hence, the weighted metric method is utilized as the objective function to achieve the desired performance. It is an extension of the sum method, defined

in (6.40), and combines the multi-objectives based on the weighted distance metric from the ideal solution [230, 231]. It is given by

$$\mathcal{F}(x) = \left(\sum_{m=1}^{M} w_m \mid f_m(x) - f_m^{\star} \mid^p \right)^{1/p}, \tag{6.42}$$

where $p \in [1, \infty]$ and $f_m^{\star}$ is the ideal objective point of each $f_m(x)$ and usually unattainable. Therefore, it is considered a reference point. When $p = 1$ the weighted metric function (6.42) becomes equivalent to the weighted sum (6.40).

Using this method, the optimization problem becomes a combination of cost functions that minimize the deviation from ideal points. This is essentially what is required to select the optimal parameters. Instead of having all the decision control criteria as f_m, the cost of the deviation of each control parameter of the vector $X_k = \left[x_{k_1}, ..., x_{k_M}\right]$ from the ideal vector denoted by $Z^{\star} = \left[z_1^{\star}, ..., z_M^{\star}\right]$ is considered as the objective functions that will be minimized [232]. This ensures a balanced consideration of all objectives and provides the flexibility to adapt to different radar scenarios. This approach shifts the decision control rules to the constraints, which are derived from the desired performance metrics, including the spatial resolution and energy control rules. Thus, the model takes the target vector as input and finds the combination of control parameters that satisfies the adaptive resolution depending on the target size and location and the energy constraint defined by the user.

The optimization function is then formulated as[2]:

$$\begin{aligned}
X_k = \arg\min_{x_k} \quad & \left\{ \sum_{m=1}^{M} w_m \frac{\mid x_{k_m} - z_m^{\star} \mid}{z_m^{\star}} \right\} \\
\text{subject to} \quad & \frac{A_{\mathrm{t}}}{N_{\mathrm{px1}}} \leq \delta_{\mathrm{r}}(Y_k, X_k)\, \delta_{\mathrm{a}}(Y_k, X_k) \leq \frac{A_{\mathrm{t}}}{N_{\mathrm{px2}}}, \\
& \frac{\delta_{\mathrm{r}}(Y_k, X_k)}{\delta_{\mathrm{a}}(Y_k, X_k)} = r_{\mathrm{D}}, \\
& g(Y_k, X_k) \geq \mathrm{SCNR}_{\mathrm{D}}, \\
& h(Y_k, X_k) \leq \mathrm{NESZ}_{\mathrm{D}}, \\
& d_{\mathrm{c}_k} + \sum_{i=1}^{n_{\mathrm{op}}} d_{c_i} \leq d_{c_{\max}}, \\
& X_k^L \leq X_k \leq X_k^U.
\end{aligned} \tag{6.43}$$

[2] The objective function is represented in a generalized form. A more detailed explicit formulation is given in Appendix A.

In the following the parameters appearing in (6.43) are detailed. The first constraint relates the range and azimuth resolution, $\delta_{\mathrm{r}}(Y_k, X_k)$ and $\delta_{\mathrm{a}}(Y_k, X_k)$, to the target size A_{t} according to the desired number of pixels on target N_{px1} and N_{px2}. A specific ratio r_{D} between the resolutions is set. The SCNR equation $g(Y_k, X_k)$, defined in (6.6), which relates the changing target vector Y_k to the control vector X_k, is used as a constraint based on the energy decision rule. The same energy level is set for all target scenarios and equals a desired value $\mathrm{SCNR}_{\mathrm{D}}$, typically defined in advance by the application requirements or the user. Additionally, the NESZ equation $h(Y_k, X_k)$, defined in (6.10), is adapted to the desired imaging quality $\mathrm{NESZ}_{\mathrm{D}}$.

The duty cycle of the entire operation is defined as the sum of the duty cycles of all operational concurrent modes and tiers, is also considered a constraint and should not exceed a specified threshold $d_{c_{\max}}$, set during the design. The last constraint in (6.43) provides the upper and lower bounds for each control parameter, denoted by $x_{k_m}^U$ and $x_{k_m}^L$, respectively. They are predefined from the instrument design limits. This structured approach is crucial to ensure that the optimized SAR parameters result in a system that meets the desired performance. The objective function is solved for each Tracking tier with distinct target properties, which are adaptively included in the constraints through the input vector X_k.

The weighting vector $W = \left[w_1, ..., w_M\right]$ is selected according to the priority of each control parameter and its deviation from its ideal value $z_m^\star$. These objective priority weights are typically fixed and predefined by the user before starting the acquisition. However, the target scenarios and user requirements can vary over time. Therefore, the priority of the different objectives and the ideal vector are adapted accordingly, as described in the following subsection.

6.4.3 Dynamic Optimization Framework

The optimization within a single Tracking tier cannot be considered independent because of the other interleaved modes and tiers. Hence, it is vital to have a dynamic framework where model parameters are adapted in real time, reflecting the ongoing operation across all modes and tiers. The optimization model is transformed into a dynamic problem, where the objective function (6.43) changes its framework over time to respond to evolving conditions and optimize the performance holistically for all dynamic scenarios. This process allows for re-evaluation and adjustment of the optimization problem based on the changing scenarios, as illustrated in Figure 6.25. The detected target properties and the status of the operation are used to execute the adaptive forcing models. The outputs of these models are then used within the optimization problem to update the constraints of the control parameters, the ideal vector, and the priority weights. The optimization is then executed for each Tracking tier by minimizing (6.43). This is done based on the MapSearch output

vector Y_k, as well as the timings of all other Tracking tiers in operation $i \in [1, n_{\text{op}}]$, their previously selected parameters X_i, and the desired performance constraints, which can be adjusted anytime.

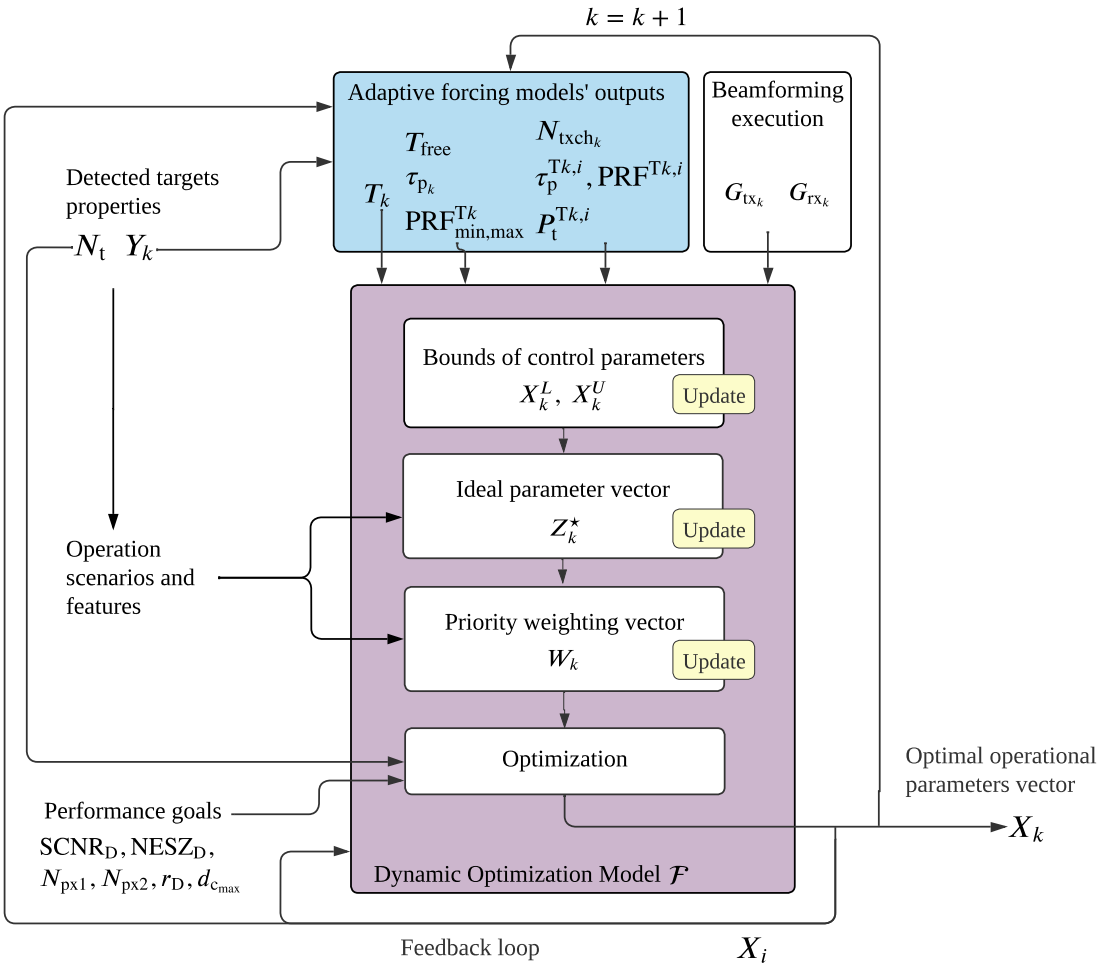

Figure 6.25: Flow chart describing the dynamic optimization model, where the bounds of the control parameters X_k, the ideal vector $Z_k^\star$, and the priority weighting vector W_k are updated for each target scenario according to their properties and the output of the adaptive forcing models.

The outputs of the adaptive forcing models, described in Section 6.2, are incorporated into the objective function. It is done through the bounds of the control parameters in the last constraint. They are updated for each new target scenario and Tracking tier. This includes updating the maximum pulse duration to

$$x_{k_6}^U = \tau_{\text{p}_k}^U = T_{\text{free}}^{\max} - 2\tau_{\text{g}}, \quad \text{for} \quad M_{\text{f}} < 1, \tag{6.44}$$

as described in the time assignment model in Section 6.2.2 and derived in (6.22), when the maximum free time margin $T_{\text{free}}^{\max}$ is not enough to schedule a new pulse for the target k with the maximum duration. The other parameter to update is the PRF, which plays a major role in the overall scheduling. Its upper and lower bounds used in the optimization are updated to

$$\begin{aligned} x_{k_5}^U &= \text{PRF}_k^U = \max\{\text{PRF}^{\text{T}k}\}, \\ x_{k_5}^L &= \text{PRF}_k^L = \min\{\text{PRF}^{\text{T}k}\}, \end{aligned} \tag{6.45}$$

where $\text{PRF}^{\text{T}k}$ is the range of all available pulse repetition frequencies obtained from the time assignment model, described in Section 6.2.2 and Figure 6.18. The antenna gain is used in the constraints through the SCNR and NESZ and is updated for each Tracking tier according to the beamforming execution described in Section 6.3.

The weighting vector W_k and the ideal parameter vector $Z_k^\star$ play a crucial role in converging the objective of the optimization. The idea consists of adapting their values according to the scenario objectives. Hence, the priority weighting vector becomes dependent on the Tracking tier index k and is denoted as $W_k = \left[w_{1_k}, ..., w_{6_k}\right]$. The same applies to the ideal vector $Z_k^\star = \left[z_{1_k}^\star, ..., z_{6_k}^\star\right]$. The objective function in (6.43) is therefore adjusted to

$$X_k = \arg\min_{x_k} \quad \left\{ \sum_{m=1}^{M} w_{m_k} \frac{\mid x_{k_m} - z_{m_k}^\star \mid}{z_{m_k}^\star} \right\}, \tag{6.46}$$

to ensure that the optimization is context-aware, focusing more on control parameters that are more critical for a given scenario. The same constraints are used. The dynamic weighting vector and ideal parameters of predefined scenarios are determined using a rule-based model. As radar scenarios evolve, this model can be updated using a feedback loop after using the selected weights and ideal vector in the final optimization function.

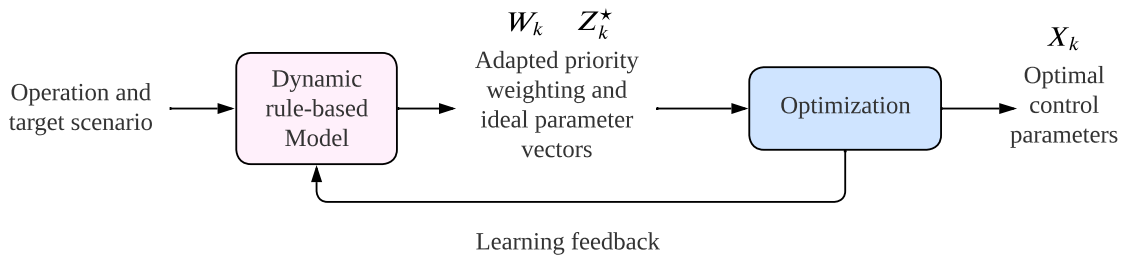

Figure 6.26: Dynamic model based on the operation and target scenario to adapt the weighting vector W_k and ideal parameters $Z_k^\star$, which are used in the framework of the optimization function. A feedback loop adjusts the model based on the selected optimal control parameters.

6.4.4 Examples of Adaptive Priority Weighting and Ideal Parameter Vectors

Five scenarios and suggestions of their respective objective priority weights and ideal vectors are derived in this section. For each scenario, the key parameters are identified, which are the most important factors the optimization function aims to minimize in terms of their deviations from the desired ideal values.

Scenario A: Multi-Mode Resource Management

In the resource management scenario, the goal of the ADOB-SAR operation is to use minimal resources. Time is critical in this scenario, as different Tracking tiers are interleaved. The priority parameters[3] include:

- $\boldsymbol{N_{\mathrm{CPI}}}$: A high number of pulses in a CPI provides better Doppler resolution, essential for accurately distinguishing between targets with different velocities. However, multi-mode interleaving requires efficient time management. Therefore the number of pulses should be kept minimum in this scenario.
- **PRF**: A higher PRF can increase the update rate and enhance the tracking of fast-moving targets, but it affects the duty cycle and time, which should be minimized.
- $\boldsymbol{\tau_{\mathrm{p}}}$: The pulse duration is directly proportional to the product of the duty cycle and PRI and determines the time available for other modes. Therefore, it should be minimized.

The corresponding weighting vector and ideal parameter vector are given in Table 6.1. The identified priority parameters get the highest priority weights, while their ideal parameter values take the lower bounds of the control parameters.

Scenario	Multi-Mode Resource Management
Priority weighting vector	$W_k = \{0.1, 0.1, 0.1, 0.2, 0.3, 0.2\}$
Ideal parameter vector	$Z_k^\star = \left\{P_{\mathrm{t}}^U, B^L, T_{\mathrm{D}}^L, N_{\mathrm{CPI}}^L, \mathrm{PRF}^L, \tau_{\mathrm{p}}^L\right\}$

Table 6.1: Dynamic priority weights and ideal parameters of scenario A.

[3] Different performance metrics often pose contradicting, i.e. opposite, requirements on the parameter values.

Scenario B: Search and Find Scenario

When searching for a specific target and identifying it, high-performance tracking is essential regardless of resource usage. Real-time processing is desired to obtain the required target details promptly. In this scenario, the priority parameters are:

- **B**: A high bandwidth provides better range resolution, allowing the radar to distinguish between closely spaced targets, especially vital in a cluttered environment.
- $\boldsymbol{T_{\mathrm{D}}}$: A long dwell time leads to a finer azimuth resolution, which can provide more detailed information about the target.
- $\boldsymbol{N_{\mathrm{CPI}}}$: To reduce computational burden and enable near real-time or real-time processing, the number of pulses is minimized. This choice enables the radar to quickly process the data and update the target's position without experiencing significant delays.
- **PRF**: A high PRF is desired to avoid Doppler ambiguities and blind velocities for moving targets. Additionally, the CPI time should be kept as small as possible to avoid motion error and target smearing effects. This can be achieved with a high PRF while maintaining the same number of pulses within each CPI.

The corresponding weighting vector and ideal parameter vector are given in Table 6.2.

Scenario	Search and Find
Priority weighting vector	$W_k = \{0.1, 0.2, 0.2, 0.2, 0.2, 0.1\}$
Ideal parameter vector	$Z_k^{\star} = \{P_{\mathrm{t}}^{U}, B^{U}, T_{\mathrm{D}}^{U}, N_{\mathrm{CPI}}^{L}, \mathrm{PRF}^{U}, \tau_{\mathrm{p}}^{U}\}$

Table 6.2: Dynamic priority weights and ideal parameters of scenario B.

Scenario C: Activation of Two Simultaneous Transmit Beams

In this scenario, two beams are generated simultaneously in different directions using the same antenna array to track two targets through individual Tracking tiers k and i. Both beams should operate with adequate energy to compensate for the halving of the peak power, as described in Section 4.6.1. A higher number of pulses with a long CPI is desired in this scenario. The first tracking tier to undergo

optimization is for the most demanding target in terms of energy and resolution. The Tracking tiers k and i are considered a pair in this scenario sharing the same pulse time slot, so equal pulse duration, bandwidth, and peak power are enforced. The second target is then optimized according to the selected output control vector of the first Tracking tier. Hence, the priority parameters are:

- $\boldsymbol{N_{\mathrm{CPI}}}$: A high number of pulses can compensate for the drop in the peak power for each Tracking tier.
- $\boldsymbol{P_{\mathrm{t}}}$: The peak power is halved between the two transmit beams and their corresponding Tracking tiers.
- $\boldsymbol{\tau_{\mathrm{p}}}$ and **PRF**: A high pulse duration is desired to increase the SNR for the first Tracking tier i. The other Tracking tier k should use the same pulse duration and PRF.

The corresponding weighting vector and ideal parameter vector for each Tracking tier are given in Table 6.3.

Scenario	Activation of Two Simultaneous Transmit Beams
Priority weighting vector	$W_i = \{0.2, 0.1, 0.1, 0.3, 0.1, 0.2\}$
Ideal parameter vector	$Z_i^\star = \left\{\frac{P_{\mathrm{t}}^U}{2}, B^L, T_{\mathrm{D}}^L, N_{\mathrm{CPI}}^U, \mathrm{PRF}^U, \tau_{\mathrm{p}}^U\right\}$
Priority weighting vector	$W_k = \{0.2, 0.1, 0.1, 0.2, 0.2, 0.2\}$
Ideal parameter vector	$Z_k^\star = \left\{\frac{P_{\mathrm{t}}^U}{2}, B^{\mathrm{T}i}, T_{\mathrm{D}}^L, N_{\mathrm{CPI}}^U, \mathrm{PRF}^U, \tau_{\mathrm{p}}^{\mathrm{T}i}\right\}$

Table 6.3: Dynamic priority weights and ideal parameters of scenario C.

Scenario D: Fast-Moving Target

For high-speed targets, the operation objective is typically to ensure consistent and accurate tracking. In this scenario, the priority parameter is the **PRF**. A higher PRF leads to a short CPI time, which is required to accurately track the position of the target. The re-evaluation of the target position should be brief enough for the beam steering to be updated at a rate high enough to ensure that the target does not move out of the beam footprint on the ground. A high PRF is also desired to avoid Doppler ambiguities and expand the exo-clutter region, as described in Section 2.3.1. The corresponding weighting vector and ideal parameter vector are given in Table 6.4.

Scenario	Fast-Moving Target
Priority weighting vector	$W_k = \{0.1, 0.1, 0.1, 0.1, 0.5, 0.1\}$
Ideal parameter vector	$Z_k^\star = \left\{P_\mathrm{t}^U, B^L, T_\mathrm{D}^L, N_\mathrm{CPI}^L, \mathrm{PRF}^U, \tau_\mathrm{p}^L\right\}$

Table 6.4: Dynamic priority weights and ideal parameters of scenario D.

Scenario E: Small Target in Near Range

Tracking small targets at near range is challenging because, at low incident angles, background clutter return is high, which can mask the weak return signals from targets of low radar cross sections, especially if they move slowly. To optimize the radar's performance for such targets, it is essential to prioritize a longer CPI time to ensure a fine Doppler resolution and perform clutter suppression. Hence, a high number of pulses $\boldsymbol{N_{\mathrm{CPI}}}$ and a high $\mathbf{PRF}$ are selected, as described in Section 2.3.1.

The corresponding weighting vector and ideal parameter vector are given in Table 6.5.

Scenario	Small Target in Near Range
Priority weighting vector	$W_{k,k+1} = \{0.1, 0.1, 0.1, 0.2, 0.4, 0.1\}$
Ideal parameter vector	$Z_k^\star = \left\{P_\mathrm{t}^U, B^L, T_\mathrm{D}^L, N_\mathrm{CPI}^U, \mathrm{PRF}^U, \tau_\mathrm{p}^L\right\}$

Table 6.5: Dynamic priority weights and ideal parameters of scenario E.

These scenarios are examples that can be extended or supplemented based on the application and the desired observations. Their use are demonstrated by the experiment described in Chapter 7.

7 Adaptive Observing SAR Reference System and Simulation

This chapter describes the design of a reference ADOB-SAR system intended for a maritime application. All instrument parameters, including the antenna configuration, are provided in Section 7.1 according to the design guidance provided in the previous chapters. To assess the performance and demonstrate the novel concept of adaptive observing SAR, a decision-making simulator is implemented and described in Section 7.2. A simulation-based scenario is provided in Section 7.3 showing the optimal Tracking parameters and performance selected automatically by the implemented dynamic decision-making processor, followed by the adaptive timing and pulse scheduling of each mode.

7.1 Reference System Design

The designed Adaptive Observing SAR sensor operates at X-band with a center frequency of $f_c = 9.65\,\text{GHz}$. It has been optimized for use on a high-altitude platform flying in the stratosphere at an altitude in the order of 20 km and a low speed of around 20 m/s. This section gives a detailed description of the designed instrument and its operational system parameters.

7.1.1 Performance Requirements

The targets of interest for this specific application are both stationary and moving ocean-floating objects. The minimum detectable radar cross section (RCS) is $\sigma_t \geq 10\,\text{dB}\,\text{m}^2$. The sensor should be capable of tracking targets with a ground velocity of $v_{tg}^{max} = 22\,\text{m/s}$, which influences the required system PRF. Examples of such targets include marine vehicles such as ships and boats, as well as oil spills and tiny islands [175, 233]. The desired performance requirements, including those of the MapSearch and Tracking modes, are provided in Table 7.1.

The goal of MapSearch, as described in Chapter 4, is to quickly identify if there are any targets in the observed area. Therefore, the detection performance is the deciding factor in selecting other key design parameters such as duty cycle and integration time. The most relevant parameters for target detection in a maritime environment

are the signal strength and the sea clutter level. A short integration time is required and a Range Doppler algorithm based solely on the range-compressed data is envisaged to perform the detection processing of moving targets with an adequate SCNR defined in (2.57). A high false detection rate during MapSearch does not pose a concern as the subsequent Tracking mode can rectify any inaccuracy. A high probability of detection ensuring a low missed detection is preferable. Therefore, a probability of detection of $P_{\mathrm{d}} \geq 0.98$ is selected leading to a required SCNR = 15 dB for a probability of false alarm $P_{\mathrm{d}} = 10^{-6}$, following the ROC curves of Figure 2.15 in Section 2.3.3.

Target Specifications	
RCS	$\sigma_{\mathrm{t}} > 10$ dBsm
Maximum velocity	$v_{\mathrm{tg}}^{\mathrm{max}} = 22\,\mathrm{m/s}$
MapSearch Mode	
Signal to clutter plus noise ratio	SCNR = 15 dB
Probability of detection	$P_{\mathrm{d}} \geq 0.98$
False alarm rate	$P_{\mathrm{fa}} = 10^{-6}$
Minimum detectable velocity	MDV = 3 m/s
Tracking Mode	
Minimum signal to clutter plus noise ratio	SCNR = 15 dB
Follow Spot SAR spatial resolution	$\delta_{\mathrm{az,el}} > 0.5\,\mathrm{m}$
Circular SAR spatial resolution	$\delta_{\mathrm{x,y}} \leq 0.5\,\mathrm{m}$

Table 7.1: Performance requirements of the designed ADOB-SAR.

For the Tracking mode, critical factors include energy and resolution performance, as well as the accuracy of estimating the moving target parameters. Given that the Tracking mode is adaptive, the performance parameters are variable and depend strongly on the user's initial operational input options, illustrated in Figure 3.1 and the physical properties of the tracked targets. Therefore, all tracking instrument parameters are designed as a range, rather than discrete values, considering the minimum and maximum performance requirements. This approach enables a more flexible and adaptable system that can adjust to different scenarios and situations during operation, especially when dealing with dynamic and unpredictable environments. In this designed reference system, the Follow Spot mode achieves a fine azimuth and range resolution of $\delta_{\mathrm{az}} = \delta_{\mathrm{el}} > 0.5\,\mathrm{m}$. In scenarios where a finer

resolution is needed, the Circular SAR mode is deployed with a resolution better than $\delta_{\mathrm{az}} = \delta_{\mathrm{el}} \leq 0.5\,\mathrm{m}$.

7.1.2 Designed Antenna System

At 20 km altitude, a HAP can achieve a maximum swath width of $W_{\mathrm{g}} = 25\,\mathrm{km}$, which is relatively remarkable compared to most airborne SAR systems. The antenna beam footprint on the ground during the Tracking mode is set to $A_{\mathrm{fa}} = 1\,\mathrm{km}$ in azimuth and $A_{\mathrm{fe}} = 5\,\mathrm{km}$ in range, which represent a careful trade-off balancing the limited size of the HAP, the system cost, and the desired coverage area on the ground. The footprint determines the antenna array size, leading to an antenna length of $D_{\mathrm{l}} = 80\,\mathrm{cm}$ and height of $D_{\mathrm{h}} = 22\,\mathrm{cm}$.

The antenna is tilted to the center of the swath in elevation with $\theta_{\mathrm{tilt}} = \theta_{\mathrm{near}} + (\theta_{\mathrm{far}} - \theta_{\mathrm{near}})/2 = 41.5°$. The near and far range angles of the MapSearch beam are set to $\theta_{\mathrm{near}} = 24°$ and $\theta_{\mathrm{far}} = 59°$ and determined by a timing analysis, resulting in an illumination beamwidth of $\Theta_{\mathrm{w}} = 35°$ defined in (4.25). As the same antenna is used for both Tracking and MapSearch, the beamwidth needs to be broadened in elevation to illuminate the entire swath W_{g}. This is done using the phase soiling subarray superposition technique, described in Section 4.3.4. During the Tracking mode, the elevation beamwidth is $\Theta_{\mathrm{e}} = 7°$ by utilizing the full height of the array, as shown in Figure 7.1.

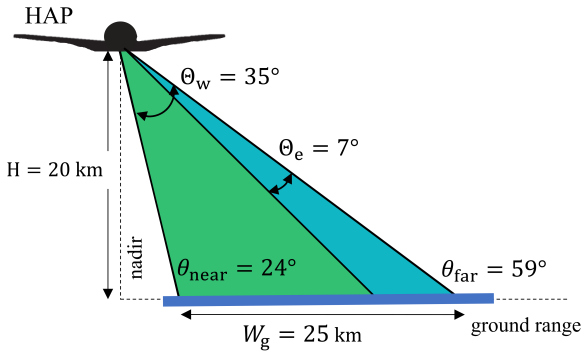

Figure 7.1: Schematic representation of the HAP side-looking geometry in elevation for the MapSearch mode (wide green beam) and the Tracking mode (narrow blue bram) with the corresponding parameters for the designed ADOB-SAR sensor.

The MapSearch receive beam is steered over time within the swath using a maximum elevation steering angle of $\theta_{\mathrm{e}}^{\mathrm{max}} = \pm\Theta_{\mathrm{w}}/2 = \pm 17.5°$, as derived in (4.38). The second

hybrid beamforming technique described in Section 4.3.5 is employed, whereby the time-variant steering in elevation is performed up to the maximum angle of $\theta_{\mathrm{eD}}^{\max} = \pm 17.5°$, and analog steering is applied at the subarray level to suppress grating lobes. The sub-aperture weights are preset with the phase shifters to the left and right extremities of the swath. First, the sub-aperture analog steering angle is set to $\theta_{\mathrm{eA}} = -17.5°$. Once the echo reaches the boresight direction defined by θ_{tilt}, the steering angle switches to $\theta_{\mathrm{eA}} = 17.5°$ according to (4.50). To ensure the grating lobe appears at the null of the sub-aperture pattern with $\theta_{\mathrm{GL}} = -17.5°$, as per (4.48), when the receive beam is steered to $\theta_{\mathrm{eD}}^{\max} = 17.5°$, the elevation sub-aperture spacing is set to $d_{\mathrm{sub,e}} = 1.6\lambda$, as derived in (4.51). The simulated 2-D antenna patterns of the MapSearch mode during transmission and reception are shown in Figure 7.2. In (a), a wide elevation beamwidth is used on transmit to cover the entire swath, and the beam is squinted to $\theta_{\mathrm{sq}} = 3°$ in azimuth. It is then narrowed on receive and steered maximally to $-17.5°$ without grating lobes.

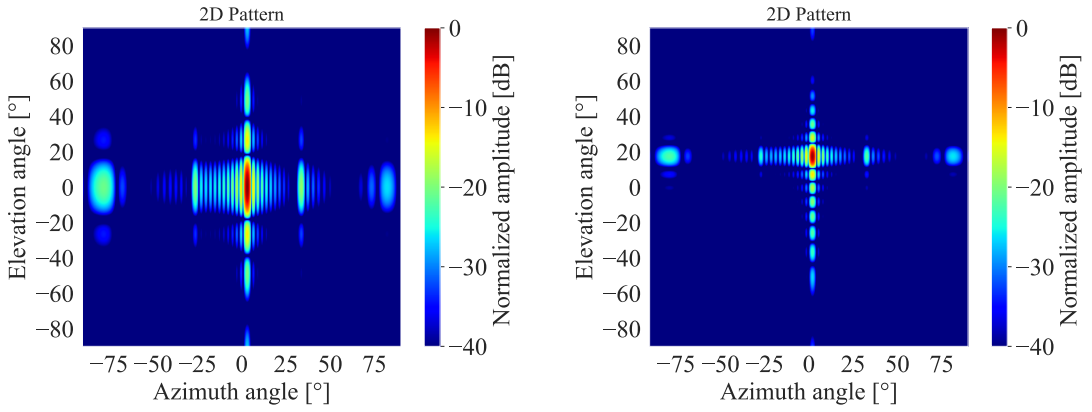

(a) Transmit pattern.

(b) Receive pattern.

Figure 7.2: Simulated 2-D antenna array pattern on transmit (a) and receive (b) snapshots during the MapSearch mode.

The value of the MapSearch azimuth squint angle is influenced by multiple factors, as derived in Section 4.3.1 and illustrated in Figure 4.11. The first parameter is the azimuth beamwidth, which is determined by the length of the antenna D_{l} and is set to $\Theta_{\mathrm{ms}} = 2°$. The squint angle also depends on the maximum Tracking illumination time T_{tr}, which is directly proportional to the finest Follow Spot azimuth resolution that the instrument is designed to achieve. Additionally, the processing time of the MapSearch CPI is set to $T_{\mathrm{procCPI}} = 5\,\mathrm{s}$, and an additional interval of $T_{\mathrm{trans}} = 5\,\mathrm{s}$ is needed to activate the concurrent new Tracking mode tier. Given these parameters results in a squint angle of $\phi_{\mathrm{sq}} = 3°$ to achieve the desired performance according to (4.12). To minimize the number of transmit/receive cores, passive subarrays having

a large inter-spacing and combining several antenna elements are used in azimuth, as described in Section 4.3.1. The subarray pattern is designed to suppress any resulting grating lobes. The azimuth subarray spacing is set to $d_{\mathrm{sa}} = 2\lambda$ according to (4.17) leading to $N_{\mathrm{as}} = 12$ subarrays. The resulting antenna pattern is depicted in Figure 7.2. Due to the large subarray spacing in azimuth, grating lobes appear on the array factor within the visible angular sector of the antenna. However, they are attenuated by the subarray pattern to less than $-20\,\mathrm{dB}$, which is acceptable.

The antenna array topology for each operation mode is illustrated in Figure 7.3.

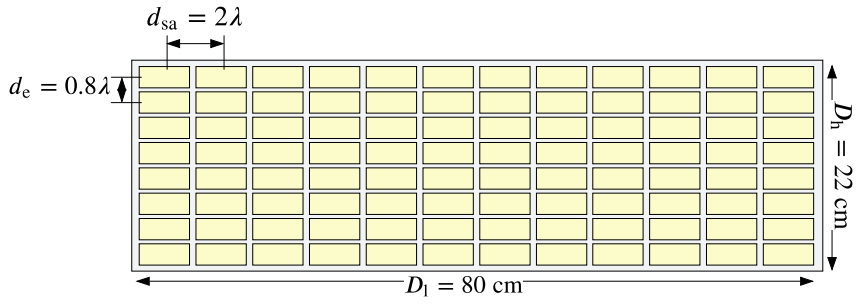

(a) Antenna array transmit configuration.

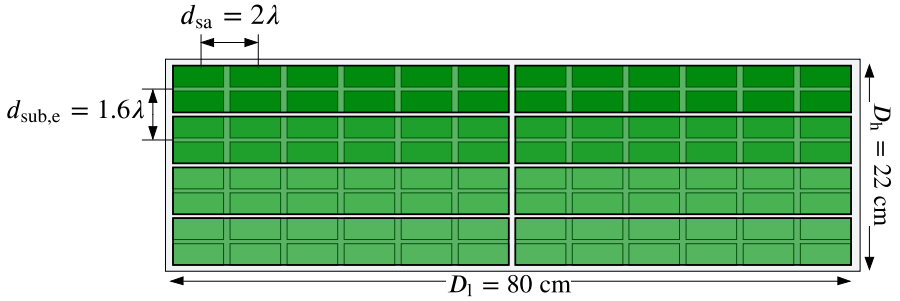

(b) Antenna array receive configuration during MapSearch.

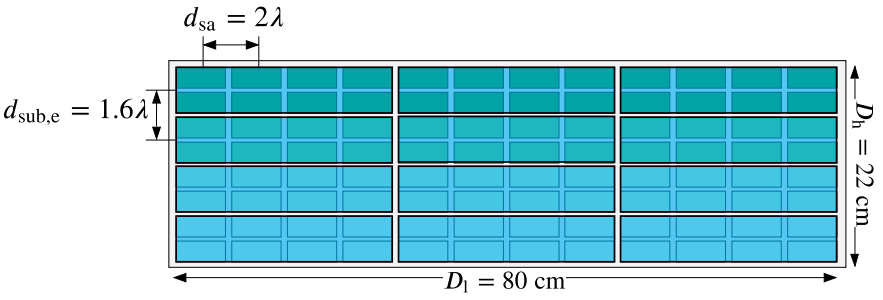

(c) Antenna array receive configuration during Tracking.

Figure 7.3: ADOB-SAR antenna array configurations. Each yellow rectangle in (a) represents a subarray with passive antenna elements. On receive, the aperture is divided into sub-apertures with $N_{\mathrm{ch,ms}} = 8$ channels for digital SCORE including two azimuth phase centers in MapSearch (b) and $N_{\mathrm{ch,tr}} = 12$ channels with 3 azimuth phase centers in Tracking (c).

A total of $N_{\text{sub,e}} = 4$ digitized sub-apertures are employed in elevation, as shown in Figure 7.3(b). In azimuth, the antenna is split into two sub-apertures, each digitized individually, resulting in a total of $N_{\text{ch,ms}} = 8$ digital channels during MapSearch.

The spacing between antenna elements in elevation is determined by the maximum steering angle $\theta_{\text{e}}^{\text{max}}$ used during the Tracking mode and derived in (4.39). According to equation (4.62), the element spacing in elevation is set to $d_{\text{e}} = 0.8\lambda$, resulting in a total of $N_{\text{e}} = 8$ antenna elements in elevation, as illustrated in the antenna topology of Figure 7.3(a). Considering the subarray formation in azimuth, a total of $N = N_{\text{e}} \times N_{\text{as}} = 12 \times 8 = 96$ subarrays are used on transmit. Each subarray is connected to a transmit/receive core and two phase shifters, as described in Section 4.5.1.

Each receive channel consists of two subarrays in elevation, as shown in Figure 7.3(b) and (c). Considering the designed ADOB-SAR application and its corresponding Maritime Moving Target Indication (MMTI), the azimuth aperture is divided into three subarrays digitized individually. The number of digital channels during Tracking increases to a total of $N_{\text{ch,tr}} = 12$, taking advantage of the available elevation channels. As described in Chapter 4, the digital channel architecture is reconfigurable and depends on the operation requirements. A different channel distribution can be applied using the available switches by deactivating some elevation channels and using them for azimuth.

The footprint size of the Tracking beam varies with the elevation steering angle and is plotted in Figure 7.4. The antenna beam footprint size is 5 km at boresight.

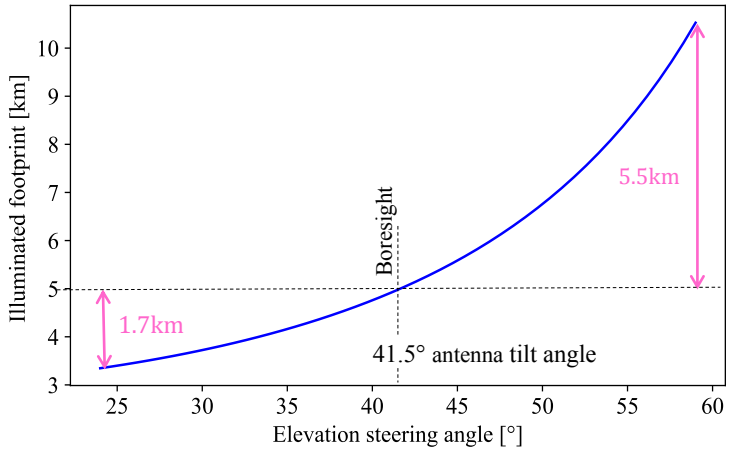

Figure 7.4: Illuminated Tracking beam footprint variation with the elevation steering angle within the MapSearch swath width W_{g}. The highlighted 5 km footprint corresponds to the boresight beam at $\theta_{\text{tilt}} = 41.5°$.

When the beam is steered, the footprint varies accordingly: it decreases by up to

1.7 km in the near-range direction, resulting in a minimum footprint of 3.3 km, and it increases by up to 5.5 km in the far-range direction, resulting in a maximum footprint of 10.5 km.

The antenna pattern of the Tracking beam is plotted in Figure 7.5 (simulated by multiplying the subarray pattern with the array factor). The final pattern shows complete suppression of the grating lobes.

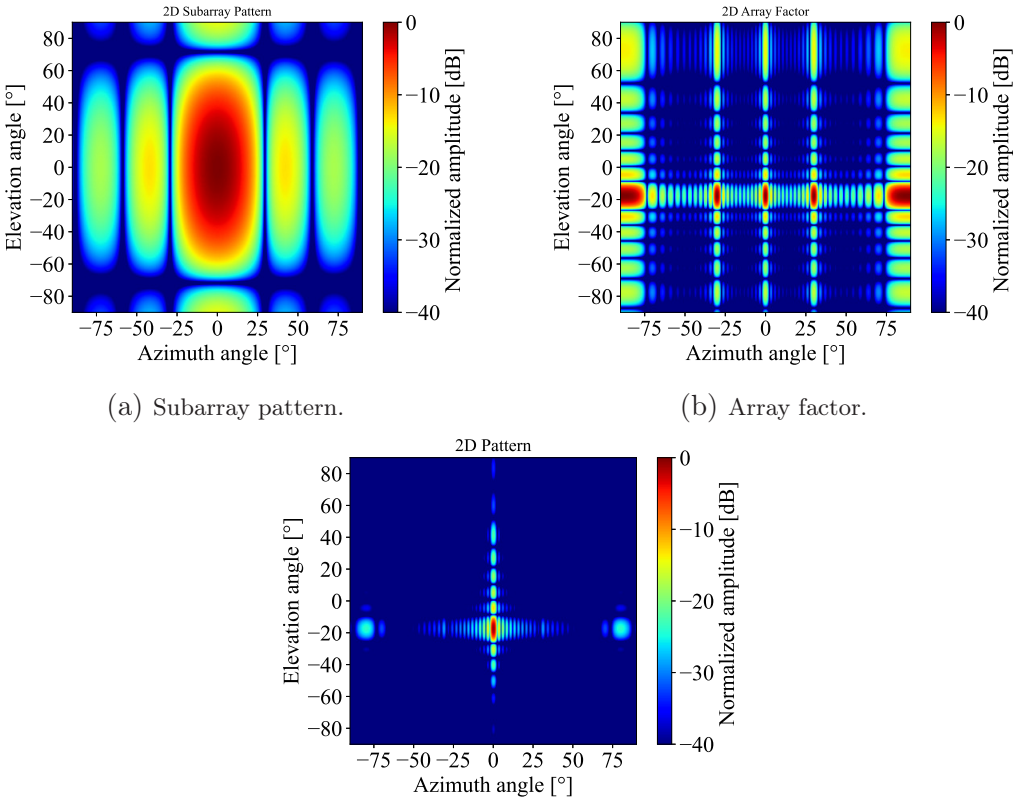

(a) Subarray pattern.

(b) Array factor.

(c) Array pattern.

Figure 7.5: Simulated 2-D antenna pattern during the Tracking mode.

7.1.3 SAR Instrument Parameters

This section provides the SAR instrument parameters for the MapSearch mode and the bounds of each control parameter during the Tracking mode, followed by a performance estimation.

For the MapSearch mode, a 15 dB SCNR is required to achieve the desired probability of detection given in Table 7.1. This gives a minimum pulse duration in the

order of $\tau_{\mathrm{p}}^{\mathrm{M}} = 12.5\,\mu\mathrm{s}$ and a chirp bandwidth of $B_{\mathrm{M}} = 20\,\mathrm{MHz}$ for a peak power of $P_{\mathrm{t}} = 50\,\mathrm{W}$ according to (2.57) using the MapSearch antenna configuration. A low bandwidth is selected for MapSearch, as the energy performance for detection purposes is more important than resolution. As described in Section 5.1.3, the choice of the PRF is influenced by many performance factors. To achieve the desired swath width of $W_{\mathrm{g}} = 25\,\mathrm{km}$ without range ambiguities, the maximum PRF should be $\mathrm{PRF}_{\mathrm{max}} = 3600\,\mathrm{Hz}$ following (5.10). This value is set as the maximum Tracking PRF the decision-maker can select. Besides, the PRF is also influenced by potential velocity ambiguities. For the desired maximum target ground velocity $v_{\mathrm{tg}}^{\mathrm{max}} = 22\,\mathrm{m/s}$, the minimum PRF should be in the order of 2400 Hz considering the far range angle $\theta_{\mathrm{far}} = 59°$ as defined in (5.13) and Figure 5.4. Based on the interleaving condition, defined (5.13), the MapSearch PRF should be an integer multiple or divisor of the Tracking PRF. As $2700\,\mathrm{Hz} \neq \mathrm{PRF}_{\mathrm{max}}^{\mathrm{T}}/n$ with n integer, the MapSearch PRF is set to $\mathrm{PRF}^{\mathrm{M}} = \mathrm{PRF}_{\mathrm{max}}^{\mathrm{T}}/2 = 1800\,\mathrm{Hz}$. This lower PRF results in ambiguous velocities, which vary depending on the target range location, as shown in Figure 7.6. Targets at far range with an incident angle of $\theta_{\mathrm{i}} = 59°$

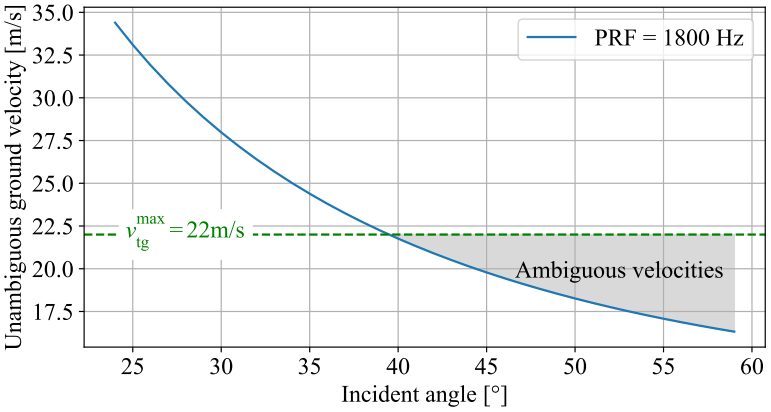

Figure 7.6: Maximum unambiguous velocities versus the incident angle for the selected MapSearch PRF of 1800 Hz.

and a ground velocity of $v_{\mathrm{tg}} > 16\,\mathrm{m/s}$ will be aliased. These targets will be displaced in the Doppler spectrum, but can still be detected, which is sufficient for the MapSearch mode. During the Tracking mode, targets at far range are observed with a higher PRF to estimate their accurate velocities. This approach aligns with the ADOB-SAR concept of resource minimization and mode rational, described in Section 3.2.2.

The resulting timing diagram illustrating the transmit and receive events as a function of the ground range is shown in Figure 7.7. The duty cycle is set to

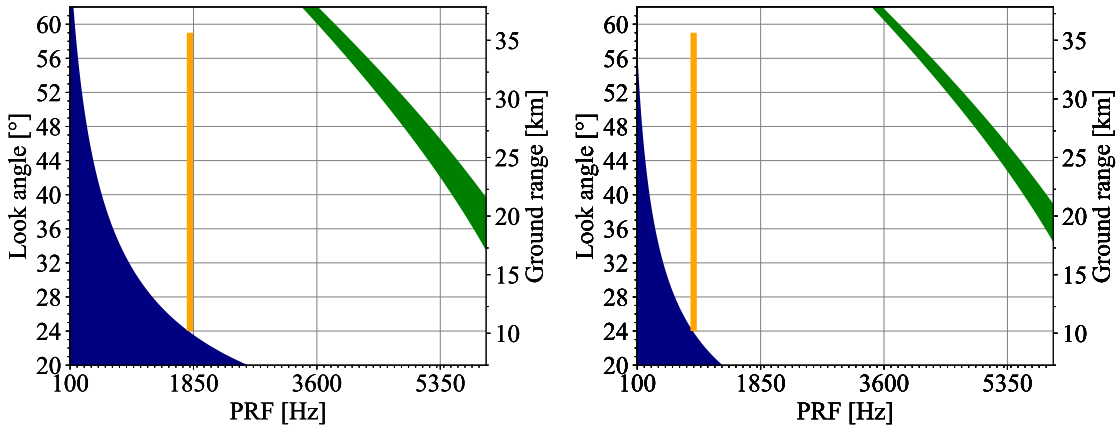

(a) $\mathrm{PRF}^{\mathrm{M}} = 1800\,\mathrm{Hz}$ at 2.25% duty cycle.

(b) $\mathrm{PRF}^{\mathrm{M}} = 900\,\mathrm{Hz}$ at 1.125% duty cycle.

Figure 7.7: Timing diagrams for a HAP with an altitude of 20 km, operating at a duty cycle of 2.25% (a) and 1.125% (b). The receive window without overlap with the transmit events (green) and nadir echoes (dark blue) is highlighted in orange.

$d_{\mathrm{c}}^{\mathrm{M}} = \mathrm{PRF}^{\mathrm{M}}\,\tau_{\mathrm{p}}^{\mathrm{M}} = 2.25\%$ for 1800 Hz. The receive window illuminating the desired swath width is free of nadir overlapping and range ambiguities, as shown in Figure 7.7(a). This duty cycle is sufficient to achieve the desired detection energy performance, as demonstrated by the simulated SCNR in Figure 7.8. The desired SCNR = 15 dB is successfully attained for a target RCS of 10 dBsm located in mid-range with $\theta_{\mathrm{i}} = 40°$. This performance simulation is based on a framework presented in [138, 234, 235].

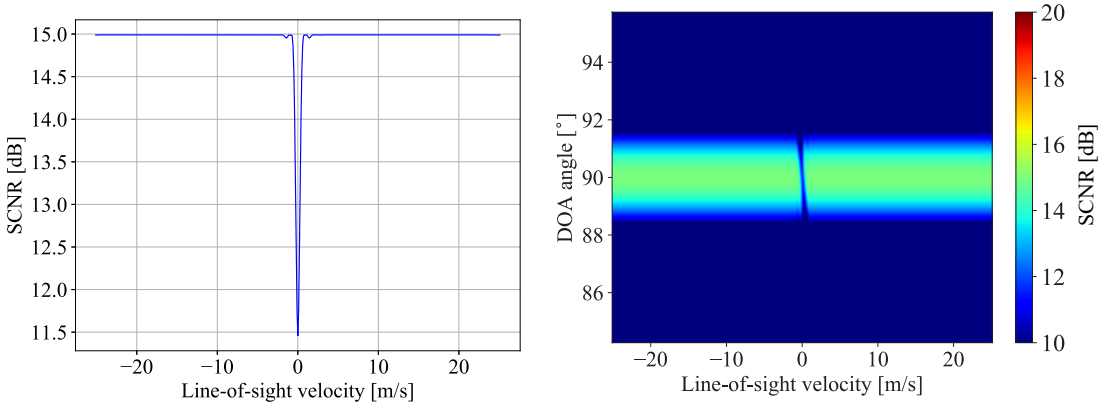

(a) (b)

Figure 7.8: Simulated SCNR during the MapSearch mode over the line-of-sight target velocity for a duty cycle of 2.25% and a PRF of 1800 Hz. In (a), the SCNR is plotted as a cut over the broadside direction of the antenna array. (b) shows the output SCNR of one azimuth receive channel.

The number of integrated pulses is $N_{\mathrm{CPI}} = 1200$ leading to a CPI time of $T_{\mathrm{CPI}} = 0.63\,\mathrm{s}$. This integration time is considered long for moving target detection when compared to airborne SAR systems like F-SAR [93, 236], which typically operates with a CPI time on the order of 0.04 s [126, 237]. However, the HAP moves slower, making motion effects such as Range Cell Migrations (RCM), defined in (2.17), negligible. This is demonstrated in Figure 7.9, which shows the range variation over the azimuth time for both platforms, and the RCM for the 0.66 s.

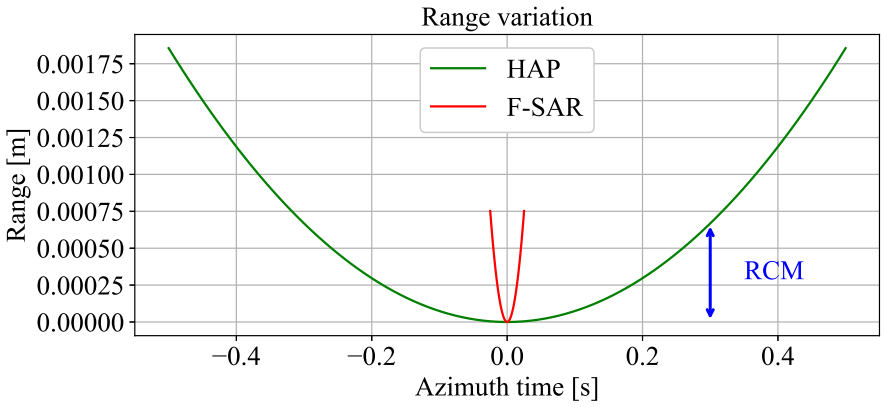

Figure 7.9: Range cell migration comparison between a HAP and the F-SAR platform in terms of CPI time.

As described in Section 5.1.5, the MapSearch is reduced when the number of targets exceeds the time capacity of the system. For this, the second operating PRF of the MapSearch mode is $\mathrm{PRF}^{\mathrm{M}} = 1800\,\mathrm{Hz}/2 = 900\,\mathrm{Hz}$. In this case, the duty cycle is reduced to $d_{\mathrm{c}}^{\mathrm{M}} = 1.125\%$, as illustrated in Figure 7.7(b). This decrease in the duty cycle is compensated by a longer integration time $T_{\mathrm{CPI}} = 1.3\,\mathrm{s}$ with the same number of pulses. To avoid moving target fluctuations caused by the longer CPI, the MapSearch burst mode with frequency alternating, described in Section 5.1.6, is activated. Following (5.19), a minimum frequency shift of $\Delta f = 90\,\mathrm{MHz}$ should be applied. Hence, the center frequencies $f_{\mathrm{c1}} = 9.65\,\mathrm{GHz}$ and $f_{\mathrm{c2}} = 9.75\,\mathrm{GHz}$ are selected. The blind velocities resulting from the low PRF are resolved by utilizing the burst mode with PRF alternating described in Section 5.1.4. A slightly different PRF in the order of 910 Hz is used for the second MapSearch burst.

The ADOB-SAR instrument parameters are listed in Table 7.2. Design-based upper and lower bounds are set for the Tracking mode parameters. The chirp bandwidth can go up to 600 MHz depending on the desired range resolution. The SAR dwell time varies depending on the azimuth resolution. The center frequency is also adapted during the Tracking mode when frequency orthogonality is needed to separate overlapping return echoes, as described in Chapter 5 Section 5.6. Therefore, the

Parameter	**MapSearch mode**	**Tracking mode**	
		Lower bound	**Upper bound**
Center frequency	9.65, 9.75 GHz	9.35 GHz	9.95 GHz
Bandwidth	20 MHz	20 MHz	600 MHz
CPI time	0.66 s 1.3 s	0.01 s	1.3 s
CPI pulses	1200	30	1200
SAR dwell time	–	5 s	60 s
Pulse duration	12.5 µs	2 µs	12.5 µs
PRF	1800 Hz 900, 910 Hz	900, 1800, 3600 Hz 910, 1820, 3640 Hz	
Peak power	50 W	25 W	50 W
Duty cycle	2.25% 1.125%	0.2%	4.5%
Antenna size (az × el)	80 × 22 cm		
Element spacing (az × el)	$2\lambda \times 0.8\lambda$		
Number of elements	12 × 8		
Number of az channels	2	3	
Number of el channels	4		
Azimuth steering	3°	0°	±3°
Elevation steering	0°	0°	±17.5°
Tx antenna gain	24 dB	30 dB	
1 Rx az channel gain	27 dB	26 dB	
System noise figure	3 dB		
Losses	7 dB		
Rx noise temperature	400 K		

Table 7.2: ADOB-SAR reference system parameters of the different operational modes.

carrier frequency interval is set to $[9.35 - 9.95\ \text{GHz}]$ based on the maximum Tracking chirp bandwidth. The pulse duration of the Tracking tiers can vary from 2 µs to 12.5 µs and can be even smaller than the pulse duration used for the MapSearch mode since the power is compensated by the narrow and high gain Tracking transmit beam. The peak power is usually fixed in radar systems and determined by the high-power amplifier design. However, activating multiple channels on transmit, as described in Sections 4.6 and 6.2.3, requires dividing the peak power between the two transmit paths, as derived in (6.30) and shown in Figure 4.38. The PRF of the Tracking mode tiers can take different discrete values depending on the moving target needs but should satisfy the interleaving condition (5.26). Therefore, the following interval $\text{PRF}^{\text{T}} = [900\,\text{Hz}, 1800\,\text{Hz}, 3600\,\text{Hz}]$ is used for Tracking.

Adaptive Tracking Performance

The optimal operational parameters for each tracking mode tier are automatically selected by the dynamic decision-making processor based on MapSearch observations, the parameter bounds defined in Table 7.2, and the specific performance requirements requested by the user. The tracking mode is designed to maintain the same SCNR for all targets, regardless of their distances, variations in RCS, and sizes. Figure 7.10 compares the SCNR variation over the target range and RCS between the desired adaptive Tracking mode and classical fixed modes such as the MapSearch mode. A uniform SCNR up to 20 dB can be achieved across all targets using the Tracking mode parameters and configuration.

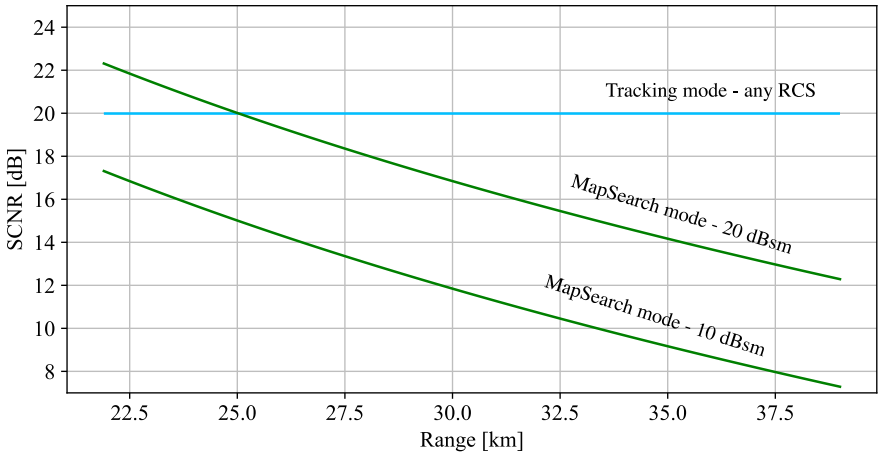

Figure 7.10: Comparison of the SCNR variation between the operating modes of the designed ADOB-SAR reference system.

The spatial resolution is also adapted so that the same target is imaged with consistent resolution regardless of its location. Figure 7.11 compares the resolution performance during Tracking and MapSearch modes. The best achievable Tracking resolution, which depends on the antenna length, is plotted here. However, the decision-maker adapts the bandwidth and dwell time from one Tracking tier to another to achieve the optimal resolution, based on the target's size, range, and the specific scenario the user wants to focus on. This approach differs from MapSearch, where the target's location influences the resulting resolution, even though the bandwidth and dwell time remain fixed.

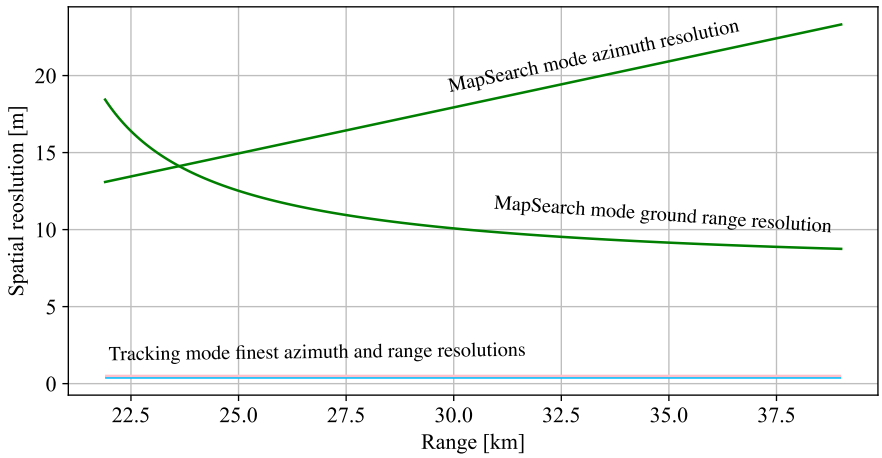

Figure 7.11: The spatial resolution performance of the ADOB-SAR sensor for the different operating modes.

7.2 DECISION Simulator

A simulator is implemented in Python to demonstrate the dynamic decision-making procedure of the designed ADOB-SAR reference system. It is named DECISION, an acronym for *Dynamic Evaluation and Control of Instrument Scheduling and Interleaved OptimizatioN*. Using this tool, it is possible to simulate a scenario, optimize the SAR instrument parameters for its Tracking acquisition, and schedule the transmit pulses and return echoes. The simulator aims to validate the novel decision-making process independently of any specific detection algorithm [126, 128]. Consequently, the detection algorithm is not included in the simulator. A knowledge-aided control is used, where the target properties are given as inputs. The detection time t_k for each target is provided, along with approximations of their sizes, backscattering coefficients, and velocities as if they were extracted by the MapSearch mode.

The structure of DECISION is illustrated in Figure 7.12. It starts by adapting the multi-mode operation by running the forcing models, described in Section 6.2. Then, the dynamic optimizer calculates the optimal SAR parameters based on the target properties given as inputs. The desired performance is typically specified by the user and given as input. It can be easily updated during the operation according to the application requirements. The adaptive scheduling algorithm, described in Chapter 5, is then activated to verify timing and echo orthogonality, adjusting the transmission time of each new Tracking tier according to the entire scenario. All results are visualized in real time, and their performance is evaluated through a feedback loop. Additionally, the simulator is adaptable to other platforms and compatible with any new SAR instrument. Therefore, the boundaries of the instrument parameters, which need to be defined during the design phase, are given as input to the simulator. In case the decision-maker fails to find an optimal solution for

a scenario not considered previously in the instrument design phase, the simulator does not abort the process but, instead, operates with the maximum performance given by the boundaries of the input system.

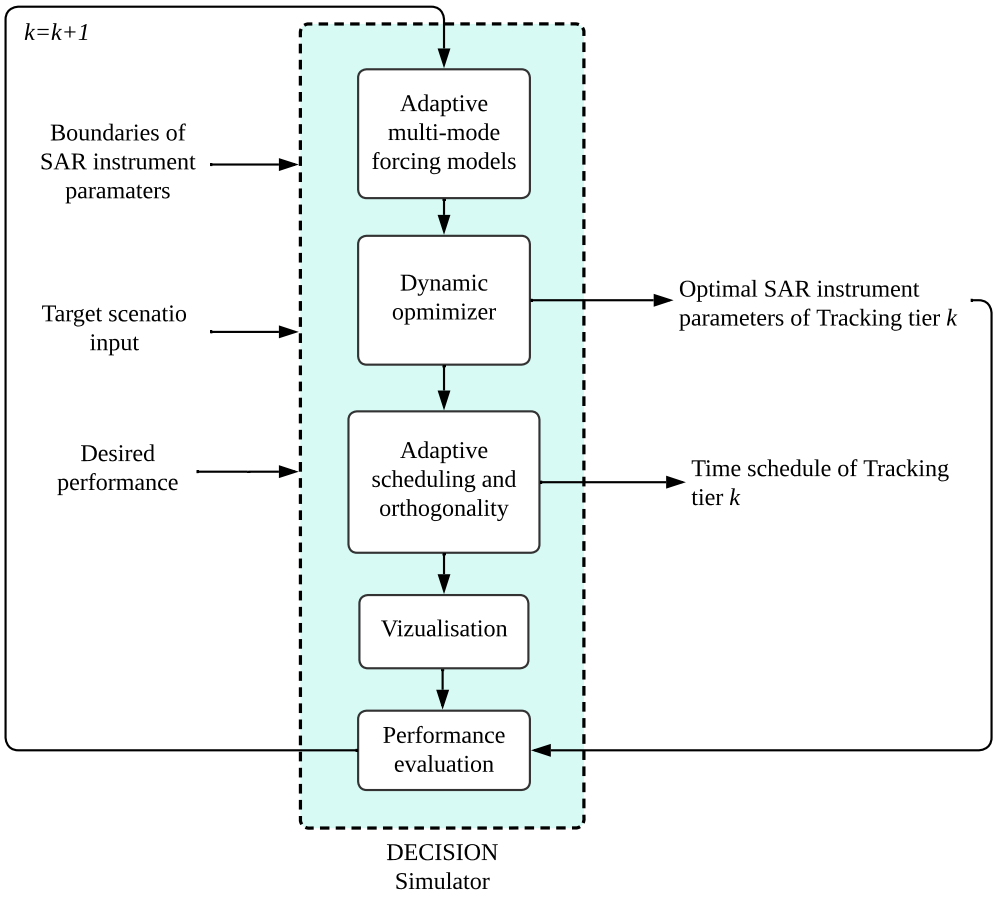

Figure 7.12: Block diagram of the DECISION simulator showing the structure of the implemented software.

The maritime application described in Section 7.1 is applied with different simulated targets detected throughout the flight. The simulator considers extended targets and incorporates a model for sea reflectivity, denoted as σ_0, which varies with the incident angle, as outlined in [155]. In a real operation, the clutter behavior is assessed continuously through the MapSearch extracted data.

DECISION takes approximately 3 s to compile and output the results on a 1.4 GHz Intel Core i5 processor, making it suitable for onboard decision-making and new mode activation capabilities.

7.3 Simulated Experiment

This section outlines a simulated experiment using the implemented DECISION software, described in Section 7.2. It includes a detailed description of the resulting dynamic decision-making behavior and the pulse-to-pulse scheduling of all optimized Tracking tiers. A HAP of an altitude of 20 km and a speed of 20 m/s is used for the simulation. The designed reference system in Section 7.1 is applied. The upper and lower bounds of the instrument parameters for the MapSearch and Tracking mode, given in Table 7.2, are used in the simulation and are fed to the dynamic optimization function (6.43).

7.3.1 MapSearch Target Scenario

In a real operation, the squinted MapSearch mode runs continuously during the flight with the task of finding the targets of interest by evaluating the signals collected within the integration time interval T_{CPI}. At each predefined time step t_k, the MapSearch mode detects N_{t} targets and determines the corresponding input parameter vector Y_k defined in (6.38) for each target k. The target scenario used in this experiment is closely aligned with the output of the MapSearch mode.

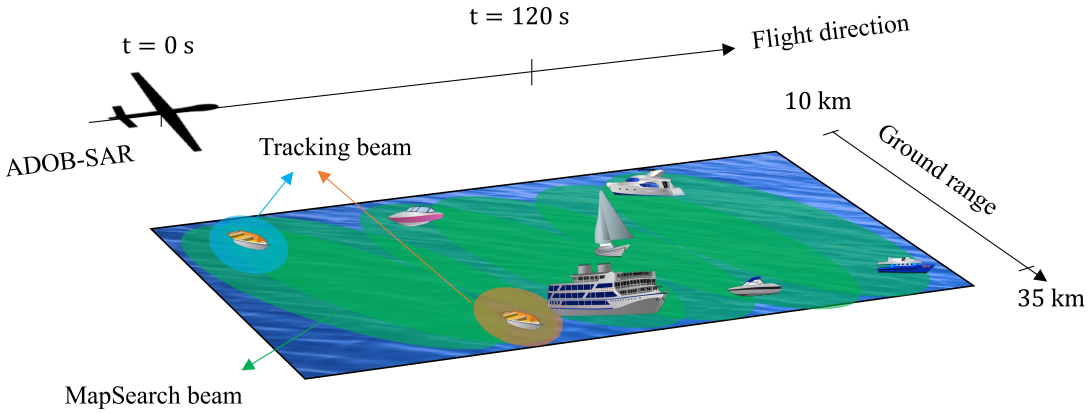

Figure 7.13: Simulated maritime scenario with eight predefined targets of different sizes, radar cross sections, and range and azimuth positions. The MapSearch and Tracking antenna beam footprints are indicated by the green and orange areas, respectively.

The implemented scenario, depicted in Figure 7.13, encompasses eight simulated targets as maritime vehicles, including boats and ships. They have distinct sizes and backscattering characteristics, as outlined in Table 7.3. It is assumed that a single target has a uniform reflectivity. The targets exhibit different detection

Target	RCS (dBsm)	Size (m × m)	Ground range (km)	Detection time (s)	Sea σ_0 (dB)	Speed (m/s)
1	10	15×5	10	5	-15	1
2	12	15×5	32	30	-28	1
3	15	50×20	14	50	-20	3
4	30	300×55	32	50	-28	3
5	13	30×10	20	60	-20	2
6	20	20×10	28	80	-25	17
7	20	150×40	10	90	-15	5
8	25	75×50	31	100	-27	16

Table 7.3: Targets and scene parameters used as inputs for the dynamic decision-making processor.

patterns. While some are identified in distinct time intervals, others, like targets 3 and 4, are detected at the same time. The total flight time considered in the simulation is 120 s, as shown in Figure 7.13

7.3.2 Dynamic Tracking Optimization and Scheduling

The dynamic decision-making processor is then executed to obtain the optimal sensor configuration and operational parameters for each Tracking acquisition of these targets. The desired performance parameters are listed in Table 7.4.

The dynamic optimizer initially sets the priority weighting vector W_0 and the ideal parameter vector $Z_0^\star$ to the configuration of scenario A, which is described in Section 6.4.4 and given in Table 6.1. For each tracking tier, the optimized instrument parameters, performance, and interleaving schedule are visualized and explained. The output of the dynamic optimizer is shown in Figure 7.14. The variation of the SAR control parameters, including the Tracking PRF, pulse duration, bandwidth, SAR dwell time, peak power, and number of CPI pulses, is plotted over the flight time. At each specific time instance, those parameters change and each marker corresponds to a new tracking tier activation.

The resulting performance metrics, including the azimuth and range resolutions, SCNR, and NESZ, for each optimized Tracking tier are presented over the flight

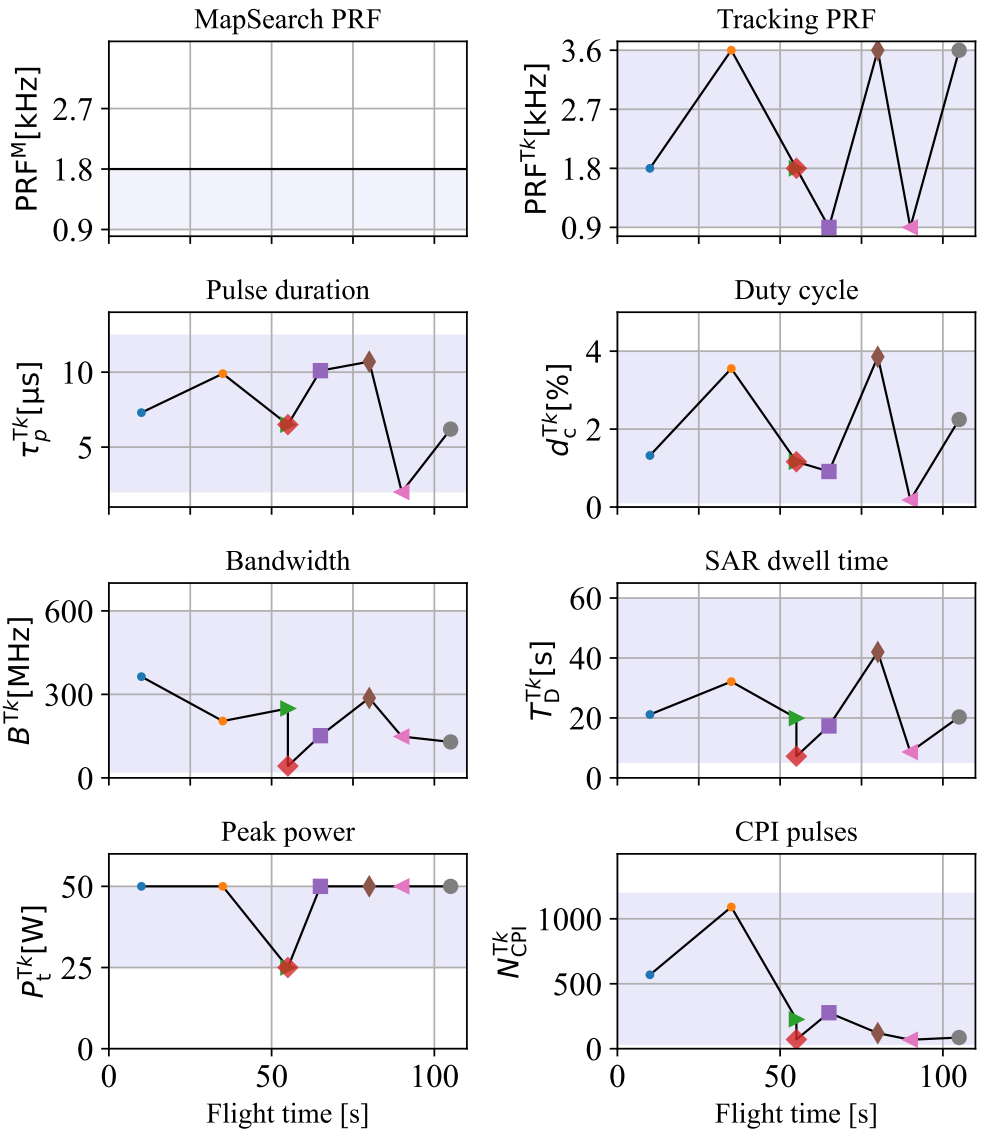

Figure 7.14: Dynamic decision-making simulation showing the instrument parameters versus time. The purple background indicates the lower and upper parameter bounds, while the markers correspond to the targets.

Parameter		Value
Desired performance		
Signal to Clutter Noise Ratio	$\mathrm{SCNR_D}$	15 dB
Noise Equivalent Sigma Zero	$\mathrm{NESZ_D}$	−22 dB
Maximum duty cycle	$d_{\mathrm{c,max}}$	30%
Resolution ratio	r_{D}	1.1
Maximum number of pixels	N_{px1}	100
Minimum number of pixels	N_{px2}	50
Optimization framework initialization		
Priority weighting vector	W_0	$\{0.1, 0.1, 0.1, 0.2, 0.3, 0.2\}$
Ideal parameter vector	$Z_0^\star$	$\{P_{\mathrm{t}}^U, B^L, T_{\mathrm{D}}^L, N_{\mathrm{CPI}}^L, \mathrm{PRF}^L, \tau_{\mathrm{p}}^L\}$

Table 7.4: Desired performance parameters and optimization model initialization.

time in Figure 7.15. The resolution is variable as it is adapted to the target size and location, while the SCNR and NESZ are constant, which aligns with the adaptive observing concept.

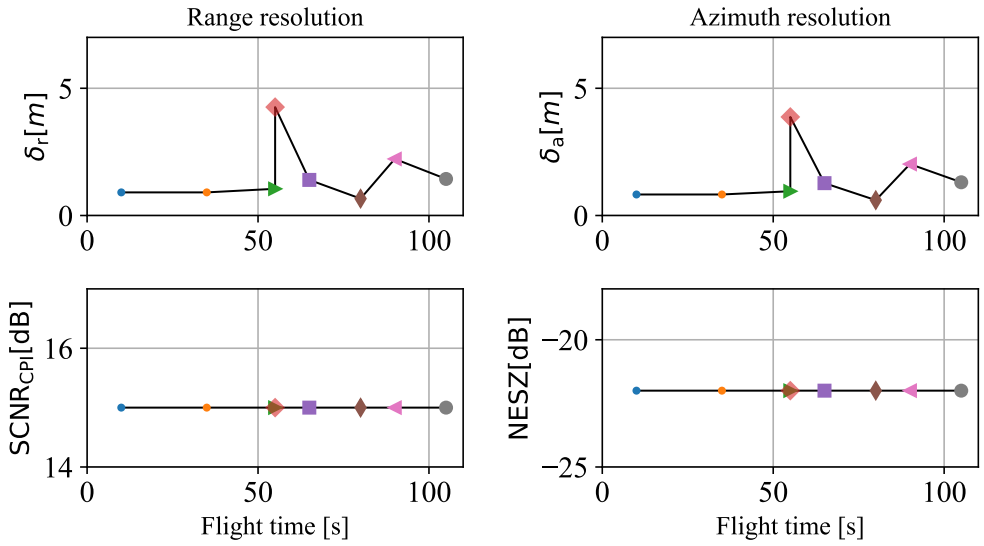

Figure 7.15: Simulated SAR performance using the automatically generated operational parameters plotted over the flight time. Each marker is assigned to a target and its corresponding Tracking tier at the start time of its acquisition.

In the following, the simulation results are described step-by-step over time. The operation starts at $t = 0\,\mathrm{s}$ and the MapSearch mode is operating with a PRF of 1800 Hz. The first target $k = 1$ is detected at $t = 5\,\mathrm{s}$. Starting from that time, the

dynamic decision-maker is executed, and the optimal operational parameters of the first Tracking tier are obtained. The target is a small boat located at a near range and moving slowly, as outlined in Table 7.3. Hence, it is difficult to track it in the presence of clutter. A high PRF is therefore forced on the ideal parameter vector following scenario E, described in Section 6.4.4. A fine resolution is needed for this small target, which is well achieved by automatically selecting large bandwidth and SAR dwell time, as depicted in Figure 7.14.

Figure 7.16 shows the simulated adaptive timing schedule starting at $t = 0\,\mathrm{s}$ with only the MapSearch and at $t = 10\,\mathrm{s}$, when the first Tracking tier is added to the schedule after obtaining the optimal parameters from the optimization model. The schedule snapshots are automatically generated by the scheduling algorithm. They showcase the real pulse and echo timings based on the target location and the Tracking beam properties.

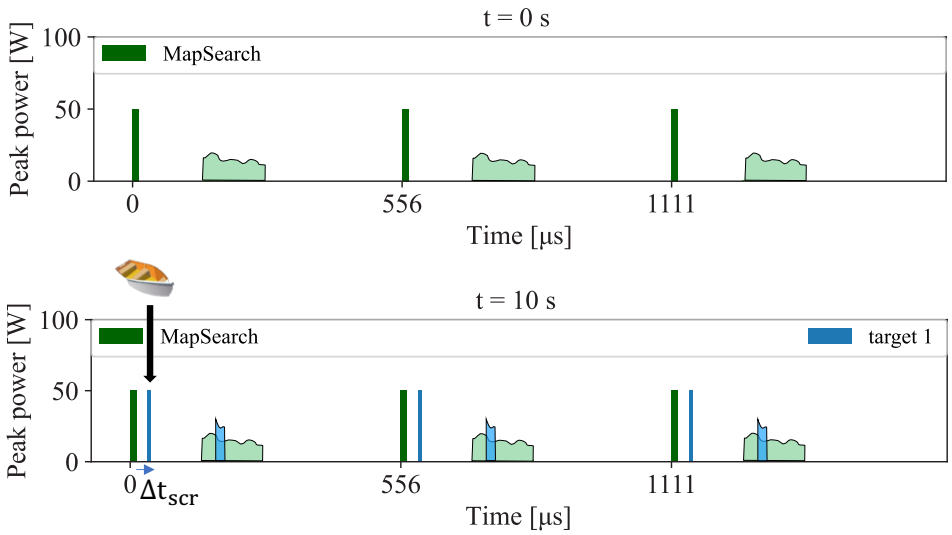

Figure 7.16: Simulated schedule snapshot of the transmit pulses and echoes versus time of the interleaved MapSearch and Tracking tier $k = 1$ at $t = 0\,\mathrm{s}$ and $t = 10\,\mathrm{s}$.

The first target transmit pulse is sent in the first free time gap corresponding to the MapSearch waiting time interval, as shown in the second diagram of Figure 7.16, where the transmit pulses and echoes are plotted over time using the obtained SAR dwell time, pulse duration, and PRF. A decision processing and Tracking activation time of 5 s after detection is considered in the simulation. Therefore, the Tracking tier $k = 1$ starts at $t = 5 + 5 = 10\,\mathrm{s}$. The scheduler searches for the best available time within the MapSearch waiting interval to place the new pulse, while avoiding unresolved time or space overlaps. Since target 1 is in near range,

its echo duration is short. The Tracking echo is received at the same time as the MapSearch echo. A SCORE time shift is, therefore, automatically applied to prevent the spatial overlapping with the MapSearch beam received from the same direction, as described in Section 5.5.2. A time shift Δt_{scr} is, therefore, applied for the first Tracking tier to reach the required spatial difference for echo separation. DBF is then used to separate the echoes in elevation.

Target 2 corresponds to a small boat, similar to target 1, and located in the far range. Therefore, the allocation of radar resources is maximized. This target scenario needs a higher energy input compared to the first target. The selection of the dynamic optimization consists of a high PRF of 3600 Hz with long pulse duration in the order of $t = 10\,\mu\mathrm{s}$, leading to a duty cycle of 3.6%. Furthermore, to achieve the desired Tracking $\mathrm{SCNR_D}$, this target requires a substantial number of CPI pulses, as shown by resulting control parameters in Figure 7.14.

Following the spatial resolution control criteria, the bandwidth and the SAR dwell time are selected based on a trade-off with other parameters. The first two targets are the smallest, which justifies the control processor's decision to utilize high bandwidth and dwell time, achieving a resolution of 0.8 m corresponding to their sizes. This is evident in the plots of the resulting performance parameters depicted in Figure 7.15. Despite their different range positions, their resolutions are consistent because they have the same size. This feature is not commonly seen in state-of-the-art systems. Adapting the resolution based on target characteristics is an effective strategy to attain the desired performance across various scenarios.

The optimal transmit time of the first Tracking tier 2 pulse is automatically determined by the scheduler following a two-step time shift and shown in Figure 7.17. Initially, the algorithm places the first pulse of the Tracking Tier 2 immediately after the MapSearch pulse. As a result, its echo overlaps with the long MapSearch echo. Given that the target is at a far range, using the SCORE shift to achieve the necessary angular separation between the beams is infeasible. Thus, temporal orthogonality is employed in this situation. The scheduler adjusts the Tx pulse such that its echo is received after both the MapSearch echo and the next pulse, as elaborated in Section 5.4 and equation (5.44). The timings for the new pulse and echo are then recalculated and compared against the pulses and echoes from other modes. Notably, the initial time shift leads to an overlap between the newly adjusted echo and the Tx pulse of Tracking tier 1. Consequently, a second time-shift is automatically initiated to distinguish the two events.

At $t = 50\,\mathrm{s}$, two targets, $N_{\mathrm{t}} = 2$, are detected at the same time within the same CPI at different range locations. Their incident angles $\theta_{\mathrm{e}3} = 32^\circ$ and $\theta_{\mathrm{e}4} = 56^\circ$ satisfy the angular separation condition (6.28). Consequently, the dynamic processor activates both transmit channels, thereby, generating simultaneous beams each pointing to one target. The time assignment model, described in Section 6.2.2, checks the free time margin T_{free} described in (6.19) and the feasibility of adding new pulses (6.20).

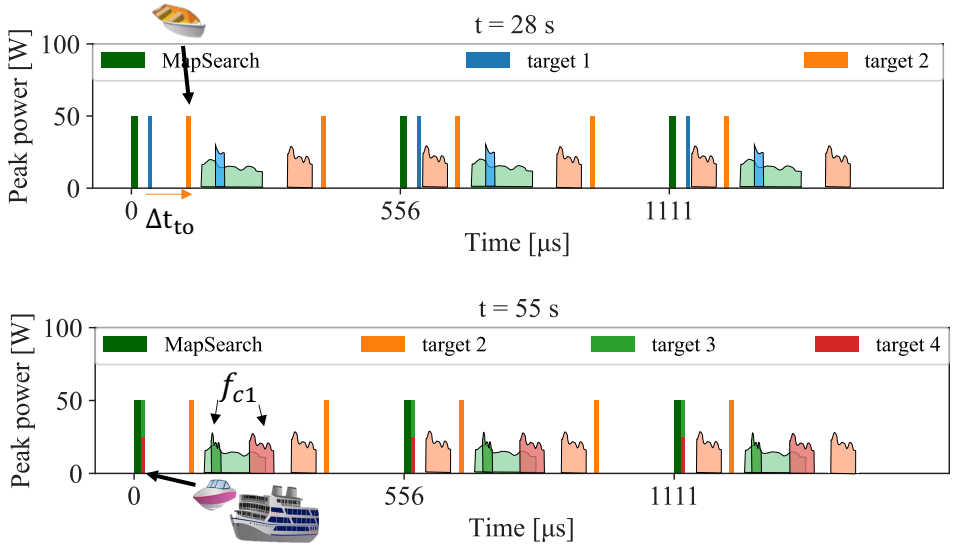

Figure 7.17: Simulated schedule snapshot of the transmit pulses and echoes versus time of the interleaved MapSearch and Tracking tiers 1,2,3, and 4 at $t = 28\,\mathrm{s}$ and $t = 55\,\mathrm{s}$.

For this specific case, there is enough time to send two individual pulses. However, activating two Tx channels here keeps a time margin for possible new future targets. The ideal vectors $Z_3^\star$ and $Z_4^\star$, as well as the priority vectors W_3 and W_4 are updated according to scenario C, described in Section 6.4.4 and given in Table 6.3. As a result of this dynamic optimization, only half of the peak power is designated for this pair of targets. The pulse duration and PRF are forced to be equal for both simultaneous Tracking tiers 3 and 4, as shown in Figure 7.14. Targets 3 and 4 have different sizes, which justifies their different resulting spatial resolutions. A higher bandwidth and a longer SAR dwell time are used for target 3 compared to target 4. Their acquisitions start at $t = 55\,\mathrm{s}$, as depicted in Figure 7.17. The scheduler decided to transmit the two-beam pulse immediately following the MapSearch pulse. Two echoes with different timings and durations corresponding to the two targets will be received simultaneously as the MapSearch echo. These echoes can potentially overlap with the transmit pulse of the ongoing Tracking tier 2 if a time shift orthogonality is applied. Therefore, frequency orthogonality was prioritized by the scheduler to resolve the time overlap between the two new echoes and the MapSearch echo. Given that the MapSearch mode operates with a bandwidth of only $B^{\mathrm{M}} = 20\,\mathrm{MHz}$ and the bandwidths of Tracking tiers 3 and 4, as determined by the dynamic optimizer, are $B^{\mathrm{T3}} = 250\,\mathrm{MHz}$ and $B^{\mathrm{T4}} = 43\,\mathrm{MHz}$ respectively, the frequency diversity conditions (5.60) and (5.59) are satisfied. Consequently, the new Tracking tiers are transmitted with a shifted center frequency of $f_{c1} = 9.79\,\mathrm{MHz}$, as described in Section 5.6.

Target 5 is located in mid-range and is moving slowly. Therefore, the optimizer follows the resource management scenario here and sets the PRF to the minimum value of 900 Hz. The sensor starts imaging target 5 at $t = 65\,\mathrm{s}$ with high resolution

following its small size, leading to longer SAR dwell time and higher bandwidth than the previous Tracking tier, as shown in Figure 7.14. As depicted in the schedule

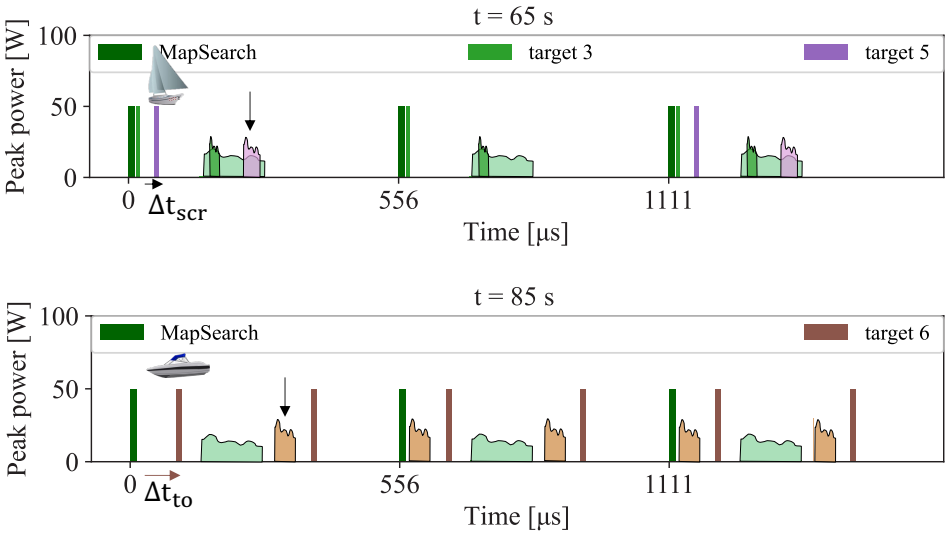

Figure 7.18: Simulated schedule snapshot of the transmit pulses and echoes versus time of the interleaved MapSearch and Tracking tiers 3,5, and 6 at $t = 65\,\mathrm{s}$ and $t = 85\,\mathrm{s}$.

of Figure 7.18, the corresponding pulse is sent with a SCORE shift to receive its echo from a different direction of arrival than the MapSearch echo return arriving simultaneously. DBF is therefore used for this Tracking tier.

The next target 6 is a small boat located at a far range. It is a fast-moving target, which needs to be observed with high accuracy. A high PRF is required to verify the Doppler shift obtained from MapSearch and expand the visible velocities. Therefore, scenario D, which is described in Section 6.4.4 and Table 6.4, is now applied. The corresponding weighting vector W_6 and ideal vector $Z_6^\star$ force the maximum Tracking PRF of 3600 Hz, as shown in Figure 7.14. A large bandwidth is selected to achieve a fine resolution. Tracking tier 6 starts at $t = 85\,\mathrm{s}$ while all previous tiers have concluded, as illustrated in Figure 7.18. The scheduler utilizes temporal orthogonality to prevent overlap with the MapSearch echo, as the target is at a far range and there is enough time available for additional pulses and echoes. The transmit time of the first pulse of Tracking tier 6 is therefore shifted.

The next detection at $t = 90\,\mathrm{s}$ consists of a large ship in near range, which typically does not require high transmit energy or a fine resolution. Besides, it is also moving slowly. For Tracking tier $k = 7$, a PRF of 900 Hz is therefore selected by the dynamic optimizer with a low pulse duration of $t = 2\,\mu\mathrm{s}$ for a duty cycle of 0.2%. Although

the smallest PRF is used for a target in near range, the nadir echo does not overlap with the Tracking echo for such a small duty cycle, which is why a higher PRF was not imposed by the model as initially expected by the PRF forcing described in Section 6.2.2. The schedule for Tracking tier 7 is shown in Figure 7.19. As the

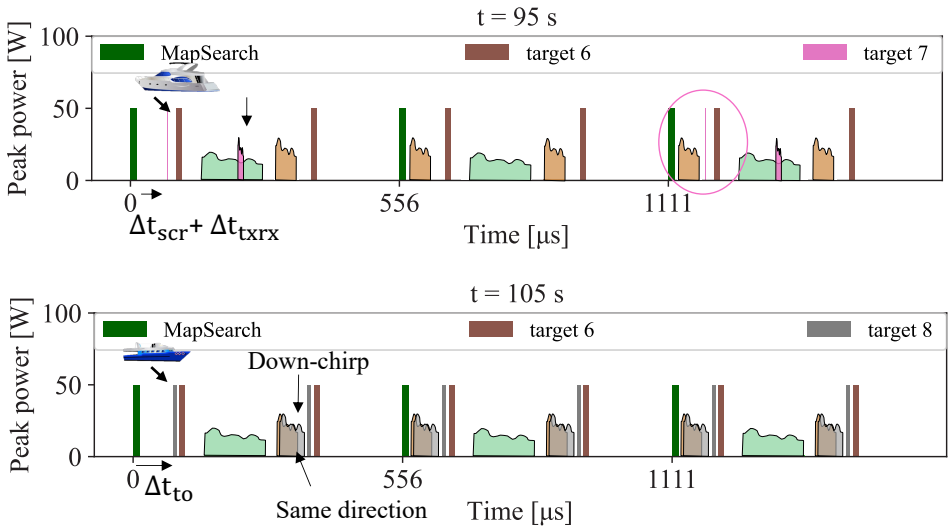

Figure 7.19: Simulated schedule snapshot of the transmit pulses and echoes versus time of the interleaved MapSearch and Tracking tiers 6,7, and 8 at $t = 95\,\mathrm{s}$ and $t = 105\,\mathrm{s}$.

target is in near range, a SCORE time shift is first applied to have the angular orthogonality with the MapSearch. Then an additional time shift is performed to avoid the overlap with the echo of tier 6, highlighted by the circle.

The last Tracking tier, $k = 8$, is initiated at $t = 105\,\mathrm{s}$ for a fast-moving target at a far range, larger than target 6. Consequently, a high Tracking PRF is selected by the optimizer, adhering to the same principle as tier 6. As the new target has a larger RCS compared to target 6, the new acquisition operates with a reduced duty cycle and, hence, a shorter pulse duration, as illustrated in Figure 7.14. Because the target is at a far range, the optimal scheduling for this Tracking tier involves shifting the first pulse to achieve temporal orthogonality with the MapSearch echo. However, this causes a temporal echo overlap with Tracking tier 6, which also originates from a similar range direction, as illustrated by the schedule in Figure 7.19. Thus, an alternative form of orthogonality is required. Given that Tracking tier 6 already operates with a large bandwidth, which limits frequency diversity, the scheduler prioritizes waveform orthogonality. Therefore, the Tracking tier 8 is operated with a down-chirp.

Simulation Summary

A key insight from the automated scheduling reveals that interleaving a distant-range target cannot rely on SCORE angular orthogonality for the MapSearch echo. An alternative form of orthogonality is necessary. The resulting SCNR for a CPI and NESZ throughout the SAR dwell time aligns with the desired values outlined in Table 7.4, and these values remain consistent across all scenarios. This underscores the objective of optimization and the essence of resource management, which employs only what is necessary. In contrast, a fixed radar configuration yields varying signal ratios based on target location and properties. In certain instances, these ratios can either surpass or fall short of the requirements. By leveraging a priori knowledge about the targets and the scene, these deviations can be avoided, ensuring that the performance is intelligently regulated to consistently achieve the same signal level.

Throughout the flight, the number of active Tracking tiers is constantly updated according to their acquisition start times and dwell durations. Figure 7.20 illustrates the timeline of the entire operation featuring the start and end times of each Tracking tier. The MapSearch mode runs continuously during the flight, while the Tracking tiers are variable. By the time Tracking tiers 3 and 4 start, Tracking tier 1 has already concluded. This sequencing is based on the SAR dwell time associated with each acquisition and selected by the dynamic decision-maker.

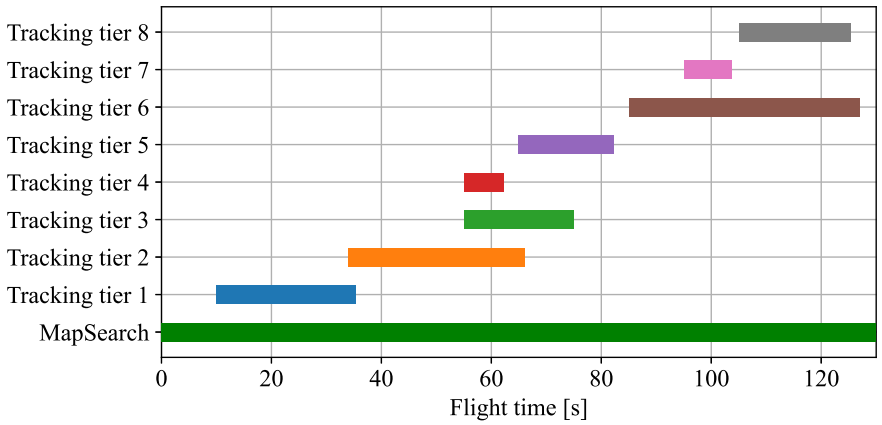

Figure 7.20: Simulated timeline illustrating the start time and duration of MapSearch and all Tracking acquisitions.

Each Tracking tier has a distinct pulse duration and PRF. This is illustrated in the simulated timing diagram of Figure 7.21, where receive events are depicted alongside the corresponding nadir and transmit events The overlap between the

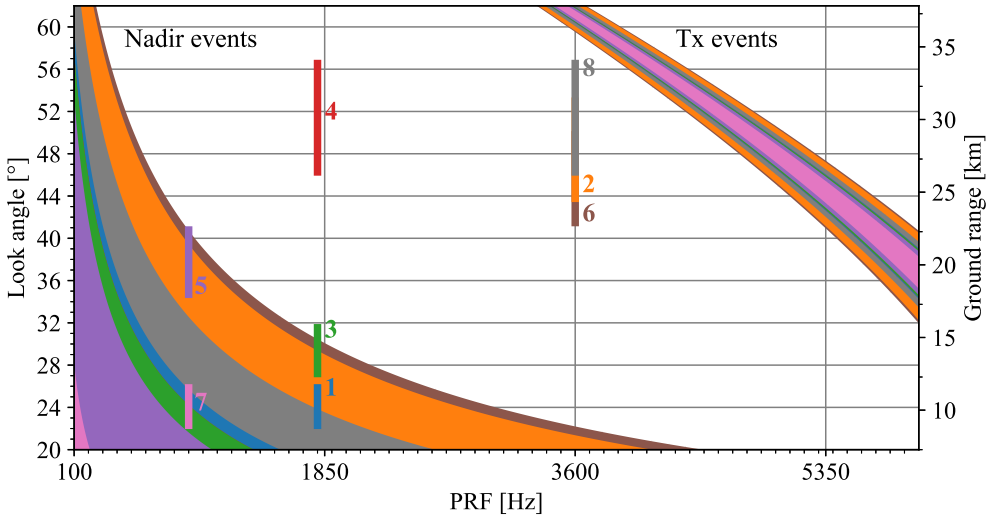

Figure 7.21: Timing diagram showing the transmit (upper right strips), nadir (lower left strips), and receive (vertical lines) events for all Tracking tiers. Each tier is represented by one color (consistent with that of the previous plots).

receive windows of some Tracking tiers with the nadir echoes of other tiers is not an issue in this concept, since waveform diversity or frequency orthogonality is used for those specific targets such as Tracking tier 3 or the relevant tiers are not operated at the same time[1].

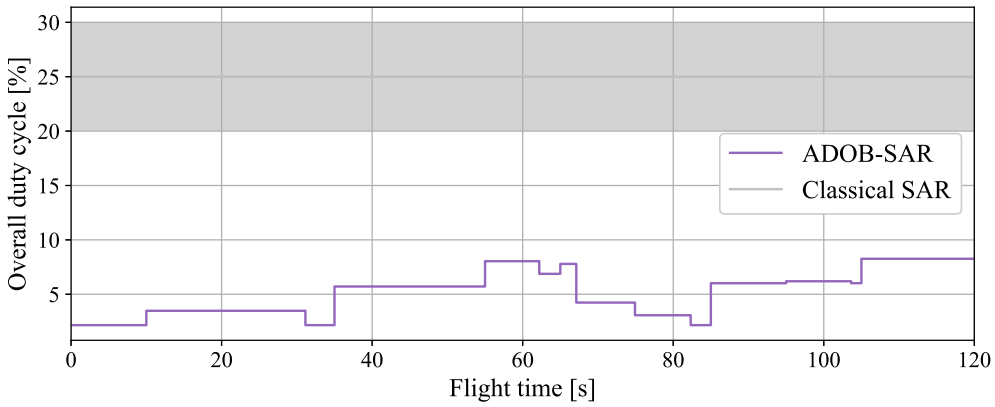

Figure 7.22: The total duty cycle of the simulated scenario over time with ADOB-SAR compared to a classical HAP SAR system operating at approximately 20 – 30%.

[1] It is worth noting that the timing diagram is not suitable to represent this level of complex beamforming and orthogonality conditions [116, 238, 239]

Compared to traditional SAR operations with fixed parameters and longer pulse durations, the ADOB-SAR system can use a reduced duty cycle thanks to its dynamic decision-making and efficient resource management, as shown in Figure 7.22. The overall duty cycle, determined by the sum of all active Tracking tiers, changes over time based on the number of tiers and their instrument parameters. When no targets are detected, the sensor operates at the minimal MapSearch duty cycle until it identifies targets of interest. A lower duty cycle enables longer flights and extended observation of the region of interest.

Reducing the downlink data rate represents a key advantage in the ADOB-SAR concept, as only the Tracking data are relevant and downlinked. It varies over time depending on the amount of information acquired, which is influenced by the Tracking instrument parameters of the different operating tiers. For the simulated scenario, the total data rate over time is plotted in Figure 7.23 based on the expression (2.18). To compare it with a classical SAR operation, the data rate of a typical HAP system is determined by using the highest bandwidth obtained in the ADOB-SAR simulation, 350 MHz specifically in Tracking tier $k = 1$. This ensures both systems can achieve the finest resolution for the same scenario. The data rate

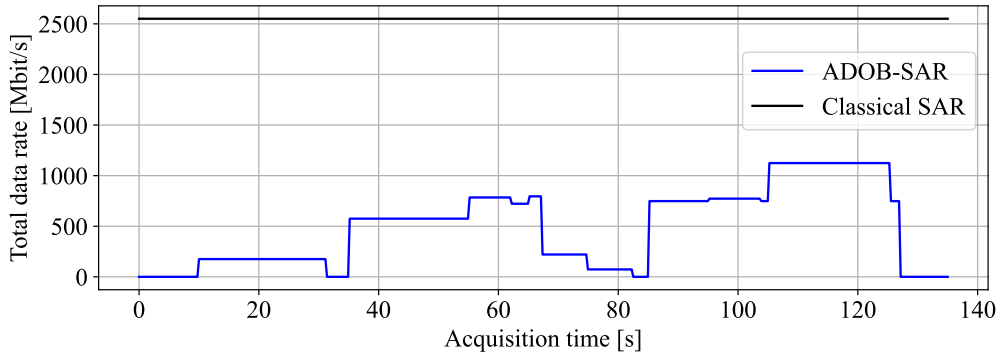

Figure 7.23: The total data rate of the simulated scenario over time with ADOB-SAR in comparison with a classical HAP SAR system operating with a bandwidth of 350 MHz considering 8 bits/sample.

of the ADOB-SAR system is significantly lower than that of classical systems and can even be zero when no Tracking tiers are in operation, which is the main feature of this intelligent system. The adaptive observation concept represents a significant advancement in minimizing the data volume in modern SAR systems. However, this comes at the cost of requiring more advanced on-board pre-processing capabilities.

8 Conclusions and Outlook

As the demand for high-resolution imaging and wide coverage of the Earth increases, innovative SAR technologies and advanced data processing techniques have been continuously emerging during the last few decades. However, current SAR systems still rely on predetermined settings without adapting their illumination to a priori information extracted from the scene, thus limiting their ability to optimize observations and minimize resources. The Earth's diverse and changing components can be effectively monitored by adapting the SAR observation during the operation based on real-time information extracted from the measured data. For instance, a forest and a lake have distinct backscattering properties, thus necessitating different imaging approaches. Current radar imaging systems are, at best, capable of generating near real-time images, but they are unable to use the sensed information to adjust the acquisition parameters.

SAR is a sensor that observes the environment and shares the same goal as a visual brain. Therefore, the core of the underlying work is to apply cognitive capabilities, inspired by human cognition, to improve performance and resource allocation. The innovative sensor is referred to as *Adaptive Observing Synthetic Aperture Radar* (ADOB-SAR). This thesis presents a step in transforming SAR into an intelligent system capable of using its acquired data to optimize performance by efficiently managing available resources. Instead of mapping a large area with the highest possible resolution (creating huge data volumes of little useful information), an intelligent ADOB-SAR sensor will focus on specific regions and scenarios of interest as requested by the user. The thesis details an instrument design and the underlying processes capable of adapting the observation in real-time utilizing an optimum acquisition mode to maximize the desired information at minimal resource consumption. The conception of the innovative ADOB-SAR system is for a high-altitude platform allowing for persistent monitoring over a long period. A dedicated continuous MapSearch mode is designed to observe the area in the flight direction of the platform while operating at minimal resources. It acquires low-resolution information utilized as a priori knowledge for the highly scene-optimized concurrent Tracking mode adapted for each target and scenario, employing intelligent resource management and a multifunctional timing operation. A new imaging technique, *Follow Spot* SAR directs the transmit beam toward areas of high interest throughout the flight while forming the required synthetic aperture dwell time to achieve an extremely high resolution. The MapSearch mode is also used to estimate the clutter statistics through a brief analysis of the real scene conditions, making it possible to

adjust the observation, such as activating more than two digital azimuth channels for clutter suppression.

To achieve this level of multi-mode operation flexibility, a reconfigurable SAR instrument is designed, which can handle both concurrent acquisition modes. It is based on a phased array front-end architecture with digital beamforming (DBF) of minimal cost and complexity capable of forming and steering the beam in 2-D during transmission and reception and adjusting the channel distribution between the different modes. The concept includes hybrid digital beamforming with multiple transmit and receive antenna beams capable of simultaneously imaging multiple targets/scenes at different positions. A considerable system-level design effort was put into designing a compact antenna system and reducing the number of transmit-receive cores and digital channels yielding a "simple" yet high-performance instrument; this is particularly significance for instruments installed on a future HAP, where the challenges of payload size and weight limitations are substantial.

The ADOB-SAR concept adheres to the principle of progressing from uncertainty to certainty. The probability of false alarms can be increased in MapSearch mode to reduce instrument resources, as false targets will be recognized and dropped during the Tracking mode. Ambiguous velocities resulting from operating with a low PRF are acceptable during MapSearch, as moving targets will be accurately observed using a higher PRF during the adaptive Tracking. Even targets that appear displaced during Mapsearch can be accurately observed during Tracking, as the system can iteratively adjust the beams and refocus them toward the correct position. Special techniques are used to avoid blind velocities and target fluctuations during MapSearch, including multi-looking based on bursts, each operating with a different center frequency or PRF. These techniques help obtain diverse backscattered information about the same area on the ground, allowing the required detection performance to be achieved without increasing the transmitted power. Thus, the designed sensor can solve operation challenges by fully leveraging the system's inherent capabilities, rather than expanding them.

To operate the multiple modes concurrently with the same SAR sensor, an adaptive scheduling algorithm is implemented. Each detected target of interest is assigned to a dedicated Tracking mode tier, specifically adapted to its extracted properties. The derived pulse-to-pulse interleaving strategy utilizes the idle window between transmitted pulses and their return echoes to add more pulses for more Tracking mode tiers. It carefully selects the PRF of each mode to prevent any pulse overlap. The implemented adaptive resource manager ensures that the increase in the number of concurrent acquisitions does not degrade the tracking of existing targets. The implemented ingenious scheduling strategy considers all dynamic operating conditions and modes' timing to automatically select the optimum parameters (pulse transmit time, bandwidth, duration, PRF, etc.) of any new Tracking acquisition. The capability to decrease the MapSearch PRF depending on the number of active

Tracking tiers offers more timing flexibility in scheduling. An innovative feature of ADOB-SAR is its ability to change the instrument settings to utilize orthogonality (temporal, waveform, frequency, and spatial), which resolves potential multi-mode echo overlapping. This includes temporal orthogonality, which prevents overlap between different echoes, and angular orthogonality, which utilizes DBF including SCORE to separate overlapped echoes in space. The thesis details how the ADOB-SAR system can smartly adjust to complex target scenarios using combinations of these techniques.

A novel adaptive decision-making algorithm is developed and implemented to coordinate all the innovative features and techniques of the ADOB-SAR instrument. The algorithm selects the optimal SAR operational parameters and beam combinations according to the extracted scene properties and the desired performance. Smart decision rules and fast dynamic scenario-dependent optimization techniques are utilized. The developed algorithm dynamically adjusts the transmitted energy based on the target range and RCS, ensuring consistent backscattered energy. It also adapts the spatial resolution depending on the target size, thereby optimizing resource management and freeing time and signal bandwidth to concurrently image other targets. An adaptive multi-objective function is derived, which selects the optimal peak power, PRF, bandwidth, pulse duration, dwell time, and number of pulses for each new Tracking acquisition. This function uses the scene properties extracted from MapSearch as input and the desired performance as constraints. The innovation here involves transforming the classical optimization problem into a dynamic function by adjusting the objectives' priorities, the ideal vector, and the parameter bounds according to the scenario. Adaptive multi-target forcing models are therefore derived, which assign beams to new targets, schedule pulses, and impose new bounds on instrument parameters based on time and hardware constraints while considering the overall acquisition schedule. This approach guarantees an optimal selection of the new configuration by considering all the dynamic scenario conditions that influence the decision.

An ADOB-SAR reference system for a maritime monitoring application has been designed and analyzed, including all instrument parameters and antenna specifications. A DECISION simulator, which integrates all the ADOB-SAR models and algorithms, has been developed and implemented (in Python). This simulator effectively combines dynamic optimization, adaptive scheduling, and decision-making processes to validate various scenarios and configurations. It was used as a proof of concept, taking a maritime scenario with simulated targets and the instrument specifications as input and providing the optimal SAR operational parameters and schedule over time as output.

It was demonstrated that the proposed ADOB-SAR system can operate with a lower duty cycle compared to state-of-the-art systems, consequently saving energy and extending flight time. Furthermore, it provides extensive coverage while reducing data

as only the relevant regions are saved and downlinked. The capability to match the operational parameters to the target and scene properties implied a simpler post-processing, as the registered data is considered optimal and does not require sophisticated post-processing algorithms. The control models are highly adjustable and can be easily reconfigured and adjusted to meet new user requirements. Although the design was initially intended for a maritime application, the simulator and all its algorithms can also be applied to other applications, including deserts or mountains. This versatility is a key feature of this underlying work.

Proofing the concept with real-world data remains challenging due to the limitations of the existing SAR sensors. These systems are not capable of providing flexibility in changing operational instrument parameters during the same acquisition or utilizing different transmit and receive beamforming and steering in all directions. Given these constraints, it becomes imperative to invest in developing advanced prototypes of intelligent SAR systems capable of utilizing the ADOB-SAR features. Potential platforms could be DLR's HAPSAR or Dronar [62, 240, 241], which are under development. Such a prototype would not only facilitate comprehensive testing of novel features through experiments but would also pave the way to establish a new domain of cognitive sensing.

A high potential exists to enhance the ADOB-SAR decision-making processor through the integration of Machine Learning (ML) techniques and the incorporation of memory capabilities. This can be applied to the selection of the ideal parameter and the priority weight vectors within the dynamic optimization model. ML algorithms are capable of using a trained model of previous operations to interpolate and predict new undefined scenarios or combinations of various rule-based scenarios. As radar scenarios evolve with time, the ML model can be updated using a feedback loop after using the determined weights and ideal vector in the final optimization function. This represents a compelling area for future research. Besides, the simulator has the potential to be further expanded to include ML-based onboard MapSearch detection algorithms to allow for faster onboard pre-processing and real-time extraction of scene properties. ML can also accelerate decision-making by bypassing the optimization process and instead using optimal instrument parameters determined from experience and learning. Future research could also explore the potential of quantum computing to enhance the onboard pe-processing capabilities and reduce complexity. The foundational mathematical models developed in this doctoral thesis are crucial for a dynamic sensor adaptation and serve as the essential basis for any future work involving the integration of ML techniques. The underlying work showcases the potential to transform SAR sensors into more autonomous, intelligent, and adaptable sensing solutions.

Bibliography

[1] L. Brown, *Technical and Military Imperatives: A Radar History of World War II.* CRC Press, 1999.

[2] J. Z. Buchwald, *The Creation of Scientific Effects: Heinrich Hertz and Electric Waves.* University of Chicago Press, 1994.

[3] C. Hülsmeyer, " Verfahren, um entfernte metallische gegenstände mittels elektrischer wellen einem beobachter zu melden," DE Patent 165 546, Apr., 1904.

[4] G. W. Stimson, *Introduction to Airborne Radar*, ser. Radar, Sonar and Navigation. Institution of Engineering and Technology, 1998.

[5] M. L. Merritt, *Introduction to Modern Traffic Flow Theory and Control: The Long Road to Three-Phase Traffic Theory.* Boston, MA: American Meteorological Society, 2015.

[6] J. D. Luse, "A Brief History of the Use of Marine Radar," *NAVIGATION: Journal of The Institute of Navigation*, vol. 28, no. 3, pp. 199–205, 1981.

[7] R. Lyons, *Understanding Digital Signal Processing*, 3rd ed. Prentice Hall Pearson Education, 2010.

[8] V. Tuzlukov, *Signal Processing in Radar Systems.* CRC Press, 2012.

[9] V. K. Madisetti and D. B. Williams, Eds., *The Digital Signal Processing Handbook.* CRC Press, 1997.

[10] J. Chitode, *Digital Signal Processing*, 1st ed. Pune: Technical Publications, 2009.

[11] C. A. Wiley, "Pulsed Doppler Radar Methods and Apparatus," U.S. Patent 3 196 436, Aug., 1954.

[12] T. Thompson and A. Laderman, "SEASAT-A Synthetic Aperture Radar: Radar System Implementation," in *OCEANS*, Washington, DC, 1976, pp. 247–251.

[13] A. Moreira, "A Golden Age for Spaceborne SAR Systems," in *20th International Conference on Microwaves, Radar and Wireless Communications (MIKON)*, Gdansk, Poland, June 2014, pp. 1–4.

[14] R. Werninghaus and S. Buckreuss, "The TerraSAR-X Mission and System Design," *IEEE Transactions on Geoscience and Remote Sensing*, vol. 48, no. 2, pp. 606–614, 2010.

[15] A. Roth, M. Eineder, and B. Schättler, "TerraSAR-X: A New Perspective for Applications Requiring High Resolution Spaceborne SAR Data," in *Joint ISPRS and EARSeL Workshop on High Resolution Mapping from Space*, Hannover, Jan 2003.

[16] S. Buckreuss and M. Zink, "The Missions TerraSAR-X and TanDEM-X: Status, Challenges, Future Perspectives," in *URSI General Assembly and Scientific Symposium*, Istanbul, 2011.

[17] P. Potin, O. Colin, M. Pinheiro, B. Rosich, A. O'Connell, T. Ormston, J.-B. Gratadour, and R. Torres, "Status And Evolution Of The Sentinel-1 Mission," in *IEEE International Geoscience and Remote Sensing Symposium*, Kuala Lumpur, 2022, pp. 4707–4710.

[18] Y. Kankaku, S. Suzuki, and Y. Osawa, "ALOS-2 Mission and Development Status," in *IEEE International Geoscience and Remote Sensing Symposium*, Melbourne, 2013, pp. 2396–2399.

[19] K. Tomiyasu, "Conceptual Performance of a Satellite Borne, Wide Swath Synthetic Aperture Radar," *IEEE Transactions on Geoscience and Remote Sensing*, vol. GE-19, no. 2, pp. 108–116, Apr 1981.

[20] M. Süss and W. Wiesbeck, "Side Looking SAR System," U.S. Patent 6 870 500, Mar. 22, 2005.

[21] M. Suess, B. Grafmueller, and R. Zahn, "A Novel High Resolution, Wide Swath SAR System," in *IEEE International Geoscience and Remote Sensing Symposium*, Sydney, July 2001, pp. 1013–1015.

[22] N. Goodman, D. Rajakrishna, and J. Stiles, "Wide Swath, High Resolution SAR using Multiple Receive Apertures," in *IEEE International Geoscience and Remote Sensing Symposium*, Hamburg, July 1999, pp. 1767–1769.

[23] M. Younis, C. Fischer, and W. Wiesbeck, "Digital Beamforming in SAR Systems," *IEEE Transactions on Geoscience and Remote Sensing*, vol. 41, no. 7, pp. 1735–1739, 2003.

[24] H. Wang, H. Zhang, S. Dai, and Z. Sun, "Azimuth Multichannel GMTI Based on Ka-Band DBF-SCORE SAR System," *IEEE Geoscience and Remote Sensing Letters*, vol. 15, no. Mar, pp. 419–423, March 2018.

[25] M. Suess, M. Ludwig, C. Schaefer, and M. Younis, "Technology Developments for the Next Generation of Spaceborne SAR Instruments Based on Digital Beamforming," in *IEEE International Geoscience and Remote Sensing Symposium*, Munich, July 2012, pp. 1529–1532.

[26] A. Moreira and G. Krieger, "Spaceborne Synthetic Aperture Radar (SAR) Systems: State of the Art and Future Developments," in *33rd European Microwave Conference*, Munich, 2003, pp. 101–104.

[27] F. Bordoni, M. Younis, and G. Krieger, "Ambiguity Suppression by Azimuth Phase Coding in Multichannel SAR Systems," *IEEE Transactions on Geoscience and Remote Sensing*, vol. 50, no. 2, pp. 617–629, 2012.

[28] T. K. Sjoegren, V. T. Vu, M. I. Pettersson, F. Wang, D. J. G. Murdin, A. Gustavsson, and L. M. H. Ulander, "Suppression of Clutter in Multichannel SAR GMTI," *IEEE Transactions on Geoscience and Remote Sensing*, vol. 52, no. 7, pp. 4005–4013, 2014.

[29] N. Gebert, G. Krieger, and A. Moreira, "Digital Beamforming on Receive: Techniques and Optimization Strategies for High-Resolution Wide-Swath SAR Imaging," *IEEE Transactions on Aerospace and Electronic Systems*, vol. 45, no. 2, pp. 564–592, 2009.

[30] G.-C. Sun, M. Xing, X.-G. Xia, Y. Wu, P. Huang, Y. Wu, and Z. Bao, "Multichannel Full-Aperture Azimuth Processing for Beam Steering SAR," *IEEE Transactions on Geoscience and Remote Sensing*, vol. 51, no. 9, pp. 4761–4778, 2013.

[31] C. Topping, A. Ahmed, W. Sullivan, C. Schaefer, and M. Ludwig, "An Active Scan-on-Receive Digital Beam Forming Unit for Synthetic Aperture Radar." in *Advanced RF Sensors and Remote Sensing Instruments*, Noordwijk, Nov 2009.

[32] H. M. Finn, "Adaptive Detection Mode with Threshold Control as a Function of Spatially Sampled Clutter-Level Estimates," *RCA Review*, vol. 29, no. 3, pp. 414–465, 1968.

[33] J. T. Rickard and G. M. Dillard, "Adaptive Detection Algorithms for Multiple-Target Situations," *IEEE Transactions on Aerospace and Electronic Systems*, vol. AES-13, no. 4, pp. 338–343, 1977.

[34] L. Brennan and L. Reed, "Theory of Adaptive Radar," *IEEE Transactions on Aerospace and Electronic Systems*, vol. AES-9, no. 2, pp. 237–252, 1973.

[35] G. van Keuk and S. Blackman, "On Phased-Array Radar Tracking and Parameter Control," *IEEE Transactions on Aerospace and Electronic Systems*, vol. 29, no. 1, pp. 186–194, 1993.

[36] S. Applebaum, "Adaptive Arrays," *IEEE Transactions on Antennas and Propagation*, vol. 24, no. 5, pp. 585–598, 1976.

[37] B. Widrow, P. Mantey, L. Griffiths, and B. Goode, "Adaptive Antenna Systems," *Proceedings of the IEEE*, vol. 55, no. 12, pp. 2143–2159, 1967.

[38] A. Farina, *Antenna-Based Signal Processing Techniques for Radar Systems*, ser. Artech House Antenna Library. Artech House, 1992.

[39] H. Shi, L. Li, C. Wang, H. Xia, and X. Liu, "Research on Moving Target Detection of Spaceborne SAR Based on STAP and CS Algorithm," in *29th Chinese Control And Decision Conference (CCDC)*, Chongqing, China, May 2017, pp. 7812–7816.

[40] W. Melvin, "A STAP Overview," *IEEE Aerospace and Electronic Systems Magazine*, vol. 19, no. 1, pp. 19–35, 2004.

[41] J. Ward, "Space-Time Adaptive Processing for Airborne Radar," in *International Conference on Acoustics, Speech, and Signal Processing*, vol. 5, Detroit, MI, USA, 1995, pp. 2809–2812.

[42] J. R. Guerci, *Space-Time Adaptive Processing for Radar*. Artech House, 2015.

[43] H. D. Griffiths and P. Mancini, "Ambiguity Suppression In SARs Using Adaptive Array Techniques," *Proceedings of the 11th Annual International Geoscience and Remote Sensing Symposium*, vol. 2, pp. 1015–1018, June 1991.

[44] S. DeGraaf, "Sidelobe Reduction via Adaptive FIR Filtering in SAR Imagery," *IEEE Transactions on Image Processing*, vol. 3, no. 3, pp. 292–301, 1994.

[45] S. Barbarossa and G. Levrini, "An Antenna Pattern Synthesis Technique for Spaceborne SAR Performance Optimization," *IEEE Transactions on Geoscience and Remote Sensing*, vol. 29, no. 2, pp. 254–259, 1991.

[46] P. Kelly, H. Derin, and K. Hartt, "Adaptive Segmentation of Speckled Images using a Hierarchical Random Field Model," *IEEE Transactions on Acoustics, Speech, and Signal Processing*, vol. 36, no. 10, pp. 1628–1641, 1988.

[47] J. Li and P. Stoica, "An Adaptive Filtering Approach to Spectral Estimation and SAR Imaging," *IEEE Transactions on Signal Processing*, vol. 44, no. 6, pp. 1469–1484, 1996.

[48] S. Haykin, "Radar Vision," in *IEEE International Conference on Radar*, Arlington, Virginia, USA, May 1990, pp. 585–588.

[49] S. Haykin, Y. Xue, and P. Setoodeh, "Cognitive Radar: Step Toward Bridging the Gap Between Neuroscience and Engineering," *Proceedings of the IEEE*, vol. 100, no. 11, pp. 3102–3130, Nov 2012.

[50] S. Haykin, *Cognitive Dynamic Systems: Perception-Action Cycle, Radar and Radio*. Cambridge University Press, 2012.

[51] M. S. Greco, F. Gini, P. Stinco, and K. Bell, "Cognitive Radars: On the Road to Reality: Progress Thus Far and Possibilities for the Future," *IEEE Signal Processing Magazine*, vol. 35, no. 4, pp. 112–125, July 2018.

[52] S. Gurbuz, H. Griffiths, A. Charlish, M. Rangaswamy, M. Greco, and K. Bell, "An Overview of Cognitive Radar: Past, Present, and Future," *IEEE Aerospace and Electronic Systems Magazine*, vol. 34, pp. 6–18, 12 2019.

[53] S. D. Blunt and E. L. Mokole, "Overview of Radar Waveform Diversity," *IEEE Aerospace and Electronic Systems Magazine*, vol. 31, no. 11, pp. 2–42, 2016.

[54] N. A. Goodman, P. R. Venkata, and M. A. Neifeld, "Adaptive Waveform Design and Sequential Hypothesis Testing for Target Recognition with Active Sensors," *IEEE Journal of Selected Topics in Signal Processing*, vol. 1, no. 1, pp. 105–113, 2007.

[55] D. Kershaw and R. Evans, "Optimal Waveform Selection for Tracking Systems," *IEEE Transactions on Information Theory*, vol. 40, no. 5, pp. 1536–1550, 1994.

[56] G. Krieger, N. Gebert, M. Younis, and A. Moreira, "Advanced Synthetic Aperture Radar Based on Digital Beamforming and Waveform Diversity," in *IEEE Radar Conference*, Rome, Italy, May 2008, pp. 1–6.

[57] A. Aubry, A. DeMaio, A. Farina, and M. Wicks, "Knowledge-Aided (Potentially Cognitive) Transmit Signal and Receive Filter Design in Signal-Dependent Clutter," *IEEE Transactions on Aerospace and Electronic Systems*, vol. 49, no. 1, pp. 93–117, 2013.

[58] J. R. Guerci, "Cognitive Radar: A Knowledge-Aided Fully Adaptive Approach," in *IEEE Radar Conference*, Arlington, VA, USA, May 2010, pp. 1365–1370.

[59] W. Melvin and J. Guerci, "Knowledge-Aided Signal Processing: a New Paradigm for Radar and other Advanced Sensors," *IEEE Transactions on Aerospace and Electronic Systems*, vol. 42, no. 3, pp. 983–996, 2006.

[60] W. Melvin and G. Showman, "An Approach to Knowledge-Aided Covariance Estimation," *IEEE Transactions on Aerospace and Electronic Systems*, vol. 42, no. 3, pp. 1021–1042, 2006.

[61] A. E. Mitchell, J. L. Garry, A. J. Duly, G. E. Smith, K. L. Bell, and M. Rangaswamy, "Fully Adaptive Radar for Variable Resolution Imaging," *IEEE Transactions on Geoscience and Remote Sensing*, vol. 57, no. 12, pp. 9810–9819, 2019.

[62] M. Jirousek, M. Peichl, S. Anger, S. Dill, and M. Engel, "Design of a Synthetic Aperture Radar Instrument for a High-Altitude Platform," in *IEEE International Geoscience and Remote Sensing Symposium*, Pasadena, CA, USA, July 2023, pp. 2045–2048.

[63] J. T. Sri Sumantyo, C. M. Yam, C. E. Santosa, A. Takahashi, and K. Ito, "Aircraft and High Altitude Platform System Onboard Circularly Polarized Synthetic Aperture Radar (CP-SAR)," in *IEEE International Geoscience and Remote Sensing Symposium*, July 2021, pp. 8515–8518.

[64] W.-Q. Wang and H. Shao, "High Altitude Platform Multichannel SAR for Wide-Area and Staring Imaging," *IEEE Aerospace and Electronic Systems Magazine*, vol. 29, no. 5, pp. 12–17, 2014.

[65] W. Yang, J. Kai, S. Lei, G. Jia-long, and Z. Qian, "Simulation Analysis and Experimental Results of Slow platform SAR System," in *CIE International Conference on Radar (RADAR)*, Guangzhou, China, Oct 2016, pp. 1–5.

[66] W.-Q. Wang, "Large-Area Remote Sensing in High-Altitude High-Speed Platform Using MIMO SAR," *IEEE Journal of Selected Topics in Applied Earth Observations and Remote Sensing*, vol. 6, no. 5, pp. 2146–2158, 2013.

[67] E. C. Zaugg, A. Margulis, J. P. Bradley, A. H. Kozak, and W. K. Roehrich, "SAR Imaging from Stratospheric Balloons: First Results," in *IEEE Radar Conference (RadarConf)*, Boston, MA, USA, Apr 2019, pp. 1–6.

[68] F. A. D'Oliveira, F. C. L. de Melo, and T. C. Devezas, "High-Altitude Platforms - Present Situation and Technology Trends," *Journal of Aerospace Technology and Management*, vol. 8, no. 3, Aug 2016.

[69] H. Alliance, "Guidlelines for Payload Operation in the Stratosphere," HAPS Alliance, Tech. Rep., Dec 2022.

[70] ——, "Diving the Potential of the Stratosphere," HAPS Alliance, Tech. Rep., Dec 2021.

[71] P. Serrano, M. Gramaglia, F. Mancini, L. Chiaraviglio, and G. Bianchi, "Balloons in the Sky: Unveiling the Characteristics and Trade-Offs of the Google Loon Service," *IEEE Transactions on Mobile Computing*, vol. 22, no. 6, pp. 3165–3178, 2023.

[72] Airbus. Zephyr, The first stratospheric UAS of its kind. [Accessed: 15 Dec 2020]. [Online]. Available: https://www.airbus.com/en/products-services/defence/uas/uas-solutions/zephyr

[73] Stratospheric Platforms. [Accessed: 10 Jan 2021]. [Online]. Available: https://www.stratosphericplatforms.com/

[74] S. H. Technology. Sunglider. [Accessed: 10 Jan 2021]. [Online]. Available: https://www.softbank.jp/en/corp/philosophy/technology/special/ntn-solution/haps/

[75] F. Baurreau, R. Staraj, F. Ferrero, L. Lizzi, J.-M. Ribero, and J.-P. Chessel, "Stratospheric Platform for Telecommunication Missions," in *IEEE International Symposium on Antennas and Propagation & USNC/URSI National Radio Science Meeting*, Vancouver, BC, Canada, July 2015, pp. 914–915.

[76] SCEYE. Stratospheric platforms to improve life on our planet. [Accessed: 10 Jan 2021]. [Online]. Available: https://www.sceye.com/

[77] Stratosyst. SkyRider. [Accessed: 10 Jan 2021]. [Online]. Available: https://www.stratosyst.com/

[78] P. Lobner, "Capgemini Engineering (formerly Altran Aerospace) - Solar Powered Drone Airships," Lynceans, Tech. Rep., Feb 2022.

[79] Y. C. Foo, W. L. Lim, R. Tafazolli, and L. Barclay, "Forward Link Power Control for High Altitude Platform Station W-CDMA System," in *54th IEEE Vehicular Technology Conference*, vol. 2, Atlantic City, NJ, USA, 2001, pp. 625–629.

[80] A. Fikes, E. Gdoutos, M. Klezenberg, A. Ayling, O. Mizrahi, J. Sauder, C. Sommer, A. Truong, A. Wen, A. Wu, R. Madonna, H. Atwater, A. Hajimiri, and S. Pellegrino, "The Caltech Space Solar Power Demonstration One Mission," in *IEEE International Conference on Wireless for Space and Extreme Environments (WiSEE)*, Winnipeg, MB, Canada, Oct 2022, pp. 18–22.

[81] W. C. Brown and E. E. Eves, "Beamed Microwave Power Transmission and its Application to Space," *IEEE Transactions on Microwave Theory and Techniques*, vol. 40, no. 6, pp. 1239–1250, 1992.

[82] K. Tomiyasu, "Tutorial Review of Synthetic-Aperture Radar (SAR) with Applications to Imaging of the Ocean Surface," *Proceedings of the IEEE*, vol. 66, no. 5, pp. 563–583, 1978.

[83] C. Elachi, T. Bicknell, R. Jordan, and C. Wu, "Spaceborne Synthetic-Aperture Imaging Radars: Applications, Techniques, and Technology," *Proceedings of the IEEE*, vol. 70, no. 10, pp. 1174–1209, 1982.

[84] J. R. Klauder, A. C. Price, S. Darlington, and W. J. Albersheim, "The Theory and Design of Chirp Radars," *The Bell System Technical Journal*, vol. 39, no. 4, pp. 745–808, 1960.

[85] M. A. Richards, J. A. Scheer, and W. A. Holm, *Principles of Modern Radar: Basic Principles*. SciTech Publishing, 2010.

[86] M. I. Skolnik, *Radar Handbook*, 3rd ed. McGraw-Hill Professional, 2008.

[87] J. Curlander and R. McDonough, *Synthetic Aperture Radar: Systems and Signal Processing*. New York: Wiley, 1991.

[88] A. Moreira, P. Prats-Iraola, M. Younis, G. Krieger, I. Hajnsek, and K. P. Papathanassiou, "A Tutorial on Synthetic Aperture Radar," *IEEE Geoscience and Remote Sensing Magazine*, vol. 1, no. 1, pp. 6–43, March 2013.

[89] A. Budillon, V. Pascazio, and G. Schirinzi, "Estimation of Radial Velocity of Moving Targets by Along-Track Interferometric SAR Systems," *IEEE Geoscience and Remote Sensing Letters*, vol. 5, no. 3, pp. 349–353, 2008.

[90] I. G. Cumming and F. H. Wong, *Digital Processing of Synthetic Aperture Radar Data*. Artech House, 2004.

[91] A. Flores, K. Herndon, R. Thapa, and E. Cherrington, *The SAR Handbook: Comprehensive Methodologies for Forest Monitoring and Biomass Estimation*. SERVIR Global, 2019.

[92] M. I. Skolnik, *Introduction to Radar Systems*. New York: McGraw-Hill, 1980.

[93] A. Reigber, R. Horn, A. Nottensteiner, P. Prats-Iraola, R. Scheiber, K.-H. Bethke, and S. Baumgartner, "Current Status of DLR's Bew F-SAR Sensor," in *Proceedings of the European Conference on Synthetic Aperture Radar (EUSAR)*, 06 2010, pp. 1078–1081.

[94] D. C. Lancashire, B. A. F. Barnes, and S. J. Udall, "Block Adaptive Quantization ," U.S. Patent US6 255 987B1, Jul. 3, 2001.

[95] R. Kwok and W. Johnson, "Block Adaptive Quantization of Magellan SAR Data," *IEEE Transactions on Geoscience and Remote Sensing*, vol. 27, no. 4, pp. 375–383, 1989.

[96] P. Guccione, M. Scagliola, and D. Giudici, "Principal Components Dynamic Block Quantization for Multichannel SAR," in *IEEE International Geoscience and Remote Sensing Symposium*, Beijing, China, July 2016, pp. 2090–2093.

[97] V. Pascazio and G. Schirinzi, "Synthetic Aperture Radar Imaging by One-Bit Coded Signals," *Electronics and Communication Engineering Journal*, vol. 10, pp. 17–28, February 1998.

[98] G. Schirinzi, "SAR Raw Data Compression Techniques," in *CEOS SAR Workshop*, ser. ESA SP-450, vol. 450, Toulouse, France, Mar 2000, pp. 193–198.

[99] R. J. Mailloux, *Phased Array Antenna Handbook*. Artech House.

[100] C. Balanis, *Antenna Theory: Analysis and Design*, 4th ed. Wiley, 2016.

[101] X. Chen, S. Zhang, and Q. Li, "A Review of Mutual Coupling in MIMO Systems," *IEEE Access*, vol. 6, pp. 24 706–24 719, 2018.

[102] P. J. Kahrilas, *Electronic Scanning Radar Systems (ESRS) Design Handbook*. Artech House, 1976.

[103] E. Brookner, *Practical Phased Array Antenna Systems*. Artech House, 1991.

[104] A. Bhattacharyya, *Phased Array Antennas: Floquet Analysis, Synthesis, BFNs and Active Array Systems*, ser. Wiley Series in Microwave and Optical Engineering. Wiley, 2006.

[105] W.-D. Wirth, *Radar Techniques Using Array Antennas*, ser. Radar, Sonar and Navigation. Institution of Engineering and Technology, 2013.

[106] J. P. Doane, K. E. Kolodziej, and B. T. Perry, "Simultaneous Transmit and Receive with Digital Phased Arrays," in *IEEE International Symposium on Phased Array Systems and Technology (PAST)*, Waltham, MA, USA, Oct 2016, pp. 1–6.

[107] T. Snow, C. Fulton, and W. J. Chappell, "Transmit-Receive Duplexing Using Digital Beamforming System to Cancel Self-Interference," *IEEE Transactions on Microwave Theory and Techniques*, vol. 59, no. 12, pp. 3494–3503, 2011.

[108] C. Fulton, M. Yeary, D. Thompson, J. Lake, and A. Mitchell, "Digital Phased Arrays: Challenges and Opportunities," *Proceedings of the IEEE*, vol. 104, no. 3, pp. 487–503, 2016.

[109] P. Barton, "Digital Beamforming for Radar," *IEE Proceedings F - Communications, Radar and Signal Processing*, vol. 127, no. 4, pp. 266–277, August 1980.

[110] H. Steyskal, "Digital Beamforming," in *18th European Microwave Conference*, Stockholm, Sweden, Sep 1988, pp. 49–57.

[111] M. Younis, F. Q. de Almeida, F. Bordoni, P. López-Dekker, and G. Krieger, "Digital Beamforming Techniques for Multi-channel Synthetic Aperture Radar," in *IEEE International Geoscience and Remote Sensing Symposium (IGARSS)*, Beijing, China, July 2016, pp. 1412–1415.

[112] M. Süss and W. Wiesbeck, "Side Looking Synthetic Aperture Radar System," European Patent 1 241 487 B1, Feb. 8, 2006.

[113] S. Huber, "Spaceborne SAR Systems with Digital Beamforming and Reflector Antenna," Ph.D. dissertation, Karlsruhe Institute for Technology, Germany, Feb 2013.

[114] E. J. Amin, G. Krieger, M. Younis, F. Bordoni, A. B. C. da Silva, and A. Moreira, "A 2-D Range Ambiguity Suppression Method Based on Blind Source Separation for Multichannel SAR Systems," *IEEE Transactions on Geoscience and Remote Sensing*, vol. 62, pp. 1–17, 2024.

[115] G. Krieger, S. Huber, M. Villano, M. Younis, T. Rommel, P. Lopez Dekker, F. Almeida, and A. Moreira, "Cross Elevation Beam Range Ambiguity Suppression (CEBRAS) for High-Resolution Wide-Swath and MIMO-SAR Imaging," in *IEEE International Geoscience and Remote Sensing Symposium IGARSS*, Milan, Italy, July 2015.

[116] M. Younis, F. Q. de Almeida, M. Villano, S. Huber, G. Krieger, and A. Moreira, "Digital Beamforming for Spaceborne Reflector-Based Synthetic Aperture Radar, Part 1: Basic Imaging Modes," *IEEE Geoscience and Remote Sensing Magazine*, vol. 9, no. 3, pp. 8–25, 2021.

[117] M. Younis, T. Rommel, F. Bordoni, G. Krieger, and A. Moreira, "On the Pulse Extension Loss in Digital Beamforming SAR," *IEEE Geoscience and Remote Sensing Letters*, vol. 12, no. 7, pp. 1436–1440, 2015.

[118] H. L. V. Trees, *Optimum Array Processing*. John Wiley & Sons, March 2002.

[119] J.-H. Kim, M. Younis, P. Prats-Iraola, M. Gabele, and G. Krieger, "First Spaceborne Demonstration of Digital Beamforming for Azimuth Ambiguity Suppression," *IEEE Transactions on Geoscience and Remote Sensing*, vol. 51, no. 1, pp. 579–590, 2013.

[120] M. B. A. Currie, "Wide-swath SAR," *IEE Proceedings: Radar and Signal Processing*, vol. 139, pp. 122–135, Apr 1992.

[121] C. Römer, "Side Looking Synthetic Aperture Radar System," European Patent 3 432 027A1, Jan. 23, 2019.

[122] S. Ogurtsov, D. Caratelli, and Z. Song, "A Review of Synthesis Techniques for Phased Antenna Arrays in Wireless Communications and Remote Sensing," *International Journal of Antennas and Propagation Hindawi*, vol. 2021, no. 5514972, pp. 1–19, 2021.

[123] P. A. Molchanov, *Seeing Invisible: Advanced Antenna Arrays*. Aalborg, Denmark: River Publishers, 2024.

[124] S.-P. Chen and H. Schmiedel, *RF Antenna Beam Forming: Focusing and Steering in Near and Far Field*. Springer, 2024.

[125] R. Klemm, U. Nickel, C. Gierull, H. Griffiths, and W. Koch, *Novel Radar Techniques and Applications Volume 1: Real Aperture Array Radar, Imaging Radar, and Passive and Multistatic Radar*, ser. Radar, Sonar and Navigation. Institution of Engineering and Technology, 2017.

[126] S. K. Joshi, "Maritime Moving Target Detection, Tracking and Geocoding Using Range-Compressed Airborne Radar Data," Ph.D. dissertation, Karlsruhe Institute for Technology, Germany, July 2022.

[127] A. Doerry, "Performance Limits for Exo-Clutter Ground Moving Target Indicator (GMTI) Radar," Sandia National Laboratories, Tech. Rep., Sep 2010.

[128] S. K. Joshi and S. V. Baumgartner, "Automatic CFAR Ship Detection in Single-Channel Range-Compressed Airborne Radar Data," in *20th International Radar Symposium (IRS)*, Ulm, Germany, 2019, pp. 1–8.

[129] A. Doerry, "A Study of Pulse-Doppler Radar Pulse Repetition Frequency," Sandia National Laboratories, Tech. Rep. SAND2023-00771, Mar 2023.

[130] J. Simpson, "PRF Set Selection for Pulse-Doppler Radars," in *IEEE Region 5 Conference: Spanning the Peaks of Electrotechnology*, Colorado Springs, CO, USA, Mar 1988, pp. 38–44.

[131] S. V. Baumgartner and G. Krieger, "Fast GMTI Algorithm For Traffic Monitoring Based On A Priori Knowledge," *IEEE Transactions on Geoscience and Remote Sensing*, vol. 50, no. 11, pp. 4626–4641, 2012.

[132] P. Lombardo, "Multichannel SAR," S&I Organization, Tech. Rep. STO-EN-SET-191, Mar 2013.

[133] R. Klemm, *Principles of Space-Time Adaptive Processing*, ser. Radar, Sonar and Navigation. Institution of Engineering and Technology, 2006.

[134] L. Lightstone, D. Faubert, and G. Rempel, "Multiple Phase Centre DPCA for Airborne Radar," in *Proceedings of the 1991 IEEE National Radar Conference*, 1991, pp. 36–40.

[135] D. Cerutti-Maori and I. Sikaneta, "A Generalization of DPCA Processing for Multichannel SAR/GMTI Radars," *IEEE Transactions on Geoscience and Remote Sensing*, vol. 51, no. 1, pp. 560–572, 2013.

[136] C. Gierull, "Statistical Analysis of Multilook SAR Interferograms for CFAR Detection of Ground Moving Targets," *IEEE Transactions on Geoscience and Remote Sensing*, vol. 42, no. 4, pp. 691–701, 2004.

[137] C. Gierull, "Moving Target Detection with Along-Track SAR Interferometry. A Theoretical Analysis," SAO/NASA Astrophysics Data System, Tech. Rep. AD-A407708, Aug 2002.

[138] A. B. C. da Silva, "A Priori Knowledge-Based Post-Doppler STAP for Traffic Monitoring with Airborne Radar," Ph.D. dissertation, Karlsruhe Institute for Technology, Germany, 2019.

[139] S. Smith, "Space-Time Clutter Covariance Matrix Computation and Interference Subspace Tracking," *Conference Record of The Twenty-Ninth Asilomar Conference on Signals, Systems and Computers*, vol. 2, pp. 1193–1197, 1995.

[140] M. Mertens, M. Ulmke, and W. Koch, "Ground Target Tracking with RCS Estimation Based on Signal Strength Measurements," *IEEE Transactions on Aerospace and Electronic Systems*, vol. 52, no. 1, pp. 123–135, 2016.

[141] S. Joshi, S. Baumgartner, and B. Tings, "Efficient Size and Heading Angle Estimation of Ships in SAR and ISAR Images," *IEEE Geoscience and Remote Sensing Letters*, vol. 21, pp. 1–5, Jan 2024.

[142] A. W. Doerry, "Performance Limits for Maritime Inverse Synthetic Aperture Radar (ISAR)," Sandia National Laboratories, Tech. Rep. SAND2013-9915, Nov 2013.

[143] L. Rosenberg, S. Watts, and M. S. Greco, "Modeling the Statistics of Microwave Radar Sea Clutter," *IEEE Aerospace and Electronic Systems Magazine*, vol. 34, no. 10, pp. 44–75, 2019.

[144] M. Allen and H. Urkowitz, "Radar Detection Performance Limitations in Sea Clutter for Conventional Noncoherent Integration," in *The Record of the 1993 IEEE National Radar Conference*, 1993, pp. 260–263.

[145] F. Luo, D. Zhang, and B. Zhang, "The Fractal Properties of Sea Clutter and Their Applications in Maritime Target Detection," *IEEE Geoscience and Remote Sensing Letters*, vol. 10, no. 6, pp. 1295–1299, 2013.

[146] V. Gracheva and D. Cerutti-Maori, "Multi-Channel Analysis of Sea Clutter for STAP Applications," in *9th EUSAR*, Nuremberg, Germany, 2012, pp. 195–198.

[147] F. Ulaby, R. Moore, and A. Fung, *Microwave Remote Sensing: Radar Remote Sensing and Surface Scattering and Emission Theory*, ser. Artech House Remote Sensing Library. Addison-Wesley, 1981.

[148] P. Lacomme, J.-P. Hardange, J.-C. Marchais, and E. Normant, *Air and Spaceborne Radar Systems: An Introduction.* SciTech Publishing, 2001.

[149] R. Touzi, F. Charbonneau, R. K. Hawkins, and P. W. Vachon, "Ship Detection and Characterization using Polarimetric SAR," *Canadian Journal of Remote Sensing*, vol. 30, pp. 552–559, 2004.

[150] Y. Allard, M. Germain, and O. Bonneau, "Ship Detection and Characterization Using Polarimetric SAR Data," in *Harbour Protection Through Data Fusion Technologies*, E. Shahbazian, G. Rogova, and M. J. DeWeert, Eds. Dordrecht: Springer, 2009, pp. 243–250.

[151] A. M. Raynal and A. W. Doerry, "Doppler Characteristics of Sea Clutter," Sandia National Laboratories, United States, Tech. Rep. SAND2010-3828, June 2010.

[152] K. Ward, R. Tough, and S. Watts, *Sea Clutter: Scattering, the K Distribution and Radar Performance*, ser. Radar, Sonar and Navigation. Institution of Engineering and Technology, 2013.

[153] L. Rosenberg and S. Watts, *Radar Sea Clutter: Modelling and Target Detection*. London, UK: The Institution of Engineering and Technology, 2021.

[154] K. Ward, R. Tough, and S. Watts, *Sea Clutter: Scattering, the K Distribution and Radar Performance*, ser. Radar, Sonar and Navigation. Institution of Engineering and Technology, 2013.

[155] L. Rosenberg and S. Watts, "High Grazing Angle Sea-Clutter Literature Review," Defence Science and Technology Organisation, Tech. Rep. ADA587307, Mar 2013.

[156] K. Ward, "Compound Representation of High Resolution Sea Clutter," *Electronics Letters*, vol. 17, pp. 561–563, August 1981.

[157] M. A. Richards, *Fundamentals of Radar Signal Processing*, 3rd ed. McGraw-Hill Education, 2022.

[158] D. Shnidman, "Determination of Required SNR Values," *IEEE Transactions on Aerospace and Electronic Systems*, vol. 38, no. 3, pp. 1059–1064, 2002.

[159] D. Barton, "Universal Equations for Radar Target Detection," *IEEE Transactions on Aerospace and Electronic Systems*, vol. 41, no. 3, pp. 1049–1052, 2005.

[160] S. Kingsley and S. Quegan, *Understanding Radar Systems*, ser. Electromagnetics and Radar. Institution of Engineering and Technology, 1999.

[161] R. McMillan and I. Kohlberg, "A Probabilistic Model of the Radar Signal-to-Clutter and Noise Ratio for Weibull-Distributed Clutter," in *IEEE National Radar Conference*, June 2010, pp. 882 – 886.

[162] E. Conte and G. Ricci, "Performance Prediction in Compound-Gaussian Clutter," *IEEE Transactions on Aerospace and Electronic Systems*, vol. 30, no. 2, pp. 611–616, 1994.

[163] X.-Y. Hou, N. Morinaga, and T. Namekawa, "Direct Evaluation of Radar Detection Probabilities," *IEEE Transactions on Aerospace and Electronic Systems*, vol. AES-23, no. 4, pp. 418–424, 1987.

[164] J. Marcum, "A Statistical Theory of Target Detection by Pulsed Radar," *IRE Transactions on Information Theory*, vol. 6, no. 2, pp. 59–267, 1960.

[165] A. Papoulis and S. U. Pillai, *Probability, Random Variables, and Stochastic Processes*, 4th ed. McGraw-Hill, 2002.

[166] K. D. Ward, "Application of the K Distribution to Radar Clutter - A Review," in *International Symposium on Noise and Clutter Rejection in Radars and Imaging Sensors*, Kyoto, Japan, Nov 1989, pp. 15–20.

[167] P. Swerling, "Detection of Fluctuating Pulsed Signals in the Presence of Noise," *IRE Transactions on Information Theory*, vol. 3, no. 3, pp. 175–178, 1957.

[168] S. Lei, Z. Zhao, Z. Nie, and Q.-H. Liu, "A CFAR Adaptive Subspace Detector Based on a Single Observation in System-Dependent Clutter Background," *IEEE Transactions on Signal Processing*, vol. 62, no. 20, pp. 5260–5269, 2014.

[169] J. Dias and P. Marques, "Multiple Moving Target Detection and Trajectory Estimation Using a Aingle SAR Sensor," *IEEE Transactions on Aerospace and Electronic Systems*, vol. 39, no. 2, pp. 604–624, 2003.

[170] Z. Jianhong and Y. Jianyu, "Signal-Clutter-Noise Power Ratio of Airborne Wideband Radar," in *International Conference on Communications, Circuits and Systems*, Kokura, Japan, July 2007, pp. 1309–1312.

[171] D. L. Bickel and A. W. Doerry, "On Minimum Detectable Velocity," in *SPIE Radar Sensor Technology XXIII*, vol. 11003, no. 110030N, 2019.

[172] F. Stambouli, M. Limbach, T. Rommel, and M. Younis, "A Cognitive Synthetic Aperture Radar Concept for Tracking and Imaging Operation," in *20th International Radar Symposium*, Ulm, Germany, July 2019, pp. 1–9.

[173] ——, "A Cognitive Maritime SAR Concept for High Altitude Platforms," in *International Radar Conference*, Toulon, France, Sep 2019, pp. 1–6.

[174] F. Stambouli, M. Younis, T. Rommel, M. Limbach, and A. Moreira, "Adaptive Observing SAR with Knowledge-Aided Control: Instrument Design and Dynamic Decision-Making," *to be submitted*, 2025.

[175] G. D. Martino and A. Iodice, Eds., *Maritime Surveillance with Synthetic Aperture Radar*, ser. Radar, Sonar and Navigation. Institution of Engineering and Technology, 2020.

[176] A. Renga, M. Graziano, M. D'Errico, A. Moccia, and A. Cecchini, "SAR-Based Sea Traffic Monitoring: a Reliable Approach for Maritime Surveillance," *Proceedings of SPIE, SAR Image Analysis, Modeling and Techniques XI*, vol. 8179, Sep 2011.

[177] M. S. Bernardi, P. C. Africa, C. de Falco, S. Serra-Capizzano, P. D. Giosa, and M. Crosetto, "On the Use of Interferometric Synthetic Aperture Radar Data for Monitoring and Forecasting Natural Hazards," *Mathematical Geosciences*, vol. 53, no. 8, pp. 1781–1812, 2021. [Online]. Available: https://doi.org/10.1007/s11004-021-09948-8

[178] K.-S. Chen, *Principles of Synthetic Aperture Radar Imaging: A System Simulation Approach*. CRC Press, Dec 2015.

[179] M. Younis, "Digital Beam-Forming for High Resolution Wide Swath Real and Synthetic Aperture Radar," Ph.D. dissertation, Universität Karlsruhe, Germany, July 2004.

[180] A. Farina, A. De Maio, and S. Haykin, *The Impact of Cognition on Radar Technology*. Scitech Publishing, 2017.

[181] W. L. Melvin and J. Scheer, Eds., *Principles of Modern Radar: Advanced Techniques*. Institution of Engineering and Technology, 2012.

[182] S. K. Joshi and S. V. Baumgartner, "Sea Clutter Model Comparison for Ship Detection using Single Channel Airborne Raw SAR Data," in *12th European Conference on Synthetic Aperture Radar*, Aachen, Germany, June 2018, pp. 1–5.

[183] A. Hees, M. Stangl, G. Adamiuk, S. Riegger, and C. Heer, "Status and Future Trends of Active Phased Array Antennas for AIRBUS Space-Borne SAR Systems," in *IEEE International Symposium on Phased Array System and Technology (PAST)*, Waltham, MA, USA, Oct 2019, pp. 1–6.

[184] A. Freeman, G. Krieger, P. Rosen, M. Younis, W. T. K. Johnson, S. Huber, R. Jordan, and A. Moreira, "SweepSAR: Beam-forming on Receive using a Reflector-Phased Array Feed Combination for Spaceborne SAR," in *IEEE Radar Conference*, Pasadena, USA, May 2009, pp. 1–9.

[185] Y. Wang, P. Xing, Q. Xie, L. Li, X. Luo, Y. Du, and B. Zhang, "Underlying Topography and Forest Height Estimation from SAR Tomography Based on a Nonparametric Spectrum Estimation Method with Low Sidelobes," *International Journal of Digital Earth*, vol. 15, pp. 2184–2201, 12 2022.

[186] T. Rommel, S. Huber, M. Younis, and M. Chandra, "Matrix Pencil Method for Topography-Adaptive Digital Beam-Forming in Synthetic Aperture Radar," *IET Radar, Sonar & Navigation*, vol. 15, no. 10, pp. 1195–1208, 2021.

[187] Y. Zhou, W. Wang, Z. Chen, Z. Lv, X. Han, J. Liu, and Q. Zhang, "Adaptive Digital Beamforming for SAR Imaging in Elevation," in *14th European Conference on Synthetic Aperture Radar*, Leipzig, Germany, July 2022.

[188] R. Kinsey, "Phased Array Beam Spoiling Technique," in *IEEE Antennas and Propagation Society International Symposium*, vol. 2, Montreal, QC, Canada, July 1997, pp. 698–701.

[189] M. C. Leifer, "Revisiting a Method of Beam Shaping Using Phase Weights," in *IEEE International Symposium on Phased Array Systems and Technology*, Waltham, MA, USA, Oct 2016.

[190] M. Zonno, F. Bordoni, J. Matar, F. Almeida, M. Sanjuan-Ferrer, M. Younis, M. Rodriguez-Cassola, and G. Krieger, "Sentinel-1 Next Generation: Trade-offs and Assessment of Mission Performance," in *ESA Living Planet Symposium*, May 2019.

[191] R. Hansen, *Phased Array Antennas*, 2nd ed., ser. Wiley Series in Microwave and Optical Engineering. Wiley, 2009.

[192] E. Sharp, "A Triangular Arrangement of Planar-Array Elements that Reduces the Number Needed," *IRE Transactions on Antennas and Propagation*, vol. 9, no. 2, pp. 126–129, 1961.

[193] K. Sayidmarie and Q. Sultan, "Synthesis of Wide Beam Array Patterns Using Quadratic-Phase Excitations," *International Journal of Electromagnetics and Applications*, vol. 3, pp. 127–135, 12 2013.

[194] G. A. T. Warren L. Stutzman, *Antenna Theory and Design*, 3rd ed. Wiley, 2012.

[195] M. Matsuki, Y. Yokota, M. Shibata, A. Karasawa, H. Fujihara, S. Nakamura, Y. Kankaku, T. Motohka, and S. Suzuki, "Phase Spoiling Technique for High Power and Wide Beam in AlOS-4," in *IEEE International Geoscience and Remote Sensing Symposium*, Yokohama, Japan, July 2019, pp. 8326–8327.

[196] D. Cerutti-Maori, J. Klare, A. R. Brenner, and J. H. G. Ender, "Wide-Area Traffic Monitoring With the SAR/GMTI System PAMIR," *IEEE Transactions on Geoscience and Remote Sensing*, vol. 46, no. 10, pp. 3019–3030, 2008.

[197] C. V. Jakowatz, D. Wahl, P. Eichel, D. Ghiglia, and P. Thompson, *Spotlight-Mode Synthetic Aperture Radar: A Signal Processing Approach.* Springer, 1996.

[198] A. Ishimaru, T.-K. Chan, and Y. Kuga, "An Imaging Technique using Confocal Circular Synthetic Aperture Radar," *IEEE Transactions on Geoscience and Remote Sensing*, vol. 36, no. 5, pp. 1524–1530, 1998.

[199] D. Nehru, V. T. Vu, T. Sjogren, and M. Pettersson, "SAR Resolution Enhancement with Circular Aperture in Theory and Empirical Scenario," in *IEEE National Radar Conference*, May 2014, pp. 0001–0006.

[200] S. Baumgartner, G. Krieger, and K.-H. Bethke, "A Large Along-Track Baseline Approach for Ground Moving Target Indication Using TanDEM-X," in *International Radar Symposium (IRS)*, Köln, Deutschland, Sep 2007, p. 5.

[201] F. Stambouli, T. Rommel, M. Younis, M. Limbach, and A. Moreira, "Adaptive Observing SAR with Knowledge-Aided Control: Multi-Mode Interleaving," *to be submitted*, 2025.

[202] A. Freeman, W. Johnson, B. Huneycutt, R. Jordan, S. Hensley, P. Siqueira, and J. Curlander, "The "Myth" of the Minimum SAR Antenna Area Constraint," *IEEE Transactions on Geoscience and Remote Sensing*, vol. 38, pp. 320 – 324, 02 2000.

[203] M. Younis, F. Q. de Almeida, T. Bollian, M. Villano, G. Krieger, and A. Moreira, "A Synthetic Aperture Radar Imaging Mode Utilizing Frequency Scan for Time-of-Echo Compression," *IEEE Transactions on Geoscience and Remote Sensing*, vol. 60, pp. 1–17, 2022.

[204] S. V. Baumgartner and G. Krieger, "A Priori Knowledge-based Post-Doppler STAP for Traffic Monitoring Applications," in *IEEE International Geoscience and Remote Sensing Symposium*, Munich, Germany, July 2012, pp. 6087–6090.

[205] A. Freeman, "On Ambiguities in SAR Design," in *EUSAR 2006: 6th European Conference on Synthetic Aperture Radar*, 2006.

[206] G. Davidson and I. Cumming, "Signal properties of spaceborne squint-mode SAR," *IEEE Transactions on Geoscience and Remote Sensing*, vol. 35, no. 3, pp. 611–617, 1997.

[207] F. Nathanson, J. Reilly, and M. Cohen, *Radar Design Principles: Signal Processing and the Environment*, ser. The SciTech Radar and Defense Series. SciTech Publishing, 1999.

[208] F. E. Nathanson, J. P. Reilly, and M. N. Cohen, *Radar Design Principles: Signal Processing and the Environment*, 2nd ed. New York: McGraw-Hill, Inc., 1990.

[209] F. Le Chevalier and N. Petrov, "Benefits of Space-Time Diversity for Radar," *Comptes Rendus Physique*, vol. 20, no. 3, pp. 183–191, 2019.

[210] H. Liu and Y. M. M. Antar, "Frequency Dependence of Radar Cross-section for Arbitrarily Shaped Targets by Model Measurement," in *Symposium on Antenna Technology and Applied Electromagnetics*, Ottawa, ON, Canada, Aug 1998, pp. 293–296.

[211] F. E. Nathanson and J. P. Reilly, "Frequency Agility for Radar Target Detection and Tracking," *APL Technical Digest*, vol. 9, no. 6, July-August 1970.

[212] J. J. Zhang and A. Papandreou-Suppappola, "MIMO Radar with Frequency Diversity," in *International Waveform Diversity and Design Conference*, Kissimmee, FL, USA, Feb 2009, pp. 208–212.

[213] B. Widrow and S. Stearns, *Adaptive Signal Processing.* New Jersey: Prentice-Hall, 1985.

[214] R. Compton, *Adaptive Antennas: Concepts and Performance.* New York: Prentice-Hall, 1988.

[215] S. Haykin, *Adaptive Filter Theory*, ser. Information and System Sciences Series. Prentice-Hall, 1986.

[216] B. Van Veen and K. Buckley, "Beamforming: a Versatile Approach to Spatial Filtering," *IEEE Acoustics, Speech, and Signal Processing Magazine*, vol. 5, no. 2, pp. 4–24, 1988.

[217] J. L. Krolik and D. H. Carlson, "Adaptive Nulling with a Steered Array," Defense Technical Information Center, Tech. Rep. ADA170537, Jan 1986.

[218] S. Chang, Y. Deng, Y. Zhang, Q. Zhao, R. Wang, and K. Zhang, "An Advanced Scheme for Range Ambiguity Suppression of Spaceborne SAR Based on Blind Source Separation," *IEEE Transactions on Geoscience and Remote Sensing*, vol. 60, pp. 1–12, 2022.

[219] J. Mittermayer and J. Martinez, "Analysis of Range Ambiguity Suppression in SAR by Up and Down Chirp Modulation for Point and Distributed Targets," in *IEEE International Geoscience and Remote Sensing Symposium*, Toulouse, France, July 2003, pp. 4077–4079.

[220] M. M. Abousetta and D. Cooper, "On the Use of Some FMCW Transmission Schemes for Radar Angular Resolution Improvement," in *International Radar Conference*, vol. 1, Brighton, UK, Oct 1992, pp. 335–339.

[221] W. Xu, P. Huang, and W. Tan, "Azimuth Phase Coding by Up and Down Chirp Modulation for Range Ambiguity Suppression," *IEEE Access*, vol. 7, pp. 143 780–143 791, 2019.

[222] G. Krieger, "MIMO-SAR: Opportunities and Pitfalls," *IEEE Transactions on Geoscience and Remote Sensing*, vol. 52, no. 5, pp. 2628–2645, 2014.

[223] G. Krieger, M. Younis, S. Huber, F. Bordoni, A. Patyuchenko, J. Kim, P. Laskowski, M. Villano, T. Romme, P. Lopez-Dekker, and A. Moreira, "MIMO-SAR and the Orthogonality Confusion," in *IEEE International Geoscience and Remote Sensing Symposium*, Munich, Germany, July 2012, pp. 1533–1536.

[224] T. Rommel, S. Huber, A. Patyuchenko, P. Laskowski, M. Younis, and G. Krieger, "An Orthogonal Waveform for MIMO-SAR Applications," in *10th European Conference on Synthetic Aperture Radar*, Berlin, Germany, June 2014, pp. 1–4.

[225] M. Mertens, M. Ulmke, and W. Koch, "Ground Target Tracking with RCS Estimation Based on Signal Strength Measurements," *IEEE Transactions on Aerospace and Electronic Systems*, vol. 52, pp. 205–220, 02 2016.

[226] K. Åström and B. Wittenmark, *Adaptive Control*, 2nd ed. New York: Dover Publications, 2008.

[227] M. Kokar, K. Baclawski, and Y. Eracar, "Control Theory-Based Foundations of Self-Controlling Software," *IEEE Intelligent Systems and their Applications*, vol. 14, pp. 37 – 45, June 1999.

[228] S.-Y. Jeon, T. Kraus, U. Steinbrecher, G. Krieger, and M. Villano, "Experimental Demonstration of Nadir Echo Removal in SAR Using Waveform Diversity and Dual-Focus Postprocessing," *IEEE Geoscience and Remote Sensing Letters*, vol. 19, pp. 1–5, 2022.

[229] R. Marler and J. Arora, "The Weighted Sum Method for Multi-objective Optimization: New Insights," *Structural and Multidisciplinary Optimization*, vol. 41, pp. 853–862, June 2010.

[230] A. Keller, *Multi-Objective Optimization in Theory and Practice I: Classical Methods*. Bentham Science Publishers, 2017.

[231] K. Miettinen, *Nonlinear Multiobjective Optimization*, ser. International Series in Operations Research & Management Science. Springer Science & Business Media, 1999.

[232] A. E. Mitchell, G. E. Smith, K. L. Bell, A. J. Duly, and M. Rangaswamy, "Fully Adaptive Radar for Variable Resolution Imaging," in *International Conference on Radar Systems*, Belfast, Oct 2017, pp. 1–6.

[233] M. Marghany, *Synthetic Aperture Radar Imaging Mechanism for Oil Spills*, ser. Gulf Professional Publishing. Elsevier Science and Technology, 2019.

[234] J. H. G. Ender, C. H. Gierull, and D. Cerutti-Maori, "Improved Space-Based Moving Target Indication via Alternate Transmission and Receiver Switching," *IEEE Transactions on Geoscience and Remote Sensing*, vol. 46, no. 12, pp. 3960–3974, 2008.

[235] A. B. C. da Silva and S. V. Baumgartner, "Novel Post-Doppler STAP with a Priori Knowledge Information for Traffic Monitoring Applications: Basic Idea and First Results," *Advances in Radio Science*, vol. 15, pp. 77–82, 2017.

[236] R. Horn, A. Nottensteiner, and R. Scheiber, "F-SAR - DLR's Advanced Airborne SAR System Onboard DO228," in *7th European Conference on Synthetic Aperture Radar*, Friedrichshafen, Germany, June 2008, pp. 1–4.

[237] S. Baumgartner and S. Joshi, "Promising Techniques for Future Maritime Surveillance Demonstrated With DLR's Airborne Radar Sensors F-SAR and DBFSAR," in *ESA Advanced RF Sensors and Remote Sensing Instruments (ARSI)*, Nov 2019.

[238] D. Thois and M. Younis, "A Synthetic Aperture Radar Imaging Mode Syntax," in *Workshop on Advanced RF Sensors and Remote Sensing Instruments*, Noordwijk, The Netherlands, November 2024, (Submitted).

[239] M. Younis, F. Q. D. Almeida, M. Villano, S. Huber, G. Krieger, and A. Moreira, "Digital Beamforming for Spaceborne Reflector-Based Synthetic Aperture Radar, Part 2: Ultrawide-Swath Imaging Mode," *IEEE Geoscience and Remote Sensing Magazine*, vol. 10, no. 4, pp. 10–31, 2022.

[240] M. Jirousek, M. Peichl, S. Anger, S. Dill, and M. Limbach, " The DLR High Altitude Platform Synthetic Aperture Radar Instrument HAPSAR ," in *European Conference on Synthetic Aperture Radar*, Munich, Germany, Apr 2024.

[241] A. Heinzel, M. Peichl, E. Schreiber, S. Dill, and M. Engel, "DRONAR - ein UHF-Breitbandradar auf Drohnen," in *Angewandte Forschung fÃ¼r Verteidigung und Sicherheit in Deutschland*, Bonn, Germany, March 2020.

[242] J. Breckling, Ed., *The Analysis of Directional Time Series: Applications to Wind Speed and Direction*, ser. Lecture Notes in Statistics. Berlin, Germany: Springer, 1989, vol. 61.

[243] P. Capece and A. Torre, *SAR Antennas*. John Wiley & Sons, Ltd, 2012, ch. 13, pp. 511–547.

[244] G. D. Callaghan, "Wide-swath space-borne SAR: Overcoming the trade-off between swath-width and resolution," Ph.D. dissertation, University of Queensland's, Uk, 1999.

[245] M. Younis and W. Wiesbeck, "SAR with Digital Beamforming on Receive Only," in *IEEE International Geoscience and Remote Sensing Symposium*, Hamburg, Germany, June 1999, pp. 1773–1775.

[246] N. Gebert, G. Krieger, and A. Moreira, "Digital Beamforming for HRWS-SAR Imaging: System Design, Performance and Optimization Strategies," in *IEEE International Symposium on Geoscience and Remote Sensing*, Denver, CO, USA, July 2006, pp. 1836–1839.

[247] G. Krieger, N. Gebert, and A. Moreira, "Multidimensional Waveform Encoding: A New Digital Beamforming Technique for Synthetic Aperture Radar Remote Sensing," *IEEE Transactions on Geoscience and Remote Sensing*, vol. 46, no. 1, pp. 31–46, Jan 2008.

[248] S. Haykin, "Cognitive Radar: a Way of the Future," *IEEE Signal Processing Magazine*, vol. 23, no. 1, pp. 30–40, Jan 2006.

[249] J. R. Guerci, R. M. Guerci, M. Ranagaswamy, J. S. Bergin, and M. C. Wicks, "CoFAR: Cognitive Fully Adaptive Radar," in *IEEE Radar Conference*, Cincinnati, OH, USA, May 2014, pp. 0984–0989.

[250] S. Haykin, A. Zia, I. Arasaratnam, and Y. Xue, "Cognitive Tracking Radar," in *IEEE Radar Conference*, Arlington, VA, USA, May 2010, pp. 1467–1470.

[251] A. B. C. da Silva and S. V. Baumgartner, "STAP Moving Target Position Estimation Accuracy Improvement and False Detection Recognition Using A Priori Road Information," in *18th International Radar Symposium*, Prague, Czech Republic, June 2017, pp. 1–7.

[252] S. Huber, F. Q. de Almeida, M. Villano, M. Younis, G. Krieger, and A. Moreira, "Tandem-L: A Technical Perspective on Future Spaceborne SAR Sensors for Earth Observation," *IEEE Transactions on Geoscience and Remote Sensing*, vol. 56, no. 8, pp. 4792–4807, Aug 2018.

[253] A. Farina and P. Neri, "Multitarget Interleaved Tracking for Phased-Array Radar," *IEE Proceedings F - Communications, Radar and Signal Processing*, vol. 127, no. 4, pp. 312–318, 1980.

[254] F. Stambouli, M. Limbach, T. Rommel, and M. Younis, "A Cognitive Maritime SAR Concept for High Altitude Platforms," in *2019 International Radar Conference (RADAR)*, Toulon, France, Sep 2019, pp. 1–6.

[255] S. Brusch, S. Lehner, T. Fritz, M. Soccorsi, A. Soloviev, and B. van Schie, "Ship Surveillance With TerraSAR-X," *IEEE Transactions on Geoscience and Remote Sensing*, vol. 49, no. 3, pp. 1092–1103, 2011.

[256] D. Cerutti-Maori, I. Sikaneta, and C. Gierull, "Ship Detection with Spaceborne Multi-Channel SAR/GMTI Radars," in *9th European Conference on Synthetic Aperture Radar*, Nuremberg, Germany, Apr 2012, pp. 400–403.

[257] J. R. Guerci, "Next Generation Intelligent Radar," in *IEEE Radar Conference*, Waltham, MA, USA, Apr 2007, pp. 7–10.

[258] M. Jin and M. Chen, "Analysis and Simulation for a Spotlight-Mode Aircraft SAR in Circular Flight Path," in *IEEE International Geoscience and Remote Sensing Symposium*, Tokyo, Japan, July 1993, pp. 1777–1780.

[259] S.-M. Hong and Y.-H. Jung, "Optimal Scheduling of Track Updates in Phased Array Radars," *IEEE Transactions on Aerospace and Electronic Systems*, vol. 34, no. 3, pp. 1016–1022, 1998.

[260] T. Nguyen and J. Branke, "Evolutionary Dynamic Optimization: A Survey of the State of the Art," *Swarm and Evolutionary Computation*, vol. 6, pp. 1–24, Oct 2012.

[261] M. Xu, N. Du, Z. Li, H. Yang, J. Wu, and J. Yang, "Cognitive SAR Waveform Design Method Based on Joint Optimization Criteria," in *6th Asia-Pacific Conference on Synthetic Aperture Radar (APSAR)*, Xiamen, China, Nov 2019, pp. 1–4.

[262] K. Aberman, S. Aviv, and Y. C. Eldar, "Adaptive Frequency Allocation in Radar Imaging: Towards Cognitive SAR," in *IEEE Radar Conference*, Seattle, WA, USA, May 2017, pp. 1348–1351.

[263] A. Maio, A. Farina, and G. Foglia, "Target Fluctuation Models and their Application to Radar Performance Prediction," *IEE Proceedings on Radar, Sonar and Navigation*, vol. 151, pp. 261 – 269, Nov 2004.

[264] S. Hovanessian, "Signal-to-Noise Ratio Calculations in Pulse and Pulse Doppler Radars," *IEEE Transactions on Aerospace and Electronic Systems*, vol. AES-17, no. 5, pp. 722–724, 1981.

[265] K. Sayidmarie and Q. Sultan, "Synthesis of Wide Beam Array Patterns Using Quadratic-Phase Excitations," *International Journal of Electromagnetics and Applications*, vol. 3, pp. 127–135, December 2013.

[266] W. Pitz and D. Miller, "The TerraSAR-X Satellite," *IEEE Transactions on Geoscience and Remote Sensing*, vol. 48, no. 2, pp. 615–622, 2010.

[267] H. M. Lyon, G. Inalhan, D. Bourne, and A. Tsourdos, "High-Altitude UAS Pseudo-Satellites: Architecture for End-to-End Military Communications," in *American Institute of Aeronautics and Astronautics Scitech Forum*, Jan 2021, pp. 2021–0521.

A ADOB-SAR Optimization Objective Function

The objective function of the ADOB-SAR decision-maker is based on a cost function minimizing the deviation from ideal values, as described in Chapter 6. The decision variables are the control parameters defined as the vector

$$X_k = \left[x_{k_1}, ..., x_{k_M}\right] = \left[P_\mathrm{t}, B, T_\mathrm{D}, N_\mathrm{CPI}, \mathrm{PRF}, \tau_\mathrm{p}\right]. \tag{A.1}$$

Substituting it in the optimization problem derived in (6.43) gives

$$\begin{aligned} X_k = \arg\min\Bigg\{ & w_1 \frac{\mid P_\mathrm{t} - P_\mathrm{t}^\star \mid}{P_\mathrm{t}^\star} + w_2 \frac{\mid B - B^\star \mid}{B^\star} + w_3 \frac{\mid T_\mathrm{D} - T_\mathrm{D}^\star \mid}{T_\mathrm{D}^\star} \\ & + w_4 \frac{\mid N_\mathrm{CPI} - N_\mathrm{CPI}^\star \mid}{N_\mathrm{CPI}^\star} + w_5 \frac{\mid \mathrm{PRF} - \mathrm{PRF}^\star \mid}{\mathrm{PRF}^\star} + w_6 \frac{\mid \tau_\mathrm{p} - \tau_\mathrm{p}^\star \mid}{\tau_\mathrm{p}^\star} \Bigg\}. \end{aligned} \tag{A.2}$$

The first constraint is related to the adaptive spatial resolution control defined in Section 6.1.1. It depends on specific target parameters of the vector $Y_k = \left[A_\mathrm{t}, R_\mathrm{t}, \sigma_\mathrm{t}, \theta_\mathrm{it}\right]$ and is given by

$$\frac{A_\mathrm{t}}{N_\mathrm{px1}} \leq \delta_\mathrm{a}(R_\mathrm{t}, T_\mathrm{D})\, \delta_\mathrm{r}(\theta_\mathrm{it}, B) \leq \frac{A_\mathrm{t}}{N_\mathrm{px2}}.. \tag{A.3}$$

Substituting (6.3) and (6.4) in (A.3) leads to

$$\frac{A_\mathrm{t}}{N_\mathrm{px1}} \leq \frac{\lambda R_\mathrm{t}}{2 v_\mathrm{p} T_\mathrm{D}} \frac{c_0}{2B \sin\theta_\mathrm{i}} \leq \frac{A_\mathrm{t}}{N_\mathrm{px2}}.. \tag{A.4}$$

The second constraint relates the azimuth resolution to the range resolution by a desired factor r_D given by the user. It is set to

$$\frac{\delta_\mathrm{a}(R_\mathrm{t}, T_\mathrm{D})}{\delta_\mathrm{r}(\theta_\mathrm{it}, B)} = r_\mathrm{D}. \tag{A.5}$$

The third constraint is based on the SCNR equation and the desired energy level required for the requested operation and is given by

$$\frac{\sigma_\mathrm{t} N_\mathrm{p}}{\frac{\lambda c_0 R_\mathrm{t} \sigma_0 \mathrm{PRF}}{4 v_\mathrm{p} \sin\theta_\mathrm{it} B} + \frac{(4\pi)^3 K T_\mathrm{s} F L R_\mathrm{t}^4}{P_\mathrm{t} \lambda^2 G_\mathrm{tx} G_\mathrm{rx} \tau_\mathrm{p}}} \geq \mathrm{SCNR}_\mathrm{D}, \tag{A.6}$$

according to (6.6).

The fourth constraint is related to the NESZ and is given by

$$\frac{4(4\pi)^3 K T_\mathrm{s} F L v_\mathrm{p}}{\lambda^3 c_0} \sin\theta_\mathrm{it} R_\mathrm{t}^3 \frac{B}{P_\mathrm{t} G_\mathrm{tx} G_\mathrm{rx} \tau_\mathrm{p} \,\mathrm{PRF}} \leq \mathrm{NESZ_D}\,. \tag{A.7}$$

The fifth constraint limits the overall duty cycle of the sensor taking into consideration all the modes and tiers in operation and the maximum duty cycle that should not be exceeded

$$d_{c_k} + \sum_{l=1}^{n_\mathrm{op}} d_{c_l} \leq d_{c_\mathrm{max}}. \tag{A.8}$$

The last constraint gives the upper and lower bound of each control parameter, as defined by the instrument design, and is given by

$$\begin{aligned}
&P_\mathrm{t}^L \leq P_\mathrm{t} \leq P_\mathrm{t}^U \\
&B^L \leq B \leq B^U \\
&T_\mathrm{D}^L \leq T_\mathrm{D} \leq T_\mathrm{D}^U \\
&N_\mathrm{CPI}^L \leq N_\mathrm{CPI} \leq N_\mathrm{CPI}^U \\
&\mathrm{PRF}^L \leq \mathrm{PRF} \leq \mathrm{PRF}^U \\
&\tau_\mathrm{p}^L \leq \tau_\mathrm{p} \leq \tau_\mathrm{p}^U\,.
\end{aligned} \tag{A.9}$$

Other constraints can be used depending on the desired performance metrics and decision criteria applied to the ADOB-SAR system.